Fabrication and Characterization of Pt and CeO_x Nanowire Interface for Improvement of Methanol Electro-oxidation Activity and Oxygen Reduction Reaction Activity on Pt

Thesis

Submitted by

Shipra Chauhan

Graduate School of Chemical Sciences and Engineering,
Hokkaido University
2014

Acknowledgements

I really thank Prof. Toshiyuki Mori for giving me a great chance to perform the interesting subject, his valuable comments, suggestions, discussions and his constant encouragement during the period of this research project.

Hearty thanks are due to Prof. Kohei Uosaki, Prof. Kei Murakoshi, and Prof. Kazuki Sada and Prof. Kazuhisa Azumi, who acted as examiner of the doctoral dissertation, for their helpful and useful suggestions.

Grateful acknowledgement is made to Dr Takuya Masuda , National Institute for Materials Science, for his suggestion, discussion and encouragements.

Special thanks to the Prof John Drennan , University of Queensland , Australia, Prof Katsuhiko Ariga, National Institute for Materials Science and Dr Jonathan Hill, National Institute for Materials Science for their encouragement and help, in my doctoral course research.

I would sincerely like to thanks Dr Gary James Richards, Tsukuba University for his suggestion and discussions.

My thanks are due to Dr Keisuke Fugane, Dr Pengfei Yan, Mr Hirotaka Togasaki, Ms Yuanyuan Wu, Mr Muhammad F. Ramadhani, Dr Breta Smid and all the students who studied together with me at the Ionics Materials Chemistry Laboratory.

I am grateful to Ms Atsuko Nagano, Ionics Materials Chemistry Laboratory for her kind help and support.

I am grateful to Dr. Uemura, Dr. Nemoto, Dr. Iiyama and Dr. Fujita for their constructive

support and assistance for the use of MANA common facilities such as SEM, EDX, TEM, N_2 sorption, Raman and other facilities. I also wish to thank Dr. Wada and Dr. Sato, NIMS XRD maintenance staff for their assistance with the XRD measurements.

For the financial support, I would like to thank the MANA Project and the NIMS. I also would like to thank Hokkaido University for encouragement by giving me the 50% tuition fee waiver throughout my Ph. D course.

Last but not least I would like to thank my parents and my sisters for their constant support, encouragement and understanding throughout my Ph.D course.

Shipra Chauhan

Tsukuba

June,2014

Contents

Chapter 1 Introduction ---1

1.1 Introduction of fuel cell ---1

1.1.1 Advantage of Fuel cell ---1

1.1.2 Theory of fuel cells ---3

1.1.2.1 A basic principle and efficiency of fuel cells ---3

1.1.2.2 Fuel cell electrochemistry ---8

1.1.3 Type of fuel cells ---9

1.1.3.1 Alkaline fuel cells (AFCs) ---10

1.1.3.2. Phosphoric Acid Fuel Cell (PAFC) ---11

1.1.3.3 Polymer Electrolyte Fuel Cells (PEFCs) ---13

1.1.3.5 Molten carbonate fuel cells (MCFCs) ---17

1.1.3.6. Solid Oxide fuel cells (SOFCs) ---18

1.2.1 Fuel cell components ---19

1.2.2.1 Membrane electrolyte ---20

1.2.2.2 Electrode-catalyst layer ---21

1.2 Electrochemistry and previously reported mechanism of CO poisoning on Pt ---23

1.3 Electrochemistry and previously reported mechanism of Oxygen Reduction Reaction (ORR) ---25

1.5 Possibility of oxide as promoter or support for electro-catalysts ---28

1.6. Fabrication of Ceria nanowire ---29

1.6.1. Soft template technique ---29

1.6.2. Hard template technique ---30

1.6.3. Non-template Technique ---31

1.7. Application of CeO_x nano-materials as promoter or support for electro-catalysts ---32

1.7.1. Carbon mono-oxide oxidation reaction ---32

1.7.2. Methanol oxidation reaction ---33

1.7.3. Limitation of previously reported electro-catalysts ---33

1.8. Outline of Thesis ---37
1.9. Outline of present thesis ---39

References ---40

Chapter 2 Experimental ---57

2-1 Material Used ---58
2-2 Synthesis of Electro catalyst ---58
2-2-1 Synthesis of Ceria Nanowire ---58
2-2-2 Synthesis of Pt loaded Ceria Nanowire ---58
2-3 Characterisation ---59
2-3-1 Morphology By Scanning Electron Microscopy(SEM) ---59
2-3-2 X-ray differaction (XRD) ---60
2-3-3 Inductively Coupled Plasma Mass Spectroscopy (ICP-MS) ---60
2-3-4 X-ray Photoelectron Spectroscopy (XPS) ---62
2-3-5 Transmission Electron Microscopy (TEM) ---63
2-3-6 Electron Energy Loss Spectroscopy (EELS) ---64
2-3-7 Electrochemical Analysis ---65
2-3-7-1 Anodic property measurement by methanol electro-oxidation reaction ---66
2-3-7-2 Cathodic property measurement by ORR (Oxygen Reduction Reaction) ---68
2-4 Atomistic simulation ---71
References ---74

Chapter 3 Fabrication of Pt loaded ceria nanowire interface for electrocatalysts ----79

3-1 Introduction ----79

3-2 Previous reported Synthesis process for ceria nanowire ----80

3-3 Optimization of fabrication condition of fine CeO_x nanowires ---81

3-3-1 Growth process analysis of CeO_x nanowire ---81

3-3-2 Influence of reaction time and reaction temperature

on change of aspect ratio of CeO_x nanowire ---82

3-3-3 Effect of urea ---91

3-3-4 Role of soft template CTAB ---93

3-3-5 Effect of water ---95

3-3-6 Formation process of CeO_x nanowire ---97

3-4 Pt particles loading on CeO_x nanowire ---99

3-5 Physical characterization of Pt loaded CeO_x nanowire ---101

3-5-1 Crystal phase identification by XRD ---101

3-5-2 Surface chemical state of Pt loaded CeO_x nanowire ---103

3-5-3 Effect of pre-treatment on surface of Pt-CeO_x nanowire/C ---104

3-5-4 Microanalysis of Pt/Ceria nanowire electrocatalyst ---106

3-7 Conclusion ---113

References ---115

Chapter 4 Improvement of anodic property (methanol electro-oxidation) on Pt loaded CeO_x nanowire/C ---120

4-1. Introduction ---120

4-2 Results and Discussion ---121

4-2-1 EASA observed for electrochemically pretreated Pt loaded CeO_x nanowire/C ....---121

4.2.1(a) Microscopic interface structure analysis of the electrochemically pre-treated Pt-CeO_x nanowire/ C electrocatalysts ---124

4-2-2 EASA observed for electrochemically pretreated Pt loaded CeO_x nanowire/C ---129

4-2-3 Comparison of EASA with other electro catalyst with respect to loading amount of Pt on support ---132

4-2-3 Methanol electro-oxidation on Pt loaded CeO_x nanowire/C ---136

4-3 Conclusion ---145

References ---149

Chapter 5 Improvement of ORR activity Pt loaded CeO_x nanowire/C electrocatalyst--157

5-1. Introduction ---157

5-2. Results and discussion ---158

5-2-1. Interfacial structural features of Pt loaded CeO_x nanowire/C ---158

5-2-1 (a). Cerium M-edge peak analysis ---158

5-2-1 (b). Oxygen K-edge peak analysis ---160

5-2-2 Oxygen Reduction Reaction (ORR) Activity on Pt/ CeO_x nanowire/C ---162

5-3 Conclusion ---182

References ---185

Chapter 6 Defect structural analysis of Pt loaded CeO_x nanowire interface by using atomistic simulation method ---188

6-1. Introduction ---188

6-2 Results and Discussion ---188

6-2-1 Defect structure simulation in Pt-CeO_x nanowire interface ----188

6-2-2 Development of defect clusters in Pt-CeO_x nanowire interface ---195

6-3 Conclusion ---225

References ---197

Chapter 7 Conclusion ---228

Chapter 1 Introduction

1.1 Introduction of fuel cell

1.1.1 Advantage of Fuel cell

Fuel cells are electrochemical devices that generate direct current (DC) electricity by converting the chemical energy of fuel and oxidant to electrical energy. The basic set up of a fuel cell consists of three compartments, which are the anode, cathode and electrolyte. The fuel is oxidized on the anode and the oxidant is reduced on the cathode. Produced ions travel from one electrode to another them through the electrolyte, which are basically charge carriers. Finally, DC current is collected via an external circuit of the cell when the ion migration occurs in the electrolyte.

It is well-known that fuel energy conversion to mechanical work in heat engines is limited by the reversible Carnot-cycle efficiency (about 70% limits) due to irreversibility of combustion process alone. The fuel energy conversion to mechanical work in the internal combustion engine includes several steps (i.e. Fig.1-1(a)). A combustion of fuel converts chemical energy of fuel into heat, then the steam is created by this heat energy. The steam is used for operation of a turbine engine that converts thermal energy into mechanical energy. Finally the electricity is generated by using

aforementioned mechanical energy. In contrast, the fuel cell converts the primary energy which is stored in a fuel (e.g. hydrogen) into DC electricity directly (Fig.1-1(b)).

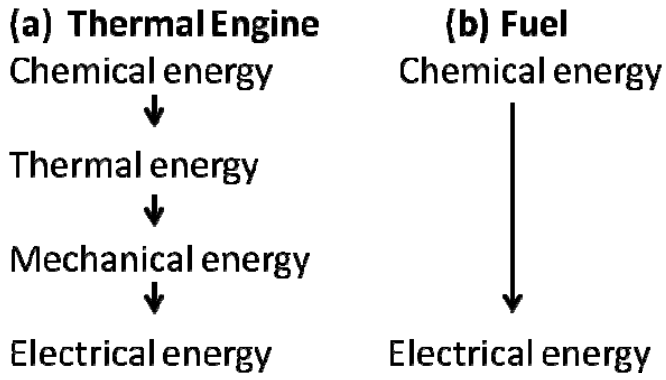

Figure 1-1 Electricity generations for a thermal engine (a) and a fuel cell (b).

The fuel cells have second advantage over the internal heat engine which produces carbon dioxide gas. The carbon dioxide produced by the combustion of a fossil fuel with oxygen gives rise to “greenhouse effect”, which will finally cause "global warming”[1]. On the other hand, the hydrogen fuel cell reaction for generating electricity is clean. An important second advantage of fuel cells is environment friendly. Other advantages are its quiet operation without mechanical vibration and its high efficiency as compared with the internal combustion engine. This point about efficiency is explained in the section of ‘1.1.2 Theory of fuel cells’ in detail.

1.1.2 Theory of fuel cells

1.1.2.1 A basic principle and efficiency of fuel cells[2,3]

The basic fuel cell reactions occurring in the hydrogen fuel cell is the water formation reaction using oxygen and hydrogen. This chemical reaction for formation of water is expressed by Eq.(1-1) to Eq.(1-3).

At the anode: $H_2 \longrightarrow 2H^+ + 2e^-$ **(1-1)**

At the cathode: $1/2O_2 + 2H^+ + 2e^- \longrightarrow H_2O$ **(1-2)**

Overall: $H_2 + 1/2O_2 \longrightarrow H_2O$ **(1-3)**

Thereby, two electrons are transferred from the hydrogen to the oxygen (i.e. from the anode to the cathode) per one molecule of water generated. This means that the hydrogen is oxidized on the anode, while the oxygen is reduced on the cathode in the fuel cells. The overall reaction (Eq.(1-3)) is the same reaction of hydrogen combustion.

$H_2 + 1/2O_2 \rightarrow H_2O + heat$ **(1-4)**

$H_2 + 1/2O_2 \rightarrow H_2O\ (l) + 286\ kJmol^{-1}$ **(1-5)**

The enthalpy in Eq.(1-5) (i.e. 286 kJ mol^{-1} at 25ºC) is called the hydrogen's heating value (or higher heating value: HHV). In contrast, the less heat energy will be created if the product (i.e. water) is the vapor form. This is also called as hydrogen's lower heating value (i.e. LHV).

The energy diagram of these reactions was summarized in **Fig. 1-3**. Under reversible conditions, the total free energy ⊿G of the reaction (i.e. Eq.(1-5)) is converted into electrical energy.

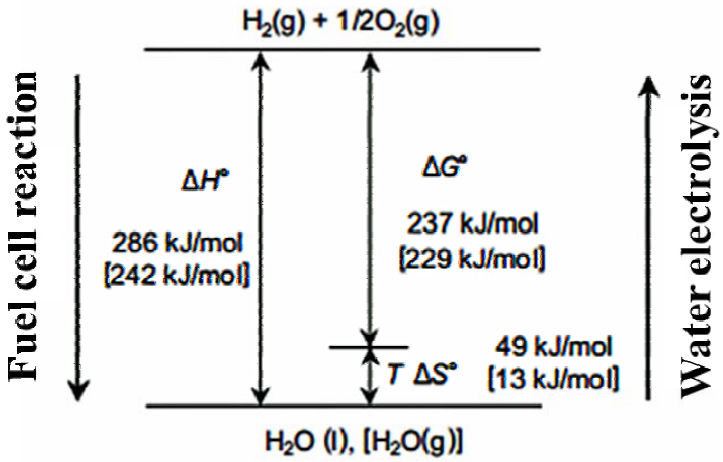

Figure 1-2 Energy diagram for the water formation reaction (25ºC) [3(a)].

The hydrogen's heating value converting to electricity in the fuel cells corresponds to Gibbs free energy and it is given by the following equation (1-6):

$$\Delta G = \Delta H - T\Delta S \qquad (1\text{-}6)$$

where ⊿G is Gibbs free energy, ⊿H is enthalpy, T is absolute temperature, and ⊿S is entropy.

The ⊿G change in the fuel cell reaction is related to the electro-motive force (i.e. emf) expressed by the Eq.(1-7) :

$$E = -\Delta G / zF \qquad (1\text{-}7)$$

where F is the Faraday constant (96485 C mol^{-1}) and z is the number of exchanged electrons in the overall reaction (z=2). The emf energy (emf E) corresponds to terminal potential of fuel cells.

Since the free energy ⊿ G is a function of temperature, the term of emf E has temperature dependence. Therefore, the change of the emf E with temperature T at constant pressures p is given by Eq. (1-8):

$$\mathbf{(dE/dT)_p = \triangle S/ zF} \qquad \mathbf{(1\text{-}8)}$$

Also, the emf E depends on the activity of the compounds involved in the reaction, Eq.(1-8) can be converted as Eq.(1-9) by using Nernst equation[4]

$$\mathbf{E = E^* - RT/ zF \ ln \ \underline{\alpha_{prod.}}/ \alpha_{react.}} \qquad \mathbf{(1\text{-}9)}$$

where E^* is the obtained emf E which is changed by the purity of the reactants and products at given temperature,

α_{react} = Activity of reactant,

α_{prod}= Activity of product.

The corresponding activities α_{react} and α_{prod} are equal to 1 if reactants and products are pure. R is the ideal gas constant (8.314 $Jmol^{-1}K^{-1}$). As ⊿S is negative, the cell potential decreases with increasing temperature, according to equation (1-8). As a result, the emf E can be calculated as a function of temperature. At the operating temperature of the

solid oxide fuel cell (SOFC) at around 800 °C, for example, the theoretical terminal potential is 1.0V (based on gaseous product water: LHV). This means that SOFC single cell is DC power supply which operates under low applied potential such as 1V. As mentioned in '1.1.1 Advantage of Fuel cell', the important advantage of fuel cell is its high efficiency. In general, the energy conversion efficiency is described by Eq. (1-9).

Efficiency ε = (obtained electrical energy) / (energy in supplied fuel) **(1-9)**

Where energy in supplied fuel is expressed by $\triangle H$ and usually, $\triangle H$ (HHV based on liquid product water) is used for calculation of efficiency of fuel cell. In contrast, $\triangle H$ (LHV based on liquid product water) is used for the calculation of efficiency of thermal engine.

To compare the fuel cell with the thermal engine, the thermal efficiency of thermal engine is given by Eq. (1-10).

Thermal efficiency (ε_c) = ($T_2 - T_1$) / T_2 **(1-10)**

where ε_c is theoretical thermal efficiency of ideal thermal engine (i,e, Carnot cycle) , T_2 is absolute temperature of high temperature heat source, T_1 is absolute temperature of low temperature heat source.

On the other hand, the theoretical efficiency of fuel cell generator is calculated by Eq.(1-11).

Theoretical efficiency of fuel cell (ε_{fc}) = ($\triangle$H - T$\triangle$S) / $\triangle$H

= $\triangle$G / $\triangle$H **(1-11)**

Equation 1-11 suggests that the obtained electrical energy from fuel cell is decreased at higher temperature. And the theoretical efficiency of fuel cell is decreased at higher temperature.

The calculated theoretical efficiency of fuel cell at 25ºC is approximately 83% by using HHV data. However, the real efficiency of fuel cell is not so high because of slow kinetics of electrode reaction and slow diffusion of mobile ion in electrolyte at low temperature. In contrast, the theoretical efficiency of fuel cells can be improved by using combined power generation system such as gas turbine and fuel cells. In order to maximize the observed efficiency of fuel cells, the design of high quality electrode and electrolyte in the fuel cells and design of combined power generator are required[5-8].

1.1.2.2 Fuel cell electrochemistry

In the case of actual fuel cell device, the ideal open circuit voltage (OCV) of the fuel cell which is around 1.2V is not attained. The OCV which is observed at zero current density is around 1.0V in the PEFC under usual operating conditions (p = 1-3bar, T = 60-80°C). This indicates that the actual cell potentials are always smaller than the theoretical ones due to irreversible losses. Voltage losses in operational fuel cells are caused by ohmic losses and polarization losses (i.e. over-potentials).

Figure 1-3 shows the current-cell potential characteristics of fuel cells which are formed by subtracting losses from the theoretical potential (E_0).

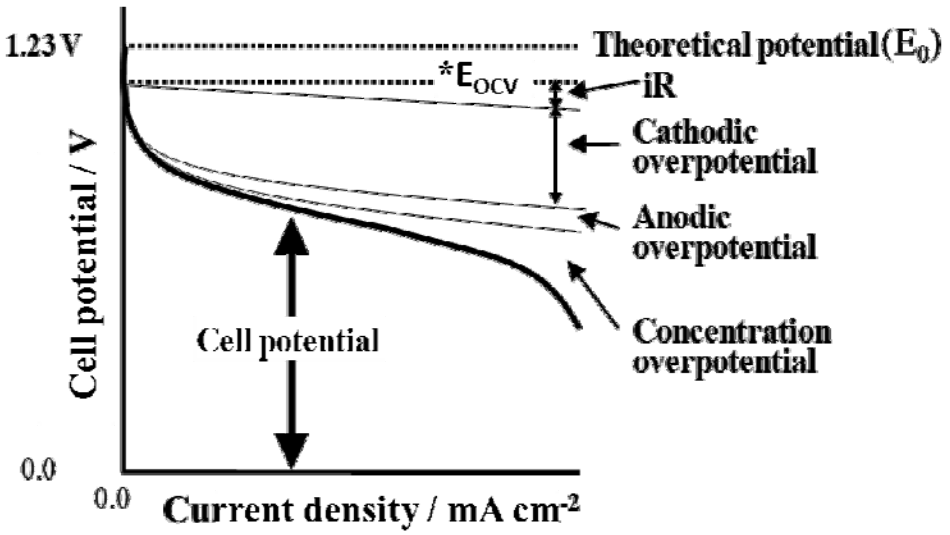

Figure 1-3 Typical current-cell potential characteristics of polymer type fuel cells; *E_{OCV}: open circuit voltage (potential) observed for fuel cells[3 (b)].

This figure indicates that the cell potential (E_{CELL}) is presented by Eq. (1-12):

$$\mathbf{E_{CELL} = E_0 - \eta_a - \eta_c - \eta_m - iR} \qquad \mathbf{(1\text{-}12)}$$

Where iR is Ohmic loss due to the internal resistance of fuel cell, $\boldsymbol{\eta}_a$ and $\boldsymbol{\eta}_c$ are anodic and cathodic over-potentials, respectively. It is attributable to slow kinetics of the electrochemical reaction, and $\boldsymbol{\eta}_m$ is concentration over-potential due to the transportation of species (H_2, O_2 and H^+).

As demonstrated in Figure 1-3, the fuel cell performance is conspicuously influenced by the cathodic over-potential ($\boldsymbol{\eta}_c$). However, the anodic over-potential ($\boldsymbol{\eta}_a$) is drastically increased when carbon monoxide (CO) molecules adsorbed on Pt electrode. It is called 'CO poisoning'. If the fuel obtained from biomass, coal, and petroleum distillates includes CO gas and its concentration will be more than 5ppm. Aforementioned CO poisoning effect will be serious for fuel cell performance. In this case, the CO tolerance of Pt should be improved for development of fuel cell devices.

1.1.3 Type of fuel cells

There is a variety of fuel cell types, which are differ from operating temperature, electrolyte used and fuel[5-8]. Mostly, the fuel cell performance is influenced by the operation temperature.

1.1.3.1 Alkaline fuel cells (AFCs) [5(a)]

The alkaline fuel cell (AFC) was developed in the beginning of 1960 for space application and one of the first modern fuel cells. This development was based, in large part, on the work initiated by Francis Thomas Bacon in the 1930s. In 1952, the performance of a 5-kW AFC which was operated by using H_2 and O_2 was demonstrated publicly.

Alkaline fuel cells use an electrolyte that is an aqueous (water-based) solution of potassium hydroxide (KOH) retained in a porous stabilized matrix. The concentration of KOH can be varied with the fuel cell operating temperature, which ranges from 60°C to 220°C. The standard operation temperature is around 70°C. The charge carrier for an AFC is the hydroxyl ion (OH^-) that migrates from the cathode to the anode where they react with hydrogen to produce water and electrons. Water formed at the anode migrates back to the cathode to regenerate OH^-. Eq.(1-13) and Eq.(1-14) depict the operating configuration of the H_2/O_2 alkaline fuel cell and a H_2/air cell . In both cases, the anode and cathode reactions can be expressed by Eq.(1-13) and Eq. (1-14), respectively:

At the anode: $\mathbf{H_2 + 2OH^- \longrightarrow 2H_2O + 2e^-}$ **(1-13)**

At the cathode: $\mathbf{\frac{1}{2}O_2 + H_2O + 2e^- \longrightarrow 2OH^-}$ **(1-14)**

The equivalent overall cell reaction is:

$$H_2 + ½O_2 \longrightarrow H_2O + \text{electric energy} + \text{heat} \quad (1\text{-}15)$$

Advantages: AFC has excellent performance on hydrogen (H_2) and oxygen (O_2) compared to other fuel cells. This is mainly result of the excellent oxygen reduction kinetics in alkaline media compared to the acidic conditions. Other attractive features of AFCs include:

- High ionic conductivity compared to other fuel cell devices is expected. It is achieved by using high hydroxide ion concentrations.
- Relatively low-cost electrodes (ex. porous Ni or silver) as compared to the platinum electrodes which are required for reactions in acidic media can be used.

Disadvantage: AFCs have the disadvantage that they need to be installed in a carbon dioxide free environment. This is to avoid poisoning of the electrolyte. If carbon dioxide comes into contact with the alkaline environment, carbonates are formed. These carbonates are insoluble salts and the porous electrodes clogged up by aforementioned salts. And they block the flow of H_2 and O_2, resulting in power failure. To prevent such an event from occurring, the input gasses need to be purified extremely well.

1.1.3.2. Phosphoric Acid Fuel Cell (PAFC)[5(b)]

PAFC uses phosphoric acid which is 100% concentrated as the electrolyte in this fuel cell, which typically operates at 150 to 220ºC. In the anode side, CO poisoning of

electro-catalyst generally occurs at lower temperatures. The matrix most commonly used to retain the acid is silicon carbide, and the electro-catalyst in both the anode and cathode is Pt. PAFCs are mostly developed for stationary applications. It is still one of the few fuel cell systems that are available for purchase. However, the development of PAFC had slowed down in the past ten years, in favor of polymer electrolyte fuel cells which were thought to have better cost potential.

Advantages: PAFCs are much less sensitive to CO poisoning as compared with PEFCs and AFCs. PAFCs tolerate to excess CO (approx. 1%) as one of impurities in the fuel. Also, PAFCs have efficiencies of 37 to 42% (based on LHV of natural gas fuel). Note that it is slightly more efficient than the combustion-based power plants, which typically operate at 33%–35% efficiency. It is lower than that of polymer electrolyte fuel cell, molten carbonate fuel cell and solid oxide fuel cell systems. In addition, the waste heat from PAFC can be readily used in most commercial and industrial co-generation application. It would technically allow the application for a topping cycle co-generation (i.e. a use of hot water by exhaust heat recovery).

Disadvantages: The disadvantages of PAFCs are summarized as follows:

•Platinum is needed as electro-catalyst.

•Cell performance is lower than that of polymer electrolyte fuel cell.

•Weight and volume are larger than that of polymer electrolyte fuel cell.

•Liquid electrolyte that can migrate is required.

In above mentioned disadvantages, the two most serious problems are the lower kinetics for the oxygen reduction reaction on the platinum cathode compared to polymer electrolyte fuel cells and the management of a liquid electrolyte.

1.1.3.3 Polymer Electrolyte Fuel Cells (PEFCs) [5(c)]

The polymer electrolyte fuel cells (PEFCs) are also referred to as proton exchange membrane fuel cell (PEMFC). Usually, the operation temperature of the PEFC is between 60 to 90°C. PEFCs consist of a thin proton conductive polymer membrane (such as perfluorosulfonic acid membrane) and Pt electrodes. These membranes, such as Nafion®, consist of a polytetrafluoroethylene (PTFE) back borne with per fluorinated-vinyl-polyerther side chains terminated by sulfonate group. Nafion® is essentially fully fluorinated. For practical use, the most suitable electro-catalyst in PEMFC has been platinum nano-particles loaded on conductive carbon so far, because the electrolyte is acid. And platinum electrode is stable and active in the acid. However, the supply of relatively pure hydrogen (less than 10ppm CO gas) into anode side is required due to CO poisoning on Pt[10]. To develop PEFC device, the CO tolerance of Pt has to be improved.

In the PEFCs, there are three types PEFCs as follows;

(i)The Hydrogen Fuelled PEFC

In the case of hydrogen fuelled PEFC system, hydrogen is stored in a suitable fuel tank, a blower or compressor is required to provide the air, and temperature control of the fuel cell stack is accomplished with a heat exchanger. In addition, a humidification section for the H_2 and air may be installed to ensure sufficient humidification of the polymer membrane. In the power electronics, the variable electrical output of the stack is regulated to a well-defined AC or DC power output. The unused hydrogen can be re-circulated using a small pump. In the last decade, there has been a tremendous effort by research groups as well as enterprises to increase the power density of the PEFC, decrease the catalyst loading, improve the electrode structure and cell design, and move towards commercialization of fuel cell components and products[11, 12]. However, kinetics on Pt cathode must be improved and Pt content in anode must be decreased for development of the hydrogen fuelled PEFCs.

(ii). The Reformate Fuelled PEFC

The Reformate Fuelled PEFC is promising concept to circumvent the problems of H_2 production, storage and transportation. It would be possible to use a variety of fuels[13]. Reformate-fuel primarily consists of hydrogen, but it contains carbon dioxide,

nitrogen and carbon monoxide as well. This mixture of gases is obtained by the steam reforming or partial oxidation of a variety of carbonaceous fuels (i.e. methanol, methane, ethanol, gasoline, biomass, and so on).

The Pt anode in PEFC is extremely sensitive to CO poisoning[9]. Therefore, the CO content in the reformate-fuel gas needs to be set to 10ppm level for prevention of serious fuel cell performance loss. The CO tolerance of Pt has to be improved for the Reformate Fuelled PEFC.

(iii).The Direct Alcohol Fuel Cell (DAFC)

From the viewpoint of system complexity associated with the Reformate Fuelled PEFC, direct electrochemical conversion of organic molecules (e.g. methanol, methane, or longer chain hydrocarbons) would be desirable. Yet, the rate of electrochemical oxidation of carbonaceous compounds on noble metal catalysts is very low in the operating temperature range of the PEFC[14]. However, the chemical energy stored in materials such as primary alcohol (i.e. methanol and ethanol) can be electrochemically converted in electricity in the operation condition of PEFC, which leads to the concept of the direct alcohol fuel cell (DAFC)[15-18]. Thereby, DAFC system supplies mixed solution of methanol (or ethanol) and water with the anode side by using a liquid feeding pump. As mentioned above, the methanol oxidation reaction is a slow process

and it involves the transfer of six electrons to the electrode for complete oxidation of carbon dioxide. Anode, cathode and overall reactions of electrochemical methanol oxidation reaction in DAFC can be expressed as follows;

At the anode reaction: $CH_3OH + H_2O \rightarrow CO_2 + 6H^+ + 6e^-$ (1-16)

At the cathode reaction: $3/2O_2 + 6H^+ + 6e^- \rightarrow 3H_2O$ (1-17)

Overall reaction: $3/2O_2 + CH_3OH \rightarrow CO_2 + 2H_2O$ (1-18)

The free energy associated with the overall reaction at 25ºC, 1 atm and the electromotive force (emf) is:

ΔG=-686 kJ mol^{-1} CH_3OH, ΔE= 1.18V[19].

As shown in aforementioned emf, the methanol / O_2 cell has a theoretical cell potential similar to the H_2 / O_2 cell (i.e. 1.2V). However, the more complex mechanism for the catalytic decomposition of the methanol molecule compared to hydrogen requires a higher anode over-potential (>250mV) to attain practical current densities. As the anode electrocatalyst activity is a strong function of the temperature, the operating temperature of the DAFC is around 60°C to obtain high power density. The targeted operating cell voltage is around 0.8V and therefore around 0.2V lower than for the hydrogen or reformate fuelled PEFC[20]. Recent reports claim a power density as high as 1 kWL^{-1} stack volume for the DMFC[21]. An essential advantage of the liquid-feed DMFC over the

PEFC is that the volume of the repetitive unit in the stack can be reduced, because the liquid water-methanol mixture can be used for cooling the stack. On the other hand, there are serious shortcomings of the DMFC, which need to be mentioned: Due to the higher anode over-potential, low conversion efficiency as compared with the hydrogen fuelled PEFC. A serious problem is the methanol crossover from the anode to the cathode through the electrolyte membrane, leading to penalties in fuel and electrochemical efficiency. From a cost viewpoint, the requirement of high catalyst loadings in the DMFC (~5gkW^{-1}) is the most severe problem for wide-scale commercialization, especially in the mobile sector.

1.1.3.5 Molten carbonate fuel cells (MCFCs)

The molten carbonate fuel cell operates at 650°C because the sufficient conductivity of carbonate electrolyte is needed. Also, this operating temperature allows the use of low-cost metal cell components. For MCFCs, the noble metal catalysts are not required due to high operating temperature for the cell electrochemical oxidation and reduction processes. Molten carbonate fuel cells are being developed for natural gas and coal-based power plants for industrial, electrical utility, and military applications[5 (d)].

Eq. (1-17) depicts the operating configuration of the molten carbonate fuel cell. The half-cell electrochemical reactions are

at the anode, $H_2 + CO_3^{2-} \rightarrow H_2O + CO_2 + 2e^-$ (1-17)

at the cathode, $\frac{1}{2}O_2 + CO_2 + 2e^- \rightarrow CO_3^{2-}$ (1-18)

The overall cell reaction is

$H_2 + \frac{1}{2}O_2 + CO_2$ **(cathode)** $\rightarrow H_2O + CO_2$ **(anode)** (1-19)

Advantage MCFCs is fuel flexibility which includes CO_2 gas, and use of variety of catalyst as compared with other fuel cell systems.

Disadvantage MCFCs have problem of limited life time which is mainly caused by the high temperature corrosion, as well as relatively unstable nickel oxide cathode. Also, MCFS take long start up time with low power density[22].

1.1.3.6. Solid Oxide fuel cells (SOFCs) [5(e)]

Solid oxide fuel cells (SOFCs) have an electrolyte that is a solid (i.e. non-porous metal oxide) thin plate or dense film. The cell operating temperature is 700 to 1000 ^{0}C where an ionic conduction by oxide ions takes place. The electrolyte is usually made from a ceramic such as zirconia doped with 8 to 10mol% yttria (yttria stabilized zirconia(YSZ)) and $(LaSr)(GaMg)O_3$. The cell is constructed with two porous electrodes that sandwich the electrolyte. Air flows along the cathode. When an oxygen molecule contacts the cathode/electrolyte interface, it acquires electrons from the

cathode. The oxide ions diffuse into the electrolyte material and migrate to the other side of the cell where they contact the anode.

Advantage: SOFC systems have demonstrated among the highest efficiencies of any power generation system, combined with minimal air pollutant emissions and low greenhouse gas emissions. These capabilities have made SOFC an attractive emerging technology for stationary power generation in the 2kW to 100s MW capacity range.

Disadvantage: low sulfur and oxidation tolerance of the anodes such as Ni/YSZ. Also, low creep strength at high operating temperature and high resistance of electrolyte/ electrode are one of disadvantages.

To use SOFCs at lower temperature such as below 500°C, Gd doped CeO_2 electrolytes which is supported by anode layer was examined. In this case, the stainless steel can be used for interconnector (i.e. separator) in the cell stack. But it is still in the research or demonstration level in the laboratory.

1.2.1 Fuel cell components

The proton conducting membrane (e.g. fluoropolymer such as Nafion®) is used as electrolyte in PEFCs. The electrodes (i.e. cathode and anode) are applied on the both sides of the proton conducting membrane. The electrodes must consist of porous structure because the reactant gases (i.e. O_2 and H_2) are fed and must reach the interface

between the electrodes and the aforementioned membrane electrolyte. That electrode consists of the electro-catalyst layer on the gas diffusion layer (GDL). Typically, platinum supported on conductive carbon (Pt/C) is used as cathode and anode. The multilayer assembly of the membrane sandwiched between the two electrodes and it is called the membrane electrode assembly (MEA). The MEA is then sandwiched between the collector/separator plates. The bipolar plate gives the MEA a pathway for flow of reactant gasses.

1.2.2.1 Membrane electrolyte

William T. Grubb in 1959 was first introduced organic-based cation exchange membranes in fuel cells. In today fuel cell system, the perfluorocarbon-sulfonic acid (PFSA) polymer membrane is commonly used. Membrane function is to provide a conductive pathway, while at the same time separating the reactant gases. The ion conduction takes place via ionic groups within the polymer structure. Ion transport at such sites is highly dependent on the bound and free water associated with those sites. PFSA polymer membrane consists of a linear chain fluorocarbon with a small percentage of sulfonic and carboxylic acid groups. These side chains are where hydrogen ions can be partially or fully exchanged with a number of differing cations. Many differing configurations were explored, but Grot eventually settled on a

polytetrafluorol backbone with polyvinyl ether pendant side groups terminated with a sulfonate ion group. The chemical formula is:

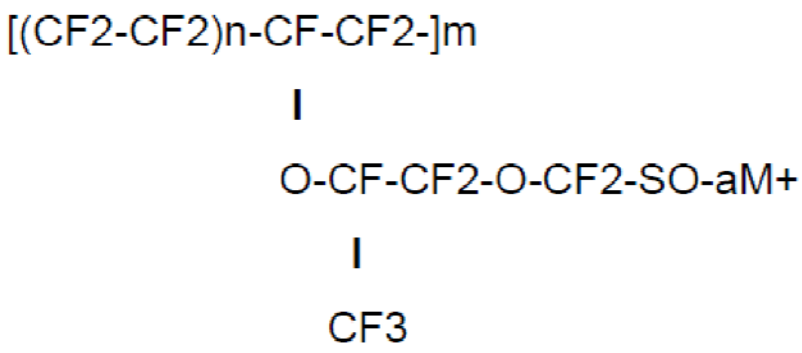

Figure 1-4 Structure of PFSA polymer (Nafion®)[23].

The M^+ can represent any number of counter ions such as H^+, Li^+, and Na^+. The membrane contains two phases of components which are the fluorocarbon and ionic phases and these phases are separated by the covalent bonds that tie them together. The structure of the membrane consists of the cluster with aforementioned aqueous ions which is imbedded in the continuous fluorocarbon phase. Each ionic phase region is connected to the other regions by small channels determining the transport properties.

1.2.2.2 Electrode-catalyst layer

Electrode-catalyst layer is important for optimal proton mobility. Typically, electrodes can be cast as thin films and transferred to the membrane or applied directly

to the membrane. The electrode-catalyst layer may be deposited onto the gas diffusion layer (GDL). There are two method of preparation of MEA. In the first method, catalyst layers apply on the GDL. Then, hot press is performed to make the MEA. In this method, hydrophobic polytetrafluroethylene (PTFE) is used as a binder on the GDL. Low platinum loading electrodes (1.0 $mg_{Pt}\,cm^{-2}$ total on the anode and the cathode) are regularly used now, and have performed as well as higher platinum loading electrodes (2.0 to 4.0 $mg_{Pt}\ cm^{-2}$) in the early stage of research. Catalyst is printed with Nafion by brushing or spraying prior to the hot pressing for ionic transport. The other method for preparation of MEA is to apply catalyst layer direct on membrane in which catalyst with ionomer solution of Nafion®) on the both sides of membrane with placing of the GDL and followed by pressing of membrane catalyst layer. These electrodes in fuel cells, which have been produced using a high-volume manufacturing process, have reached high level such as $600mAcm^{-2}$ at 0.7V of the cell potential. Recent advances in MEA performance and durability have led to tests with reformate in excess of 10,000 hours with the 3M 7-layer MEA. This MEA is produced using high-speed, continuous, automated assembly equipment. To overcome the challenges of operating of fuel cell on low temperature attempts have been made to develop so-called intermediate-temperature PEFC, which would operate in the temperature ranging from 120°C to

160°C. New or modified ion exchange membranes would be needed to allow this, because Nafion® dehydrates rapidly at such temperatures unless high (greater than 10 bar) pressures are applied. One candidate material is phosphoric acid doped polybenzimidizole (PBI). The higher operating temperature eliminates CO poisoning by eliminating CO poisoning on the platinum surface.

1.3 Electrochemistry and previously reported mechanism of CO poisoning on Pt

Recently, polymer electrolyte membrane fuel cells (PEMFCs) have reached to the commercialization stage due to impressive research efforts. PEMFCs performance degrades when CO presents in the fuel, this is referred as "CO poisoning effect". In an effort to enhance the catalytic activity on Pt, electro-catalyst development has been increasingly employing smaller catalyst particle size and metal alloys instead of single Pt catalysts. Adsorption of CO molecule on Pt catalyst surface reduces the surface available for the electrochemical hydrogen adsorption-desorption reaction. CO species can be bonded by linear or bridged form on the catalyst surface[24]. Such strong binding has been explained by 5σ donation of CO orbital to the metal and subsequent transfer of two electron of metal d orbital to the anti-binding $2\pi^*$ CO orbital as shown in Figure 1-5. This process is known as back donation.

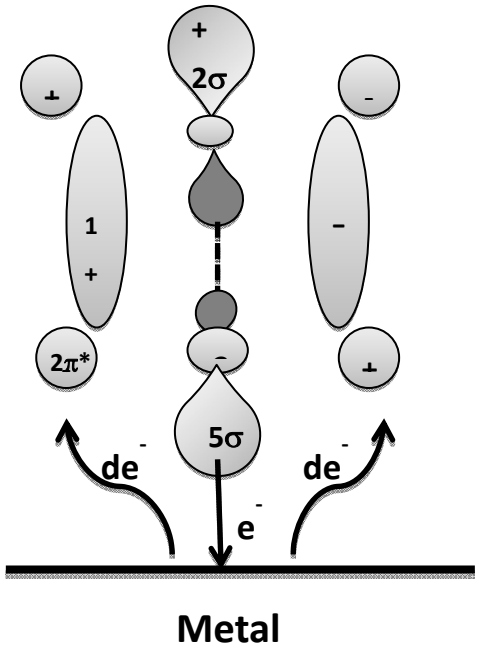

Figure 1-5 5σ donation of CO orbital to the metal and subsequent transfer of two electron of metal d orbital to the anti-binding $2\pi^*$ CO orbital [24(a)].

The bi-functional mechanism of electrocatalysis was proposed by Watanabe and colleagues[25-27] to account for the change in electro catalytic activity of these multi-component systems. This idea is presupposed on the mixture of electro catalysts—with different adsorption properties—on the atomic scale. Watanabe's work demonstrated how oxidation of organic molecules over platinum was improved by the atomic level addition of other electrocatalysts (i.e., gold, ruthenium) that could access lower energy pathways for the adsorption of reactive species. Effectively, one metal acts as sites for organic species and another metal acts as sites for oxygen-containing species. Complex

reactions involving various species and reaction pathways will thus occur more efficiently at metal interfaces. De Souza et al. conducted a study of ethanol oxidation over a PtRh based alloy electrode[28]. Using differential electrochemical mass spectroscopy (DEMS) and Fourier transform infrared spectroscopy (FTIR) [29]; their work demonstrated that the addition of Rh to a Pt catalyst increases the selectivity towards the complete oxidation of ethanol to CO_2, while decreasing selectivity to acetaldehyde. Ethanol oxidation requires C-H bond and C-C bond dissociation, in addition to CO-O bond coupling. De Souza's work suggests that because Pt has relatively low bond energy for CO and O adsorption, Pt and PtRh based catalysts are more likely than Rh to have a lower CO_2 activation energy. A linear sweep voltammetric study of adsorbed CO on Pt surface suggests that Rh ad-atoms modify the electro catalytic properties of Pt to promote the partial oxidation of CO[28] While in a bimetallic system; Rh continues to play the role one would expect it to perform in a single catalyst system.

1.4 Electrochemistry and previously reported mechanism of Oxygen Reduction Reaction (ORR)

In proton exchange membrane fuel cell, the ORR reaction occurs at the cathode side. The mechanism of ORR reaction is quite complicated and involved many intermediates. Primarily, it's depending on the nature of electrode and electrolyte. The ORR reaction is

a multi-electron process with a number of elementary steps, involving different reaction intermediates. The simplified mechanism shown in Figure 1-6, in which major product are H_2O and H_2O_2 .Oxygen reduction process is major four electron transfer process from O_2 to H_2O in both acidic and alkaline medium. Also, Figure 1-6 shows that O_2 can be reduced either directly to water (4 electron reduction process) with rate constant k_1 or to adsorbed hydrogen peroxide ($H_2O_{2,ad}$) with rate constant k_2 , and it can be further reduced to water with rate constant k_3, chemically decomposed on electrode surface (k_4) or desorbed into electrolyte solution (k_5).

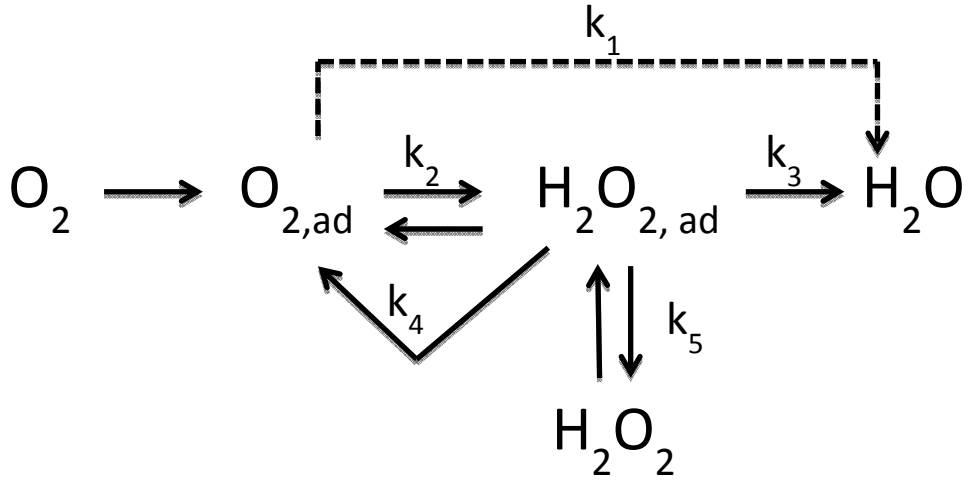

Figure 1-6 ORR mechanism on Pt[24(b)].

Oxygen reduction reaction on cathode side in acidic solution is expressed by

$$\mathbf{O_2 + 4H^+ + 2e^- \longrightarrow 2H_2O} \qquad \mathbf{E^0 = 1.229V} \qquad \mathbf{(1\text{-}20)}$$

Reaction which is expressed by Eq.(1-20) is the four electron process by four hydrogen and oxygen bond splitting. Elementary reactions in over-all reaction (i.e. Eq.(1-20)) are as follows;

$$O_2 + * \longrightarrow O_2* \quad (1\text{-}21)$$

$$O_2* + (H^+ + e^-) \longrightarrow HO_2* \quad (1\text{-}22)$$

$$HO_2* + (H^+ + e^-) \longrightarrow H_2O + O* \quad (1\text{-}23)$$

$$O* + (H^+ + e^-) \longrightarrow HO* \quad (1\text{-}24)$$

$$HO* + (H^+ + e^-) \longrightarrow H_2O + * \quad (1\text{-}25)$$

(where * denotes a site on Pt surface)

Electrode potential plays very important role in changing the Pt surface structure in presence of oxygen. At higher potential, electrode surface is a mixture of Pt and oxide layer. At lower potential, Pt surface is bare Pt. Two tafel slops are observed for ORR on Pt surface in 1M H_2SO_4 aqueous solution. At high current density (low potential), a value of Tafel slope is -120mVdec^{-1} and in at low current density (high potential), a Tafel slop obtained -60mVdec^{-1}. Tafel slop indicates that the oxide layer formation reaction on Pt and ORR on bare Pt. For the examination of ORR activity on electrode,

the analysis of intersect of Tafel line and potential axis in Tafel plot is important. Also, the argument of number of electron in the electrochemical reaction is important. As a consequence of this, the Tafel analysis and Koutecky–Levich (K-L) plot analysis are important for characterization of ORR reaction on electrodes.

1.5 Possibility of oxide as promoter or support for electro-catalysts

Semi-conducting nanomaterial such as nanowire and nanotube consists of unique nanostructure which has diameter in nano-scale. Synthesis and characterization of the semi-conducting nanomaterials have been take major in last few year research[30-32]. In this race of semiconductor nanowire and nanotubes are the most popular category which is prepared by different method[33-38].

So far, aforementioned semi-conducing nanomaterials such as semiconductor nanowire and nanotubes have been examined as thermal activated catalysts. There are no previously reported papers about development of promoter or support for electro-catalyst by using aforementioned semiconductor nanowires and nanotubes. In fuel cell field, only oxide particles have tried to use promoter for electro-catalysts. However, a lowering of Pt amount in the electrodes was hard because of small activity observed for Pt loaded oxide electro-catalysts.

In the present thesis, I will focus on the role of Pt and CeO_x nanowire interface for enhancement of methanol electro-oxidation reaction and design of ORR activity on the electrodes.

To highlight the novelty and uniqueness of the present work, previously reported methods for fabrication of CeO_x nanowires and its application are introduced in following chapter 1.6.

1.6. Fabrication of Ceria nanowire

Cerium is most abundant material and attractive material due to its wide range of application[38-41]. In past decade, the control synthesis of ceria nanowire with uniform structure has been challenging job. Not only physical property, its chemical property is also responsible for the catalytic activity[42]. And following techniques are useful for the fabrication of ceria nanowires[42-45].

1.6.1. Soft template technique

The soft template techniques for development of CeO_x nanowire are very harmless and less time consuming way to develop the nanowire. In this technique, the surfactant have most important role. Most commonly use surfactants are cetyl-trimethyl-ammonium bromide (CTAB), poly-vinyl-pyrrolidone (PVP), tetra-butyl-ammonium bromide (TBAB), and poly-ethylene glycol (PEG). The cerium salts are mostly nitrate

and chloride. The synthesis method carried out under the basic condition. Nanowire size and shape differ by reaction rate, reaction temperature, holding time at the fixed reaction temperature, and surfactant amount in the preparation reaction of the nanowires. Son et al.[46], Gu et al.[47], Andreescu et al.[48], Gasser-Ramirez and coworker[49] performed the research in the development of CeO_x nanomaterials by using soft template method. In previously reported works, the amorphous phase were remained on the surface of CeO_x nanowires. And the crystallinity of fabricated CeO_x nanowires became low level when morphology of wire is clear. To use the surface of CeO_x nanowire surface as promoter or support for electrocatalysts, the crystallinity of CeO_x nanowire surface has to be improved for enhancement of charge transfer from active metal electrode surface to interface of Pt-oxide nanowire interface. The control of experimental parameters for fabrication of nanowire and optimization of its fabrication condition are required for application of electrodes in fuel cell reaction.

1.6.2. Hard template technique

In hard template method, adequate surfactant, template, and ultrasonic treatment condition have to be selected for a preparation of nanowire. The hydrothermal method which is by using optimized preparation temperatures, aging time, and acidic treatment condition may provide nanowires higher thermal, chemical, and structural stability[50,51].

In this hard template method, higher-temperature treatment was carried out for the removal of the templates[53-55]. The formation of CeO_x nanostructure is assisted with different methods like ultra-sonication, facile solvothermal method, and boiling reflux of ethylene glycol[56, 57] by hard template method.

The surface activity of CeO_x nanowire was lost when hard template was removed. To design the active Pt-CeO_x nanowire interface for application of electrodes in fuel cell reaction, the hard template method is not useful.

1.6.3. Non-template Technique

In this method, the solvent composition and cerium source precursor have important role in the final product morphology[58-60]. For the formation of ceria nanostructure, Urea has a significant effect[61, 62]. Hirano and Kato[62]showed that the angular nano-crystalline ceria with a cubic fluorite structure was hydrothermally synthesized in the presence of different concentration urea and three different types of cerium source such as cerium(III) chloride ($CeCl_3 \cdot 7H_2O$), and cerium(III) sulfate $Ce_2(SO_4)_3 \cdot 8H_2O$), cerium(III) nitrate (Ce $(NO_3)_3 \cdot 6H_2O$). In the previously reported works, the synthesis methods of CeO_x nanorods were relatively complicated and always needed high-temperature, high-pressure, or long-time treatments[63-66]. Previously reported non-template techniques were not suitable for application of electrodes in fuel cell reaction.

However, the one-step synthesis of CeO_x nanowires is still a challenge. As a consequence, in the present thesis, the fabrication of CeO_x nanowire is examined by using single step process.

1.7. Application of CeO_x nano-materials as promoter or support for electro-catalysts

CeO_x compounds are one of important components in catalysis for their oxygen storage property which is thermal activated property (not application for electrodes). The several examples of catalysis on CeO_x nano-materials are summarized below.

1.7.1. Carbon mono-oxide oxidation reaction

CeO_x nanomaterial structural defect and vacancies have a positive impact on CO oxidation reaction on thermal activated CeO_x surface[65]. Zhang et al.[66-68] synthesized various CeO_x micro/nanostructures such as spheres, spindles, columns, spheres, and rods. And they investigated the thermally activated catalytic activity in the oxidation of carbon monoxide. The physical and chemical properties of CeO_x nanostructured catalysts were increased by doping with different metals .Au, Cu, Pr, and Sn[69-71]. However, application as electrode support or promoter in the electrochemistry was quite limited in the previously reported works.

1.7.2. Methanol electro-oxidation reaction

Methanol is a useful fuel for use in the development of portable devices and electric vehicle applications. Pt loaded CeO_x nano-material composite electrodes were reported in the methanol electro-oxidation field as well as metal alloys electro-catalysts. Since several metal alloys are useful and show high activity for methanol oxidation reaction[72-82] by the bi functional mechanism and ligand field effect, the activity of methanol electro-oxidation on metallic alloy electrodes were better than that of previously reported activity observed for Pt loaded CeO_x nano-material composite electrodes in methanol electro-oxidation reaction.

I summarized limitation of previously reported electro-catalysts including previously reported Pt loaded CeO_x nanomaterial electrodes in the Chapter 1.7.3.

1.7.3. Limitation of previously reported electro-catalysts

There are some demerits of previously reported electro-catalysts such as high loading of noble metal, weak interaction between oxide support and active metal electrode. Since the resources of those noble metals are very limited on our planet, we need to focus on a lowering of the noble metal amount in the electro-catalysts and maximization of electro-catalytic activity in the fuel cells.

In general, the CO tolerance of Pt in reaction of electro-oxidation of methanol can be estimated by using both of the onset potential of methanol oxidation reaction and intensity ratio of observed peak current intensities in the forward and backward potential sweep (I_f / $I_{b)}$. High I_f / I_b value indicates that the carbonaceous species as intermediates easily formed on Pt surface in the forward scan and direct methanol oxidation without formation of H^+ on Pt in the backward scan is suppressed. As results, the six electron-processes for the formation of H^+ become easy on Pt surface. As consequence, the activity of methanol electro-oxidation on Pt becomes high. Also, I_f / I_b would be inversely proportional to the observed onset potential of methanol electro-oxidation reaction on Pt. It was observed on the surface of PtRu electro-catalyst. In the case of PtRu electro-catalysts, aforementioned I_f / I_b values were from 1.8 to 3.46[83] and obtained values of onset potential of methanol electro-oxidation reaction were from 0.26 to 0.38 V vs. RHE [84-87]. But these bimetallic electro-catalysts have limitation. One of important problems was optimum composition ratio between Pt and Ru. To maximize the CO tolerance of Pt in PtRu alloy electro-catalysts, the optimum atomic ratio between Pt and Ru was 1:1. It gives the lowest on-set potential of methanol oxidation reaction and high activity of methanol electro-oxidation on the PtRu/C electro-catalysts. However, both metals are precious metals whose resources are limited on our planet.

Also, it is hard to reduce the content of Pt in aforementioned bi-metallic electro-catalyst to keep both high CO tolerance of Pt and high catalytic activity. To overcome this problem, the new concept for a design of high activity of methanol electro-oxidation on Pt and a lowering of Pt amount in the anodes is required.

To develop the design paradigm for fabrication of electro-catalysts with high methanol electro-oxidation on Pt, the promotion effect of CeO_x nano-particles for improvement of methanol electro-oxidation activity on Pt was examined in the previous works[88]. Also, the effect of variation of conductive carbon (i.e. carbon-nanotube, graphene, and graphite) in Pt-CeO_x nano-particles/C electro-catalysts towards improvement of methanol electro-oxidation activity on Pt was examined. The observed I_f / I_b values were from 1.05 to 6.52. Also, the observed onset potential values of methanol electro-oxidation reaction were from 0.32 to 0.47 V vs. RHE[89-94]. This means that the level of both observed I_f / I_b values and on-set potential values of methanol electro-oxidation reaction could not reach the level of the PtRu/C electro-catalysts because the interface between Pt and CeO_x nano-particles are limited (i.e. low population of Pt-CeO_x interface).

To maximize the promotion effect of CeO_x for improvement of activity of methanol electro-oxidation on Pt, the population of Pt-CeO_x interface on Pt has to be maximized

by proposal of unique preparation method. Also, the detail analysis of Pt-CeO_x interface structure on Pt with improved activity of methanol electro-oxidation activity has to be clarified.

In the case of improvement of ORR activity on Pt, the role of high conductive carbon such as carbon nano-tube (CNT), graphene, and organic support[95-97] was examined. The observed EASA values from the surface of Pt on aforementioned conductive carbons were high. Unfortunately, the improvement of ORR activity on Pt was not conspicuously observed by using aforementioned various kinds of conductive carbons.

In contrast, Fugane et al. reported higher ORR activity on Pt surface in Pt-CeO_x nano-particles/C as compared with conventional Pt/C cathode. But, previously reported Pt-CeO_x nano-particles/C electrodes which include low amount of Pt less than 10wt% cannot keep high ORR activity as well as higher amount of Pt such as more than 20wt% in Pt-CeO_x nano-particles/C cathodes.

To minimize the Pt content and maximize the ORR activity on Pt in Pt-CeO_x system, the population of Pt-CeO_x interface on Pt should be maximized as well as aforementioned anode case (i.e. for electro-oxidation of methanol on anode). Also, the high functional Pt-CeO_x interface which can maximize the promotion effect of CeO_x for

improvement of ORR activity on Pt has to be designed for development of high quality cathode materials in fuel cells.

1.8. Outline of Thesis:

Why Pt/CeO_x nanowire /C electro-catalyst?

Aim of Thesis

Cerium oxide (CeO_x) nanowire synthesis will be helpful for minimizing Pt metal loading in the electro-catalysts and maximizing both methanol electro-oxidation activity and ORR activity on Pt. In the case of CeO_x nanoparticles, the surface area of CeO_x nano-particles can be high level such as around $50 m^2 g^{-1}$ [98]. But the agglomeration level of nano-particles will be increased. Then, the possibility of formation of Pt-CeO_x interface would become low. In order to maximize the formation of Pt-CeO_x interface on Pt, the active CeO_x surface at nano-scale has to be prepared.

In the present thesis work, the surface activity of CeO_x nanowire was focused for this challenge, even though BET surface area observed for CeO_x nanowire (approximately $38 m^2 g^{-1}$) is not conspicuously high as compared with CeO_x nano-particles. The surface of CeO_x nanowire consists of smooth surface in macro-scale. But this surface would be bumpy in nano-scale. Also, the surface of CeO_x nano-wire has basicity because of adsorption of OH^- species in the aqueous solution. Since Pt resources for formation of

Pt nano-particles are Pt-chlorine compound which has solid acidity, many acid–base reaction spaces in nano-scale can be expected on CeO_x nano-wires. It suggests that nano-reaction space for formation of large amount of Pt-CeO_x interface can be expected on well dispersed and well-crystalline CeO_x nanowire.

For preparation of aforementioned nano-reaction space on CeO_x nanowire, the growth process of CeO_x nanowire is examined in the present thesis. Also, the expected nano-reaction space for formation of large amount of Pt-CeO_x interface is characterized in chapter 3 in the present thesis. After the interface and surface of Pt-CeO_x nanowire interface on Pt, the effect of improvement of activity of methanol electro-oxidation and ORR activity on Pt on formation of Pt-CeO_x nanowire interface is examined. Also, the defect structure features of the Pt-CeO_x nanowire interface which is different from Pt-CeO_x nano-particles is characterized by using atomistic simulation method. Based on all experimental results, the guide to design of high functional Pt-CeO_x interface can be proposed. The main aim of this thesis work is development of design paradigm for fabrication of high quality and less amount Pt electrodes which have high activity of methanol electro-oxidation and high ORR activity through aforementioned research process using CeO_x nanowire surface**.**

1.9. Outline of present thesis

In **chapter 1**, background of the fuel cell science and technology are introduced. Also electro-catalysis in fuel cell reaction and its related catalysis and catalysts are introduced from previously reported literatures.

Chapter 2 contains experimental details for characterization of Pt-CeO_x nanowires on conductive carbon electro-catalysts

Chapter 3 is for synthesis and characterization of Pt-CeO_x nanowires on conductive carbon electro-catalysts. In this chapter, detail discussion about how we design Pt-CeO_x nanowire/C electro-catalysts and confirm Pt-CeO_x nanowire interface interaction with different technique.

Chapter 4: Anodic property of Pt-CeO_x nanowire electro catalysts will be there in detail.

Chapter 5: ORR property observed for Pt-CeO_x nanowire electro-catalysts discussed with the help of rotating disk electrode.

Chapter 6 is for atomistic simulation work for characterization of the interface of Pt and CeO_x nanowires.

And we conclude the results of present thesis in **Chapter 7**.

References

1. D. Hart, "Sustainable Energy Conversion Fuel Cells the Competitive Option?", *J. Power Sources* , **86** , pp.23-27(2000).

2. Editorial committee of fuel cell generation system (ed.), 'Fuel Cell Generation System', Ohm Ltd., Tokyo, Japan, pp.48-51(1993).

3. K.Ota, "Principle of Fuel Cells for Application (Review)", *GS Yuasa Technical Report*, **2**(1), pp.1-5(2005), 3(a) K.Ota, "Principle of Fuel Cells for Application (Review)", *GS Yuasa Technical Report*, **2**(1), p.2(2005), 3(b) K.Ota, "Principle of Fuel Cells for Application (Review)", *GS Yuasa Technical Report*, **2**(1), p.4(2005).

4. L. Gubler, "Operating Polymer Electrolyte Fuel Cells with Reformed Fuel",Chapter 2 "Fundamentals of Fuel Cells" of a dissertation submitted to the Swiss Federal Institute Technology Zurich, pp.29 - 30(2001),

5(a) J. Larminie and A. Dicks, *Fuel Cell Systems explained*. 2nd ed. West Sussex: John Wiley & Sons Ltd, pp.121 – 137(2003), 5(b) J. Larminie and A. Dicks, *Fuel Cell Systems explained*. 2nd ed. West Sussex: John Wiley & Sons Ltd, pp.177 – 184(2003), 5(c) J. Larminie and A. Dicks, *Fuel Cell Systems explained*. 2nd ed. West Sussex: John Wiley & Sons Ltd, pp.177 – 184(2003), 5(d) J. Larminie and A. Dicks, *Fuel Cell Systems explained*. 2nd ed. West Sussex: John Wiley & Sons Ltd, pp.187 – 207(2003),

and 5(e) J. Larminie and A. Dicks, *Fuel Cell Systems explained*. 2nd ed. West Sussex: John Wiley & Sons Ltd, pp.207 – 228(2003).

6. H. Zhang, and P. K. Shen," Recent Development of Polymer Electrolyte Membranes for Fuel Cells" *Chem. Rev*. ,**112**, pp.2780−2832(2012).

7. T.N.Veziroglu, (ed.), "Hydrogen Energy and Transportation ",*Conf. Plenum Press, New York*, pp.1-13(1975).

8. A. Heinzel, C. Hebling, M. Muller, M. Zedda, and C. Muller, "Fuel Cells for Low Power Applications", *Journal of Power Sources* , **105** ,pp.250–255(2002).

9. C.K. Dyer, "Fuel Cells for Portable Applications ", *Journal of Power Sources,***106**, pp.31-34 (2002).

10. H.P. Dhar, L.G. Christner, and A.K Kush, "Nature of CO Adsorption during H_2 Oxidation in Relation to Modeling of CO Poisoning of a Fuel Cell Anode", *J. Electrochem. Soc*., **134**, pp.3021-3026 (1987).

11. T.R. Ralph, GA. Hards, J.E. Keating, S.A. Campbell, D.P. Wilkinson, M. Davis, J. St-Pierre, and M.C. Johnson, "Low Cost Electrodes for Proton Exchange Membrane Fuel Cells Performance in Single Cells and Ballard Stacks, ", *J. Electrochem. Soc*.,**144**, pp. 3845-3857 (1997).

12. T.R. Ralph, "Proton Exchange Membrane Fuel Cells, Progress in Cost Reduction of the Key of componants", *Plat. Met. Rev*., **41**, pp. 102-113 (1997).

13. T. Gilchrist, "Fuel Cells to the Fore", IEEE Spectrum, **11**, pp. 35-40 (1998).

14. J.H. Hirschenhofer, D.B. Stauffer, R.R. Engleman, and M.G. Klett, "Fuel Cell Handbook", Fourth edition, U.S. Department of Energy, pp. 157-170(1998).

15. A. Brouzgou, F. Tzorbatzoglou, and P. Tsiakaras, "Direct Alcohol Fuel Cells: Challenges and Future Trends", *Energetics (IYCE), Proceedings of the 2011 3rd International Youth Conference on*, pp.1-6(2011).

16. M.P. Hogarth, and G.A. Hards, "Direct Methanol Fuel Cells, Technology Advances and Further Requirements", *Plat. Met. Rev*., **40**, pp. 150-159 (1996).

17. GT. Burstein, C.J. Barnett, A.R. Kucernak, and K.R. Williams, "Aspects of the Anodic Oxidation of Methanol", *Catal. Today*, **38**, pp. 425-437 (1997).

18.A. Hamnett, "Mechanism and Electrocatalysis in the Direct Methanol Fuel Cell", *Catal. Today*, **38**, pp. 445-457 (1997).

19. B.Braunchweig, D.Hibbitts, M.Neurock, and A.Wieckowski, "Electrocatalysis: A Direct Alcohol Fuel Cell and Surface Science Perspective", *Catal. Today*, **202**, pp.197-209(2013).

20. A.S.Arico, S.Srinivasan, and V.Antonucci, "DMFCs: From Fundamental Aspects to Technology Development", *Fuel Cells*, **1**, pp.133-161(2001).

21. X. Ren, P. Zelenay, S. Thomas, J. Davey, and S. Gottesfeld, "Recent Advances in Direct Methanol Fuel Cells at Los Alamos National Laboratory", *J. Power Sources*, **86**, pp.111-116 (2000).

22. J.R.Selman, "Molten-Salt Fuel Cell – Technical and Economic Challenges", *J. Power Sources*, **160**, pp.852-857(2006).

23. K.A.Mauritz and R.B.Moore, "State of Understanding of Nafion", *Chem. Rev.*, **104**, pp.4535-4585(2004).

24 (a). S.Ye, "Chapter 16: CO-tolerant Catalysts" of "PEM Fuel Cells Electro-catalysts and Catalysts Layers, Fundamentals and Applications " edited by J. Zhang, Springer-Verlag London Limited, p.765(2008), 24 (b). C.Song and J.Zhang, "Chapter 2: Electrocatalytic Oxygen Reduction Reaction" of "PEM Fuel Cells Electro-catalysts and Catalysts Layers, Fundamentals and Applications" edited by J. Zhang, Springer-Verlag London Limited, pp. 110-111(2008).

25. M. Watanabe and S. Motoo,"Electrocatalysis by Ad-atoms. Part 1. Enhancement of Oxidation of Methanol on Platinum and Palladium by Gold Ad-atoms", *Journal of Electroanalytical Chemistry*, **60**, pp. 259-266(1975).

26. M. Watanabe and S. Motoo,“Electrocatalysis by Ad-atoms. Part 2. Enhancement of Oxidation of Methanol on Platinum by Ruthenium Ad-atoms”, *Journal of Electroanalytical Chemistry*, **60**, pp. 267-273(1975).

27. M. Watanabe and S. Motoo, “Electrocatalysis by Ad-atoms. Part 3. Enhancement of Oxidation of Carbon-monoxide on Platinum by Ruthenium Ad-atoms”, *Journal of Electroanalytical Chemistry*, **60**, pp.275-283(1975).

28. J.P.I. de Souza, S.L. Queiroz, K. Bergamaski, E.R. Gonzalez, and F.C. Nart, “Electro-Oxidation of Ethanol on Pt, Rh, and PtRh Electrodes. A Study Using DEMS and in-Situ FTIR Techniques”, *J. Phys. Chem. B*, **106**, pp.9825-9830 (2002).

29. V. Stamenkovic, M. Arenz, B.B. Blizanac, C.A.Lucas, P.N. Ross, and N.M. Markovic, "Surface Science Studies of the Fuel Cell Reactions on Model Electrocatalysts", *Surf. Scie. Rep*., **45**, pp. 117-229 (2002).

30.Q. Yuan, H.H. Duan, L.L. Li, L.D. Sun, Y.W. Zhang, and C.H. Yan, "Controlled Synthesis and Assembly of Ceria-Based Nanomaterials", *Journal of Colloid and Interface Science*, **335**, pp. 151–167(2009).

31. J. Hu, T.W Odom, and C.M. Lieber,"Chemistry and Physics in One-Dimension: Synthesis and Properties of Nanowires", *Acc Chem. Res*.; **32**, pp. 435-445(1999).

32. Y. Xia, P. Yang, Y. Sun, Y.Wu ,B. Mayers, B. Gates, Y. Yin, F. Kim, and Y. Yan," One Dimensional Nanostructures: Synthesis, Characterization, and Applications", *Adv Mater*, **15**,pp.353-389 (2003).

33. Z.L. Wang, "Splendid One-diementional Nanostructure of Zinc Oxide: A New Nanomaterial Family for Nanotechnology", *ACS Nano*, **2**, pp. 1987-1992(2008).

34. M J. Bruchez, M. Moronne, P. Gin, S. Weiss, and A.P. Alivisatos, "Semiconductor Nanocrystals as Fluorescent Biological Labels", *Science*, **281,** pp. 2013-2016(1998).

35. X. Wang, J. Zhuang, Q. Peng, and Y.D. Li, "A General Strategy for Nanocrystal Synthesis ", *Nature*, **437**, pp.121-124 (2005).

36. B.C.H. Steele, and A. Heinzel, "Materials for Fuel-Cell Technologies", *Nature*, **414**, pp.345-352(2001).

37. R.X. Li, S. Yabe, M. Yamashita, S. Momose, S. Yoshida, S. Yin, and T. Sato, “Synthesis and UV Shielding Properties of ZnO- and CaO-doped CeO_2 via Soft Solution Chemical Process", *Solid State Ionics*, **151**, pp.235-241(2002).

38. L.J. Wu, H.J. Wiesmann, A.R. Moodenbaugh, R.F. Klie, Y.M. Zhu, D.O. Welch, and M.L.J. Suenaga, "Oxidation State and Lattice Expansion of CeO_{2-x} Nanoparticles as a Function of Particle Size", *Phys. Rev.* B,.**69**, pp.125415-125424(2004).

39. S. Tsunekawa, T. Fukuda, and A. Kasuya,"X-ray Photoelectron Spectroscopy of Monodisperse CeO_{2-x}Nanoparticles", *Surf. Sci*., **457**, pp.437-440(2000).

40. S. Carrettin, P. Concepcion, A. Corma, J.M.L. Nieto, and V.F.A. Puntes, " Nanocrystalline CeO_2 increases the Activity of Au for CO Oxidation by Two Orders of Magnitude" , *Angew. Chem. Int. Ed***. , 43**, pp.2538-2540 (2004).

41. D. Terribile, A. Trovarelli, J. Llorca, C. De Leitenburg, and G. Dolcetti, "The Synthesis and Characterization of Mesoporous High Surface Area Ceria Prepared Using a Hybrid Organic/Inorganic Route", *Journal of Catalysis*, **178**, pp.299-308 (1998).

42. M. Yada, S. Sakai, T. Torikai, T. Watari, S. Furuta, and H. Katsuki, "Cerium Compound Nanowires and Nanorings Templated by Mixed Organic Molecules", *Advanced Materials*, **16,** pp.1222-1226 (2004).

43. C. Sun, H. Li, Z. Wang, L. Chen, and X. Huang, "Synthesis and Characterization of Polycrystalline CeO_2 Nanowires" ,*Chemistry Letters*, **33**, pp.662-663 (2004).

44. L. Yan, X. Xing, R. Yu, J. Deng, J. Chen, and G. Liu, “Facile Alcohothermal Synthesis of Large-Scale Ceria Nanowires with Organic Surfactant Assistance”, *Physica B*, **390**, pp.59-64 (2007).

45. R. Yang and L. Guo, “Synthesis of cubic fluorite CeO nanowires”, *Journal of Materials Science*, **40**, pp.1305-1310(2005).

46. J. H. Son, S. W. Kim, and D. S. Bae, “Synthesis and Characterization of CeO_2-Doped SiO_2 Nanoparticles by a Reverse Micelle and Sol-Gel Processing”, *Materials Science and Engineering A*, **498**, pp.2-4(2008).

47. F. Gu, Z. Wang, D. Han, C. Shi, and G. Guo, “Reverse Micelles Directed Synthesis of Mesoporous Ceria Nanostructures”, *Materials Science and Engineering B*, **139,** pp**.** 62-68 (2007).

48. D. Andreescu, E. Matijevi´c, and D. V. Goia, “Formation of Uniform Colloidal Ceria in Polyol”, *Colloids and Surfaces A*, **291**, pp.93-100(2006).

49. J. L. Gasser-Ramirez, B. C. Dunn, and D. W. Ramirez, “A Simple Synthesis of Catalytically Active High Surface Area Ceria Aerogels”, *Journal of Non-Crystalline Solids*, **354**, pp.5509-5514 (2008).

50. R. O. Fuentes, L. M. Acuna, and M. G. Zimicz, "Formation and Structural Properties of Ce-Zr Mixed Oxide Nanotubes," *Chemistry of Materials*, **20**, pp.7356-7363 (2008).

51. G. Chen, S. Sun, X. Sun, W. Fan, and T. You, "Formation of CeO_2 Nanotubes from $Ce(OH)CO_3$ Nanorods through Kirkendall Diffusion," *Inorganic Chemistry*, **48**, pp.1334-1338(2009).

52. D. Zhang , F. Niu , H. Li , L. Shi , and J. Fang, "Uniform Ceria Nanospheres: Solvothermal Synthesis, formation Mechanism, Size-control and Catalytic activity" *Powder Technology*, **207**, pp.35–41(2011).

53. D. Zhang, C. Pan, J. Zhang, and L. Shi, "Solvothermal Synthesisof Necklace-like Carbon Nanotube/Ceria Composites", *Materials Letters*, **62**, pp.3821-3823(2008).

54. Y. Li, J. Ding, and J. Chen, "Preparation of Ceria Nanoparticles Supported on Carbon Nanotubes", *Materials Research Bulletin*, **37**, pp.313-318 (2002).

55. J.Wei, J. Ding, and X. Zhang, "Coated Double-Walled Carbon Nanotubes with Ceria Nanoparticles", *Materials Letters*, **59**, pp.322-325 (2005).

56. D. Zhang, T. Yan, L. Shi, C. Pan, and J. Zhang, "Ethylene Glycol Reflux Synthesis of Carbon Nanotube/Ceria Core-Shell Nanowires", *Applied Surface Science*, **255**, pp.5789-5794(2009).

57. C. Sun, H. Li, H. Zhang, Z. Wang, and L. Chen, "Controlled Synthesis of CeO_2 Nanorods by a Solvothermal Method", *Nanotechnology*, **16,** pp. 1454-1463 (2005).

58. C. Ho, J. C. Yu, T. Kwong, A. C. Mak, and S. Lai, "Morphology-Controllable Synthesis of Mesoporous CeO_2 Nano- and Microstructures" , *Chemistry of Materials*, **17**, pp.4514-4522 (2005).

59. B. Tang, L. Zhuo, J. Ge, G. Wang, Z. Shi, and J. Niu, "A Surfactant Free Route to Single Crystalline CeO_2 Nanowires", *Chemical Communications*, **28**, pp.3565-3567 (2005).

60. C. Pan, D. Zhang, and L. Shi, "CTAB Assisted Hydrothermal Synthesis Controlled Conversion and CO Oxidation Properties of CeO_2 Nanoplates, Nanotubes, and Nanorods ", *Journal of Solid State Chemistry*, **181**, pp.1298-1306 (2008).

61. D. E. Zhang, X. J. Zhang, X. M. Ni, J. M. Song, and H. G. Zheng, "Optical and Electrochemical Properties of CeO_2 Spindles", *Chem. Phys. Chem.*, **7**, pp.2468-2470(2006).

62. M. Hirano and E. Kato, "Hydrothermal Synthesis of Two Types of Cerium Carbonate particles", *Journal of Materials Science Letters*, **18**, pp. 403-405(1999).

63. R. J. Qi, Y. J. Zhu, G. F. Cheng, and Y.H. Huang, "Sonochemical Synthesis of Single-Crystalline $CeOHCO_3$ Rods and Their Thermal Conversion to CeO_2 Rods", *Nanotechnology*, **16,** pp.2502-2506 (2005).

64. D. Zhang, H. Fu, and L. Shi, "Synthesis of CeO_2 Nanorods via Ultrasonication Assisted by Polyethylene Glycol", *Inorganic Chemistry*, **46**, pp.2446 -2451(2007).

65. C. Ho, J. C. Yu, T. Kwong, A. C. Mak, and S. Lai, "Morphology Controllable Synthesis of Mesoporous CeO_2 Nano and Microstructures", *Chemistry of Materials,* **17**, pp.4514-4522(2005).

66. D. Zhang, H. Mai, L. Huang, and L. Shi, "Pyridine-Thermal Synthesis and High Catalytic Activity of CeO_2/CuO/CNT Nanocomposites", *Applied Surface Science,* **256**, pp.6795-6800(2010).

67. F. Niu, D. Zhang, and L. Shi, "Facile Synthesis, Characterization and Low-Temperature Catalytic Performance of Au/CeO_2 Nanorods", *Materials Letters*, **63**, pp.2132 -2135(2009).

68. D. Zhang, F. Niu, T. Yan, L. Shi, X. Du, and J. Fang, "Ceria Nanospindles: Template Free Solvothermal Synthesis and Shape Dependent Catalytic Activity", *Applied Surface Science*, **257**, pp. 10161-10167 (2011).

69. R. S. Sundar and S. Deevi, “CO Oxidation Activity of Cu-CeO_2 Nano-Composite Catalysts Prepared by Laser Vaporization and Controlled Condensation”, *Journal of Nanoparticle Research*, **8**, pp.497-509 (2006).

70.C. Sun, H. Li, and L. Chen, “Study of Flowerlike CeO_2 Microspheres used as Catalyst Supports for CO Oxidation Reaction”, *Journal of Physics and Chemistry of Solids*, **68**, pp.1785-1790 (2007).

71. J. Guzman, S. Carrettin, and A. Corma , “Spectroscopic Evidence for the Supply of Reactive Oxygen during CO Oxidation Catalyzed by Gold Supported on Nanocrystalline CeO_2”, *Journal of the American Chemical Society*, **127**, pp.3286-3287 (2005).

72. P. Costamagna, and S. Srinivasan, "Quantum Jumps in the PEMFC Science and Technology from the 1960s to the year 2000 Part I. Fundamental Scientific Aspects", *J. Power Sources*, **102**, pp. 242-252 (2001).

73. Y.Y. Tong, H.S. Kim, P.K. Babu, P. Waszczuk, A. Wieckowski, and E. Oldfield, **"**An NMR Investigation of CO Tolerance in a Pt/Ru Fuel cell Catalyst", *J. Am. Chem. Soc*., **124**, pp. 468-473 (2002).

74. Y.M. Liang, H.M.Zhang, B.L.Yi, Z.H.Zhang, and Z.C.Tan, "Preparation and Characterization of Multi-walled Carbon Nanotubes Supported PtRu Catalysts for Proton Exchange Membrane Fuel Cells", *Carbon*, **43**, pp. 3144 -3152 (2005**).**

75. C. Bock, C.Paquet, M.Couillard, G.A.Botton, and B.R.MacDougall, "Size-Selected Synthesis of PtRu Nano-Catalysts: Reaction and Size Control Mechanism"*, J. Am. Chem. Soc*., **126**, pp. 8028-8037 (2004**).**

76. B.Yang, Q.Lu, Y.Wang, L.Zhuang, J.Lu, P.Liu, J.Wang, and R.Wang, " Simple and Low-Cost Preparation Method for Highly Dispersed ",*Chem. Mater*., **15**, pp. 3552-3557 (2003).

77. G. Samjeske , H. Wang, T. Loffler, and H. Baltruschat, "CO and Methanol Oxidation at Pt-Electrodes Modified by Mo", *Electrochim. Acta*, **47**, pp.3681-3692 (2002)**.**

78. D.C.Papageorgopoulos, M.Keijzer, and F.A. de Bruijn, "The Inclusion of Mo, Nb and Ta in Pt and PtRu Carbon Supported Electro-catalysts in the Quest for Improved CO tolerant PEMFC anodes", *Electrochem. Acta*, **48**, pp. 197-204 (2002).

79. K.W. Park, J.H. Choi, B.K. Kwon, S.A. Lee, Y.E. Sung, H.Y. Ha, S.A. Hong, H.Kim, and A.Wieckowski,"Chemical and Electronic Effects of Ni in Pt/Ni and

Pt/Ru/Ni Alloy Nanoparticles in Methanol Electro oxidation", *J. Phys. Chem. B*, **106**, pp. 1869 -1877 (2002).

80. T.C. Deivaraj, W.Chen, and J.Y.Lee, "Preparation of PtNi Nanoparticles for the Electro-catalytic Oxidation of Methanol ", *J. Mater. Chem*., **13**, pp .2555-2560 (2003).

81. K.W.Park, J.H.Choi, B.K.Kwon, S.A.Lee, C.Pak, H.Chang, and Y.E.Sung," Pt Ru Rh Ni Nanoparticle Electrocatalyst for Methanol Electro-oxidation in Direct Methanol Fuel Cell", *J. Catal*., **224**, pp. 236-242 (2004).

82. H.R. Mercado-C, H. Kim, and B.N. Popov, "Durability Study of Pt_3Ni Catalysts as Cathode in PEM fuel cells", *Electrochem. Commun,* **6**, pp.795-799(2004).

83. Z. Liu, X. Y. Ling, X.Su, and J. Y. Lee, "Carbon-Supported Pt and PtRu Nanoparticles as Catalysts for a Direct Methanol Fuel Cell", *J. Phys. Chem. B*, **108**, pp.8234-8240(2004).

84. E.V Spinacé, A.O Neto and M Linardi, "Electro-oxidation of Methanol and Ethanol using PtRu/C Electrocatalysts Prepared by Spontaneous Deposition of Platinum on Carbon-Supported Ruthenium Nanoparticles," *Journal of Power Sources*, **129**, pp. 121–126(2004).

85. A. V, Palenzuela, F. Centellas, J. A. Garrido, C. Arias, R. M. Rodríguez, E. Brillas and P.-L. Cabot, "Kinetic analysis of carbon monoxide and methanol oxidation on high performance carbon-supported Pt–Ru electro-catalyst for direct methanol fuel cells", *Journal of Power Sources*, **196** ,pp.3503–3512(2011).

86. G. Garcíaa, J. F.-Montano, A.H.Creusa, E.Pastora and G.A. Planesb, "Methanol Electrooxidation at Mesoporous Pt and Pt–Ru Electrodes: A Comparative Study with Carbon Supported Materials", *Journal of Power Sources*, **196**, pp.2979–2986(2011).

87. J. Lu, L.Hong , Y. Yang , S. Xu , S. Wang , J. Yuan and Li Niu,"Phosphotungstic Acid-Assisted Preparation of Carbon Nanotubes-Supported Uniform Pt and Pt Bimetallic Nanoparticles, and their Enhanced Catalytic Activity on Methanol Electro-oxidation*", Journal of Nanoparticle ResearchDecember*, **16**, pp.1-11 (2013).

88. T. Mori, D. R. Ou, J. Zou, and J. Drennan, "Present status and future prospect of design of Pt-cerium oxide electrodes for fuel cell applications", *Progress in Natural Science: Materials International*, **22**, pp.561-571(2012).

89. L. Dong, R. R. S. Gari, Z. Li, M. M. Craig and S. Hou, "Graphene-Supported Platinum and Platinum–Ruthenium Nanoparticles with high Electrocatalytic Activity for Methanol and Ethanol Oxidation", *Carbon*, **48**, pp.781-787(2010).

90. M. Takahashi, T. Mori, A. Vinu, H. Kobayashi, J. Drennan, and D.R. Ou, "Preparation and Anode Property of Pt-CeO_2 Electrodes Supported on Carbon Black for Direct Methanol Fuel Cell Applications", *Journal of Materials Research*, **21**, pp. 2314-2322*(*2006).

91. M. Takahashi, T. Mori, F. Ye, A. Vinu, H. Kobayashi, and J. Drennan, "Design of High-Quality Pt-CeO_2 Composite Anodes Supported by Carbon Black for Direct Methanol Fuel Cell Application", *Journal of American Ceramic Society*, **90**, pp.1291-1294(2007).

92. M. Takahashi, T. Mori, A. Vinu, D. R. Ou, H. Kobayashi and J. Drennan, "Development of High Quality Pt–CeO_2 Electrodes Supported on Carbon Black for Direct Methanol Fuel Cell Applications", *IEEE Polytronic Conference*., pp.251-256 (2007).

93. A.M. Scibioh, S.K. Kim, E.A.Cho, T.H.Lim, S.A.Hong, and H.Y.Ha, "Pt-CeO_2/C Anode Catalyst for Direct Methanol Fuel Cells", *Applied Catalysis B Environmental*, **84**, pp.773-782(2008).

94. D.J. Guo, and Z.H. Jing, "A Novel Co-Precipitation Method for Preparation of Pt-CeO_2 Composites on Multi-walled Carbon Nanotubes for Direct Methanol Fuel Cells", *Journal of Power Sources,* **195**, pp.3802-3805(2010).

95. B.M. Babi, L.M. Vracar, V. Radmilovi, and N.V. Krstaji, "Carbon Cryogel as Support of Platinum Nano-sized Electro-catalyst for the Hydrogen Oxidation Reaction", *Electrochimica Acta*, **51**, pp. 3820–3826(2006).

96. Z. Yan, J. Xie, S. Zong, M. Zhang, Q. Sun and M. Chen,"Small Sized Pt Particles on Mesoporous Hollow Carbon Spheres for Highly Stable Oxygen Reduction Reaction", *Electrochimica Acta*, **109**, pp.256– 261(2013).

97. R. Siburian, T. Kondo and J. Nakamura,"Size Control to a Sub-Nanometer Scale in Platinum Catalysts on Graphene", *J. Phys. Chem. C*, **117**, pp.3635−3645 (2013).

98. J. G. Li, T. Ikegami, Y. Wang, and T. Mori, "Reactive ceria nanopowders via carbonate precipitation", *Journal of the American Ceramic Society*, **85**, pp.2376-2378(2002).

Chapter 2 Experimental

2-1 Material Used

Starting materials which were used for fabrication of samples were cerium chloride ($CeCl_3 \cdot H_2O$, Nacalai Tesque Company, Japan), cetyltetraethylammonium bromide ($C_{19}H_{42}BrN$, Wako Pure Chemical Industries Ltd., Japan, 98% purity), urea ($(H_2N)_2CO$, Nacalai Tesque Company, Japan, 99.99% purity), and dehydrated ethanol (Wako Pure Chemical Industries Ltd., Japan, 99.99% purity). Potassium tetrachloroplatinate (II) ($K_2PtCl_4 \cdot H_2O$, Sigma-aldrich Ltd., Japan, 98.9% pure) were used for Pt resources. Sodium borohydride ($NaBH_4$, Singma Aldrich, 98 % purity) was used as reducing agent. Carbon black (C, 99.99% purity, Vulcan XC-72R, Cabot Co.) was used for preparation of electro-catalysts. Other materials used were potassium chloride (KCl, Kishida chemical Co. Ltd., Japan, 99.5 % purity) and ammonium by-carbonate ($(NH_4)_2CO_3$, Kishida chemical Co. Ltd., Japan, 98.9% purity). 20wt% Pt/C (Hispec3000) as comparative electro-catalyst was purchased from Johnson Matthey Company. Water as solvent was purified by using reverse osmosis-electro-deionization system (Elix Advantage system, Merck MILLPRE Cooperation, USA). High purity nitrogen and oxygen gases which were supplied from National Institute for Materials Science were used for control of experimental atmosphere.

2-2 Synthesis of Electro-catalysts

2-2-1 Synthesis of Ceria Nanowire

The CeO_x nanowire was synthesized by using alcohol-thermal process. $CeCl_3 \cdot H_2O$, $C_{19}H_{42}BrN$ and $(H_2N)_2CO$ powders were dissolved into the dehydrated ethanol and mixed using magnetic stirrer at room temperature for one hour in dry nitrogen atmosphere. $C_{19}H_{42}BrN$ and $(H_2N)_2CO$ were used as the surfactant for micelle formation and as a base for a control of pH in micelle formation reaction, respectively. The mixed solution was filtered by using ultra filtration. Half amount of filtrate was transferred into 25ml Teflon autoclave. The formation reaction of CeO_x nanowire took place into 25ml Teflon autoclave at 80°C for 4 days in electric oven. After filtration and rinsing, the mixture was dried at room temperature in a N_2 gas flow.

2-2-2 Synthesis of Pt loaded Ceria Nanowire

To impregnate fine Pt particles on the CeO_x nanowire, $K_2PtCl_4 \cdot H_2O$ powder was dissolved into distilled water and mixed for one hour. The K_2PtCl_4 aqueous solution was dropped into the previously prepared CeO_x nanowire solution in which the CeO_x nanowires were dispersed in the distilled water. The mixture was left at room temperature for 12h. The platinum complex in the mixture was reduced at room temperature for 1h in $NaBH_4$ aqueous solution. The mixture was rinsed by distilled

water and ethanol. And it was dried at room temperature in nitrogen atmosphere. In the final stage, the prepared Pt-CeO_x nanowire and carbon black (CB) were dispersed in ethanol and dried in a N_2 gas flow.

2-3 Characterizations

2-3-1 Morphology by Scanning Electron Microscopy (SEM)

Scanning electron microscope (SEM) is a type of electron microscope that produces images of a sample by scanning it with a focused beam of electrons. Once the beam hits the sample, electrons and X-rays are ejected from the sample. The beam travels through electromagnetic fields and lenses, which focus the beam down toward the sample. The electrons interact with atoms in the sample, producing various signals that can be detected and that contain information about the sample's surface topography and composition.

For preparation of SEM sample, ethanol dispersed Pt/CeO_x nanowire electro-catalyst takes place. Then they were put on carbon tape or on sample holder of SEM. Morphology of CeO_x nanowire was confirmed by using field emission scanning electron microscopy (FE-SEM, SU-8000 Hitachi, Japan). All samples were sputtered with Tungsten for 30 sec by SEM coater. The sample morphologies were characterized by accelerating voltage of 2-5kV and emission current in the range of 10mA.

2-3-2 X-ray diffraction (XRD)

The crystal phases of the samples were characterized by using X-ray diffraction analysis. XRD patterns of the samples were recorded on Rigaku Ultima plus X-ray diffractometer using Cu Kα (λ= 1.5405 Å). Target voltage and target current were 40kV and 40mA, respectively. Divergence, scattering, and receiving slits used were 0.5deg, 0.5deg, and 10mm, respectively. Scan axes were 2θ/θ. Scan angle is 10 to 90 degree. Scan speed is 2 degree·min^{-1}. And the step of scan is 2degree.

2-3-3 Inductively Coupled Plasma Mass Spectroscopy (ICP-MS)

Inductively Coupled Plasma Mass Spectrometry (ICP-MS) is an analytical technique used for elemental determinations. In ICP-MS technique, samples are introduced into argon plasma as aerosol droplets and this plasma dries the aerosol, dissociates the molecules, and then removes an electron from the components, thereby forming singly-charged ions, which are directed into a mass filtering device known as the mass spectrometer. In ICP-MS systems employ a quadrupole mass spectrometer which rapidly scans the mass range. At any given time, only one mass-to-charge ratio will be allowed to pass through the mass spectrometer from the entrance to the exit upon exiting the mass spectrometer, ions strike the first dynode of an electron multiplier, which serves as a detector. The impact of the ions releases a cascade of

electrons, which are amplified until they become a measureable pulse. The software compares the intensities of the measured pulses to those from standards, which make up the calibration curve, to determine the concentration of the element. For each element measured, it is typically necessary to measure just one isotope, since the ratio of the isotopes, or natural abundance, is fixed in nature.

An ICP-MS consists of the following components:

• **Sample introduction system** – composed of a nebulizer and spray chamber and provides the means of getting samples into the instrument

• **ICP torch and RF coil** – generates the argon plasma, which serves as the ion source of the ICP-MS

• **Interface** – links the atmospheric pressure ICP ion source to the high vacuum mass spectrometer

• **Vacuum system** – provides high vacuum for ion optics, quadrupole, and detector

• **Collision/reaction cell** – precedes the mass spectrometer and is used to remove interferences that can degrade the detection limits achieved. It is possible to have a cell that can be used both in the collision cell and reaction cell modes, which is referred to as a universal cell

• **Ion optics** – guides the desired ions into the quadrupole while assuring that neutral species and photons are discarded from the ion beam

• Mass spectrometer – acts as a mass filter to sort ions by their mass-to-charge ratio (m/z)

• **Detector** – counts individual ions exiting the quadrupole

• **Data handling and system controller** – controls all aspects of instrument control and data handling to obtain final concentration results.

For the analysis of Pt-CeO_x/C nanowire catalysts, ELAN 6100DRC has been used for tracing all elements in the electro-catalysts. Several reviews on atomic mass spectrometry[1-7] have included significant developments in instrumentation, methodology, and understanding of the fundamentals of ICP-MS.

2-3-4 X-ray Photoelectron Spectroscopy (XPS)

X-ray photoelectron spectroscopy (XPS) works by irradiating a sample material with mono energetic soft x-rays causing electrons to be ejected. Identification of the elements in the sample can be made directly from the kinetic energies of these ejected photoelectrons. The relative concentrations of elements can be determined from the photoelectron intensities. An important advantage of XPS is its ability to obtain information on chemical states from the variations in binding energies, or chemical

shifts of the photoelectron lines. The relationship governing the interaction of a photon with a core level is:

KE= *h*ν - BE –Φ[8] **(2-1)**

KE =Kinetic Energy of ejected photoelectron

*h*ν =characteristic energy of X-ray photon

BE= Binding Energy of the atomic orbital from which the electron originates.

Φ =spectrometer work function

The surface composition and surface chemical states of Pt loaded CeO_x nanowire/C were characterized by using RIGAKU XPS7000 and Thermo Scientific theta probe equipment. AlKα X-ray source (hυ =1486.6 eV) was used for surface characterization. Binding energies of Pt4*f* and Ce3*d* core level peaks were corrected by using C1*s* core level peak which is located at 284.5ev. Peak separation and analysis of XPS raw data were performed by using software UNIFIT2009 (Leipzing University, Germany).

2-3-5 Transmission Electron Microscopy (TEM)

Transmission electron microscopy (TEM) is used for characterization of the internal microstructure of Pt loaded CeO_x nanowire. The principle of TEM observation is explained by using "Bragg's law" which is expressed by Eq. (2-2).

$2d(hkl) \sin\theta = n\lambda$ **(2-2)**

In reciprocal lattice, tiny crystallographic information in real lattice space is maximized based on “Bragg’s law”. TEM observation provides us the lattice image by Fourier transformation of the information of reciprocal lattice. For detail analysis of interface structural feature well, the diffraction pattern analysis, image analysis, and other analysis using non-elastic scattering beam (i.e. electron energy-loss spectroscopy (EELS) which can show us information of valence of cation, length between atoms and coordination number of oxygen around absorbed atom) are required. That is important aspect of the analytical TEM analysis.

The preparation of TEM sample takes place by sonicating Pt loaded CeO_x nanowire in ethanol for 5 min and then dispersed on copper grid for analysis. JEM-200EX (JEOL, Japan) electron microscope and Tecnai F20 with EELS detector (FEI, Japan) were used at 200kV for microstructural analysis.

2-3-6 Electron Energy Loss Spectroscopy (EELS)

Electron energy-loss spectroscopy (EELS) involves analyzing the energy loss distribution of initially mono-energetic electrons after they have interacted with a specimen. In electron energy-loss spectroscopy, it mainly focuses on the primary process of electron excitation, which results into the energy lost with the losing of

electron. High-resolution electron spectrometer separates the electrons according to their kinetic energy and produces an electron energy-loss spectrum. There are many articles in which EELS analysis explained in detail[9-17]. EELS study generally performed with the help of STEM mode of TEM instrument. EELS data analysis and processing was done by GATAN imaging filtering system.

2-3-7 Electrochemical Analysis

The electrochemical properties observed for Pt loaded CeO_x nanowire catalyst consist of following parts;

2-3-7-1 Anodic property measurement by methanol electro-oxidation reaction

(a) EASA (electrochemically active surface area) measurement

(b) Activity measurement of methanol electro-oxidation reaction

2-3-7-2 Cathodic property measurement by ORR (Oxygen Reduction Reaction)

(a) Geometrical surface area measurement

(b) Activity measurement of oxygen reduction reaction

2-3-7-1 Anodic property measurement by methanol electro-oxidation reaction

The activities of methanol electro-oxidation reaction on Pt in Pt loaded CeO_x nanowire/C anode were examined by using cyclic voltammetry (CV) in a mixed solution of 0.5M H_2SO_4 and 0.5M CH_2OH_5 in the potential range from -0.2 to 1.3V (vs. Ag/AgCl). The water was purified using RO (reverse osmosis) – EDI (electro-deionization) system (Merck MILIPORE, Elix Advantage, Japan), and the ultrapure grade H_2SO_4 (Kishiada Chemicals Company, Japan) was used for preparation of electrolyte solution. The electrochemical measurements were carried out by using standard three-electrode glass cell at 28°C. The samples for the electrochemical measurement were prepared from suspensions of Pt-CeO_x nanowire/C samples (2mg·ml^{-1}) in the ethanol solution. The suspension was spread out on a Au electrode (area: 0.197cm^2) by using a micropipette containing 5 μ L of solution. The quantity of Pt in the commercially available Pt/C and Pt-CeO_x nanowire/C anodes was 2 μ g. Prior to the electrochemical measurements, the electrochemical pre-treatment for conditioning of the anode surface was carried out and the electrochemically active surface area was estimated as follows:

(a) Electrochemical active surface area (EASA) measurement

The electrochemical pre-treatment for conditioning of the anode surface was carried out into 0.5M H_2SO_4 aqueous solution by means of 300 cycle sweeps in the potential range from -0.2 to 1.3 V (vs. Ag/AgCl). A Pt foil and Ag/AgCl were used as counter and reference electrodes, respectively. The sweep rate during the conditioning process was 50mVsec^{-1}. The electrochemically active surface area (EASA) of Pt in Pt loaded CeO_x nanowire/C anodes was determined by using the amount of charge of the electro-desorption of hydrogen from the Pt surface in the anode at 28°C. For this analysis, the sweep rate was 20mVsec^{-1}. The value of EASA was calculated by using Eq.(2-3).

EASA ($m^2 \cdot g$)= QH/ ([Pt] x 0.21) **(2-3)**

where QH is average charge for hydrogen desorption in mCcm^{-2}, [Pt] is loading of platinum in mgcm^{-2}, and 0.21 is charge (in mC) required to oxidize one monolayer of hydrogen from 1 cm^{2}of platinum black **(**Ralph *et al.*, [18] Pozio *et al.*[19]).

(b) Activity measurement of methanol electro-oxidation reaction

After aforementioned conditioning process, the electrolyte solution was changed from 0.5M H_2SO_4 aqueous solution to a mixed solution of 0.5M H_2SO_4 and 0.5M CH_2OH_5. Prior to the measurement of the activity on anodes, the stability of CV signal was examined by means of 30 cycle sweeps in the potential ranging from -0.2 to 1.3 V

(vs. Ag/AgCl). For measurement of CV curves in the methanol oxidation reaction, the sweep rate was 20mVsec^{-1}. The observed current in CV measurement was normalized by using aforementioned EASA values.

The onset potential of methanol electro-oxidation reaction is estimated using the potential value which conspicuously deviates from the base-line of the forward sweep curve (i.e. positive going scan curve). To estimate the onset potential correctly, a slow sweep rate (i.e. 1 mVsec^{-1}) was selected because of the effect of high sweep rate on baseline drift of CV curves. The measured potentials were converted to the reversible hydrogen electrode (RHE) scale.

2-3-7-2 Cathode property by ORR (Oxygen Reduction Reaction)

Cathode property on Pt in Pt-CeO_x nanowire/C electro-catalyst was examined by using voltammetry in 0.5M H_2SO_4 aqueous solution in the potential ranging from 0.8 to 0V (vs. Ag/AgCl). The water was purified as well as measurement of anode property on the anode, and the ultrapure regent grade of H_2SO_4 was used for preparation of electrolyte solution. The electrochemical measurements were carried out by using standard three-electrode glass cell with a rotating disk electrode after pretreatment at 28°C. A Pt foil and Ag/AgCl were used as counter and reference electrodes, respectively. The samples for the electrochemical measurement were prepared from

suspensions of Pt-CeO_x nanowire/C samples ($2mgml^{-1}$) in ethanol solution. The suspension was spread out on a glassy carbon electrode (area: $0.385cm^2$) by using a micropipette containing 5 μ L of solution. The quantity of Pt in the commercially available Pt/C and Pt-CeO_x nanowire/C anodes was 2 μ g. Prior to the electrochemical measurements, the electrochemical pre-treatment for conditioning of the cathode was carried out and electrochemically active surface area was estimated as follows:

(a) Geometrical surface area measurement

Prior to the measurement of electrochemistry, the electrochemical pre-treatment for conditioning of the cathode surface was carried out into 0.5M H_2SO_4 aqueous solution by means of 300 cycle sweeps in the potential range from 0 to 0.8 V (vs. Ag/AgCl). A Pt foil and Ag/AgCl were used as counter and reference electrodes, respectively. The sweep rate during the conditioning process was $50mVsec^{-1}$.

To compare the activity of ORR between Pt-CeO_x nanoparticles/C and Pt-CeO_x nanowires/C cathodes, the observed current was normalized by using geometrical surface area of cathode on working electrode (i.e. glassy carbon electrode). Since the oxidation of surface of Au electrode give influence for estimation of onset potential of ORR, the glassy carbon electrode was used as working electrode in the present work. And the geometrical surface area was calculated by using Levich equation[20] (Eq. 2-4) .

$$I_d = 0.62\ nFAD^{2/3} C\nu^{-1/6}\omega^{1/2} \qquad (2\text{-}4)$$

where I_d is limited current density, n is the number of transferred electrons (=4), F is Faraday constant (=96490Cmol^{-1}), A is geometric surface area, D is the diffusion coefficient (=1.15×10^{-5}cm^{2}sec^{-1}), C is solubility (=1.61×10^{-6}molcm^{-3}), ν is Kinematic viscosity (=0.00839cm^{2}sec^{-1}), and ω is angular velocity (=14.47sec^{-1}). The sweep rate is 10mVsec^{-1}.

(b) Activity measurement of ORR

Prior to the measurement of the ORR activity on cathodes, the stability of electrochemistry signal was examined by means of additional cycle sweeps in the potential ranging from 0 to 0.8V (vs. Ag/AgCl). Then, the ORR activity was examined in O_2-saturated 0.5M H_2SO_4 aqueous solution. Aforementioned additional cycle sweeps were varied by the composition of cathodes. The number of cycle sweeps for homemade Pt/C, 20wt%Pt-CeO_x nanoparticles/C, 5wt%Pt-CeO_x nanowires/C, 10wt%Pt-CeO_x nanowires/C and 50wt% Pt-CeO_x nanowires/C were 30, 30, 50, 70 and 120 cycle sweeps, respectively. Then, ORR activity was measured by linear voltammograms which were observed in O_2-saturated 0.5 MH_2SO_4 aqueous solution. The final linear voltamometric curves were determined by the subtraction of observed hydrodynamic voltammograms in N_2-saturated 0.5M H_2SO_4 aqueous solution from the aforementioned

observed hydrodynamic voltammograms in O_2-saturated 0.5M H_2SO_4 aqueous solution at the same rotation rate (2000 rpm).

In the electrochemical measurement, the potential was swept from the positive side to the negative side. The sweep rate was 10 $mVsec^{-1}$. For a fair comparison, the same amount of each catalyst by mass was loaded on a glassy carbon rotation disk electrode, and the observed current density was normalized by using aforementioned geometric surface area. The measured potentials were converted to the reversible hydrogen electrode (RHE) scale.

2-4 Atomistic simulation

To the conclusion the influence of interface defect structure of Pt-CeO_x nanowire on anodic and cathodic properties, the atomistic simulation work was performed by using GULP code. The atomistic simulation is based on Born model[21, 22] description of an ionic crystal which the lattice energy consists of three sources: long-range Coulombic forces, short-range interactions, and polarization between cation and anion in the ionic crystals. The Coulombic forces are summed using Ewald's method to provide convergence[23]. The short-range interactions were captured by Buckingham pair potential in the form of $E(r_{ij}) = A \exp(-r_{ij}/\rho) - Crij^{-6}$, where r_{ij} is the atomic distances and A, ρ, and C are adjustable parameters (see Table 2-1). Since short-range interactions

decrease quickly with increasing atomic distances, it is necessary to consider that those ions are separated less than a certain cut-off distance (20Å in this study). Shell model expressed polarizability of ions[24, 25]. This consists of a mass less shell with charge Y|e| that is allowed to move to a massive core with charge X|e|, resulting in the overall charge state of each ion equal to (X + Y)|e|. The shell is bound to the core by an isotropic harmonic spring with force constant k, and the displacement of the shell relative to the core gives a good description of electronic polarization. In this study, O^{2-} and Ce^{4+} ions are treated as polarizable and their shell parameters are listed in Table 2-2. To calculate the intrinsic defect energy in bulk lattice, Mott-Littleton two-region method[26] was applied, which is coded in GULP code[27]. To approach simulation of the accommodation of the defect clusters in perfect crystal, the lattice around defect center is divided into two spherical regions (I and II) together with an interfacial region II a. Ions in region I are allowed to be explicitly relaxed related to the defect, which is introduced to the center of region I, while ions in region IIa are assumed to be weakly perturbed and thereby vary via the Mott-Littleton approximation. Meanwhile, the interaction between region I and II ions are explicitly calculated. In order to ensure that the defect energy is sufficiently converged with respect to the region radii, an inner region I with a radius $3a_0$ (a_0= 5.411Å, the lattice constant of ceria) and the interfacial

region IIa with a radius $6a_0$ were used for calculation. Explicitly, the positive defect energy means the energy required to form the defect. Therefore, defects with the lowest energy are preferred as stable in the crystal lattice. On the other hand, for defect clusters with different number of defect components, binding energy ΔE_b is calculated to investigate the preference and stability of defect clusters, with the following formula:

$$\Delta E_b = E_{isolated} - E_{cluster}. \quad \textbf{(2-5)}$$

where $E_{isolated}$ refers to the sum of defect energies of all components in the defect cluster, and $E_{cluster}$ is the defect energy of the cluster itself. From Eq. (2-5), it can be noticed that a positive binding energy implies a preference of the formation of defect cluster over its individual components. Therefore, the higher binding energy indicates greater stability of defect cluster. Combing the exact defect and binding energy, we can thus predict the formation and evolution of stable defect clusters in bulk materials.

Table 2-1 Short-range pair parameters.

Species	**A(eV)**	**ρ(Å)**	**C(ev Å^6)**	**References**
Ce^{4+}-O^{2-}	1986.8	0.3511	20.40	28
Pt^{2+}-O^{2-}	2561.61	0.3200	0.00	
O^{2-}-O^{2-}	22764.3	0.149	45.83	29

Table 2-2 Shell parameter.

Species	Y (lel)	K (eV Å^{2-})	References
Ce^{4+}	7.7	291.8	29
O^{2-}	-6.1	419.9	30

References

1. J. R. Bacon, K. L Linge, and L. J.Van Vaeck, "Atomic Spectrometry Update. Atomic Mass Spectrometry", *Anal. At. Spectrom*, **20**, pp. 763-802 (2005).

2. J. S. Becker," Trace and Ultratrace Analysis in Liquids by Atomic Spectrometry", *Trends Anal. Chem*., **24**, pp.243-254(2005).

3. N. H. Bings, A. Bogaerts and J. A. C. Broekaert, "Liquid Sample Introduction in ICP Spectrometry*", Anal. Chem*., **76**, pp. 3313-3336 (2004).

4. J. S. Becker," Inductively Coupled Plasma mass Spectrometry (ICP-MS) and Laser Ablation ICP-MS for Isotope Analysis of Long-lived Radionuclides", *Int. J. Mass Spectrom*., **242**, pp. 183-195(2005).

5. H. J Haraguchi, "Metallomics as Integrated Biometal science*", Anal. At. Spectrom*., **19**, pp. 5-14 (2004).

6. A.Fisher, P. S. Goodall, M. W. Hinds, S. N. Nelms, and D. M. Penny, "Atomic Spectrometry Update: Industrial Analysis: Metals, Chemicals and Advanced Materials", *J. Anal. At. Spectrom*., **18**, pp. 1497-1528(2003).

7. A Fisher, P. S.Goodall, M. W. Hinds, S. N. Nelms and D. M. Penny, "Industrial Analysis: Metals, Chemicals and Advanced Materials", *J. Anal. At. Spectrom*, **19**, pp. 1567-1595 (2004).

8. D. Briggs and J.T. Grant, "Surface Analysis by Auger and X-ray Photoelectron Spectroscopy," *Publications and Surface Spectra Limited,* **6**, pp 769-779 (2003).

9. P. E. Batson, "Parallel Detection for High-Resolution Electron Energy Loss Studies in the Scanning Transmission Electron Microscope", *Rev. Sci. Instrum*. **59**, pp.1132–1138 (1988).

10. P. E. Batson, "Electron Energy Loss Studies in Semiconductors", In Transmission Electron Energy Loss Spectrometry in Materials Science, *The Minerals, Metals and Materials Society*, **2**, pp. 217–240(1992).

11. P. E. Batson, "Spatial Resolution in Electron Energy Loss Spectroscopy", *Ultramicroscopy* , **47**, pp. 133–144 (1992).

12. P. E. Batson, "Simultaneous STEM Imaging and Electron Energy-Loss Spectroscopy with Atomic Column Sensitivity", *Nature,* **366**, pp. 727–728(1993).

13. P. E. Batson, "Distortion of the Core Excitation by the Swift Electron and Plasmon Wake in Spatially Resolved Electron-Energy-Loss Scattering", *Phys. Rev. B* ,**47**, pp. 6898–6910 (1993).

14. P. E. Batson, "Silicon *L*23 Near-edge Fine Structure in Confined Volumes", *Ultramicroscopy,* **50**, pp. 1–12(1993).

15. P. E. Batson, "Conduction Band structure in Strained Silicon by Spatially Resolved Electron Energy-Loss Spectroscopy ", *Ultramicroscopy,* **59**, pp. 63–70 (1995).

16. P. E. Batson, and J. Bruley, "Dynamic Screening of the Core Exciton by swift Electron Energy-Loss Spectroscopy ", *Phys. Rev. Lett*., **67**, pp.350–353 (1991).

17. P. E Batson, and A. J. Craven, "Extended Fine Structure on the Carbon Core-Ionization Edge Obtained from Nanometer-sized Areas with Electron Energy-Loss Spectroscopy", *Phys. Rev. Lett*., **42**, pp. 893–897(1979).

18. T. R. Ralph, G. A. Hards, and J. E. Keating ,"Low Cost Electrodes for Proton Exchange Membrane Fuel Cells", *J. Electrochem. Soc.,***144**, pp. 3845-3857(1997).

19. A. Pozio, M. D. Francesco, A. Cemmi, F. Cardellini, and L. Giorgi,"Comparison of High Surface Pt/C Catalysts by Cyclic Voltammetry", *Journal of Power Sources*, **105**, pp.13–19(2002).

20. A.J.Bard, and L.R.Faulkner, "*Electrochemical Methods: Fundamentals and Applications*", 2nd ed.; Wiley &Sons: New York, p.339 (2000).

21. M. Born and J. E. Mayer, "Zur Gittertheorie der Ionenkristalle", *Z. Phys*., **75**, pp.1-5 (1932).

22. M. R. Welton and W. Barndt, "A LEED Study of the MgO (100) Surface: Identification of a Finite Rumple", *J. Phys. C,* **15**, pp.5691-5700 (1982).

23. P. P. Ewald, "Die Berchnung Optischer und Elektrostatischer Gitterpotentiale", *Ann. Phys*, **64**, pp. 253-257 (1921).

24. B. G. Dick and A. W. Overhauser, "Theory of the Dielectric Constants of Alkali Halide Crystals", *Phys. Rev*., **112**, pp.90-103 (1958).

25. G. V. Lewis and C. R. Catlow, "Potential Models for Ionic Oxides", *J. Phys. C*, **18**, pp. 1149 -1161(1985).

26. N.F.Mott and M.J.Littleton, "Conduction in Polar Crystals", *Trans. Faraday Soc.*, **34**, pp.485−499(1938).

27. J.D. Gale, "GULP: A Computer Program for the Symmetry-Adapted Simulation of Solids", *J. Chem. Soc., Faraday Trans.*, **93**, pp.629-637 (1997).

28. D. J. Binks and R. W. Grimes, "Incorporation of Monovalent Ions in ZnO and Their Influence on Varistor Degradation", *J. Am. Ceram. Soc*., **76**, pp. 2370- 2372 (1993).

29. V. Bulter, C. R. Catlow, B. E. Fender, and J. H. Harding, "Dopant Ion Radius and Ionic Conductivity in Cerium Dioxide", *Solid State Ionics*, **8**, pp. 109-113 (1983).

30. S. Vyas, R. W. Grimes, D. H. Gay, and A. L. Rohl, "Structure, Stability and Morphology of Stoichiometric Ceria Crystallites", *J. Chem. Soc. Faraday Trans*., **94**, pp. 427-434(1998).

Chapter 3 Fabrication of Pt loaded ceria nanowire interface for electro catalysts

3-1 Introduction

Variety of nanowires materials has paid much attention due to their application in chemical sensors[1], electronic devices, and interconnect[2, 3]. Nanowire can be produced by various growth techniques such as hydrothermal process[4], thermal decomposition process[5], templating sol-gel process[6]. But those applications need the development of techniques to control size of nanowire for large scale integaration[7-10]. There are significant researches for the growth of nanowire includes solution based growth[11], template based growth[12], and thermal oxidation[13-15]. However, those reports cannot clearly explain the growth process of nanowire by alcohothermal process whose alias is solvothermal process. Alcohothermal process utilizes a solvent under pressures and temperature above its critical point to increase solubility to speed up reactions between solids. Heath and co-workers introduced the alcohothermal process for fabrication of semiconducting nanowires[16]. They synthesized Ge nanowire by using $GeCl_4$ with sodium in an alkenes solvent which was heated and pressurized. After their works, Wang, Lu and Li and co–workers exploited extensively this method by to process variety of nanowires[17], nanotubes[18], and wiskers[19]. The alcohothermal process is complicated and its growth mechanism is largely affected by the parameters such as reaction time and reaction temperature. For the understanding of fundamental growth mechanism of oxide nanowire which is developed by using alcohothermal method, we examine the growth process of CeO_x nanowire to prepare the active reaction space (or stage) for the fabrication of Pt-CeO_x nanowire interface on the electrodes.

The interface design of electro-catalysts which promote the electro-oxidation of methanol and reduction of oxygen is important for development for fuel cell device. It is known that Pt-oxide support series such as Pt-CeO_x nano-particles/carbon (C) [20-28] anode and cathode in fuel cells are unique system due to the electrochemical interaction between Pt and CeO_x at room temperature. Pt loaded cerium oxide (CeO_x) nano-particle supports/C as electro-catalysts have attracted attention due to aforementioned unique interactions between Pt and CeO_x. In the present work, in order to maximize the interaction between Pt and CeO_x, and improve the activity of methanol electro-oxidation reaction on Pt and oxygen reduction reaction activity on Pt, the CeO_x nanowires rather than CeO_x nanoparticles is fabricated using the alchothermal method. The growth process of CeO_x nanowire is examined and optimized for preparation of active surface of CeO_x nanowires. Also, the surface and interface of Pt loaded CeO_x nanowire were characterized by using scanning electron microscopy (SEM), transmission electron microscopy (TEM), selected area electron diffraction pattern (SAEDP), X-ray photoelectron spectroscopy (XPS) and X-ray diffraction (XRD) analysis.

3-2 Previous reported Synthesis process for ceria nanowire

In the previous reported papers mainly CeO_x nanowire synthesized by surfactant assisted method[29], template method[30], and sol-gel[31]. For template method different templates, such as organic macromolecules[32], surfactants[33], nanometer-sized granular of silica[34], polycarbonate membranes, and anodic alumina membranes (AAM) [36, 37] were used. From all of those template methods, anodic alumina membrane is most attention seeking material due to its structure property and controlled size.

La et al.[30] prepared uniform array of CeO_x nanowire of 60 nm diameter with alumina template. Disadvantage of template method is the several step long procedures and removing

template using harsh chemical. Yu et al.[37] synthesized CeO_x nanowires from the non-hydrolytic sol–gel reaction of cerium(III) nitrate and diphenyl ether in the presence of appropriate surfactants with less diameter, but this synthesis route has an unavoidable drawback that the surface of the nanowire is not ‘‘clean”, which have large amounts of organic species, covering the CeO_x surface. CeO_x material is very useful for catalysis so designing of CeO_x material will be helpful for development of electro-catalysts. In this chapter, synthesis and growth of CeO_x nanowire will be explain in detail later. And we prepared CeO_x nanowire by using alchothermal because of difficulties in the hard template method.

3-3 Optimization of fabrication condition of fine CeO_x nanowires

To design the active interface between Pt and CeO_x nanowire, the fabrication of fine CeO_x nanowire which has active surface is required. As mentioned in the present chapter, previously reported CeO_x nanowire as active metal support or promoter is not preferable because of less active surface for fabrication of Pt-CeO_x interface such as its thick diameter and low aspect ratio. To design the active Pt-CeO_x interface on Pt, the preparation process should be examined to optimize the fabrication condition of fine CeO_x nanowires.

3-3-1 Growth process analysis of CeO_x nanowire

Nanowires of CeO_x were grown by alcohothermal process using soft template surfactant cetyltriethylammonium bromide (CTAB). Surfactant molecules spontaneously organized into micelles when their concentration reached to critical value[29]. These anisotropic structures can be immediately used as soft template to promote the formation of nanowire when coupled with an appropriate chemical and electrochemical reaction. Mann and co-workers and Yang and co-workers explained synthesis of nanorodes[30] based on this idea.

We saw that in growth process of CeO_x nanowire, micelle formed at initial stage of CeO_x formation process. Then, CeO_x nanowires were slowly developed at 80°C in alchohothemal process (shown in Figure 3-1).

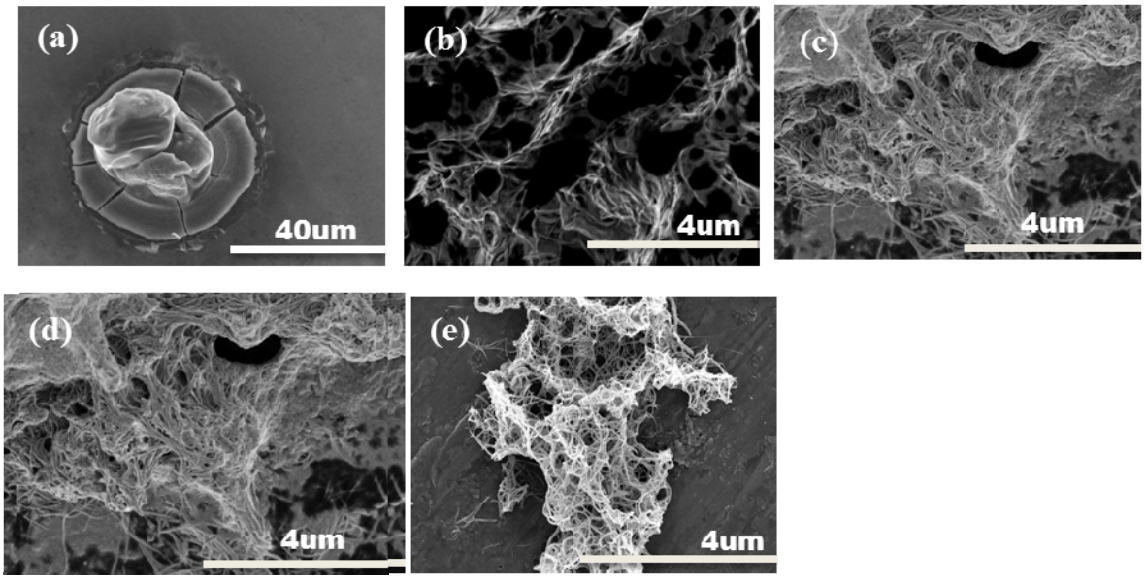

Figure 3-1 Scanning electron microscopy images observed for developed CeO_x nanowire, starting material (a), product after 24h reaction (b), product after 48h reaction (c), product after 72h reaction (d) and product after 96h reaction at 80°C.

3-3-2 Influence of reaction time and reaction temperature on change of aspect ratio of CeO_x nanowire

To examine aforementioned growth process of CeO_x nanowires in detail, the influence of the reaction time and reaction temperature on the change of the aspect ratio of fabricated CeO_x nanowires was examined. Figure 3-2 shows the reaction time dependence of the observed aspect ratio of CeO_x nanowires which was examined at 80°, 100°, 125°, and 150°C. The reaction time varied from 1, 2, 3, 4 and 5h at each reaction temperature. After each growth period, the prepared

CeO_x nanowires were rinsed by distilled water (2 times) and ethanol (1 time) to remove the remained impurity from CeO_x nanowire surface. The aspect ratio which is ratio between length and diameter of CeO_x nanowires was estimated at aforementioned fixed reaction temperature and reaction time by using SEM, as shown in Figure 3-2.

(a)

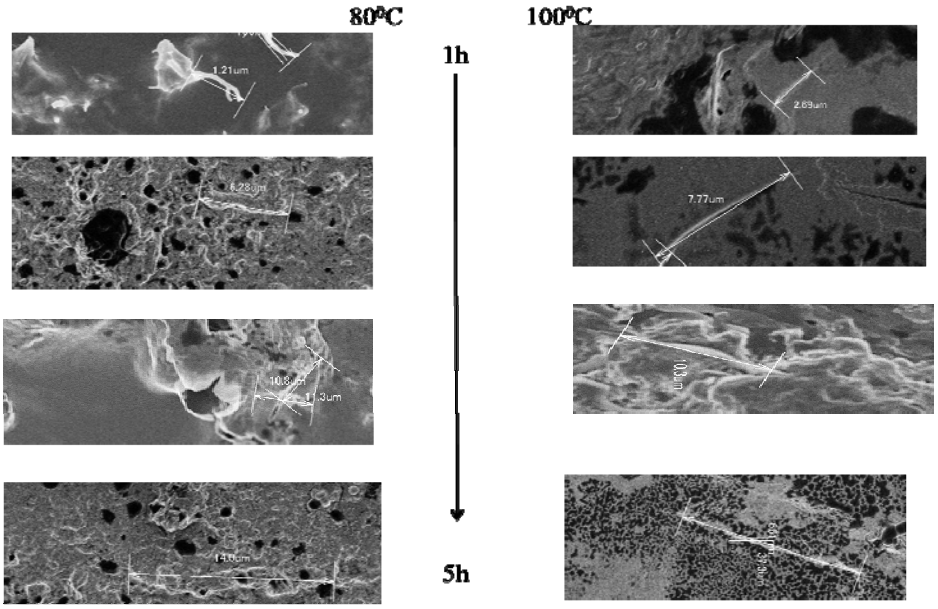

(b)

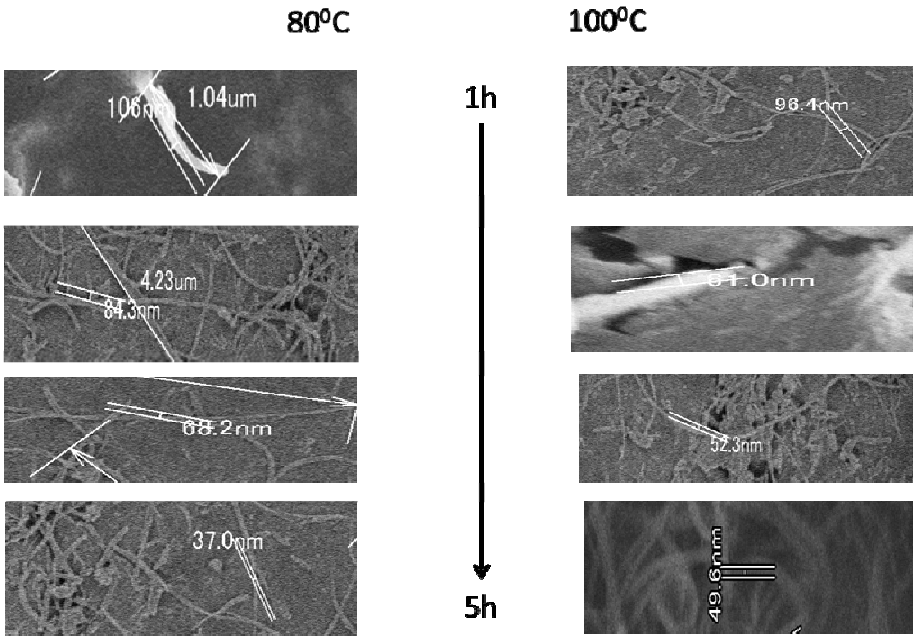

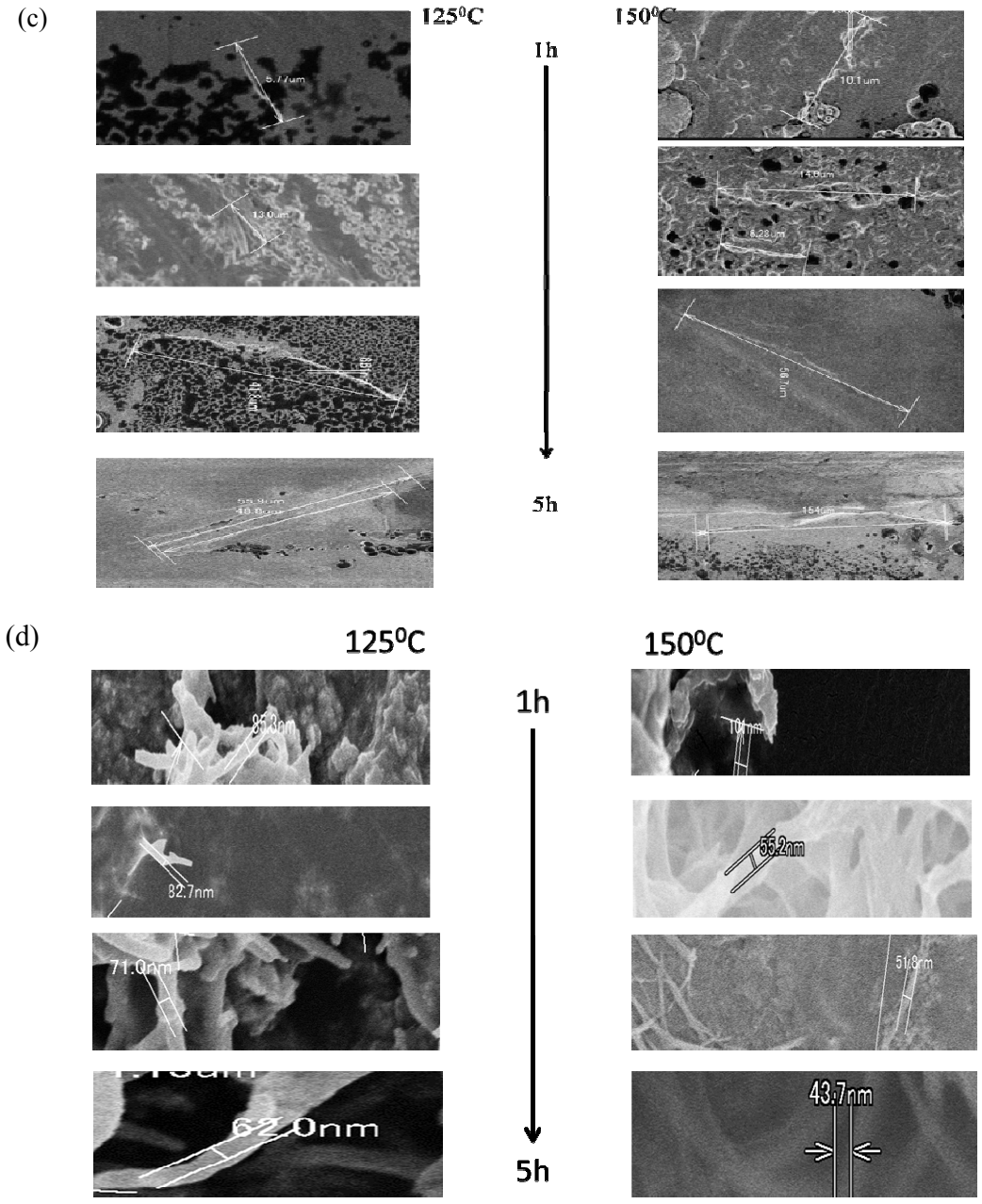

Figure 3-2 Representative morphology change of CeO_x nanowire at fixed time and fixed temperature; (a): representative length observation data at 80°C and 100°C for 1 to 5h, (b): representative width observation data at 80°C and 100°C for 1 to 5h, (c): representative length observation data at 125°C and 150°C for 1 to 5h, (d): representative width observation data at 125°C and 150°C for 1 to 5h.

A control of aspect ratio of CeO_x nanowire would be important for fabrication of useful reaction stage on CeO_x nanowire. In the present thesis work, it is expected that CeO_x nanowire with large aspect ratio will create large opens space around CeO_x nanowires and provide the surface of CeO_x nanowire the wide reaction space for fabrication of large amount of Pt-CeO_x interface.

To estimate the aspect ratio of prepared CeO_x nanowires, approximately 10 samples of CeO_x nanowire were observed at each fixed reaction time and fixed reaction temperature. Then, the average aspect ratio values observed in SEM pictures of Figure 3-2 were plotted in Figure 3-3.

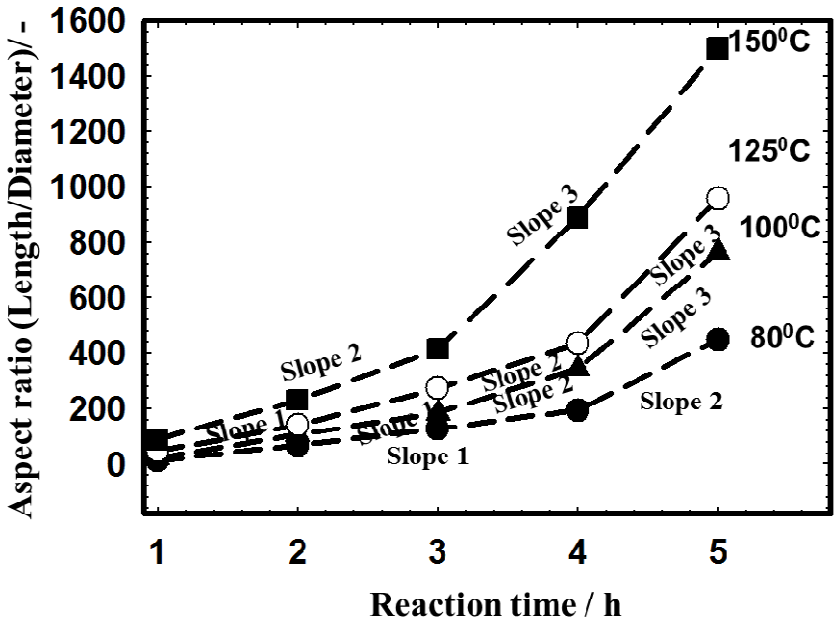

Figure 3-3 Relationship between aspect ratio (Length/Diameter) of CeO_x nanowire and reaction time at fixed reaction temperature, reaction temperature: 80°C, 100°C, 125°C, and 150°C. Three kinds of slopes were noticed in each curve (i.e. slope 1, slope 2 and slope 3).

In Figure 3-3, the aspect ratio observed for fabricated CeO_x nanowire increased with increasing reaction time at each reaction temperature. To characterize the growth process of CeO_x nanowire, the characterization of initial stage of growth of CeO_x nanowire is important. In the middle and final stage of growth process, it becomes hard to estimate the aspect ratio of CeO_x nanowire in the present fabrication process. Figure 3-3 tells that the different three slopes were observed in each curve. The observed slopes were summarized in Table 3-1. Table 3-1 suggests that there are three different steps in the initial stage of growth process of CeO_x nanowires in the present alcoho-thermal process.

Table 3-1 observed slopes in Figure 3-3.

Slope	observed slope / h^{-1}
1	79 - 84
2	117- 283
3	400 - 560

To characterize each step, the crystal phases observed for the products in each step were examined by using XRD. Figures 3-4(a) to 3-4(e) were XRD profiles observed for reaction products after 1h reaction, 2h reaction, 3h reaction, 4h reaction and 5h reaction, respectively.

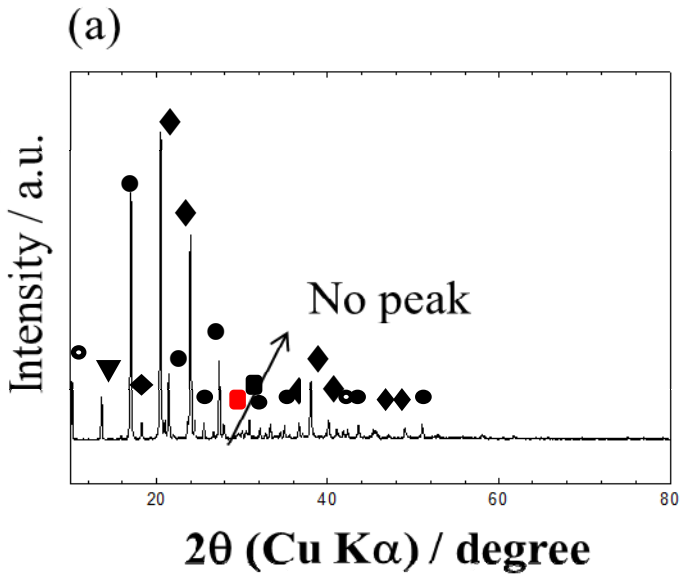

$$\frac{I_{CeO2}(111)}{I_{CeCl3}(100) + I_{CeO2}(111)} \times 100 = 2.1 \text{ / vol\%}$$

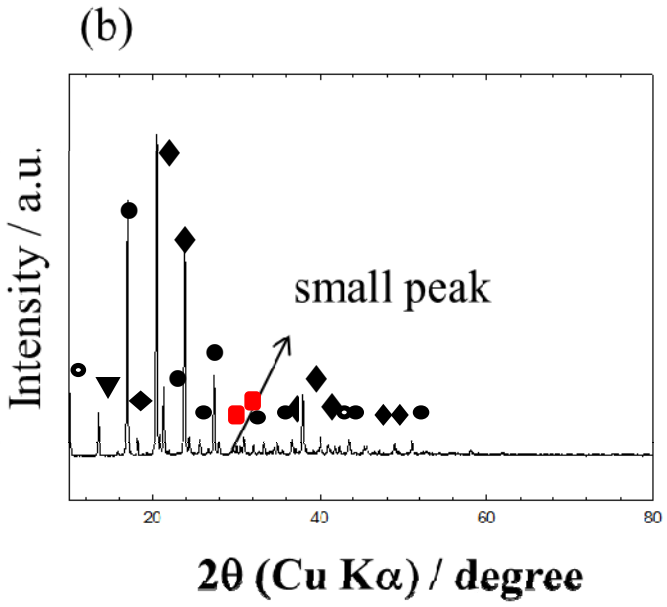

$$\frac{I_{CeO2}(111)}{I_{CeCl3}(100) + I_{CeO2}(111)} \times 100 = 3.3 \text{ / vol\%}$$

(c)

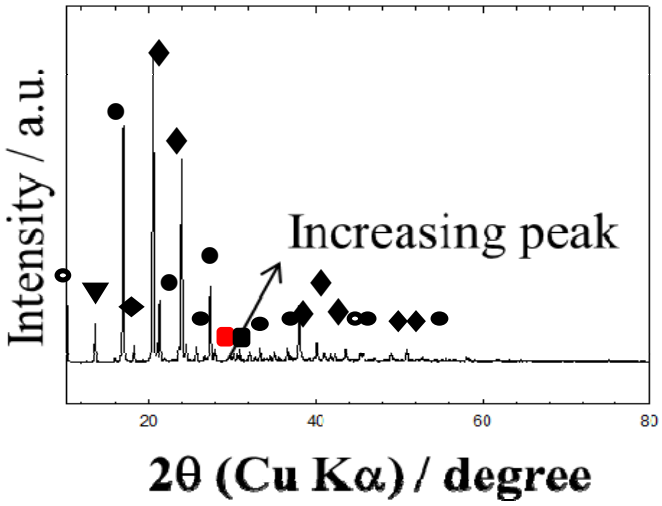

$$\frac{I_{CeO2}(111)}{I_{CeCl3}(100) + I_{CeO2}(111)} \times 100 = 3.3 \text{ / vol\%}$$

(d)

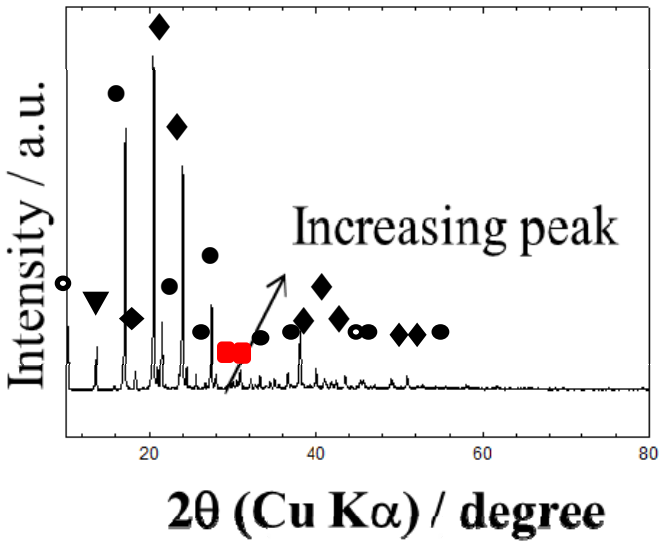

$$\frac{I_{CeO2}(111)}{I_{CeCl3}(100) + I_{CeO2}(111)} \times 100 = 3.3 \text{ / vol\%}$$

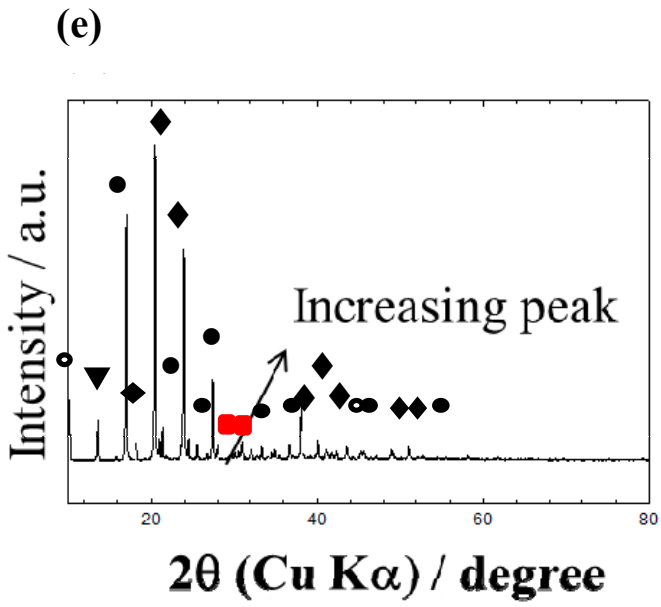

$$\frac{I_{CeO2}(111)}{I_{CeCl3}(100) + I_{CeO2}(111)} \times 100 = 4.0 \text{ / vol\%}$$

$CeCl_3$: ●, $(H_2N)_2CO$: ♦, $Ce(OH)_3$:○, CeO_2: ■ NH_4CO: ▼

Figure 3-4 Effect of reaction time on crystal phases observed for fabricated CeO_x nanowire at 80°C. Reaction time: 1h (a), 2h (b), 3h (c), 4h (d) and 5h (e).

Figure 3-4 (a) indicates that the observed phases mainly consist of crystalline $CeCl_3$ and urea. Since soft template CTAB is amorphous, no XRD peaks taken from CTAB are observed in the XRD profiles. In contrast, small peak which can be assigned by CeO_2 was detected in Figure 3-4 (b). Also the intensity of CeO_2 peak and peak intensity ration between $CeCl_3$ and CeO_2 increased with increasing reaction time, although the peak intensity of CeO_2 was small. Those XRD

analysis data suggest that oxidation of $CeCl_3$ is quite slow, but aforementioned slow oxidation process of $CeCl_3$ to CeO_x would be important process for formation of CeO_x nanowire in the present work.

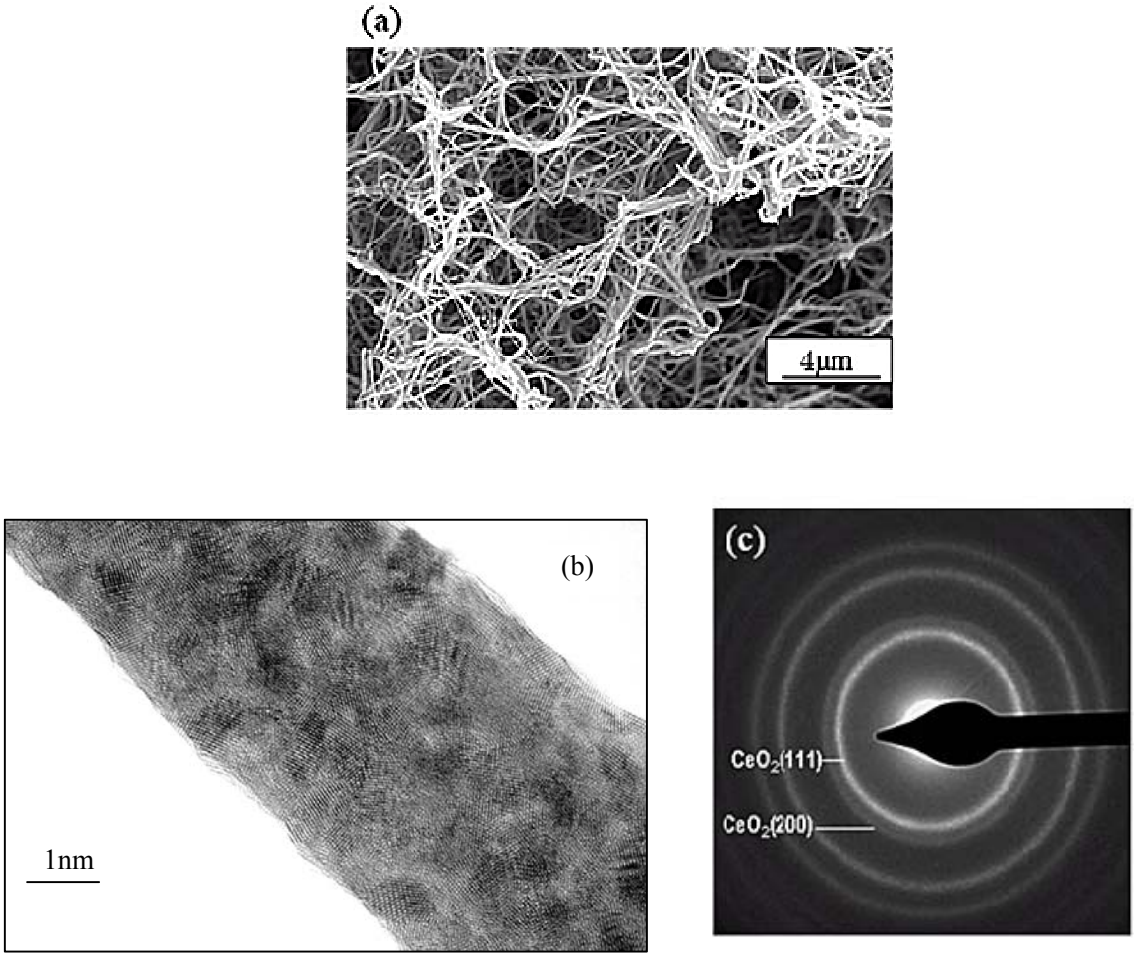

Figure 3-5 SEM photograph (a), TEM image (b) and selected area electron diffraction (c) taken from CeO_x nanowires which were prepared at 80°C, 96h.

Figure 3-5 presents the morphology and crystal phase observed for CeO_x nanowires which were prepared at 80°C for 96h. This figure suggests that the width of prepared CeO_x nanowire is

around 20nm and the observed aspect ratio is more than 1000. And the observed crystal phase of CeO_x nanowire mainly consists of Ce^{4+}. Based on the conclusion of Table 3-1, the expected whole length of CeO_x nanowire prepared at 80°C for 96h which is displayed in Fig. 3-5 is approximately 36μm (= (400*90)nm) or more. Also its expected aspect ratio of CeO_x nanowire prepared at 80°C for 96h is 1800 or more. Those expected length and aspect ratio based on Figure 3-3 and Table 3-1 are reasonable as compared with SEM and TEM observation results.

Based on all experimental data, it is concluded that the oxidation process of $CeCl_3$ in soft template CTAB is important for a control of aspect ratio of CeO_x nanowire and preparation of active reaction space on CeO_x nanowire in the present synthesis process.

3-3-3 Effect of urea

To control the oxidation process, the selection of oxidizing regent is also important for preparation of fine CeO_x nanowire.

In general, urea gives the reactants OH^- ion and hydrolysis process is promoted. Zhong et al.[38] examined the role of urea in other reaction system, and that work suggests that no hydrolyzed precipitation was observed in their reaction without urea. This clearly indicates the role of urea in hydrolysis and oxidation process.

To apply this important result to the present work, we examined the role of urea before we examined the relationship between aspect ratio (Length/Diameter) of CeO_x nanowire and reaction time at fixed reaction temperature (i.e. Figure 3-3). Figure 3-6 demonstrates the XRD analysis results for reaction products which were obtained by without urea and with urea reactions.

(a)

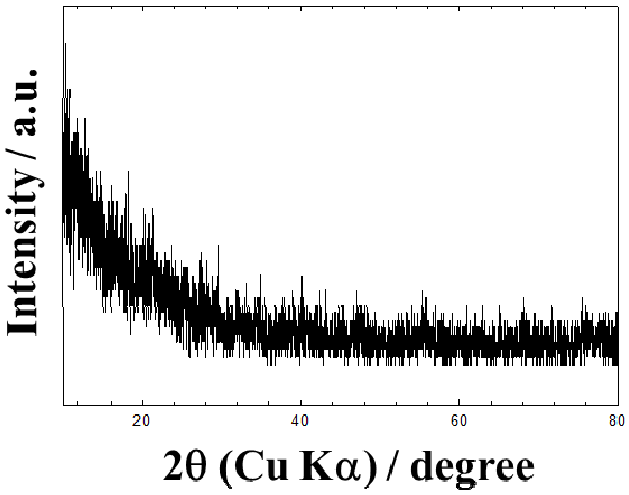

(b)

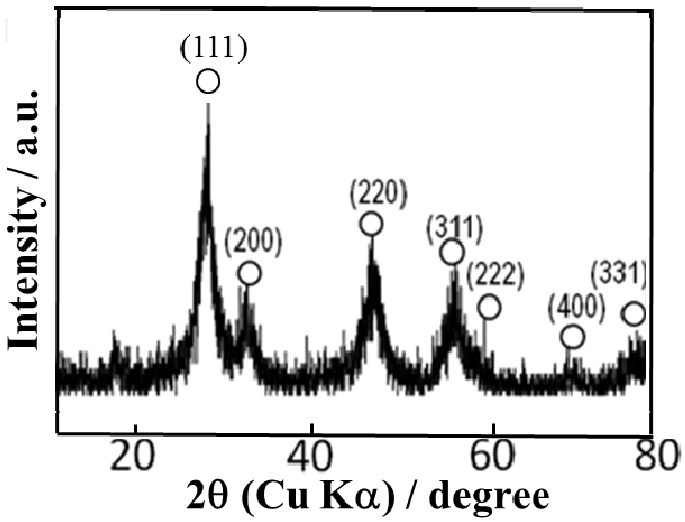

Figure 3-6 XRD profiles taken from the reaction products which were obtained by without urea reaction (a) and urea reaction (b) at 80°C for 96h. (○ : Cerium oxide)

In addition, Figure 3-7 presents the photograph taken from the reaction products which were obtained by without urea reaction (a) and urea reaction (b) at 80°C for 96h. As shown in this

figure, no clear precipitants were observed in the reaction products which were obtained without urea reaction.

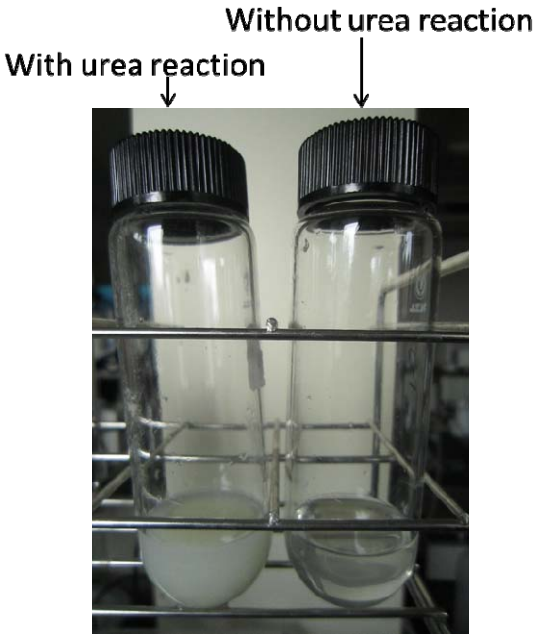

Figure 3-7 Comparison of the reaction products which were obtained by without urea reaction (a) and urea reaction (b) at 80°C for 96h (urea is not in the reaction system) .

This data also clearly suggests that the combination reaction of hydrolysis and oxidation reaction of the mixture of $CeCl_3$ and soft template CTAB by using urea plays key role for fabrication of fine CeO_x nanowires in the present alcohothermal process.

3-3-4 Role of soft template CTAB

For optimizing process of CeO_x nanowire, the different surfactants like sodium dodecyl sulfate ($CH_3(CH_2)_{11}OSO_3Na$) was examined instead of CTAB.

Figure 3-8 shows SEM photograph taken from reaction products which were obtained at 80°C for 96h in the alcohothermal process by using $CH_3(CH_2)_{11}OSO_3Na$ as soft template.

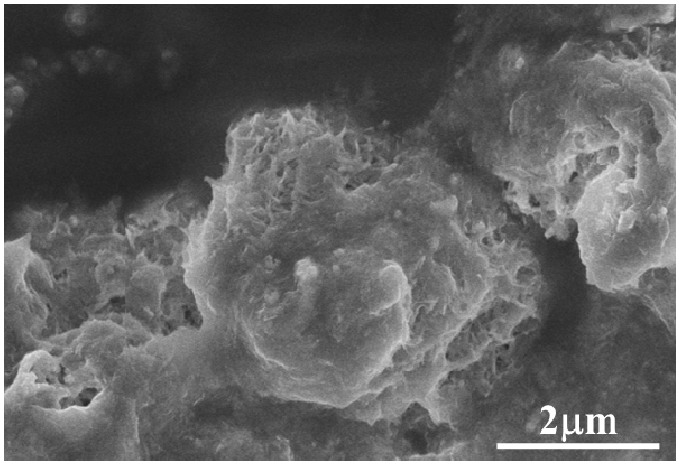

Figure 3-8 SEM photograph taken from sodium dodecyl sulfate soft template product.

In Figure 3-8, no CeO_x nanowires morphology were observed at all. To compare the role of surfactants (i.e soft templates), crystal phases of products which were prepared by using sodium dodecyl sulfate were examined by using XRD analysis. As shown in Figure 3-9, the starting materials were remained after 4 days synthesis. Also, CeO_2 phase was observed in the XRD profile. The morphology of the products was just agglomerated particles which were shown in the SEM image (i.e. Figure 3-8).

The different morphology which looks like micelle was observed when CTAB was used. Also each micelle like particle lined up during preparation process when CTAB was used.

Based on those results, the following results can be concluded. The starting materials $CeCl_3$ and urea were absorbed on CTAB molecule as surfactant. The CTAB molecule with aforementioned starting materials made the micelle like in alcohol solvents. The micelle like particle lined up under the applied pressure in the reactor (i.e diffusion process which was

described in the present Chapter 3). Then, the starting materials $CeCl_3$ was slowly oxidized in the micelle like particles. Also, the CTAB was slowly oxidized as well in the present process. Eventually, CeO_x nanowire with one dimensional structure would be formed in the present process. The growth process of CeO_x nanowire was summarized in Figure 3-11.

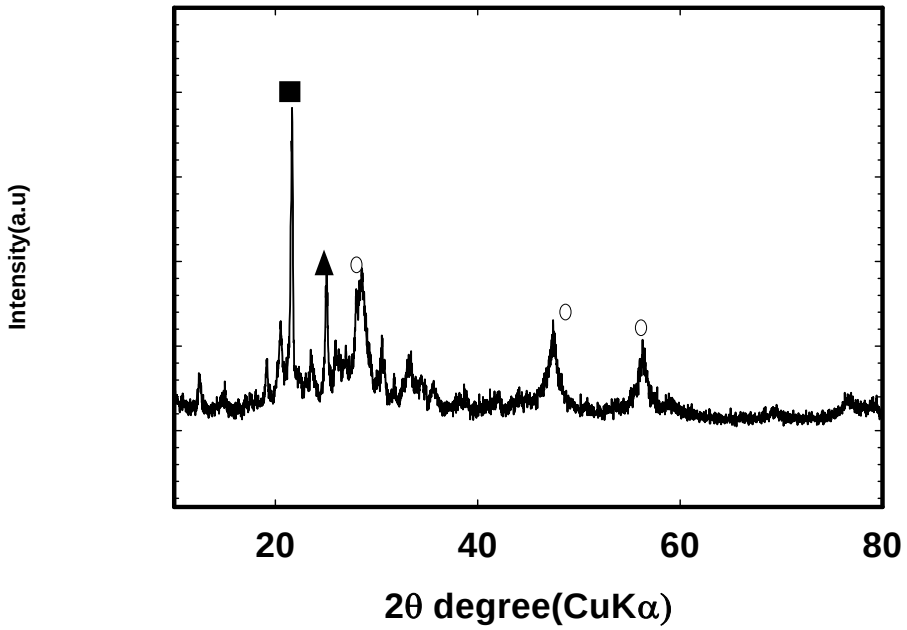

Figure 3-9 XRD profile taken from the reaction product which were obtained by sodium dodecyl sulfate ($CH_3(CH_2)_{11}OSO_3Na$)) .

▲ :$CeCl_3$, ○ : CeO_2, ■: NaCl

3-3-5 Effect of water

Solvent in the present process is one of the important factors for fabrication of CeO_x nanowire. The morphology difference of reaction products using different solvent was shown in Figure 3-10 (a). As shown in Figure 3-10(a), if solvent was water, the morphology of reaction products are round shaped big particles. This result suggests that CeO_x nanowires can be created

by using dehydrated ethanol. Also, XRD profile taken from product (Figure 3-10(b)) indicates that product is mainly consists of $CeCl_3$ (i.e one of starting materials) and NH_4Cl (i.e. by product). In addition, it is conclude that the urea ($CO(NH_2)_2$) is dissolved into water and the desired reaction space with the micelle like structure for fabrication of CeO_x nanowires is not formed when solvent is water. The urea molecule would help the formation of $Ce(OH)_3$ in the present hydrolysis process. To prepare the CeO_x nanowire, the alcohol solvent is required.

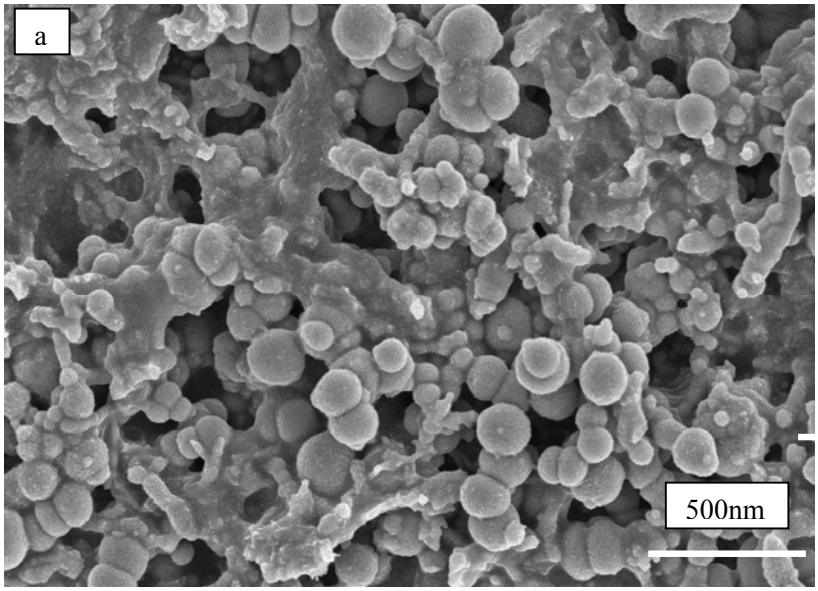

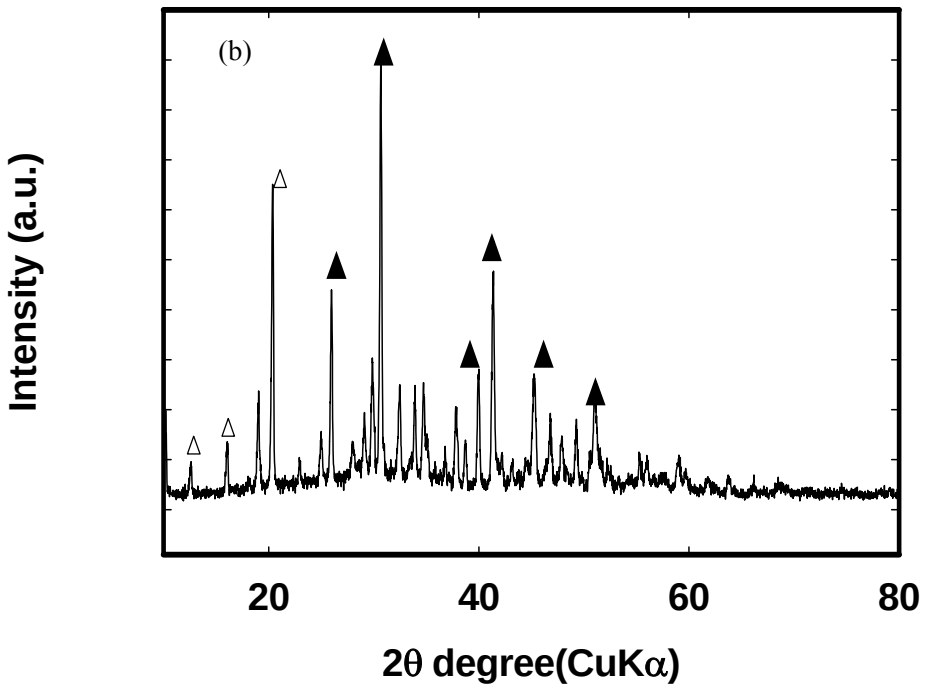

Figure 3-10 a) SEM image and b) XRD profile taken from the reaction products which were obtained by using water as solvent for fabrication of CeO_x nanowire at 80°C for 96h.

3-3-6 Formation process of CeO_x nanowire

There are significant researches for the growth of nanowire includes solution based growth[11], template based growth[12], and thermal oxidation[13-15]. However, those reports cannot clearly explain the detailed growth process of nanowire by alcohothermal process whose alias is solvothermal process. In the previous reported papers, various templates were used for development of 1 dimensional nanomaterials and self-assembly 0 dimensional nanostructure. Also, various kinds of growth process of oxide nanowire were proposed such as nucleation and growth mechanism on the anisotropic crystallographic structure of solid, effect of liquid droplet

formed by the vapor on the substrate, and kinetic control for size reduction of 1 dimensional nanostructure. But those methods have poor responsibitlity[39].

Based on the experimental results in the present Chapter, the formation process of CeO_x nanowire was briefly summarized as follows; in the first step of synthesis, CTAB molecules with $CeCl_3$ was appeared in the reaction space which is micelle like morphology. Gentle oxidation reaction of $CeCl_3$ was occurred in the reaction space which is micelle like morphology. And $Ce(OH)_3$ was formed in there. In the autoclave, the micelles with $Ce(OH)_3$ lined up under the applied pressure. Subsequently, CeO_x nanowire which consists of well crystalline CeO_x primarily particles is formed by the slow oxidation of both surfactants with micelle like morphology and $Ce(OH)_3$ in the micelles. Aforementioned formation process of CeO_x nanowire in the present thesis work was summarized in Figure 3-11.

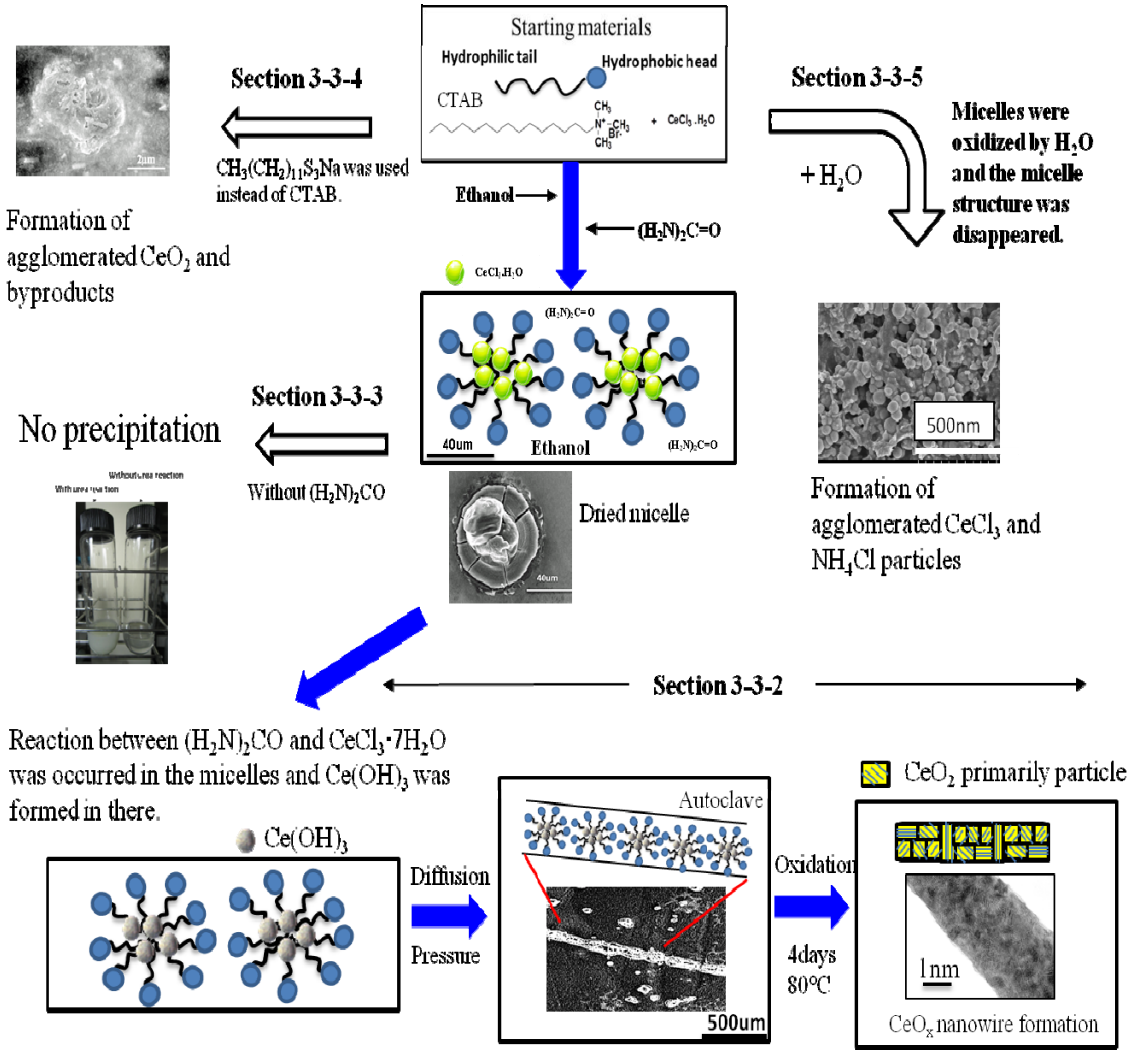

Figure 3-11 Schematic diagram for summary of formation process of CeO_x nanowire.

3-4 Pt particles loading on CeO_x nanowire

To impregnate the fine Pt particles on the CeO_x nanowire, $K_2PtCl_4 \cdot H_2O$ powder was dissolved in distilled water and the suspension was mixed for 1h. The K_2PtCl_4 aqueous solution was dropped into the previously prepared CeO_x nanowire solution in which the CeO_x nanowires were dispersed in the distilled water. The mixture was left at room temperature for 12h. The platinum complex in the mixture was reduced at room temperature for 1h in sodium borohydride

($NaBH_4$) aqueous solution. The mixture was rinsed by water and ethanol. And it was dried at room temperature in nitrogen atmosphere. In the final stage, the prepared Pt-CeO_x nanowire and carbon black (CB, Vulcan XC-72R, Cabot Co.) were dispersed in ethanol and dried in a N_2 gas flow. The morphology of prepared Pt loaded CeO_x nanowires was observed using SEM.

After Pt particles were loaded on CeO_x nanowires, the width of CeO_x nanowires conspicuously differed from Pt unloaded CeO_x nanowires as shown in **Fig.3-12(a) and 3-12(b)**. The observed diameters of nanowires which Pt particles were impregnated varied from 40 to 200nm.

In the present work, the following equilibriums could be considered for the formation of nano-sized Pt particles on CeO_x nanowires.

$$\mathbf{CeO_x\text{-}wire\ (CeO_2, Ce_2O_3) + H_2O + K_2PtCl_4 \cdot H_2O \leftrightarrow Ce_2O_3PtClCeO_2 + 2KOH + 3/2Cl_2 + H_2} \quad \mathbf{(3\text{-}1)}$$

$$\mathbf{2(Ce_2O_3PtClCeO_2) + 6H_2O \leftrightarrow 3Ce(OH)_3\text{-}O\text{-}PtCl + ClPt\text{-}O\text{-}(Ce_2O_3, CeO_2) + 3/2H_2} \quad \mathbf{(3\text{-}2)}$$

$NaBH_4$ addition:

$$\mathbf{Ce(OH)_3\text{-}O\text{-}PtCl + ClPt\text{-}O\text{-}(Ce_2O_3, CeO_2) \leftrightarrow Ce(OH)_3\text{-}O\text{-}Pt + Pt\text{-}O\text{-}(Ce_2O_3, CeO_2) + Cl_2} \quad \mathbf{(3\text{-}3)}$$

During the reduction reaction of K_2PtCl_4 by using $NaBH_4$, $Ce(OH)_3$ layer would cover the rough surface of CeO_x nanowire through Eq.(3-1) to Eq. (3-3). Also, it is concluded that the interface between $Ce(OH)_3$ and CeO_x nanowire can be useful reaction space for the formation of nano-sized Pt particles. In addition, $Ce(OH)_3$-O-Pt and Pt-O-(Ce_2O_3, CeO_2) shown in Eq.(3-3) would be formed on the CeO_x nanowire in the present process.

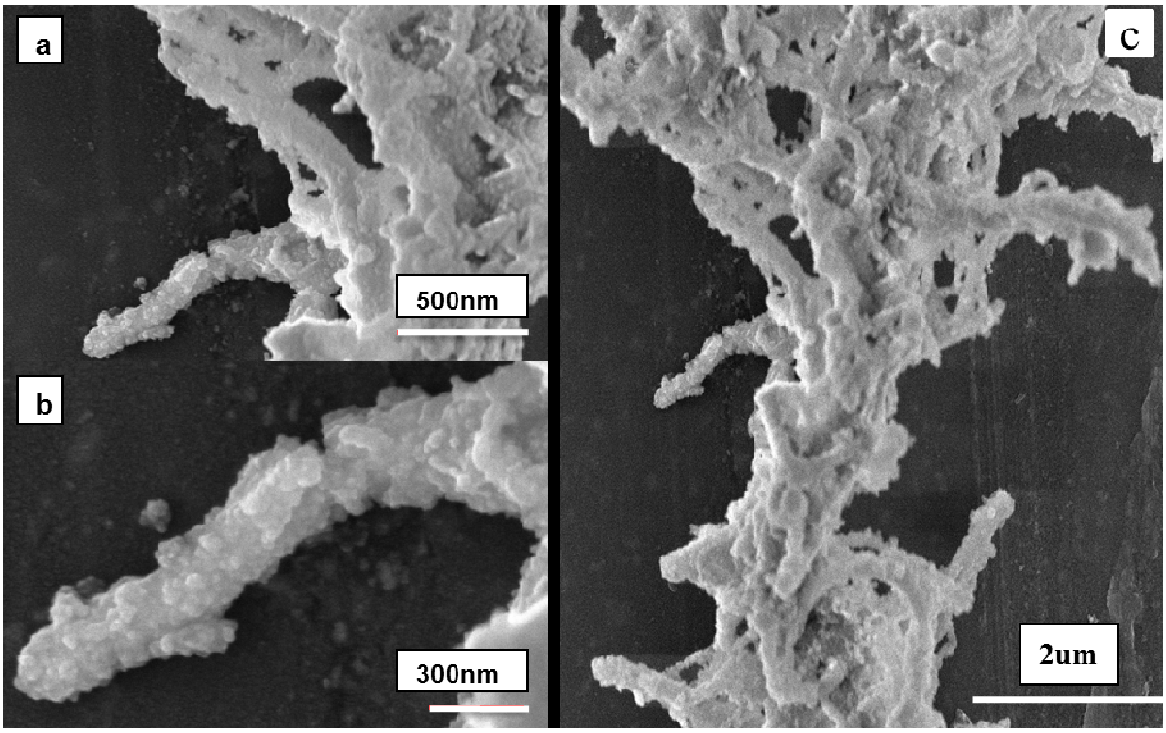

Figure 3-12 (a)-(c) SEM images of CeO_x nanowire after Pt loading.

3-5 Physical characterization of Pt loaded CeO_x nanowire

3-5-1 Crystal phase identification by XRD

After loading of Pt on CeO_x nanowire, the identification of the crystal phases of the CeO_x nanowire and the nanosized Pt-loaded CeO_x nanowire/C at larger length scale (i.e. not only at the nanoscale) were performed by using XRD analysis as shown in Figure 3-13. The XRD profile obtained from the CeO_x nanowire (Figure 3-13(a)) indicates that simple fluorite CeO_2 pattern is observed. And it agrees with the phase analysis result of selected area electron diffraction pattern in Figure 3-16(b). Pt, CeO_2 and Ce $(OH)_3$ phases can be clearly observed during the Pt embedding process at the interfacial space between CeO_x nanowire and $Ce(OH)_3$ (Figure 3-13(b)). After the electrochemical pretreatment process, the diffraction peaks due to $Ce(OH)_3$

were absent from the electrochemically pre-treated specimen as shown in Figure 3-13(c). It indicated that $Ce(OH)_3$ was removed from the Pt loaded CeO_x nanowire/C and Pt particles appeared on the CeO_x nanowires among low crystallinity C particles (Figure 3-13(c)).

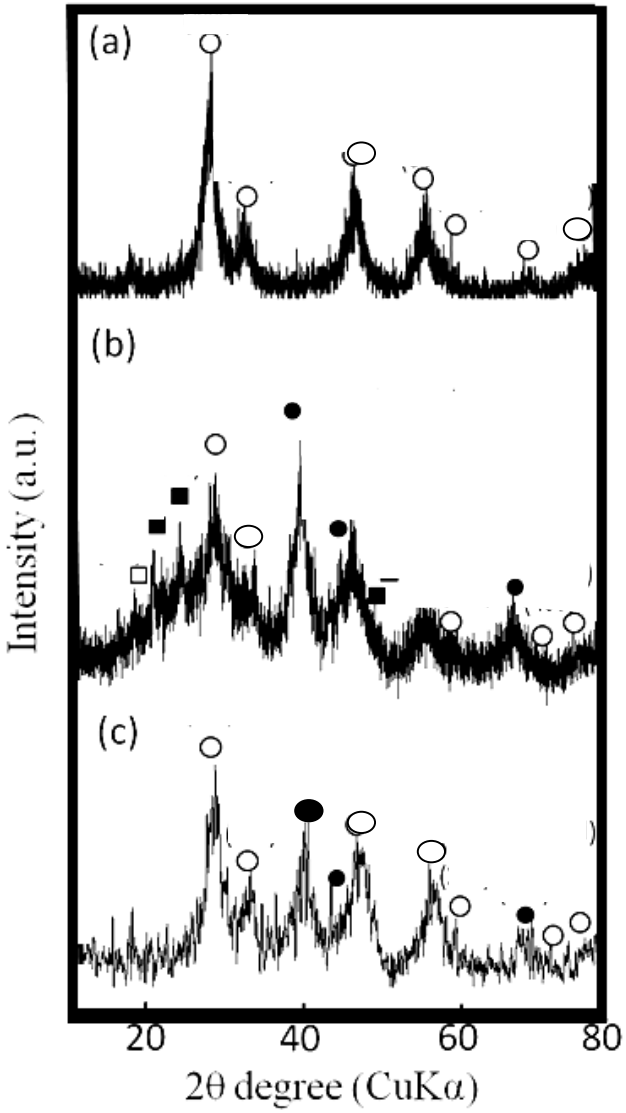

Figure 3-13 XRD profiles taken from the prepared CeO_x nanowire (a), Pt loaded CeO_x nanowire prior to the electrochemical pre-treatment, and (b) Pt loaded CeO_x nanowire/C after the electrochemical pre-treatment (c). **●: Pt, ○: CeO_2, ■: $Ce(OH)_3$.**

3-5-2 Surface chemical state of Pt loaded CeO_x nanowire

To examine the composition at the interface and surface of the sample prior to the electrochemical pre-treatment, Pt loaded CeO_x nanowire was characterized by using XPS. The Pt 4*f* spectrum in Figure 3-14(a) presents two spin-orbital splitting doublets Pt $4f_{7/2}$ - $4f_{5/2}$. The peaks at 70.9 and 72.6eV are attributable to metallic Pt (Pt^0)[20] and divalent Pt (Pt^{2+}, PtO) [21], respectively, while the peak at 73.5eV is due to tetravalent Pt (Pt^{4+}, PtO_2)[22]. The other peak at binding energy of 71.9eV, labelled as Pt-O-X (X: $Vo^{\cdot\cdot}$, Ce), could correspond to slightly ionized Pt, which is attributed to the formation of Pt-O-Ce bonds at the interface between Pt and CeO_x nanowires. A similar slightly ionized Pt peak has been also reported by Fugane et al.[23] Fugane et al. suggested that the slightly ionized Pt peak midway between metallic Pt and Pt^{2+} is attributable to the formation of Pt-O-Ce bonds at the interface between Pt and CeO_x. Also, formation of Pt-O-Ce bonds at the interface is supported by the first principle calculation of Yang et al.[24].

Ce 3*d* spectra show many characteristic peaks due to spin orbital splitting of $3d_{5/2}$ and $3d_{3/2}$ states. In Figure 3-14(b), the symbols ν, u, ν″, u″, ν□ and u□ correspond to $3d_{5/2}$ and $3d_{3/2}$ states observed for Ce^{4+} species and the other symbols ν^0, u^0, ν′ and u′ correspond to $3d_{5/2}$ and $3d_{3/2}$ states observed for Ce^{3+} species[34]. The XPS spectra indicate that the surface and interface consist of CeO_x species (CeO_2 and Ce_2O_3) and $Ce(OH)_3$.

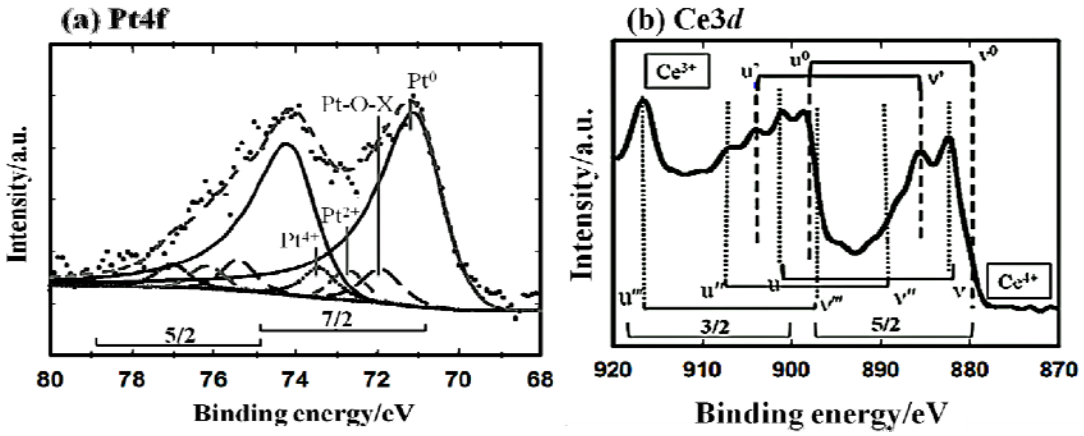

Figure 3-14 Pt 4*f* XPS spectrum (a) and Ce3*d* XPS spectrum (b) observed for 0.975mgml^{-1} Pt loaded CeO_x nanowire/C prior to the electrochemical pre-treatment process. Rough dotted line Pt 4*f* spectrum in Figure 3 (a) is observed Pt 4*f* XPS spectrum. Weak dashed line profile in Figure 3 (a) is the constructed spectrum using separation peaks. Pt-O-X indicates that X means $V_o^{\cdot\cdot}$(=oxygen vacancy) or Ce cation.

3-5-3 Effect of pre-treatment on surface of Pt-CeO_x nanowire/C

To characterize the surface and interface of the electrochemically pre-treated Pt-loaded CeO_x nanowire/C, the chemical compositions of Pt-loaded CeO_x nanowire/C after the electrochemical pre-treatment process were observed using XPS. The key peak at the binding energy of 71.9eV which is labeled as Pt-O-X can be clearly observed in Pt 4*f* spectra (Figure 3-15(a)). The peak intensity ratio between Pt-O-X peak and metallic Pt was approximately 0.27. Since the previously reported peak intensity ration between Pt-O-X peak and metallic Pt which was observed for electrochemically pre-treated Pt loaded CeO_x nano-particles/C was approximately 0.14[32], the observed peak intensity ratio between Pt-O-X peak and metallic Pt observed for the electrochemically pre-treated Pt loaded CeO_x nanowires/C was approximately twice as compared with that observed for the electrochemically pre-treated Pt loaded CeO_x nano-particles/C. And Ce^{3+} peaks which are labelled as v^0, v^0, v′ and u′ and Ce^{4+} speaks labelled as v, u, v″, u″, v‴ and

u‴ in Figure 3-15(b) was clearly observed as well as the Ce3*d* spectrum observed for Pt loaded CeO_x nanowire/C prior to the electrochemical pre-treatment process. Fugane et al.[23,28] observed the surface and interface composition on Pt loaded CeO_x nano-particle/C using XPS analysis. In their works, the observed Ce3*d* spectra became quite low intensity after the electrochemical pre-treatment process because only small amount of remained CeO_x partially covered the Pt surface after the pre-treatment process in their works. In contrast, the quite strong Ce3*d* spectra was observed for the electrochemically pretreated Pt loaded CeO_x nanowire/C. This suggests that the interaction between Pt and CeO_x is maximized on CeO_x nano-wire in the present work.

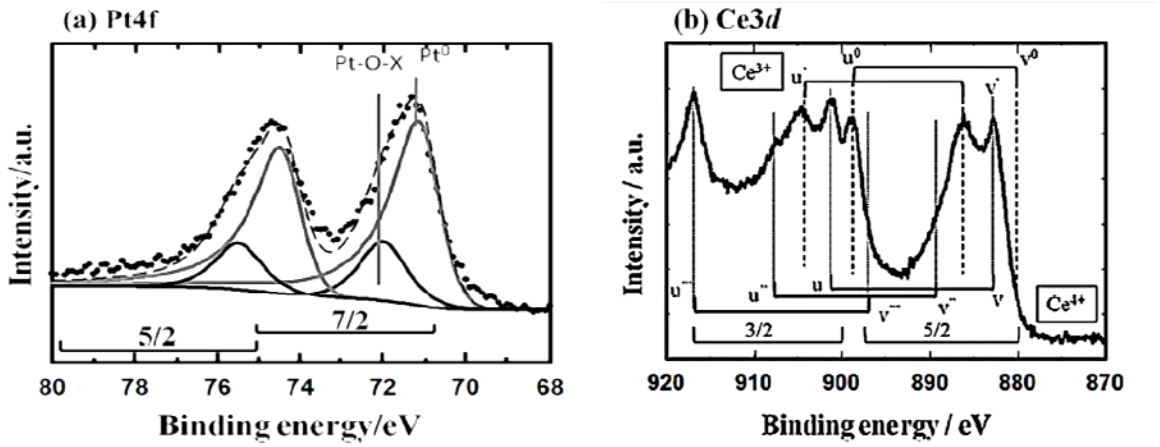

Figure 3-15 Pt 4*f* XPS spectrum (a) and Ce3*d* XPS spectrum (b) observed for 5% Pt loaded CeO_x/C after the electrochemical pre-treatment. Rough dotted line Pt 4*f* spectrum in Figure 3-15 (a) is the observed Pt 4*f* XPS spectrum. Dashed line profile in Figure 3-15 (a) is the constructed spectrum using separation peaks. Pt-O-X indicates that X means $V_o^{\cdot\cdot}$(=oxygen vacancy) or Ce cation.

Table 3-2 shows the presence of Pt cations in the Pt –ceria nanowire electro catalyst. After the electrochemical pre-treatment, Pt-O-X content on the surface of the sample was estimated as

12.03vol%. This information about Pt-O-X species which was formed on the surface indicates the presence of Pt-CeO_x bond. Since the content of Pt-O-X species observed for electrochemically pretreated Pt loaded CeO_x nanowire/C was much higher than that on Pt loaded CeO_x nanopartcile/C, it is concluded that the Pt-CeO_x nanowire interface formation on the Pt loaded CeO_x nanowire/C after electrochemical pre-treatment will be helpful in the electro catalysis which will be examined in Chapter 4 and Chapter 5 of the present thesis.

Table 3-2 Surface Pt composition observed for Pt loaded CeO_x nanowire by SXPS.

	Pt^0	Pt-O-X	Pt^{2+}	Pt^{4+}
Before pre-treatment	**43.33**	**22.52**	**27.14**	**7.01**
After pre-treatment	**44.34**	**12.03**		

3-5-4 Microanalysis of Pt-CeO_x nanowire electro catalyst

3-5-4 (a) CeO_x nanowire

Microstructure and crystal phase were characterized by using TEM as shown in Figure 3-16(a) and 3-16(b). Surfaces of CeO_x nanowire are rough at the nano-scale and have protrusions which consist of well crystalline CeO_x particles (Figure 3-16(b)). Electron diffraction rings can be assigned to CeO_2 (i.e. CeO_2 (d(111) ≈ 3.1Å, d(200) ≈ 2.7Å, d(220) ≈ 1.9Å) in the selected area electron diffraction pattern (SAEDP). CeO_x nanowire surface looking smooth in the macro scale, but in the nanoscale rough surface of CeO_x nanowires can be seen which make them suitable for fabrication of functional interfaces between nanosized Pt and CeO_x nanowire surface.

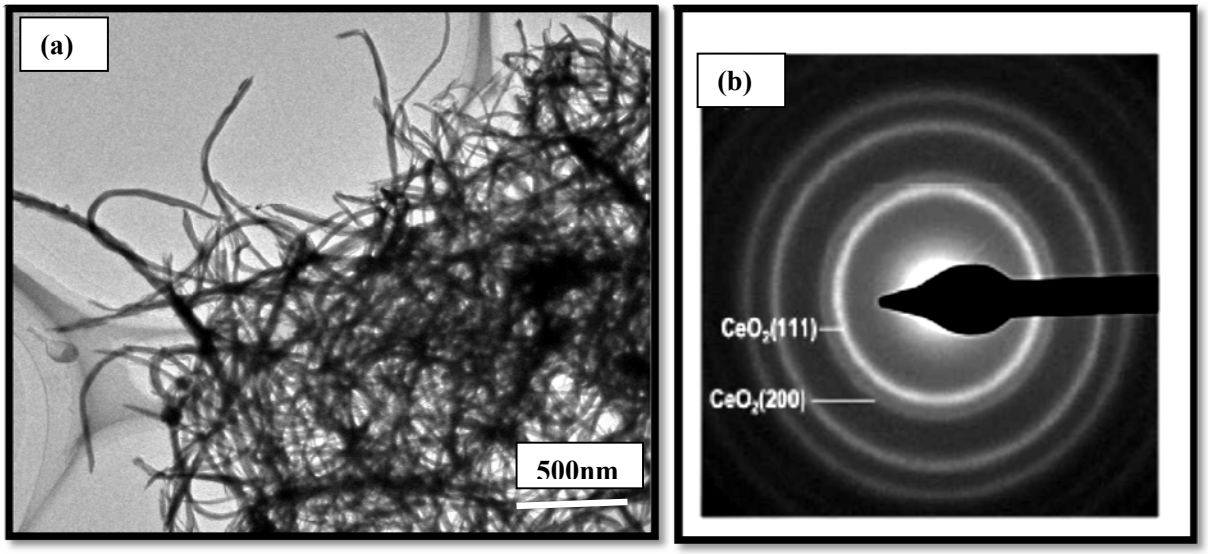

Figure 3-16 (a) High resolution TEM image and (b) selected area electron diffraction pattern taken from as prepared CeO_x nanowire.

3-5-4 (b) Pt loaded CeO_x nanowire microstructure

Pt particles were loaded on CeO_x nanowires, the width of CeO_x nanowires differed conspicuously from that of Pt-free CeO_x nanowires as shown in Figure 3-17(a) and (b). The observed diameters of nanowires impregnated with Pt particles varied from 40 to 200nm. The observed diffraction rings in Figure 3-14(c) can be assigned to CeO_x (i.e. CeO_2: (d(111) ≈ 3.1Å, d(200) ≈ 2.7Å), Ce_2O_3: d(222) ≈ 3.2Å, d(400) ≈ 2.8Å), Pt (i.e. d(111) ≈ 2.3Å, d(200) ≈2.0Å, d(220) ≈1.4 Å)) and $Ce(OH)_3$ (i.e. d(211) ≈1.8 Å). Also, small diffraction spots within the diffraction rings due to Pt in the SAEDP such that the Pt is present in a nano-crystalline form. In addition, TEM image of Figure 3-17 (d) shows that the weak contrast layer covers the surface of strong contrast part. As mentioned in the section of synthesis procedure of Pt loaded CeO_x nanowire, CeO_x nanowire and K_2PtCl_4 acidic salt were mixed in the distilled water for the loading of nano-sized Pt particle on CeO_x nanowires. During this mixing process, OH^- species

would adsorb on the CeO_x nanowire surface which makes surface basic. Since K_2PtCl_4 salt which is Pt resources shows acidic behavior in the aqueous solution, K_2PtCl_4 acidic salt would interact with OH^- basic species on the CeO_x nanowire surface. Also, CeO_x nanowire surface was covered by $Ce(OH)_3$ species during reducing process in the present work as shown in Figure 3-17. It is because two different contrasts were clearly observed in TEM image. Lighter contrast area would be $Ce(OH)_3$ and darker area would be CeO_x nanowire. The selected area electron diffraction pattern recorded from the surface of Pt-CeO_x nanowire which is reduced by $NaBH_4$ agreed with this interpretation of TEM observation result. Since Ce $(OH)_3$ species which were formed in reducing process shows the acidic property in the aqueous solution as well as $(OH)^-$ species on CeO_x nanowire, another acid–base reaction sites between K_2PtCl_4 salt and $Ce(OH)_3$ would be expected in the present process. Based on all characterization results, it is concluded that large amount of interaction between Pt and Ce species is occurred on the surface of CeO_x nanowire. In other words, the surface of CeO_x nanowire can be active nano-reaction stage for fabrication of Pt-CeO_x interface and provide the surface of electro-catalysts the large amount of Pt-CeO_x interface on Pt which would contribute to enhancement of electro-catalytic activities. That is unique role of CeO_x nanowire which cannot be observed on the surface of nano-sized CeO_x particles in the previously reported works.

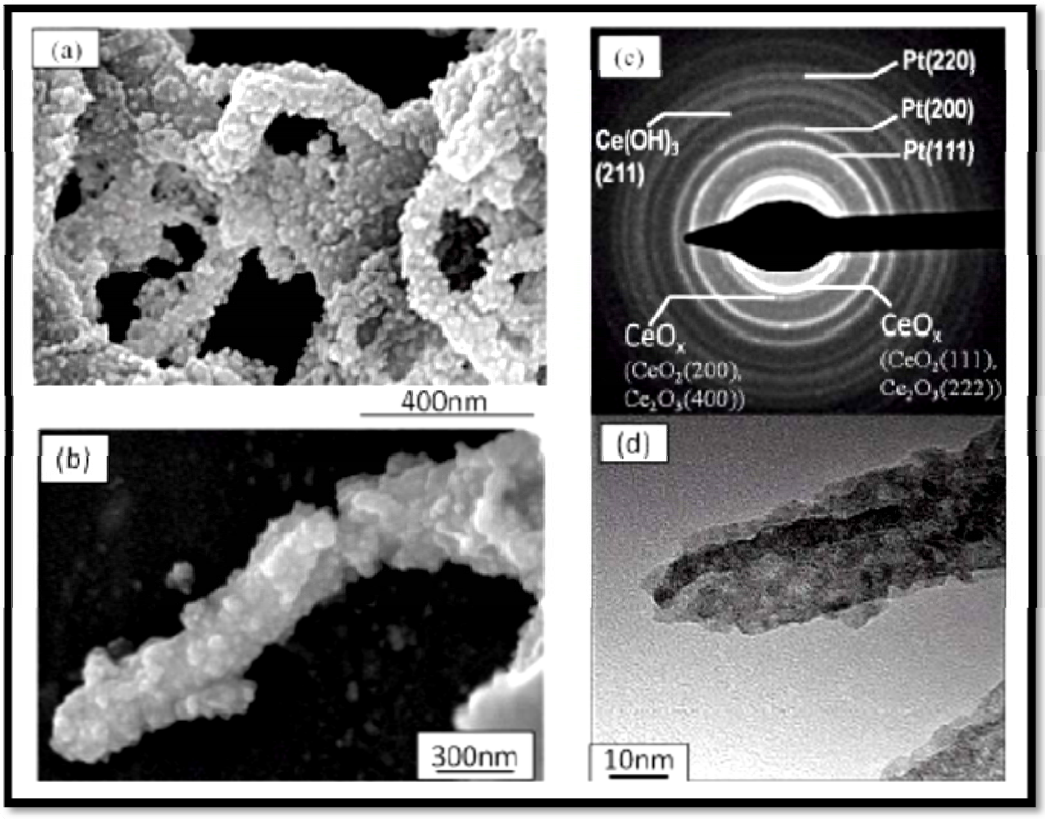

Figure 3-17 SEM images (a and b), selected area electron diffraction pattern (c) and TEM image (d) taken from Pt loaded CeO_x nanowire without carbon prior to the electrochemical pre-treatment.

3-5-4 (c) Microanalysis for electrochemically pretreated electro-catalysts

Prior to the electrochemical measurements, a surface cleaning/conditioning process of Pt-CeO_x nanowire is required. Pt-CeO_x nanowire and carbon black (C) particles were mixed for this surface cleaning/conditioning process of Pt-CeO_x electrodes. Following the electrochemical pre-treatment (i.e. conditioning process) by potential ranging from 0 to 1.5V (vs. RHE) in H_2SO_4 aqueous solution, the Pt loaded CeO_x nanowires were observed using SEM and TEM. SEM micrograph in Figure 3-18(a) presents the aspect of electrochemically pre-treated Pt loaded CeO_x

nanowires. The round shaped C particles were mainly observed in Figure 3-18(a). SAEDP (Figure 3-18(b)) taken from the electrochemically pre-treated Pt loaded CeO_x nanowire/C consists of the diffraction rings which can be assigned as Pt and CeO_x (i.e. CeO_2 and Ce_2O_3). No diffraction rings of C were observed in SAEDP because C particles mainly consist of amorphous carbon. In addition, no other diffraction rings such that the $Ce(OH)_3$ presents in the specimen prior to the electrochemical pre-treatment process was observed in the SAEDP. Also, the small diffraction spots within the diffraction rings due to Pt in the SAEDP such that the Pt is present in a nano-crystalline form as well as Figure 3-17(c). This clearly indicates that the surface impurity (i.e. $Ce(OH)_3$) observed for Pt loaded CeO_x nanowires as shown in Figure 3-17(c) was removed after the electrochemical pre-treatment process. To observe the Pt loaded CeO_x nanowires among C particles, low magnification (Figure 3-18(c)) and high magnification (Figure 3-18(d) and 3-18(e)) TEM observation were performed. The high resolution TEM images taken from the thin areas of the electrochemically pre-treated Pt loaded CeO_x nanowire/C which are marked by using circles in the low magnification TEM image show that nanosized Pt particles (black dots in Figures 3-18(d) and 3-18(e)) appear on the lighter contrast CeO_x nanowire. The particle sizes of nano-crystalline form Pt varied from 2nm to 4nm. The particle sizes of Pt on the CeO_x fat nano-wire and CeO_x thin nano-wire were approximately 3nm and 2nm, respectively.

The microanalysis results shown in Figure 3-17 and Figure 3-18 indicate that Pt particle size would be controlled less than 4nm in the nano-reaction space at the interface between CeO_x nanowire and $Ce(OH)_3$ prior to the electrochemical pretreatment process. And the nano-crystalline form Pt loaded CeO_x nano-wires among round shaped C particles come up after the removal of $Ce(OH)_3$ layer from the surface of the electrochemically pre-treated Pt-CeO_x nanowires/C.

The microstructure change of surface and interface of electrochemically pretreated Pt-CeO_x/C which was prepared by using Pt nanoparticles and CeO_x nanoparticles was previously observed by using TEM[26, 27]. In their works, the small amount of remained CeO_x partially covered the surface of Pt after similar electrochemical pre-treatment in H_2SO_4 aqueous solution. Fugane et al indicated that large amount of CeO_x which has no Pt-O-Ce bond was dissolved from Pt-CeO_x nano-particles/C into H_2SO_4 aqueous solution during the electrochemical pretreatment process and the small amount CeO_x with Pt-O-Ce bond was remained on Pt surface in Pt-CeO_x nano-particles/C [23]. The small amount of remained CeO_x on Pt surface was observed by TEM. In contrast, the exterior of CeO_x nanowire can be clearly observed in conductive carbon particles after electrochemical pre-treatment process. In Figure 3-18 (a) and (b), the conductive carbon particles which were agglomerated around CeO_x nano-wires were observed by using microscopes (i.e. SEM and TEM). In the agglomerated conductive carbon particles, Pt loaded CeO_x nanowires were observed as shown in Figure 3-18 (d) and (e). Since conductive carbon consists of amorphous nature, the diffraction rings of conductive carbon cannot be observed in the selected area electron diffraction pattern recorded from electrochemically pre-treated sample. But the ring patterns of CeO_x and Pt were observed in this selected area electron diffraction pattern. As demonstrated in Figure 3-15(b) of Chapter 3, the peak intensity of Ce3*d* XPS profile observed for the electrochemically pre-treated samples was quite clear and strong as compared with that observed for electrochemically pre-treated Pt-CeO_x nano-particles/C sample[23]. This indicates that the amount of remained CeO_x in Pt-CeO_x nanowire/C electro-catalysts were much higher than that in Pt-CeO_x nano-particles/C electro-catalysts. This suggests that large amount of interface between Pt and CeO_x nanowires was prepared in the present work as compared with previously reported Pt-CeO_x nano-particles/C electrodes, even though the width of CeO_x

nanowire changed from 35nm to 10nm or less after the electrochemical pre-treatment process because of the dissolution of large amount of CeO_x component with no Pt-O-Ce bond from Pt-CeO_x nanowire/C into the acidic solution during the electrochemical pretreatment process.

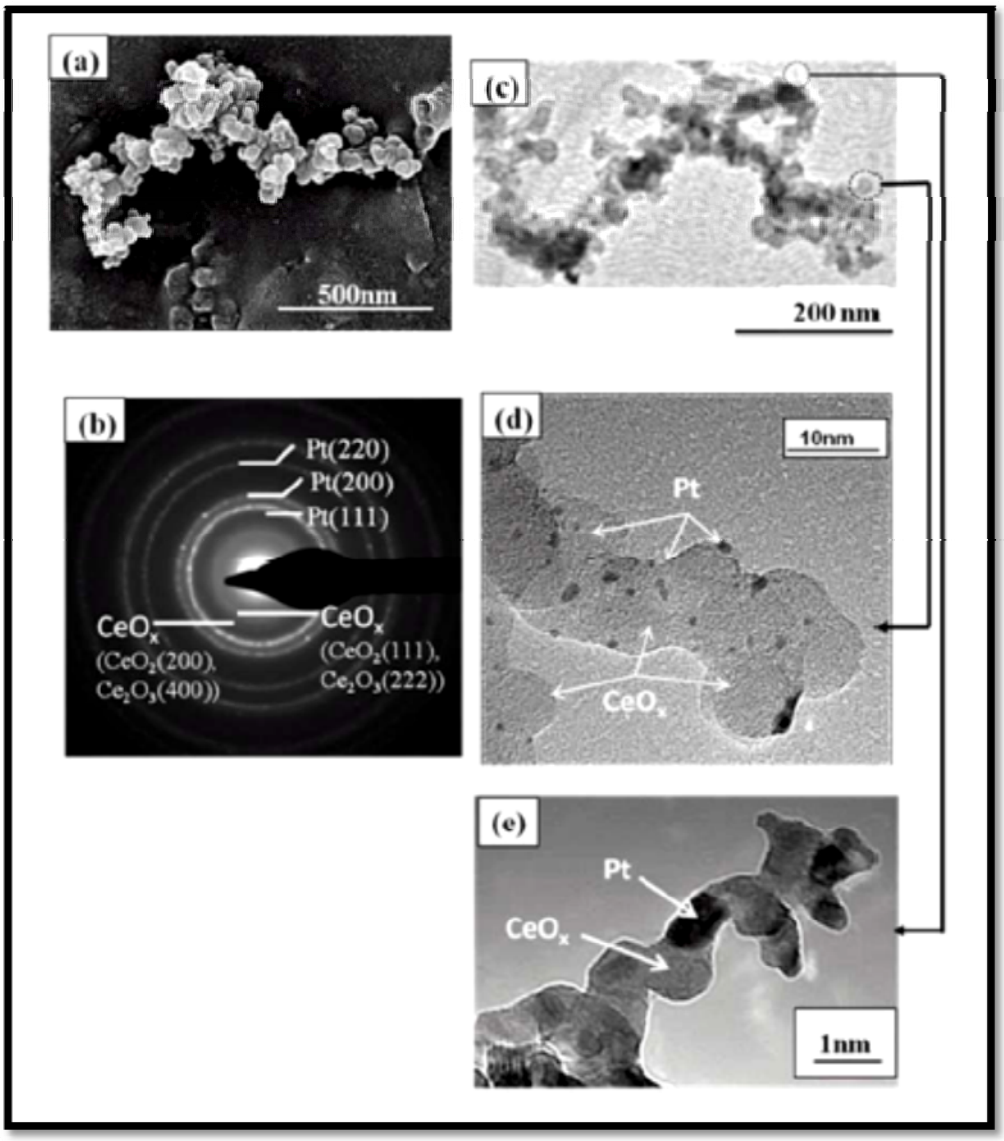

Figure 3-18 SEM image (a), selected area electron diffraction pattern (b), low magnification TEM image (c) and high resolution TEM images (d) and (e) focused on the circles which are in low magnification TEM image (c) taken from 5wt% Pt loaded CeO_x nanowire on conductive amorphous carbon particles after the electrochemical pre-treatment.

3-6 Conclusion

In this chapter we highlighted the role of CeO_x nanowire surface for fabrication of Pt-CeO_x interfaces. In the case of nanowire from Figure 3-4(a), CeO_x nanowire has so wide reaction spaces for formation of Pt-CeO_x nanowire interface. In contrast, the reaction space on Pt-CeO_x nanoparticle/C was limited to the contact point of Pt nanoparticle and CeO_x nanoparticle (i.e. point contact between Pt and CeO_x). So, after Pt loading procedure, the Pt particles were captured by these CeO_x nanowire spaces due to acid-base interaction at the interface. And we got large amount of Pt-CeO_x nanowire interface on Pt in the present work.

Since CeO_x nanowire surface is useful for fabrication of Pt-CeO_x interface which would help the enhancement of activity on electro-catalyst, in this chapter, the effect of different physical factors for the synthesis of fine CeO_x nanowire was discussed. Based on the experimental results, it was found that the urea and soft template CTAB were needed for the oxidation of $CeCl_3$. Also, water content has to be controlled in extremely low level for preparation of fine CeO_x nanowire.

In the first step of the formation process of CeO_x nanowire, growth of micelle structure which consists of soft template CTAB, $CeCl_3$ and urea was observed and gentle oxidation of $CeCl_3$ give rise $Ce(OH)_3$ in that micelle structure. Eventually, fine CeO_x nanowires were formed from slow oxidation of $Ce(OH)_3$.

Based on all experimental results, we concluded that there were following three steps involved in CeO_x nanowire formation process, it is because three type slopes were observed in Figure 3-3 and Table 3-1.

Step 1: Diffusion

$$CeCl_3. + CO(NH_2)_2 + CTAB \xrightarrow{\text{Diffusion}} CeCl_3.\,CO(NH_2)_2\,.CTAB$$

Step 2: Diffusion + Oxidation

$CeCl_3 .\ 7\ H_2O\ .CO(NH_2)_2\ .CTAB \longrightarrow Ce(OH)_x .\ CTAB + Byproduct\ (NH_3, Cl_2, CO_2) \uparrow$

Step 3: Oxidation

$Ce(OH)_x\ .CTAB \longrightarrow CeO_x(nanowire) + Byproduct\ (H_2, CO_2, Br_2\ ) \uparrow$

After loading of Pt, we proposed acid–base reaction was going on between $Ce(OH)_3$, CeO_x nanowires and Pt. Due to acid–base reaction, there was unique and large interfacial interaction has been noticed. Prior to the electrochemical pre-treatment of Pt loaded CeO_x nanowire/C, the microanalysis in the present work shows that the unique interface between $Ce(OH)_3$ and CeO_x nanowire can be reaction space for Pt particle synthesis. Selected area electron diffraction pattern recorded from Pt-CeO_x nanowire/C prior to the electrochemical pre-treatment indicates that $Ce(OH)_3$ covered the surface of CeO_x nanowire, as shown in figure 3-17.

Based on the microanalysis data, it is concluded that Pt resources (i.e. K_2PtCl_4) is in between $Ce(OH)_3$ and CeO_x nanowire. The surface of CeO_x nanowire would be covered by OH^- species. It means that the surface of CeO_x nanowire is base. Also, the surface of $Ce(OH)_3$ has basic nature. This indicates that the acid-base reaction between Ce and Pt can be expected in many places on CeO_x nanowire. This acid-base reaction site on CeO_x nanowire looks reaction space for fabrication of Pt-CeO_x interface. And the surface of Pt loaded CeO_x nanowire/C was activated through the electrochemical pre–treatment.

In the case of Pt loaded CeO_x nanoparticles/C, there was really less contact point between CeO_x nanoparticle and Pt nanoparticle in the previously reported works. In contrast, the interaction between Pt and CeO_x was enhanced in aforementioned reaction space on CeOx nanowire. Finally, we proposed that Pt particles were prepared in the interface between $Ce(OH)_3$ and CeO_x nanowires due to acid base reaction, which increased interaction of Pt and CeO_x

nanowire. Also, it is expected that the formation of Pt-CeO_x nanowire interface on the electrochemically pre-treated sample will be useful for enhancement of anode and cathode properties in the fuel cell reactions. In the later chapters (i.e. Chapter 4 and Chapter5), the interface of Pt-loaded CeO_x nanowire/C were fully characterized using scanning electron microscopy (SEM), transmission electron microscopy (TEM), selected area electron diffraction pattern (SAEDP), X-ray photoelectron spectroscopy (XPS) and X-ray diffraction (XRD) analysis. Also, the effect of formation of Pt-CeO_x nanowire interface on enhancement of electro-catalytic activities in fuel cell reactions was examined.

References

1. D.H. Zhang, Z.Q. Liu, C. Li, T. Tang, X.L. Liu, S. Han, B. Lei, and C.W. Zhou, "Detection of NO_2 Down to ppb Levels Using Individual and Multiple In_2O_3 Nanowire Devices", *Nano Lett.*, **4**, pp.1919-1925 (2004).

2. S.H. Jo, D. Banerjee, and Z.F. Ren,"Field Emission of Zinc Oxide Nanowires Grown on Carbon Cloth" *Appl. Phys. Lett.*, **85**, pp. 1405-1406, (2004).

3. Z.H. Zhong, D.L. Wang, Y. Cui, M.W. Bockrath, and C.M. Lieber "Nanowire Crossbar Arrays as Address Decoders for Integrated Nanosystems", *Science*, **302**, pp.1377-1383 (2003).

4. X.P .Gao, J.L. Bao, G.L. Pan, H.Y. Zhu, P.X. Huang, F. Wu and D.Y Song, "Preparation and Electrochemical Performance of Polycrystalline and Single Crystalline CuO Nanorods as Anode Materials for Li ion Battery", *J. Phys. Chem. B*, **108**, pp .5547-5551 (2004).

5. R. Yang, and L Gao, "Novel Way to Synthesize CuO Nanocrystals with Various Morphologies", *Chem. Lett.*, **33**, pp.1194-1195 (2004).

6. Y.K. Su, C.M. Shen, H.T. Yang, H.L. Li, and H.J.Gao, "Controlled Synthesis of Highly Ordered CuO Nanowire Arrays by Template-Based Sol-Gel Route", *Trans Nonferrous Met. Soc. China*, **17**, pp.783-786 (2007).

7. Y. Cui, L.J. Lauhon, M.S. Gudiksen, J.F. Wang, and C.M. Lieber, "Diameter-Controlled Synthesis of Single Crystal Silicon Nanowires", *Appl. Phys. Lett*., **78**, pp.2214-2220 (2001).

8. C.L. Cheung, A. Kurtz, H. Park, and C.M. Lieber, "Diameter Controlled Synthesis of Carbon Nanotubes*", J. Phys. Chem. B*, **106**, pp. 2429-2432(2002).

9. T.E. Bogart, S. Dey, K.K. Lew, S.E. Mohney, and J.M. Redwing, "Diameter Controlled Synthesis of Silicon Nanowires using Nanoporous Alumina Membranes", *Adv. Mater*., **17**, pp.114-120 (2005).

10. N. Chopra, P.D. Kichambare, R. Andrews, and B.J. Hinds, " Control of Multiwalled Carbon Nanotube Diameter by Selective Growth on the Exposed Edge of a Thin Film Multilayer Structure", *Nano Lett.*, **2**, pp. 1177 -1189(2002).

11. W.Z. Wang, G.H. Wang, X.S. Wang, Y.J. Zhan, and Y.K. Liu, "Synthesis and Characterization of Cu_2O Nanowires by Novel Reduction Route", *Adv. Mater.*, **14,** pp.67-70(2002).

12. C.T. Hsieh, J.M. Chen, H.H. Lin, and H.C. Shih, "Synthesis of Well Ordered CuO Nanofibers by a Self-Catalytic Growth Mechanism", *Appl. Phys. Lett*., **82**, pp. 3316 -3320 (2003).

13. K. Jiang, T. Herricks, and Y. Xia, "CuO Nanowires can be Synthesized by Heating Copper Substrates in Air", *Nano Lett.*, **2**, pp.1333-1340 (2002).

14. L.S. Huang, S.G. Yang, T. Li, B.X. Gu, Y.W. Du, Y.N. Lu, and S.Z. Shi, "Preparation of Large Scale Cupric Oxide Nanowires by Thermal Evaporation Method", *J. Cryst. Growth*, **260,** pp.130-132 (2004).

15. S. Wang, "Thermal Oxidation of Cu_2S Nanowires: A Template Method for the Fabrication of Mesoscopic CuxO (x = 1, 2) Wires", *Phys. Chem. Chem. Phys.*, **4,** pp. 3425-3430 (2002).

16. J.R Heath, and F.K. Le Goues, "One-Dimensional Nanostructures: Synthesis, Characterization and Applications", *Chem. Phys. Lett.*, **20**, pp. 263-270(1999).

17. X.Wang, and Y.Li," A General Strategy for Nanocrystal Synthesis", *J. Am. Soc*., **124**, pp. 2880-2990 (2002).

18. Q.Lu, F.Gao, and D.Zhao, "One-step Synthesis and Assembly of Copper Sulfide Nanoparticles to Nanowires, Nanotubes, and Nanovesicles by a Simple Organic Amine-Assisted Hydrothermal*", Nano Lett*., **2**, pp. 725-730 (2002).

19. Y. Li, M. Sui, Y. Ding, G. Zhang, J. Zhuang, and C. Wang, " Preparation of Mg $(OH)_2$ Nanorods*", Adv. Mater*., **12**, pp.818-825(2000).

20. K.S.Kim, N.Winograd,and R.E.Davis, "Electron Spectroscopy of Platinum-Oxygen Surfaces and Application to Electrochemical Studies*", J.Am.Chem.Soc.*, **93**, pp.6296-6305 (1971).

21. Q.Fu, H.Saltsburg, and M.Flytzani-Stephanopoulos, "Active-Non-Metallic Au and Pt Species on Ceria-based Water-gas shift Catalysts", *Science*, **301**, pp. 935-950(2003).

22. M.Václavů, I. Matolínová, J.Mysliveček, R. Fiala, and V.Matolin, "Anode Material for Hydrogen Polymer Membrane Fuel Cell:Pt–CeO_2 RF-Sputtered Thin Films*", J. Electrochem. Soc.*, **156**, pp .B938.-947 (2009).

23. K. Fugane, T.Mori, D.R.Ou, A. Suzuki, H.Yoshikawa, T.Masuda, K.Uosaki, Y.Yamashita, S.Ueda, K.Kobayashi, N.Okazaki, I.Matolinova, and V.Matolin, "Activity of Oxygen Reduction

Reaction on Small Amount of Amorphous CeO*x* Promoted Pt Cathode for Fuel cell Application *", Electrochimica Acta*, **56**, pp .3874-3883 (2011).

24. Z.X. Yang, Z.S. Lu, and G.X.Luo, "Hybrid Functionals Based on a Screened Coulomb Potential", *Phys. Rev.B*, **76**, p.p.235431-235445(2007).

25. F. Zhang, P. Wang, J. Koberstein, S. Khalid, and S.-W.Chan, "Cerium Oxidation State in Ceria Nanoparticles Studied with X-ray Photoelectron Spectroscopy and Absorption Near Edge Spectroscopy", *Surf. Sci.*, **563**, pp.74-82(2004).

26. D.R.Ou, T.Mori, K.Fugane, H.Togasaki, F.Ye and J. Drennan, "Stability of Ceria Supports in Pt–CeO_x/C Catalysts*", J. Phys. Chem. C*, **115**, pp. 19239-19245 (2011).

27. D.R. Ou, T. Mori, T.Togasaki, M.Takahashi, F.Ye, and J.Drennan, "Microstructures and Metal-Support Interaction of the Pt-CeO_2/C Catalysts for Direct Methanol Fuel Cell Application", *Langmuir*, **27**, pp.3859-3866(2011).

28. K.Fugane, T.Mori, D.R.Ou, P.F.Yan, F.Ye, H.Yoshikawa, and J.Drennan, "Improvement of Cathode Performance on Pt-CeO_x by Optimization of Electrochemical Pretreatment Condition for PEFC Application", *Langmuir*, **28**, pp. 16692-16770 (2012).

29. L. Yan, X. Xing, R. Yu, J. Deng, J. Chen, and G. Liu, "Facile Alcohothermal Synthesis of Large-Scale Ceria Nanowires with Organic Surfactant Assistance", *Physica B*, 390**,** pp.59–64 (2007).

30. R.-J. La, Z.-A. Hua, H.-L. Lib, X.-L. Shanga, and Y.-Y. Yang, "Characterization and Optical Properties of Pole-like Nano-CeO_2 Synthesized by a Facile Hydrothermal Method", *Materials Science and Engineering A*, 368, pp.145–148 (2004).

31. Q. Yuan, H.H. Duan, L.L. Li, L.D. Sun, Y.W. Zhang, and C.H. Yan, "Characteristics of Carbon Nanotube Polymer Composites", *Journal of Colloid and Interface Science*, **335**, pp.151-167(2009).

32. C.Y. Wang, M.H. Chen, G.M. Zhu, and Z.G. Lin, "Measurement of the Zeta Potential of Gas Bubbles in Aqueous Solutions by Micro-electrophoresis Method", *J. Colloid Interface Sci*., **243** , pp. 362-370(2001).

33.Y. Li, X.L. Li, Z.X. Deng, B.C. Zhou, S.S. Fan, J.W. Wang, and X.M. Sun, "From Surfactant–Inorganic Mesostructures to Tungsten Nanowires", *Angew. Chem*., **114**, pp.343-350(2002).

34. T. Linssen, K. Cassiers, P. Cool, and E.F. Vansant, "Mesoporous Templated Silicates: an Overview of their Synthesis, Catalytic Activation and Evaluation of the Stability", *Adv. Colloid Interface Sci*., **103**, pp.121-147(2003).

35. C.R. Martin,"Membrane-based synthesis of nanomaterials", *Science*, **9**, pp.266-278(1994).

36. A.P. Li, F. Müller, A. Birner, K. Nielsch, and U. Gösele, " Ultrahigh-Density Nanowire Arrays Grown in Self-Assembled Diblock Copolymer Templates ", *J. Appl. Phys.*, **84**, pp.6023-6029(1998).

37. T. Yu, J. Joo, Y.I. Park, and T. Hyeon,"Single Unit Cell Thick Samaria Nanowires and Nanoplates*", Angew. Chem. Int. Ed*., **44**, pp.7411-7420(2005).

38. L.S. Zhong, J.S. Hu, H.P. Liang, A.M. Cao, W.G. Song, and Li-Jun Wan, "Self-Assembled 3D Flowerlike Iron Oxide Nanostructures and their Application in Water Treatment", *Advanced Materials*, **18**, pp. 2426–2431(2006).

Chapter 4 Improvement of anodic property (methanol electro-oxidation) on Pt loaded CeO_x nanowire/C

4-1. Introduction

In the Chapter 3, the influence of some preparation factors on growth process of CeO_x nanowire and optimization of Pt loading procedure was examined. Also, the Pt-CeO_x nanowire interface was analyzed by using XPS and TEM microanalysis. The results in Chapter 3 suggest that base and acid reaction was happening among cerium hydroxide, CeO_x and Pt. And it is expected that wider area of Pt-CeO_x nanowire interface as compared with previously reported Pt-CeO_x nanoparticle interface is fabricated on Pt in the present work.

In the present chapter, to examine the effect of Pt-CeO_x nanowire interface formation on the enhancement of methanol electro-oxidation activity observed for Pt surface, the influence of electrochemical conditioning process on the electrochemical reactions observed for the anodes and the influence of formation of Pt-CeO_x nanowire interface on a lowering of Pt amount in the anodes are examined.

To develop the high quality anodes for methanol electro-oxidation reaction (i.e. for DMFCs), Pt based alloys[1-27]such as Pt doped with Ru[1-15], Mo[16, 17,21], Sn[17,18,19], Bi[18], Pb[18], Sb[18], W[17,20], Nb[21], Ta[21],Ni[22-25], Mn[26] and Zn[27] have been developed for the improvement of activity on Pt anode in methanol electro-oxidation reaction. Of those candidates, PtRu alloy leads to the best improvement in performance of the Pt based alloys examined. This is due to the lower potential required for formation of Ru-OH compared to the formation of Pt-OH while activated OH on Ru can additionally oxidize CO to CO_2 on Pt. This phenomenon is referred to as a bifunctional mechanism. However, PtRu alloy is still not sufficient for effective application of fuel cells and this electro-catalyst still contains a high platinum content making it less industrially attractive.

This bifunctional mechanism of the methanol oxidation reaction is operated when metal oxides are added to Pt/ conductive carbon (C) as oxide supports. The effects of oxide supports such as RuO_x[28-30], SnO_x[29], $InSnO_x$[29], MoO_x[31], NiO[32], TiO_2[33], and $NbRu_xO_y$[34]on the electro-oxidation of alcohols have also been examined for improvement of the activity of alcohol electro-oxidation on Pt in those anodes. Moghaddam et al.[29] examined the role of RuO_x, SnO_x and $InSnO_x$ supports for the electro-oxidation of alcohol on Pt anode surface. Their work suggests that Sn based oxides (i.e. SnO_x and $InSnO_x$) promote the CO oxidation by an electronic effect (i.e. ligand effect) which weakens the Pt-CO_{ad} bond while the effect of RuO_x can be attributed to enhancement of the aforementioned bifunctional mechanism. A similar electronic effect (i.e. ligand effect) was also reported by using other Pt-oxide supports. Of the Pt-oxide support series, Pt-CeO_x particle/C [35-44] has attracted attention due to the unique interactions between Pt and CeO_x.

In the present work, in order to maximize the interaction between Pt and the CeO_x support, and enhance the actiity of methanol electro-oxidation on Pt, Pt loaded CeO_x nanowires/C rather than Pt loaded CeO_x nanoparticles/C was fabricated, as shown in Chapter 3. Also, the activity of alcohol electro-xoidation on Pt in Pt loaded CeO_x nanowire anodes was examined using the electro-oxidation reaction of methanol in mixed solution of H_2SO_4 and CH_3OH.

4-2 Results and Discussion

4-2-1 EASA observed for electrochemically pretreated Pt loaded CeO_x nanowire/C

The extra CeO_x without Pt-CeO_x interaction which presents in the electro-catalyst would suppress the charge transfer process between Pt and CeO_x. To increase the charge transfer on electrode surface, the conditioning process (i.e. electrochemical pre-treatment) of electro-catalyst surface is required. After the electrochemical pre-treatment of Pt loaded CeO_x nanowire surface,

the observed electrochemical active surface area (EASA) of anode would be maximized. Also, the effect of formation of Pt-CeO_x nanowire interface on enhancement of methanol electro-oxidation activity observed for Pt surface would become clear.

As a consequence, influence of cycle number of CV in H_2SO_4 aqueous solution was examined at first. The electrochemical pretreatment process was performed in N_2-saturated 0.5 M H_2SO_4 aqueous solution. The suspension was spread on glassy carbon electrode by using micropipette in which amount was 5μl. The measured potentials were converted to the reversible hydrogen electrode (RHE) scale. Prior to the electrochemical measurements, the electrochemical pre-treatment as conditioning process of anode surface was carried out in the potential ranging from 0 to 1V (vs. Ag/AgCl). The sweep rate in the conditioning process was $50mVs^{-1}$.

In the case of fabrication of Pt loaded CeO_x nanowire/C, as shown in last chapter, the platinum nano-particles were formed in the interface which would be nano-scale reaction space between CeO_x nanowire and reducing agent sodium borohydride ($NaBH_4$). This suggests that the large amount of remained $NaBH_4$ is on the surface of Pt loaded CeO_x nanowire and the remained impurity has to be removed by using electrochemical pre-treatment process (i.e. electrochemical conditioning process) of Pt.

The influence of cycle number of CV on the current density which was observed in 0.5M H_2SO_4 aqueous solution by using potential ranging from 0.0 to 1.5V (vs. RHE) was examined by using 5wt% Pt loaded CeO_x nanowires/C, as shown in Fig.4-1.

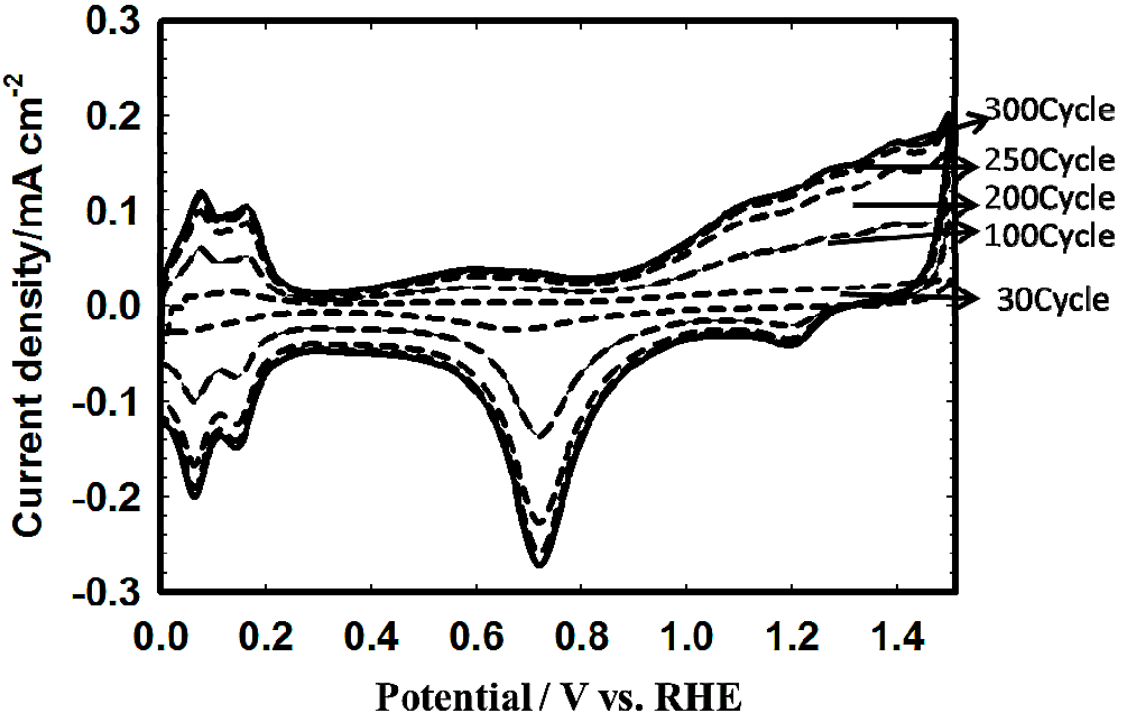

Figure 4-1 Relationship between current density and cycle number of CV observed for 5wt% Pt loaded CeO_x nanowire/C in 0.5M H_2SO_4 aqueous solution at 28°C.

In the case of Pt loaded CeO_x nano-particles/C, the stationary state can be observed by approximately 30 cycle sweeps in the conditioning process. In contrast, the observed current on 5wt% Pt loaded CeO_x nanowire/C was quite low level after 30 cycle sweeps. The observed current on aforementioned sample becomes high during long cycle sweep as demonstrated in Fig. 4-1. Then, the observed electrochemical data reached to the stationary state after 300 cycle sweeps in the present conditioning process. In the case of 50wt% Pt loaded CeO_x nanowire/C and 10wt% Pt loaded CeO_x nanowire/C, the cycle sweep dependence of current density was almost same to this case. Based on those results, it is concluded that the larger area Pt-CeO_x

interface is formed on the Pt-CeO_x nanowire/C electrode surface as compared with previously reported Pt loaded CeO_x nanoparticle/C electrodes. It is because the cycle number for conditioning of Pt-CeO_x nanowire/C surface is approximately 10 times bigger than that of previously reported Pt loaded CeO_x nanoparticle/C. Also, the current density observed for the electrochemically pretreated Pt-CeO_x nanowire/C surface was larger than Pt loaded CeO_x nanoparticle/C surface.

4.2.1(a) Microscopic interface structure analysis of the electrochemically pre-treated Pt-CeO_x nanowire/C electro-catalysts

After 300 cycle sweeps in the present condition process of Pt-CeO_x nanowire/C in H_2SO_4 aqueous solution, fine Pt particles on CeO_x nanowires were seen properly in TEM images which were shown in Figures 4-2 (a) to 4-2 (c).

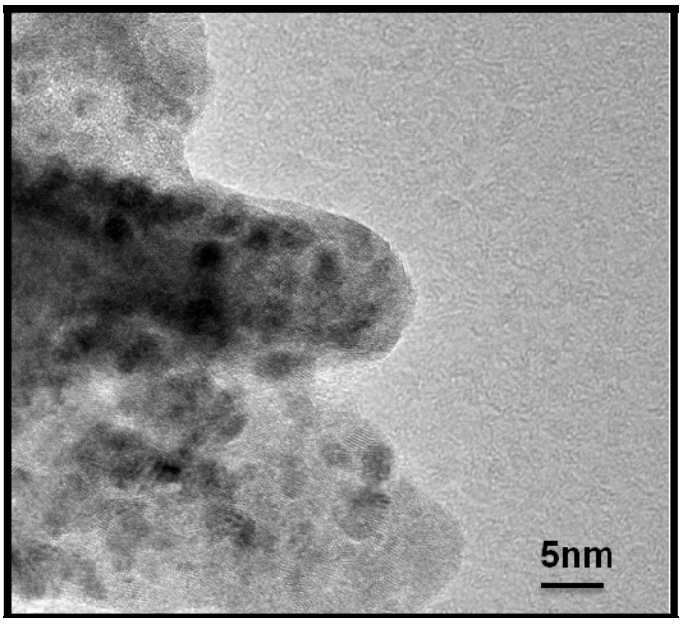

Figure 4-2(a) 50wt% Pt loaded CeO_x nanowire/C after 300 cycles electrochemical pre-treatment.

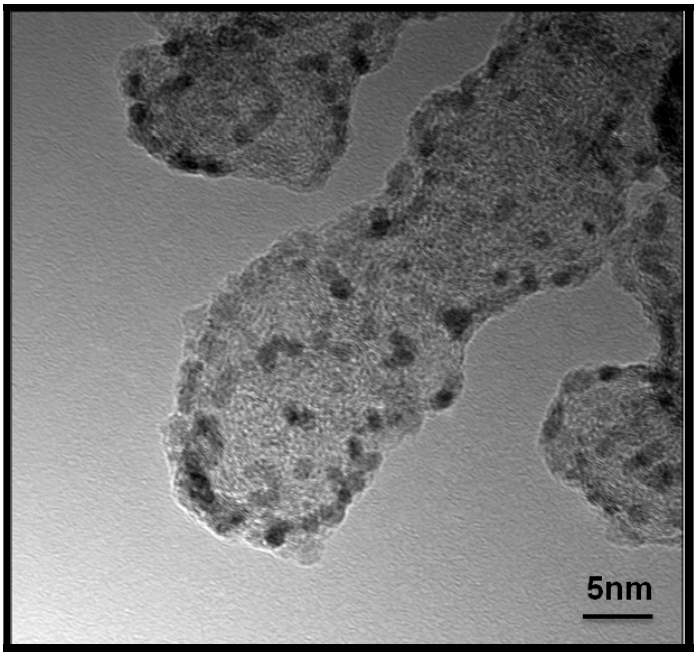

Figure 4-2(b)10wt% Pt loaded CeO_x nanowire/C after 300 cycles electrochemical pre-treatment.

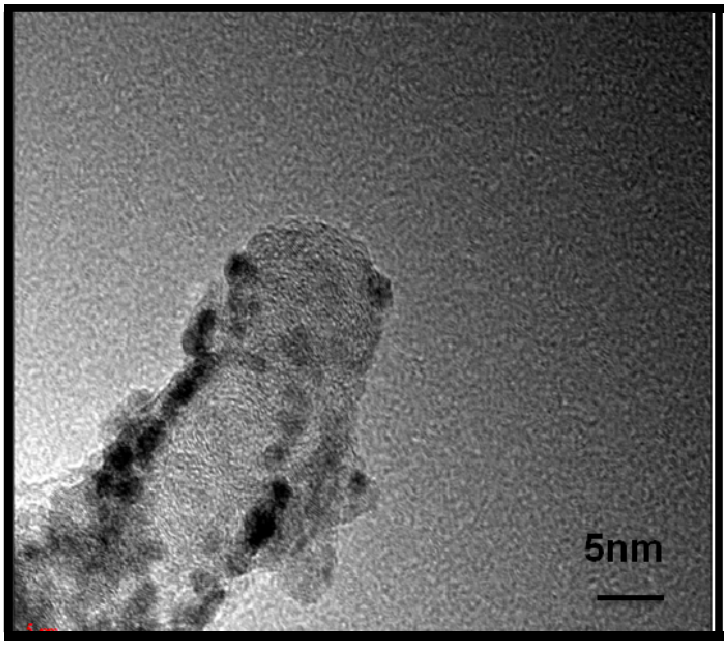

Figure 4-2(c)5wt% Pt loaded CeO_x nanowire/C after 300 cycles electrochemical pre-treatment.

Also, the selected area electron diffraction pattern (SAEDP) recorded from 5wt% Pt loaded CeO_x nanowire/C was demonstrated in Figure 4-2(d) as well.

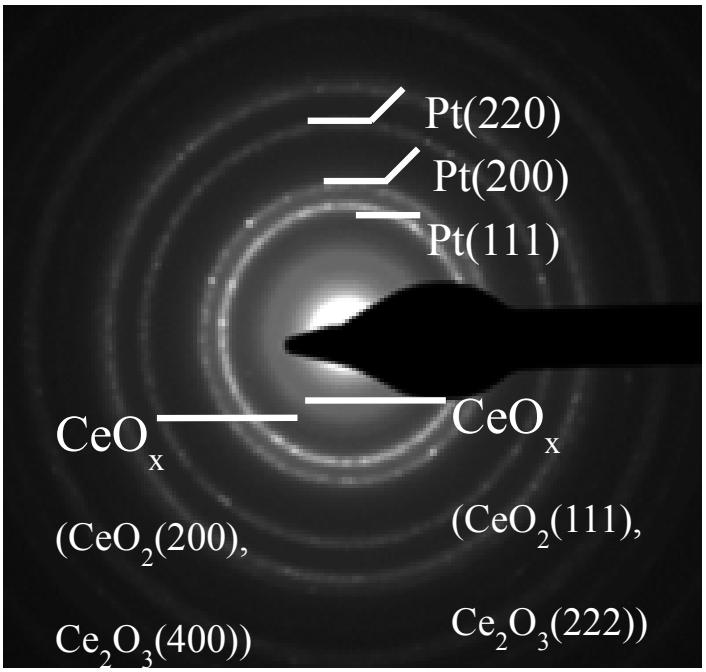

Figure 4-2(d) Selected areaelectron differaction pattern (SAEDP) recoreded from sample of Figure 4-2(c).

In the TEM images, the black color spots indicate Pt particles and light contrast areas are CeO_x. From high amount Pt electro-catalyst (i.e. 50wt% Pt loaded CeO_x nanowire/C) to low amount Pt electro-catalyst (i.e. 5wt% Pt loaded CeO_x nanowire/C), Pt particle distribution is going uniform and clear. And the diffraction rings were assigned to metallic Pt and CeO_x in the SAED pattern in Figure 4-2 (d) which was performed by 300 cycle sweeps of electrochemical pre-treatment. In the SAEDP, small spots were observed in the diffraction rings of Pt. It means that nano-sized Pt particles were in the observed area. Since conductive carbon mainly consists of amorphous phase, there is no diffraction rings in the SAEDP. In addition, no other diffraction rings such as $Ce(OH)_3$, Pt oxide and reducing agent of Pt were observed in the SAEDP taken from 300 cycles electrochemical pretreatment samples. Based on the experimental results in

Chapter 4, it can be concluded that active nano-sized Pt particles were appeared on CeO_x nanowire surface after 300 cycle sweeps of electrochemical pretreatment process.

To characterize the Pt loaded CeO_x nanowire/C electro-catalysts, the particle size distribution of Pt on CeO_x nanowire was observed by using TEM photographs of Figures 4-2(a) to 4-2(c). Also, the average particle size of Pt was estimated and noted in each figure. As we can see in the Figures 4-3(a) to (c), the particle size distribution and average size of Pt taken from 50wt% Pt loaded CeO_x nanowire/C was different from 10wt% Pt loaded CeO_x nanowire/C and 5wt% Pt loaded CeO_x nanowire/C.

(a)

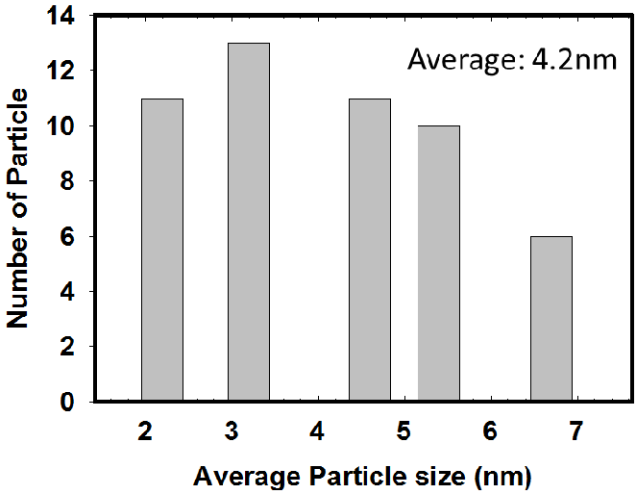

(b)

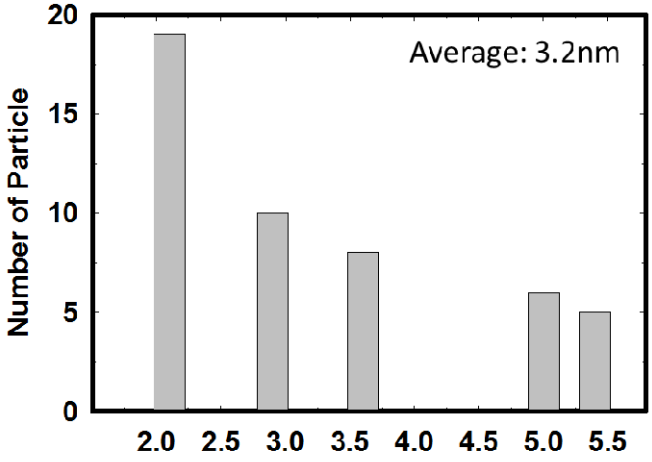

(c)

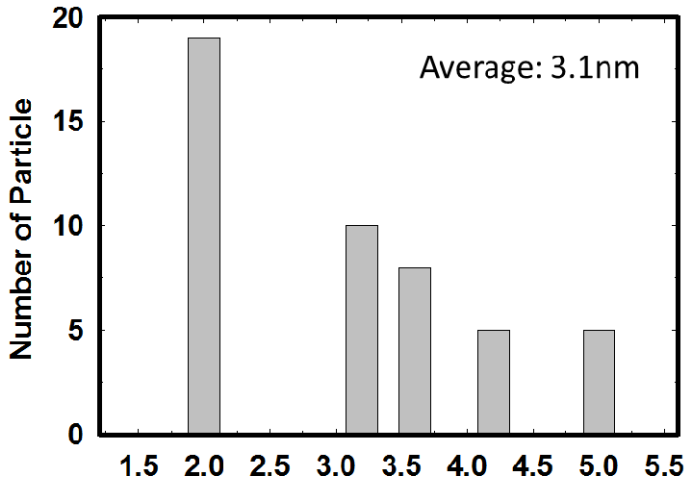

Figure 4-3 Platinum particle size distribution by using histograms obtained from (a) 50wt%, (b) 10wt%, and (c) 5wt% Pt loaded CeO_x nanowire/C electro-catalysts.

The average particle sizes observed for 5wt% Pt loaded CeO_x nanowire/C and 10wt% Pt loaded CeO_x nanowire/C were around 3nm which are similar to the commecially available Pt/C and smaller than home-made Pt/C (i.e. approximately 10nm). In cotrast, the particle size distribution obtained from 50wt% Pt loaded CeO_x nanowire/C indicated that Pt particles were agglomerated on CeO_x nanowire. Also, the average particle size of Pt in 50wt% Pt loaded CeO_x nanowire/C was approximately 4nm which is slightly bigger than 5wt% Pt loaded CeO_x nanowire/C and 10wt% Pt loaded CeO_x nanowire/C.

To conclude the relationship between the obseved Pt partcile sizes and electrode properties, the electrochemical active surface area (EASA) was examined by using 50wt% Pt loaded CeO_x nanowire/C, 10wt% Pt loaded CeO_x nanowire/C, 5wt% Pt loaded CeO_x nanowire/C and commecially available Pt/C.

4-2-2 EASA observed for electrochemically pretreated Pt loaded CeO_x nanowire/C

In the case of Pt loaded CeO_x nanowire/C, Pt nano-particles were formed in the interface which would be nano-scale reaction space between CeO_x nanowire and reducing agent sodium borohydride ($NaBH_4$) (see the results of Chapter 3). This suggests that the large amount of $NaBH_4$ is remained on the surface of Pt loaded CeO_x nanowire and the remained impurity has to be removed by using electrochemical pre-treatment process (i.e. electrochemical conditioning process) of Pt. As shown in Figure 4-1, 300 cycle sweeps in the electrochemical pre-treatment is required to confirm the steady state in electrochemistry. Based on this data, EASA value was estimated by using the current peak intensity of H desorption as follows;

Usually, EASA is calculated by using following equation[2]

EASA ($cm^2 g^{-1}_{Pt}$)

= Charge ($\mu C\ cm^{-2}$) / [210 ($\mu C\ cm^{-2}$) $Pt_{loading}$($g\ cm^{-2}$)] (4-1)

Figures 4-4 (a) to 4-4(c) demonstrate the cyclic voltammograms in 0.5M H_2SO_4 aqueous solution recorded from 50wt% Pt loaded CeO_x nanowire/C, 10wt% Pt loaded CeO_x nanowire/C and 5wt% Pt loaded CeO_x nanowire/C for EASA calculation, respectively. Also, the estimated EASA values for aforementioned three Pt loaded CeO_x nanowire/C electro-catalysts were summarized in Table 4-1.

(a)

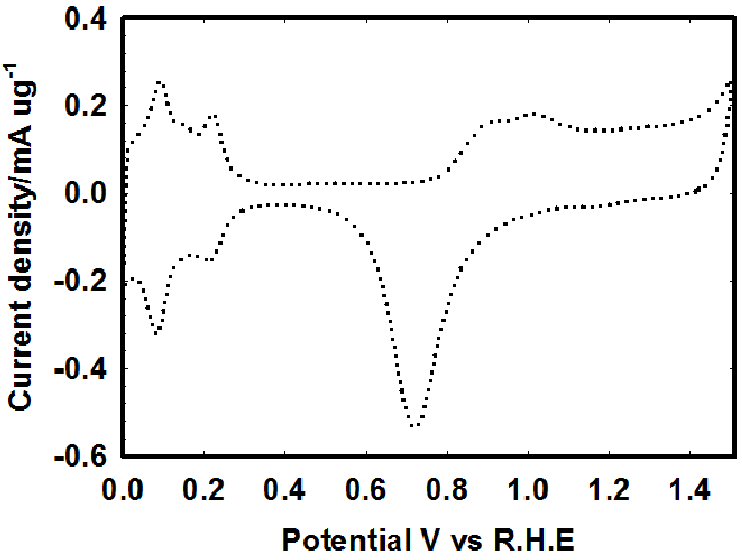
Current density/mA ug-1
0.4
0.2
0.0
-0.2
-0.4
-0.6
0.0
0.2
0.4
0.6
0.8
1.0
1.2
1.4
Potential V vs R.H.E

(b)

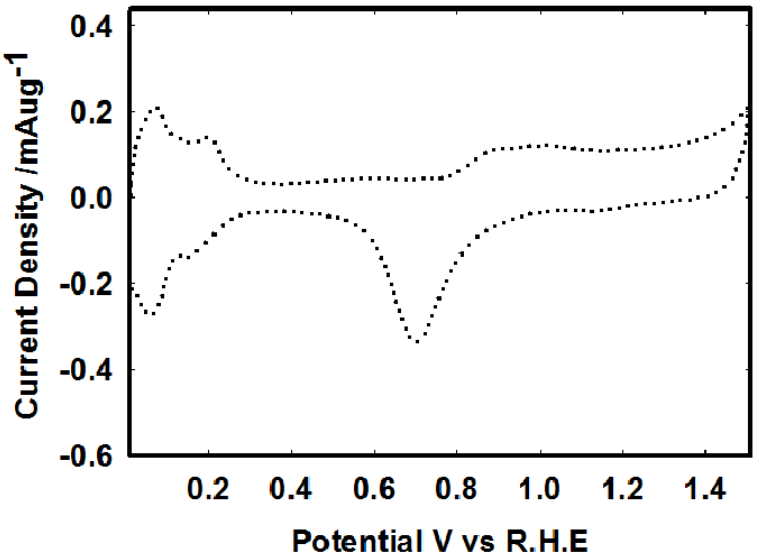
Current Density /mAug-1
0.4
0.2
0.0
-0.2
-0.4
-0.6
0.2
0.4
0.6
0.8
1.0
1.2
1.4
Potential V vs R.H.E

(c)

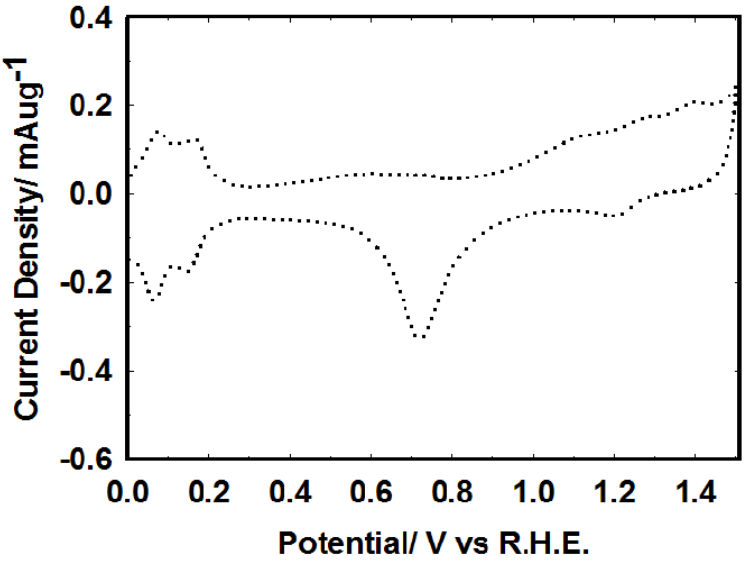

Figure 4-4(a) Cyclic voltammograms in 0.5M H_2SO_4 aqueous solution recorded from 50wt% Pt loaded CeO_x nanowire/C (a), 10wt% Pt loaded CeO_x nanowire/C (b) and 5wt% Pt loaded CeO_x nanowire/C (c) for EASA calculation.

Table 4-1 Estimated EASA values for Pt loaded CeO_x nanowire/C electro-catalysts by using H desorption peak intensity.

Pt (wt%)	EASA ($m^2 \cdot g_{Pt}^{-1}$)
50	90.7
10	136.2
5	152.1

4-2-3 Comparison of EASA with other electro catalyst with respect to loading amount of Pt on support

Figure 4-4(d) shows the relationship between Pt content in the electro-catalysts and the EASA values observed for Pt particle loading on different support material like carbon nanotube[52], graphene[53], organic moiety[50, 51]. Also, the EASA values observed for Pt loaded CeO_x nanoparticles/C were demonstrated in this figure. Figure 4-4(d) indicates that the EASA value observed for 10wt% Pt loading on graphene sheet and 10wt% Pt loaded on carbon nanotube electro-catalysts are in the quite high level such as approximately $170 cm^2 g^{-1}_{Pt}$ and $163 cm^2 g^{-1}_{Pt}$, respectively. It is because the average particle sizes of Pt in aforementioned Pt loaded carbon is in subnano-scale.

In contrast, the EASA observed for 10wt% Pt loaded CeO_x nanoparticles/C (i.e. approximately 40 $cm^2\ g^{-1}_{Pt}$) was much lower than 10wt% Pt loading on graphene sheet and 10wt% Pt loaded on carbon nanotube. In the case of Pt loaded CeO_x nanoparticles/C, the observed particle size of Pt in the electro-catalysts was approximately 3 to 5nm. On the other hand, the Pt particle size observed for Pt/graphene was in sub-nano scale. The big difference of observed EASA from the surface of electro-catalysts would be attributable to this Pt particle size difference among Pt/graphene, Pt/carbon nanotube and Pt-CeO_x nanoparticles/C.

The important point in the result of Figure 4-4(d) is the relationship between average particle size of Pt which is shown in Figure 4-3 and EASA values observed for 10wt% Pt loaded CeO_x nanowire/C and 5wt% Pt loaded CeO_x nanowire/C electro-catalysts. As shown in Figure 4-3, the average particle size which was observed by TEM was around 3nm. It is similar to 10wt% Pt-CeO_x nano-particles/C electro-catalysts which has lower EASA value (i.e. around 40 $cm^2\ g^{-1}_{Pt}$) as compared with 10wt% Pt-CeO_x nanowire/C (i.e. approximately $140 cm^2 g^{-1}_{Pt}$). This clearly

indicates that large amount of Pt-CeO_x interface was formed around Pt bulk particles on CeO_x nanowire. It is concluded that the large area of Pt-CeO_x nanowire interface which was formed on CeO_x nanowire increased the observed EASA values (i.e. 40 cm^2 g^{-1}_{Pt} to 140 $cm^2g^{-1}_{Pt}$) on the surface of Pt-CeO_x based electro-catalyst system. Also, it is expected that electro-catalytic performance on Pt in Pt-CeO_x nanowire/C will be conspicuously improved as compared with Pt-CeO_x nano-particles/C series.

To develop aforementioned working hypothesis, the activity observed for Pt surface in Pt-CeO_x nanowire/C in methanol electro-oxidation reaction was examined in this Chapter 4 as well.

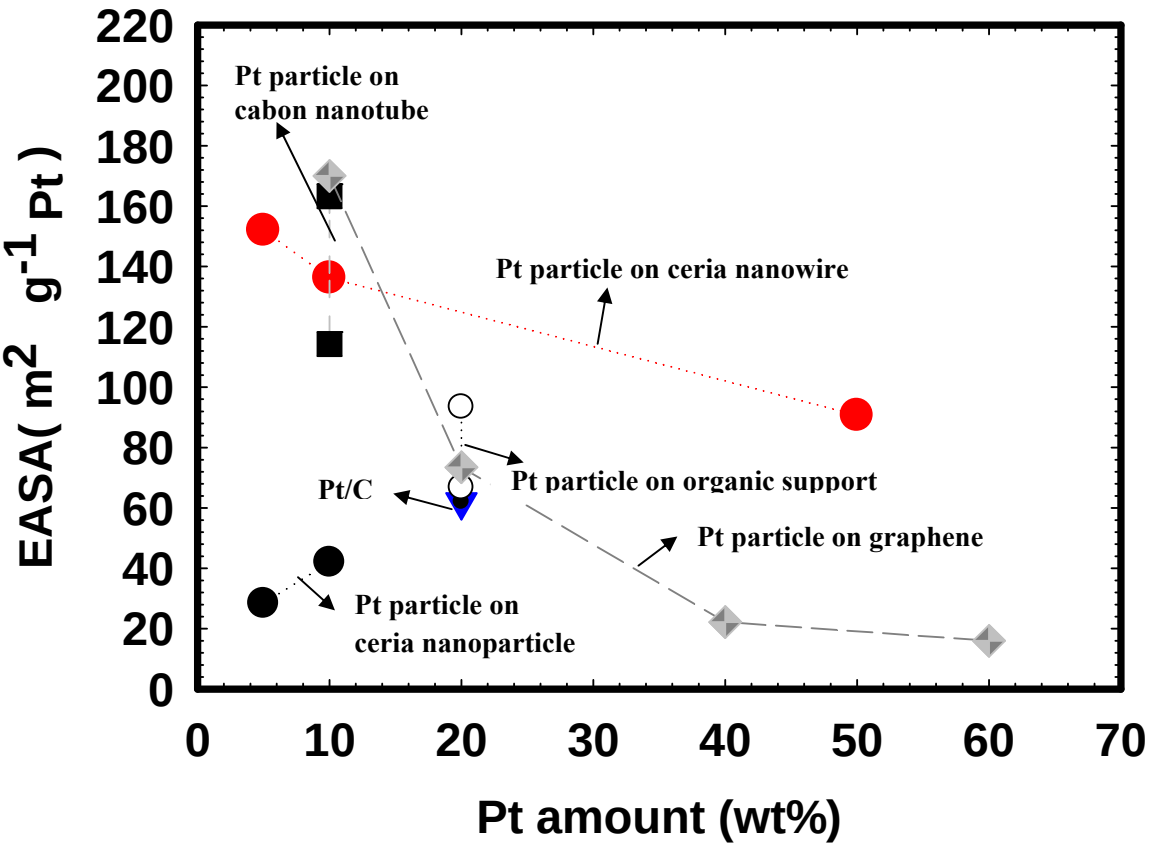

Figure 4-4(d) EASA comparison of Pt loaded CeO_x nanowire with various previously reported electro-catalysts.

The measurement results of EASA obtained from Pt/graphene and Pt/CNT in Figure 4-4(d) are large due to conjugated graphene network which provides charge transfer from graphene or CNT surface to metal surface, but these catalyst supports are not enough to reduce the Pt amount. On the other hand, we reduced the Pt amount with the help of CeO_x nanowire as support. In the case of Pt-CeO_x nano-particles/C, it is concluded that EASA is not improved due to less interaction between Pt and CeO_x particle. To confirm the validity of this conclusion, the EASA values observed for Pt-CeO_x nano-particles/C compared with aforementioned EASA values observed for Pt loaded CeO_x nanowire/C samples. Figures 4-5 (a) and 4-5 (b) demonstrate the cyclic voltammograms in 0.5M H_2SO_4 aqueous solution recorded from 5wt% Pt loaded CeO_x nano-particle/C (a) and 10wt% Pt loaded CeO_x nano-particles/C (b). Also, Table 4-2 summarizes the EASA values observed for 5wt% Pt loaded CeO_x nano-particles/C and 10wt% Pt loaded CeO_x nano-particles/C by using H desorption peak intensity. As reference data, EASA observed for home-made 20wt% Pt/C was shown in Table 4-2 as well. EASA values observed for Pt loaded CeO_x nano-particles/C were much lower than that of Pt loaded CeO_x nanowire/C series. It is because Pt and CeO_x nano-particles were contacted at limited area and small amount of Pt-CeO_x interface would be formed through this point contact between Pt and CeO_x particle.

Based on all experimental data, it is expected that Pt-CeO_x nanowire interface on Pt loaded CeO_x nanowire/C will provide the wide and active reaction space which was different from Pt-CeO_x nano-particle/C for improvement of electrode performance.

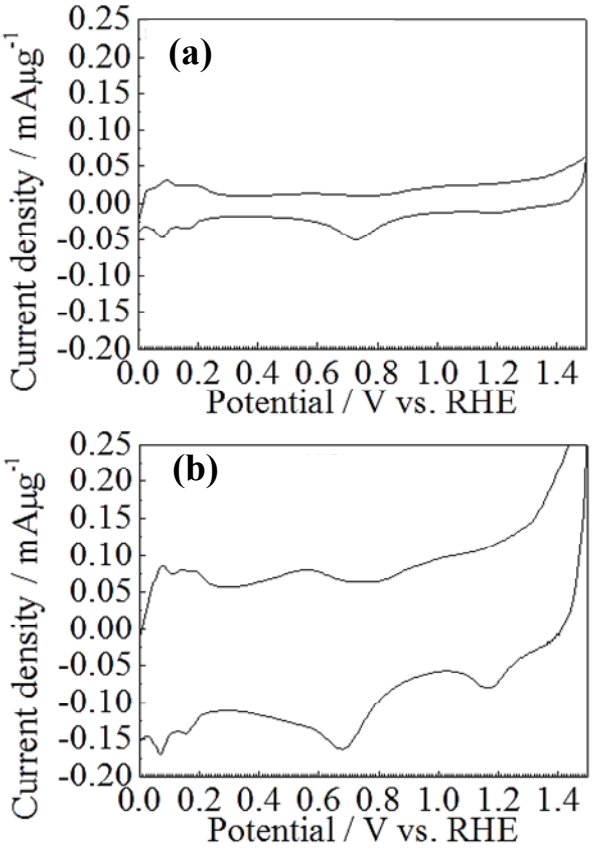

Figure 4-5 Cyclic voltammograms in 0.5M H_2SO_4 aqueous solution recorded from 50wt% Pt loaded CeO_x nanoparticle/C (a), and 10wt% Pt loaded CeO_x nanoparticle/C (b) for EASA calculation.

Table 4-2 Estimated EASA values for Pt loaded CeO_x nano-particles/C electro-catalysts by using H desorption peak intensity.

	EASA / $m^2g_{pt}^{-1}$
(a) 5 wt% Pt-CeO_2 particles /C	28.4
(b) 10 wt% Pt-CeO_2 particles /C	42.0
(c) home-made 20wt% Pt /C	62.4

4-2-4 Methanol electro-oxidation on Pt loaded CeO_x nanowire/C

Based on the results of 4-2-1 and 4-2-2, the anode properties on electrochemically pretreated Pt loaded CeO_x nanowire mixed with C were examined by cyclic voltammetry (CV) in mixed aqueous solution of 0.5M CH_3OH and 0.5M H_2SO_4 in the potential ranging from 0 to 1.5V (vs. Ag/AgCl). Electrochemical measurements were carried out by using a standard three-electrode glass cell at 28°C. To estimate the onset potential of methanol electro-oxidation reaction, a slow sweep rate (i.e. $1mVs^{-1}$) was selected because of the effect of high sweep rate on baseline drift of CV curves. For this analysis, a sweep rate was $20mVs^{-1}$. The observed current in CV measurement was normalized by using EASA values. For comparison of anodic properties observed for commercially available materials, the electro-catalytic activity of methanol electro-oxidation observed for Pt/C (Johnson Matthey Co., HiSPEC 8000) was also examined.

The representative anode activities observed for the electrochemically pre-treated Pt-CeO_x nanowire/C electro-catalysts are demonstrated in Figures 4-6(a) to 4-6(c). The observed CV curves show the typical forward and reverse sweep curves as compared with previously reported Pt/C in the methanol electro-oxidation reaction. The intensity of the peak between 0.8 and 0.9V (vs. RHE) observed for 50wt% Pt loaded CeO_x nanowire (i.e. Figure 4-6(a)) is almost same to the 10wt% Pt loaded CeO_x nanowire/C because of agglomeration of Pt and relatively small Pt-CeO_x interface area on anode.

(a)

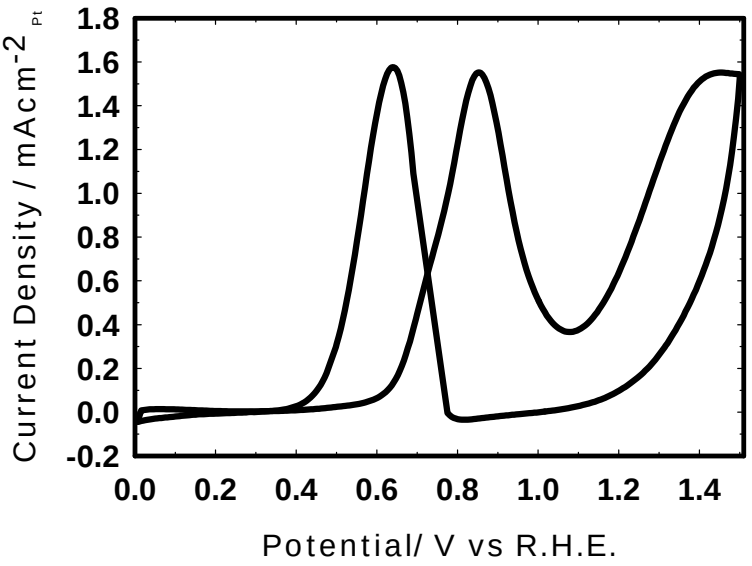
Current Density / mAcm-2 Pt
1.8
1.6
1.4
1.2
1.0
0.8
0.6
0.4
0.2
0.0
-0.2
0.0 0.2 0.4 0.6 0.8 1.0 1.2 1.4
Potential/ V vs R.H.E.

(b)

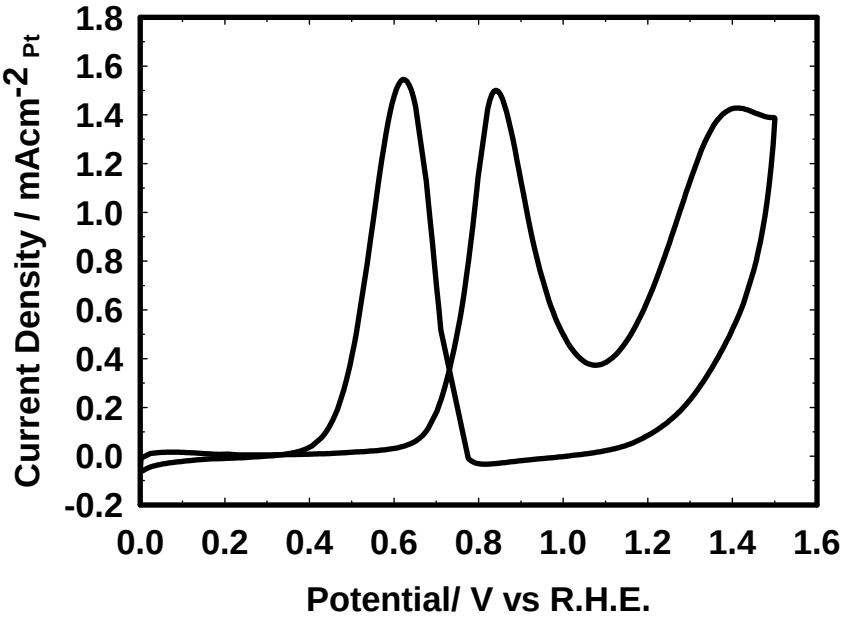
Current Density / mAcm-2 Pt
1.8
1.6
1.4
1.2
1.0
0.8
0.6
0.4
0.2
0.0
-0.2
0.0 0.2 0.4 0.6 0.8 1.0 1.2 1.4 1.6
Potential/ V vs R.H.E.

(c)

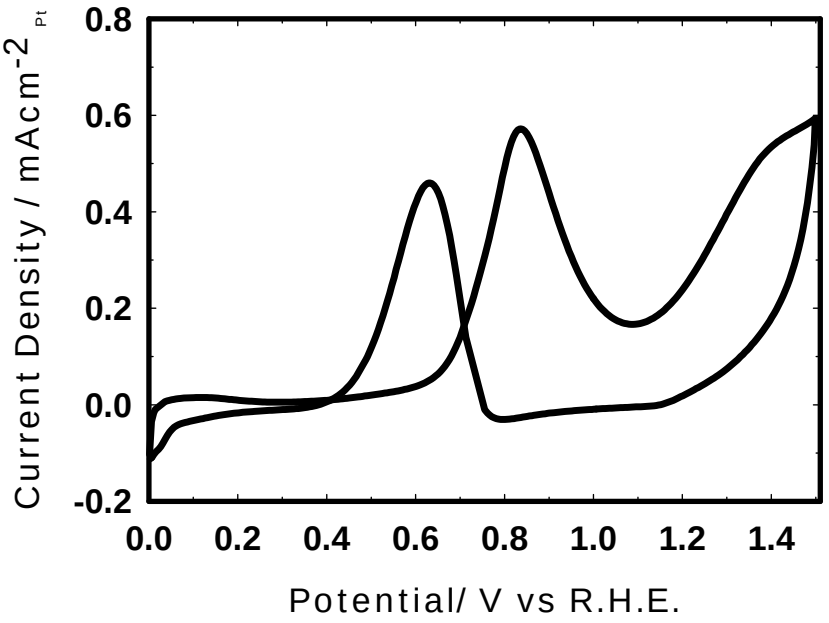

Figure 4-6 Cyclic voltammograms of methanol electro-oxidation in both forward and back sweeps on 50wt% Pt-CeO_x nanowire/C anode (a), 10wt% Pt-CeO_x nanowire/C anode (b), 5wt% Pt-CeO_x nanowire/C anode (c) at 28°C in the mixed solution of 0.5M aqueous H_2SO_4 solution and 0.5M aqueous CH_3OH solution at $10mVs^{-1}$. Number of sweeps: 30 cycles.

The onset potential of the methanol electro-oxidation reaction can be estimated using the potential value which conspicuously deviates from the base-line of the forward sweep curve. To estimate the onset potential correctly, the slow sweep rate (i.e. $1mVsec^{-1}$) was used in the present work. Figure 4-7 indicates that the estimated onset potential of the commercially available 20wt% Pt/C was approximately 0.5V (vs. RHE). This is similar to the previously reported value observed for Pt/C (i.e. 0.5V vs. RHE). In contrast, the methanol electro-oxidation on 5wt% Pt loaded CeO_x nanowires/C commenced from approximately 0.19V (vs. RHE), which is much

lower than that of the aforementioned commercially available Pt/C. Also, this onset potential of methanol electro-oxidation reaction observed for Pt-CeO_x nanowires/C was conspicuously lower than previously reported Pt-CeO_x nano-particles/C or carbon-nanotube (and PtRu-CeO_x nano-particles/C (0.30V[46] vs. RHE) in similar experimental conditions. This clearly indicates that the methanol electro-oxidation of Pt in Pt loaded CeO_x nanowires/C, which has the interface of Pt and CeO_x nanowire, is superior to Pt in commercially available Pt/C and previously reported Pt-CeO_x nanoparticles/C. However, the CV data obtained from the lower amount of Pt (i.e. 1wt% Pt) in Pt loaded CeO_x nanowires/C showed the noisy and low reliability data. In the case of aforementioned lower amount of Pt in the samples, it would be difficult to prepare homogeneous and well dispersed Pt-CeO_x nanowires in the conductive carbon particles by using preparation method in the present work. Based on those experimental data, 5wt%Pt-CeO_x nanowires/C anode showed the lowest onset potential of CH_3OH electro-oxidation in all prepared Pt-CeO_x nanowires/C in the present work.

The observed I_f / I_b peak intensity ratio and onset potential of methanol electro-oxidation reaction were summarized in Table 4-3. However, there is small inconsistency in the relationship between I_f/I_b and onset potential of methanol oxidation in Table 4-3. For example, I_f/I_b observed for commercially available Pt/C is higher than 20wt% Pt loaded CeO_x nano-particle/C, although the onset-potential observed for aforementioned Pt/C was higher than 20wt% Pt loaded CeO_x nano-particle/C.

In the case of Pt electro-catalyst supported by conductive C, carbon-nanotube and graphene, the previously reported I_f / I_b ratio values taken from aforementioned Pt electro-catalyst was improved by using graphene support. I_f / I_b ratio taken from Pt/graphene was around 6.52, although I_f / I_b ratio taken from Pt/graphite C was approximately 1.03. In this case, the onset

potential was not affected by the change of carbon supports. Similar results which are for comparison of effect of carbon supports were reported before[56,59,60] .

The experimental results Table 4-3 and aforementioned previously reported data suggest that the design of multifunctional active site has to be designed on the anodes. The conspicuous improvement of methanol electro-oxidation of Pt in 5wt% Pt loaded CeO_x nanowire/C should be concluded based on aforementioned point (i.e. possibility of multifunction on active sites).

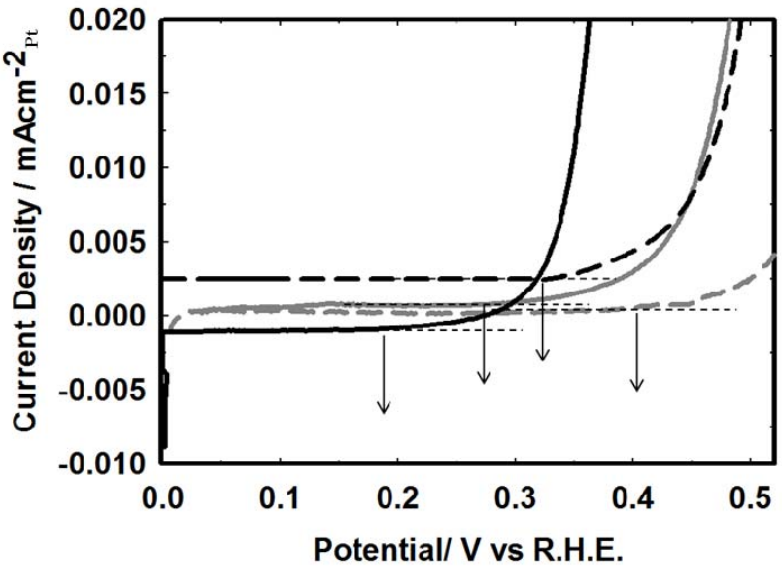

Figure 4-7. Onset potential of methanol oxidation in forward sweep on 5wt% Pt-CeOx/C (solid black line), 10wt% Pt-CeO_x/C anode (solid gray line), 50wt% Pt-CeO_x /C anode (dashed black line), and commercially available 20wt% Pt/C anode (dashed gray line) at 28°C in the mixed solution of 0.5M aqueous H_2SO_4 solution and 0.5M aqueous CH_3OH solution at $1mVs^{-1}$. Arrows indicate the on-set potentials of electrochemical CH_3OH oxidation reaction.

Table 4-3 Estimated current peak intensity ratio (I_f / I_b) and onset potential values of methanol electro-oxidation reaction obtained from Pt loaded CeO_x nano-particles/C electro-catalysts.

Catalyst	I_f / I_b	Onset Potential (V vs. RHE)
50 Pt-CeO_x nanowire/C	**0.98**	**0.32**
10 Pt-CeO_x nanowire/C	**1.98**	**0.29**
5 Pt-CeO_x nanowire/C	**2.21**	**0.19**
20Pt/C(commercial)	**1.39**[58]	**0.5**[58]
PtRu/C	**3.46**[56]	**0.26**[57]
20wt% Pt/ CeO_xnano-particle/C	**1.13**[38]	**0.45**[38]

It is known that both I_f / I_b peak intensity ratio and onset potential of methanol electro-oxidation reaction can be useful factors. For the improvement of methanol electro-oxidation reaction on Pt, I_f / I_b peak intensity ratio has to be in high level. In the forward potential sweep from lower potential region to higher potential region, the formation of intermediates in 6 electron process on Pt is promoted by applied potential. Then, enough amount of H^+ formation from methanol is expected for fuel cell reaction. In the higher potential region, however, oxidation of Pt surface is started and oxide thin film is formed on Pt surface in this forward potential sweep. In the forward sweep, the formation of intermediates reaction and Pt surface oxidation are taking place simultaneously. In higher potential region, the formation of intermediates in 6 electron process is suppressed by the surface oxidation of Pt surface. As a

consequence of this, enhancement of observed current on Pt is suppressed and peak current is appeared in this forward potential sweep process.

On the other hand, the methanol electro-oxidation proceeds on the oxidized Pt surface in the backward potential sweep from high potential region to low potential region. In this process, adsorption of CO molecules on Pt takes place as well as methanol oxidation on Pt. Then, I_b current peak value is suppressed by adsorption of created CO on the Pt surface.

If the Pt surface has high activity of methanol electro-oxidation, the adsorbed CO molecule on Pt can be easily removed from Pt surface in the forward potential sweep which comes after aforementioned backward potential sweep of CV. This makes peak intensity in forward potential sweep (I_f) high. So, overall conclusion is this for high methanol electro-oxidation on electro-catalysts, I_f / I_b peak intensity ratio should be high. Also, the onset potential observed for Pt surface becomes low.

In the previously reported electro-catalysts such as PtRu/C and Pt/C, I_f / I_b values were around 1.8 to 3.46[56] and obtained onset potential values of methanol electro-oxidation reaction were 0.26 to 0.38V (vs. RHE) [56-59] , as shown in Table 4-3. In the case of PtRu/C, Pt-Ru combination needs to choose 1:1 ratio of both metal atoms for higher activity of methanol electro-oxidation reaction on PtRu/C. In this combination, aforementioned good atomic ratio between Pt and Ru is fixed. If we try to reduce the Pt amount in PtRu/C, we cannot be able to see high methanol electro-oxidation property.

On the other hand, Pt loaded CeO_x nanoparticle/C anodes have been developed instead of alloy electro-catalysts. Xu et al. initially reported the stable anode performance of Pt-CeO_x particle/C in alkaline media such as a mixed solution of alcohol and KOH[35-37] and Takahashi et al. reported the improvement of methanol electro-oxidation activity observed for Pt in the acidic

media which corresponds to the operation condition of DMFCs using Pt-CeO_x nanoparticle support[38]. Takahashi et al. proposed that the anode performance observed for Pt-CeO_x nanoparticle/C in acidic media was improved by the high oxygen storage capacity of CeO_x surface, which is related to the electrochemical redox reaction between $Ce^{(Ce4+)}O_2$ and reduced $Ce^{(Ce4+,\ Ce3+)}O_{2-x}$.[39-41] Also, Scibioh et al.[42] examined the anodic reaction mechanism on Pt-CeO_x particle/C in the acidic media and they proposed the bifunctional-like mechanism similar to that observed in the Pt-RuO_x/C series. In addition, Guo et al.[43] and Tabet-Aoul et al.[44] fabricated Pt-CeO_x particle/C nanotube electrodes and improved the anode performances of Pt-CeO_x particle/C systems. In those cases, the nanotube substrate enhanced the charge transfer between Pt and CeO_x particle, and maximized the effect of the electrochemical redox reaction of CeO_x ($Ce^{4+} \leftrightarrow Ce^{3+}$) on the enhancement of CO oxidation reaction activity on Pt surface. But aforementioned previously reported cases give the bifunctional mechanism which is similar to PtRu/C.

In the previously reported Pt-CeO_x nanoparticles/C system, the remained CeO_x on Pt was quite small and it mainly consists of Ce^{3+} cation. It would be hard to accept aforementioned idea because the ratio of Ce^{4+} in the interface is quite low level. In this case, it is not so easy to transfer the electron from adsorbed methanol to the surface/ interface on anode under the applied potential.

To conclude the role of active site for enhancement of methanol electro-oxidation process on Pt-CeO_x nanoparticles/C system, in-situ analysis on anodes is required. Since the observed results of in-situ FT-IR analysis (shown in conclusion part of Chapter 4) in the methanol electro-oxidation reaction suggests that ligand mechanism contributes to the enhancement of activity of methanol electro-oxidation reaction, the electrochemical reduction reaction of Ce^{4+} to Ce^{3+} (i.e. **$Ce^{4+} + e^- \Rightarrow Ce^{3+}$**) can be assumed on the Pt–CeO_x nanoparticle/C electro catalyst surface.

As the mentioned above, the surface of previously reported Pt–CeO_x nanoparticle/C electro catalyst mainly consists of Ce^{3+} cation. The content of Ce^{4+} was in low level. It means that total amount of Ce^{4+} which contributes to aforementioned electro-chemical reduction reaction of Ce^{4+} to Ce^{3} was really low level. As a consequence of this, it is concluded that the effect of lowering of onset potential of methanol electro-oxidation reaction and enhancement of current peak intensity ratio of forward and backward sweep (I_f / I_b) by formation of Pt–CeO_x interface in the previous reported Pt–CeO_x nanoparticle/C electro-catalyst was insufficient level as compared to conventional PtRu/C.

In the contrast, the surface and interface of Pt loaded CeO_x nanowire/C mainly consists of Ce^{4+} cation. The area of the Pt-CeO_x nanowire interface which can be estimated by measurement of electrochemical active surface area was much higher than previously reported Pt–CeO_x nanoparticle/C electro-catalyst. The enhancement of area of Pt - CeO_x nanowire interface would contributes to improvement of current peak intensity ratio of forward and backward sweep (I_f / $I_{b)}$. To decrease the onset potential of methanol electro-oxidation reaction on Pt–CeO_x system, additional mechanism (i.e. not only $\mathbf{Ce^{4+} + e^{-} => Ce^{3+}}$)[47] would be required for design of quality Pt–CeO_x electro-catalyst system.

Since the onset potential of methanol electro-oxidation reaction observed for Pt-CeO_x nanowire/C was lower than Pt–CeO_x nanoparticle/C and it becomes close to conventional PtRu/C, I assumed the formation of unique Pt-CeO_x nanowire interface by different incorporation of Pt into CeO_x lattice. It is formation of interstitial oxygen site (i.e. $\mathbf{O^{"}_i}$) into the oxygen lattice sites. The electrochemical reduction reaction (i.e. $\mathbf{1/2O_O^X + e^{-} => 1/2\ O^{"}_i}$) in Pt-CeO_x nanowire interface would be occurred by small applied potential and contribute to enhancement of charge transfer from Pt surface to Pt-CeO_x nanowire interface (i.e ligand mechanism) and a lowering of

onset potential of methanol electro-oxidation reaction. Due to the multifunction such as electrochemical reduction reaction of Ce^{4+} (i.e. $\mathbf{Ce^{4+} + e^- => Ce^{3+}}$) and lattice oxygen (i.e. $\mathbf{1/2O_O^X + e^- => 1/2\ O^{"}_i}$) in the interface of Pt-CeO_x nanowire interface, it is conclude that lower onset potential of methanol electro-oxidation reaction and higher current peak intensity ratio of forward and backward sweep (I_f / I_b) which are close to the conventional PtRu/C were observed on the surface and interface of Pt-CeO_x nanowire/C.

4-3 Conclusion

From Chapter 4, I concluded that the formation of interface between Pt and CeO_x contributes to the improvement of the EASA and methanol oxidation property. In the case of 5wt% Pt loaded CeO_x nanowire/C, the observed EASA was approximately 5 times higher than 5wt% Pt loaded CeO_x nanoparticles/C. Also, the amount of Pt in Pt-CeO_x nanowire/C was reduced without decrease of activity of methanol electro-oxidation reaction on Pt-CeO_x nanowire/C as compared with Pt- CeO_x nanoparticle/C. To conclude why the improvement of methanol electro-oxidation activity was observed on 5wt% Pt-CeO_x nanowire/C, the multifunction such as electrochemical reduction reaction of Ce^{4+} (i.e. $\mathbf{Ce^{4+} + e^- => Ce^{3+}}$) and lattice oxygen (i.e. $\mathbf{1/2O_O^X + e^- => 1/2\ O^{"}_i}$) were assumed in the Pt-CeO_x nanowire interface. Aforementioned two kinds of electrochemical reduction reaction in the Pt-CeO_x nanowire interface would contribute to promotion of Pt surface activity (i.e lower onset potential of methanol electro-oxidation reaction and higher current peak intensity ratio of forward and backward sweep (I_f / I_b)).

To conclude the basic mechanism of improvement of activities of methanol electro-oxidation reaction on Pt, the in-situ FT-IR observation which is direct observation of methanol electro-oxidation reaction on Pt was performed using the home-made 20wt% Pt/C and 20wt% Pt loaded CeO_x nano-particles/C anodes.

Supporting Information Figure 4-1(a) and 4-1(b) demonstrate the adsorption potential dependence of absorbance profiles which were observed for the home-made 20wt% Pt/C and 20wt% Pt-CeO_x nano-particles/C, respectively. Besides the two strong absorption bands for adsorbed CO on Pt in the 2000–2100cm^{-1} frequency region, one weak absorption band at 2106 cm^{-1} was observed in aforementioned figure. This absorption band at 2106 cm^{-1} corresponds to the adsorbed CO on Au electrode. Alternatively, the strong absorption bands at 2030cm^{-1} and 2012cm^{-1} in Supporting Information Fig 4-1(a) and 2052cm^{-1} in Supporting Information Fig 4-1(b) at 50mV were assigned to the linear bonded CO (CO_L) on Pt. The two well-defined peaks at higher frequency (2030cm^{-1} and 2052cm^{-1}) and lower frequency (2012cm^{-1}) were assigned to CO at terrace and step edge sites, respectively.

Since absorption band centers observed for the surface of Pt in the 20wt% Pt-CeO_x nano-particles/C shifted to the higher wave number region as compared with home-made 20wt% Pt/C, it suggests that the absorption strength of CO molecule on Pt surface in Pt-CeO_x nano-particles/C becomes weak as compared with that of home-made 20wt% Pt/C.

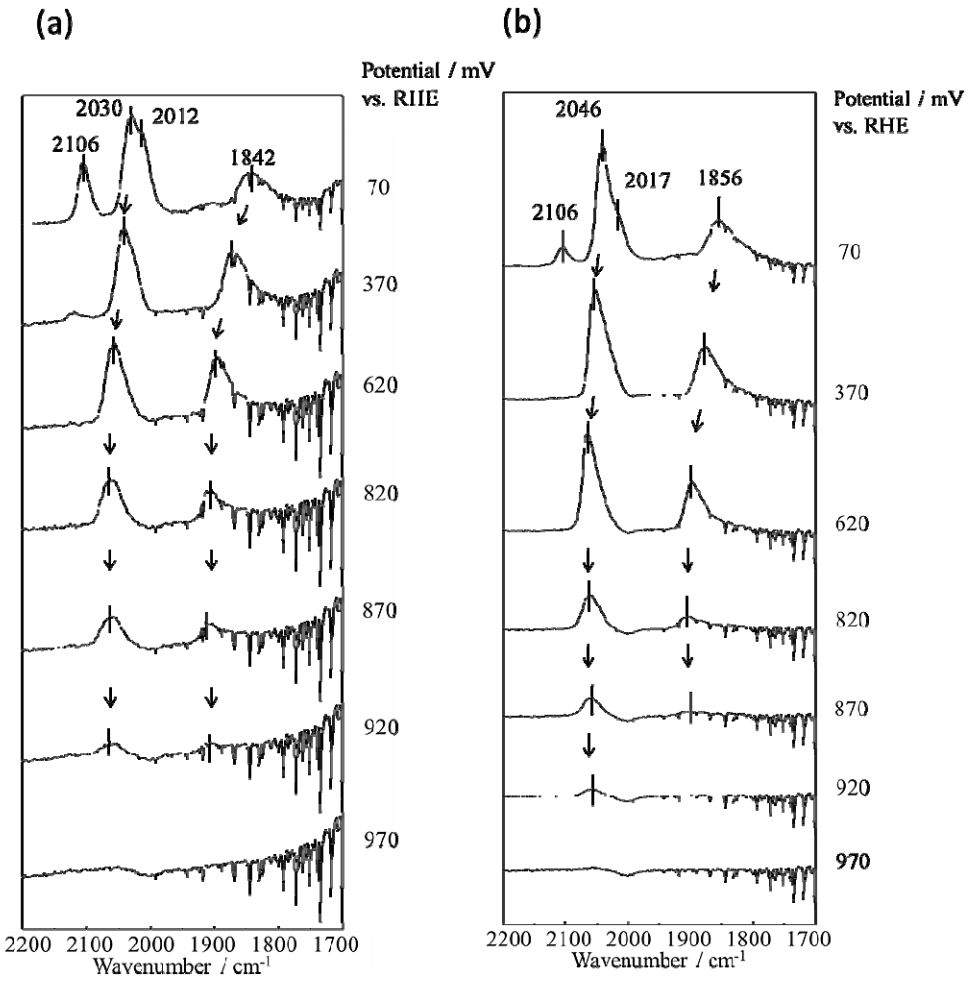

Supporting Information Figure 4-1 for conclusion In-situ IR spectra recorded from home-made 20wt% Pt/C (a) and 20wt%Pt-CeO_x nano-particles/C (b) at 1700cm^{-1} to 2200cm^{-1}.

In general, methanol electro-oxidation on Pt electrocatalyst proceeds as follows;[48]

$$\mathbf{Pt + CH_3OH \rightarrow Pt\text{-}(CH_3OH)_{ads}} \qquad \mathbf{(4\text{-}2)}$$

$$\mathbf{Pt\text{-}(CH_3OH)_{ads} \rightarrow Pt\text{-}(CH_3O)_{ads} + H^+ + e^-} \qquad \mathbf{(4\text{-}3)}$$

$$\mathbf{Pt\text{-}(CH_3O)_{ads} \rightarrow Pt\text{-}(CH_2O)_{ads} + H^+ + e^-} \qquad \mathbf{(4\text{-}4)}$$

$$\mathbf{Pt\text{-}(CH_2O)_{ads} \rightarrow Pt\text{-}(CHO)_{ads} + H^+ + e^-} \qquad \mathbf{(4\text{-}5)}$$

$$\mathbf{Pt\text{-}(CHO)_{ads} \rightarrow Pt\text{-}(CO)_{ads} + H^+ + e^-} \quad \textbf{(4-6)}$$

$$\mathbf{Pt + H_2O \rightarrow Pt\text{-}OH + H^+ + e^-} \quad \textbf{(4-7)}$$

$$\mathbf{Pt\text{-}(CO)_{ads} + Pt\text{-}OH \rightarrow 2Pt + CO_2 + H^+ + e^-} \quad \textbf{(4-8)}$$

In the above reactions, the step 5 (i.e. Eq.4-6) shows the CO poisoning of Pt based electro-catalyst. If the concentration of adsorbed CO is high enough, it will be hard to move on the next step (i.e. from Eq.4-6 to Eq.4-7). In the previously reported Pt-CeO_x nano-particle/C system, CeO_x which is electrode support would convert CO_x by taking electron from Pt-(CO) species.[49] It means that the electrochemical reduction reaction of Ce^{4+} to Ce^{3+} (i.e. $\mathbf{Ce^{4+} + e^- => Ce^{3+}}$) is assumed on the Pt–$CeO_x$ electro-catalyst. In the case of Pt-CeO_x nanoparticles/C, this proposed mechanism was not obviously observed in the activity of methanol electro-oxidation reaction because of low level Pt-CeO_x interface area and small amount of Ce^{4+} species in the interface.

In contrast, Pt-CeO_x nanowire/C has high Pt-CeO_x interface area which has electrochemical reduction reaction of Ce^{4+} (i.e. $\mathbf{Ce^{4+} + e^- => Ce^{3+}}$) and lattice oxygen (i.e. $\mathbf{1/2O_O^X + e^- => 1/2\ O''_i}$) in the interface of Pt-CeO_x nanowire interface. It is conclude that lower onset potential of methanol electro-oxidation reaction and higher current peak intensity ratio of forward and backward sweep (I_f / I_b) which were close to the conventional PtRu/C observed by aforementioned two electro-chemical reduction reactions in the Pt-CeO_x nanowire interface in Pt-CeO_x nanowire/C.

References

1. P. Costamagna, and S. Srinivasan, "Quantum Jumps in the PEMFC Science and Technology from the 1960s to the year 2000: Part I. Fundamental Scientific Aspects", *J. Power Sources*, **102**, pp.242-245 (2001).

2. E. E. Antolin, "Formation of Carbon-Supported PtM Alloys for Low Temperature Fuel Cells", *Mater. Chem. Phys.*, **78**, pp. 563-573 (2003).

3. E.Antolini, "Recent Developments in Polymer Electrolyte Fuel Cell Electrodes", *J. Appl. Electrochem*., **34**, pp. 563-576 (2004).

4. Y.Y. Tong, H.S. Kim, P.K. Babu, P. Waszczuk, A. Wieckowski, and E. Oldfield, **"**An NMR Investigation of CO Tolerance in a Pt/Ru Fuel Cell Catalyst", *J. Am. Chem. Soc*., **124**, pp. 468-473 (2002).

5. T.J. Schmidt, M. Noeske, H.A. Gasteiger, R.J. Behm, P. Britz, W. Brijoux, and H. Bönnemann**,** **"**Electrocatalytic Activity of PtRu Alloy Colloids for CO and CO/H_2 Electro-oxidation: Stripping Voltammetry and Rotating Disk Measurements**",** *Langmuir*, **13**, pp. 2591-2595 (1997).

6 . Y.Takasu, T.Fujiwara, Y.Murakami, K.Sasaki, M.Oguri, T.Asaki, and W.Sugimoto, "Effect of Structure of Carbon-Supported PtRu Electrocatalysts on the Electrochemical Oxidation of Methanol"*, J. Electrochem. Soc.*, **147**, pp. 4421-4427 (2000).

7. Y.M. Liang, H.M.Zhang, B.L.Yi, Z.H.Zhang, and Z.C.Tan, "Preparation and Characterization of Multi-walled Carbon Nanotubes Supported PtRu Catalysts for Proton Exchange Membrane Fuel Cells", *Carbon*, **43**, pp. 3144 -3152 (2005)**.**

8. V. Radmilovic,H.A.Gasteiger, and P.N.Ross, "Structure and Chemical Composition of a Supported Pt-Ru Electrocatalyst for Methanol Oxidation"*, J. Catal*., **154**, pp. 98-106 (1995).

9. C. Bock, C.Paquet, M.Couillard, G.A.Botton, and B.R.MacDougall, "Size-Selected Synthesis of PtRu Nano-Catalysts: Reaction and Size Control Mechanism", *J. Am. Chem. Soc*., **126**, pp. 8028-8037 (2004).

10. H.A.Gasteiger, N. M.Marković, P.N. Jr. Ross, and E.J.Cairns, "CO Electro-Oxidation On Well Characterized PtRu alloy", *J. Phys. Chem.*, **97**, pp.12020-12029 (1993).

11. H.A. Gasteiger, N. M.Marković,P.N. Jr Ross., and E.J.Cairns, "Carbon Monoxide Electro-oxidation on Well-Characterized Platinum-Ruthenium Alloys", *J. Phys. Chem*., **98**, pp. 617-625 (1994).

12. A.V. Tripković, K. D. Popović, B.N.Grgur, B.Blizanac, P.N. Jr. Ross, and N. M. Marković, "Methanol Electrooxidation on Supported Pt and PtRu Catalysts in Acid and Alkaline Solutions ", *Electrochimica Acta*, **47**, pp. 3707-3714 (2002).

13. B.Yang, Q.Lu, Y.Wang, L.Zhuang, J.Lu, P.Liu, J.Wang, and R.Wang, "Simple and Low-Cost Preparation Method for Highly Dispersed", *Chem. Mater.*, **15**, pp. 3552-3557 (2003).

14. G.A. Camara, M.J. Giz, V.A. Paganin, and E.A. Ticianelli, "Correlation of Electrochemical and Physical Properties of PtRu Alloy Electrocatalysts for PEM Fuel Cells", *J. Electroanal. Chem*., **537**, pp. 21 -29 (2002).

15. Z.L. Liu, X.Y. Ling, X.D. Su, and J.Y. Lee, "Carbon-Supported Pt and PtRu Nanoparticles as Catalysts for a Direct Methanol Fuel Cell", *J.Phys. Chem. B,* **108**, pp. 8234-8240 (2004).

16.G. Samjeske, H. Wang, T. Loffler, and H. Baltruschat," CO and Methanol Oxidation at Pt-Electrodes Modified by Mo", *Electrochim. Acta*, **47**, pp. 3681-3692 (2002)**.**

17. M. Gotz, and H.Wendt, "Binary and Ternary Anode Catalyst Formulations Including the Elements W, Sn and Mo for PEMFCs Operated on Methanol or Reformate Gas", *Electrochem. Acta***, 43**, pp .3637-3644 (1998).

18.E.C. Rivera, D.J. Volpe, L. Alden, C. Lind, C. Downie, T.V. Alvarez, A.C.D. Angelo, F.J.DiSalvo, and H.D. Abruña, "Electrocatalytic Activity of Ordered Intermetallic Phases for Fuel Cell Applications", *J.Am.Chem.Soc.*, **126**, pp.4043-4049 (2004).

19. Y.Liu, D.G. Li, V.R. Stamenkovic, S. Soled, J.D. Henao, and S.H. Sun, "Synthesis of Pt_3Sn Alloy Nanoparticles and Their Catalysis for Electro-Oxidation of CO and Methanol", *ACS Catalysis*, **1**, pp. 1719-1725 (2011).

20. P.Shen, K.Chen, and A.C.C.Tseung, "CO Oxidation on Pt/Ru/WO_3 Electrodes", *J. Electrochem. Soc.*, **142**, pp. 85-86 (1995).

21 D.C.Papageorgopoulos, M.Keijzer, and F.A. de Bruijn,"The Inclusion of Mo, Nb and Ta in Pt and PtRu Carbon Supported Electro-catalysts in the Quest for Improved CO tolerant PEMFC anodes", *Electrochim. Acta*, **48**, pp. 197-204(2002).

22. K.W. Park, J.H. Choi, B.K. Kwon, S.A. Lee, Y.E. Sung, H.Y. Ha, S.A. Hong, H.Kim, and A.Wieckowski,"Chemical and Electronic Effects of Ni in Pt/Ni and Pt/Ru/Ni Alloy Nanoparticles in Methanol Electrooxidation", *J. Phys. Chem. B*, **106**, pp. 1869 -1877 (2002).

23. T.C. Deivaraj, W.Chen, and J.Y.Lee, "Preparation of PtNi Nanoparticles for the Electro-catalytic Oxidation of Methanol", *J. Mater. Chem*., **13**, pp .2555-2560 (2003).

24. K.W.Park, J.H.Choi, B.K.Kwon, S.A.Lee, C.Pak, H.Chang, and Y.E.Sung, "Pt Ru Rh Ni Nanoparticle Electrocatalyst for Methanol Electro-oxidation in Direct Methanol fuel cell", *J. Catal*.,**224**, pp. 236-242 (2004).

25. H.R. Colon-Mercado, H. Kim, and B.N. Popov, "Durability Study of Pt_3Ni Catalysts as Cathode in PEM fuel cells", *Electrochem. Commun. ,* **6**, pp. 795-799(2004).

26.Y.Kang, and C.B.Murray, "Synthesis and Electrocatalytic Properties of Cubic Mn−Pt Nanocrystals (Nanocubes)", *J. Am. Chem. Soc.*, **132**, pp.7568-7569 (2010).

27. Y.Kang, and C.B.Murray,"Synthesis and Electrocatalytic Properties of Cubic Mn−Pt Nanocrystals (Nanocubes)", *J. Am. Chem. Soc.*, **132**, pp.7568-7569 (2010).

28. L. Jörissen,K.A.Friedrich, and J.Garche, "The function of Ruthenium Oxide in Pt-Ru Catalysts for Methanol Electro-Oxidation at Low Temperatures", *J. Solid State Electrochem*.,**7**, pp. 619-632 (2004).

29. R.B.Moghaddam, and P.G. Pickup, "Support Effect on the Oxidation of Methanol at Platinum Nanoparticle", *Electrochimica Acta*, **65**, pp.210-212(2012).

30. J.J.Pietron, M.B.Pomfret, C.N.Chervin, J.W.Long, and D.R. Rolison, "Direct Methanol Oxidation at Low Overpotentials using Pt Nanoparticle Electrodeposited at Ultrathin Conductive RuO_2 Nanoskins", *J.Mater.Chem.*, **22**, pp. 5197-5204 (2012).

31. H. Zhang, Y.Wang, E.R.Fachini, and C.R.Cabrera, "Electrochemically Co-deposited Platinum/Molybdenum Oxide Electrode for Catalytic Oxidation of Methanol in Acid Solution ". *Electrochemical and solid-state letter*, **2**, pp.437-439(1999).

32. R.S.Amin, R.M.Abdel Hameed, K.M.El-Khatib, M.Elsayed Youssef, and A.A.Elzatahry, "Pt–NiO/C Anode Electrocatalysts for Direct Methanol Fuel Cells", *Electrochimica Acta*, **59**, pp.499-508(2012).

33. C.T. Lin, H.J.Huang, Jr.J.Yang, and M.H.Shiao, "A Simple Fabrication Process of Pt–TiO_2 Hybrid Electrode for Photo-Assisted Methanol Fuel Cells", *Microelectronic Engineering*, **88**, pp.2644-2647 (2011).

34. D.A. Konopka, M. Li, K. Artyushkova, N. Marinkovic, K. Sasaki, R. Adzic, T.L. Ward, and P. Atanasov, "Highly Dispersive Pt Atoms on the Surface of RuNi Nanoparticles with Remarkably Enhanced Catalytic Performance for Ethanol-Oxidation", *J. Phys. Chem. C*, **115**, pp.3043-3044(2011).

35.C.W. Xu, and P.K.Shen, "Ethanol Electro-Oxidation on Pt/C and PtSn/C Catalysts in Alkaline and Acid Solutions", *Chem.Comm*, **19**, pp.2238-2242 (2004).

36. C.W. Xu, and P.K.Shen, "Electrochamical Oxidation of Ethanol on Pt-CeO_2/C Catalyst", *Journal of Power Sources*, **142**, pp.27-29 (2005).

37. C.W. Xu, R.Zeng, P.K.Shen, and Z.Wei, "Synergistic Effect of CeO_2 Modified Pt/C Catalysts on the Alcohols Oxidation", *Electrochimica Acta*, **51**, pp.1-5 (2005).

38. M. Takahashi, T. Mori, D. R. Ou, F. Ye, and J. Drennan ,"Anode Properties of Pt-CeO_2 Composite Electrode Material for Direct Methanol Fuel Cells Application", *Transactions of the Materials Research Society of Japan*, **32,** pp.967-970(2007).

39. M. Takahashi, T. Mori, A. Vinu, H. Kobayashi, J. Drennan,and D.R. Ou, "Preparation and Anode Property of Pt-CeO_2 Electrodes Supported on Carbon Black for Direct Methanol Fuel Cell Applications", *Journal of Materials Research*, **21**, pp. 2314-2322*(*2006).

40.M.Takahashi, T. Mori, F. Ye, A. Vinu, H. Kobayashi,and J. Drennan,"Design of High-Quality Pt-CeO_2 Composite Anodes Supported by Carbon Black for Direct Methanol Fuel Cell Application", *Journal of American Ceramic Society*, **90**, pp.1291-1294(2007).

41. M. Takahashi,T. Mori, A. Vinu, D. R. Ou, H. Kobayashi and J. Drennan ,"Development of High Quality Pt–CeO_2Electrodes Supported on Carbon Black for Direct Methanol Fuel Cell Applications", *Adv. Appl. Ceram*.,**107**, pp.57-63(2008).

42. A.M.Scibioh, S.K. Kim, E.A.Cho, T.H.Lim, S.A.Hong,and H.Y.Ha,"Pt-CeO_2/C Anode Catalyst for Direct Methanol Fuel Cells", *Applied Catalysis B: Environmental*, **84**, 773-782(2008).

43. D.J.Guo,and Z.H. Jing, "A Novel Co-Precipitation Method for Preparation of Pt-CeO_2 Composites on Multi-walled Carbon Nanotubes for Direct Methanol Fuel Cells", *Journal of Power Sources,* **195**, pp.3802-3805(2010).

44. A. Tabet-Aoul, M. Mohamedi, "Interrelated Functionalities of Hierarchically CNT/CeO_2/Pt Nanostructured Layers: Synthesis, Characterization, and Electroactivity", *Physical Chemistry Chemical Physics,* **14**, pp. 4463-4474(2012).

45. J.Wang, A.Deng, J.Xi, L.Chen, W.Zhu, and X.Qiu, "Promoting the Current for Methanol Electro-oxidation by Mixing Pt-based Catalysts with CeO_2 Nanoparticles", *J. Power Sources*, **170**, pp.297-302 (2007)**.**

46. S.Y.Huang, C.M.Chang, and C.T.Yeh, **"**Promotion of Platinum-ruthenium Catalyst for Electro-oxidation of Methanol by Ceria", *J. Catal.*, **241**, pp.400-406(2006).

47. T. Masuda,H. Fukumitsu,K. Fugane,H. Togasaki,D. Matsumura,K. Tamura,Y. Nishihata,H. Yoshikawa,K. Kobayashi,T. Mori,and K. Uosaki, "Role of Cerium Oxide in the Enhancement of Activity for the Oxygen Reduction Reaction at Pt–CeO_x Nanocomposite Electrocatalyst - An in Situ Electrochemical X-ray Absorption Fine Structure Study", *J. Phys. Chem. C*, **116**, pp.10098−10102 (2012).

48. J.M. Legar,"Mechanistic Aspect of Methanol Oxidation on Platinum based Electrocatalyst", *Journal of Applied Electrochemistry*, **31**, pp.767-771(2001).

49. F. Xiaojuan S. Yanlong and Z. Huijuan, "Electrocatalytic Enhancement of Methanol Oxidation by Adding CeO_2 Nanoparticle on Porous Electrode", *Journal of Rare Earth*, **30**, pp.29-33(2012).

50. B.M. Babi, L.M. Vracar, V. Radmilovi, and N.V. Krstaji, "Carbon Cryogel as Support of Platinum Nano-sized Electro-catalyst for the Hydrogen Oxidation Reaction", *Electrochimica Acta* ,**51**, pp. 3820–3826(2006).

51. Z. Yan, J. Xie, S. Zong, M. Zhang, Q. Sun and M. Chen," Small Sized Pt Particles on Mesoporous Hollow Carbon Spheres for Highly Stable Oxygen Reduction Reaction", *Electrochimica Acta*, **109** , pp.256– 261(2013).

52. G. Centi , M. Gangeri , M. Fiorello , S. Perathoner , J. Amadou , D. Be' gin , M.J. Ledoux ,C. Pham-Huu , M.E. Schuster , D.S. Su , J.P. Tessonnier and R. Schlogl,"The Role of Mechanically Induced Defects in Carbon Nanotubes to Modify the Properties of Electrodes for PEM fuel cell", *Catalysis Today*,**147**, pp. 287–299(2009).

53. R. Siburian, T. Kondoand J. Nakamura, "Size Control to a Sub-Nanometer Scale in Platinum Catalysts onGraphene", *J. Phys. Chem. C*, **117**, pp.3635−3645(2013).

54. E.V SpinacéA.O Neto and M Linardi, "Electro-oxidation of Methanol and Ethanol using PtRu/C Electrocatalysts Prepared by Spontaneous Deposition of Platinum on Carbon-Supported Ruthenium Nanoparticles,"*Journal of Power Sources*, **129**, pp. 121–126(2004).

56. L. Dong ,R. R. S. Gari , Z. Li , M. M. Craig and S. Hou, "Graphene-Supported Platinum and Platinum–Ruthenium Nanoparticles with high Electrocatalytic Activity for Methanol and Ethanol Oxidation", *Carbon*, **48**, pp.781-787(2010).

57.Z. Liu, X. Y. Ling, X.Su, and J. Y. Lee, "Carbon-Supported Pt and PtRu Nanoparticles as Catalysts for a Direct Methanol Fuel Cell", *J. Phys. Chem. B*, **108**, pp.8234-8240(2004).

58.A. V, Palenzuela, F. Centellas, J. A. Garrido and C. Arias, R. M. Rodríguez, E. Brillas and P.-L. Cabot, "Kinetic analysis of carbon monoxide and methanol oxidation on high performance

carbon-supported Pt–Ru electro-catalyst for direct methanol fuel cells", *Journal of Power Sources*, **196**, pp.3503–3512(2011).

59. G. Garcíaa, J. F.-Montano, A.H.Creusa, E.Pastora and G.A. Planesb, "Methanol Electrooxidation at Mesoporous Pt and Pt–Ru Electrodes: A Comparative Study with Carbon Supported Materials", *Journal of Power Sources* , **196**, pp.2979–2986(2011).

60. J. Lu, L.Hong, Y. Yang, S. Xu, S. Wang, J. Yuan and Li Niu, "Phosphotungstic Acid-Assisted Preparation of Carbon Nanotubes-Supported Uniform Pt and Pt Bimetallic Nanoparticles, and their Enhanced Catalytic Activity on Methanol Electro-oxidation *", Journal of Nanoparticle Research*, **16**, pp.1-11 (2013).

Chapter 5 Improvement of ORR activity on Pt loaded CeO_x nanowire/C electrocatalyst

5-1. Introduction

In last chapter, I discussed the role of Pt-CeO_x interface on the anodic property (i.e. electro-oxidation of methanol) based on the experimental data. The Pt-CeO_x interface which was formed on CeO_x nanowire loaded Pt whose particle size were 3 to 4 nm contributed to the improvement of anodic property in the observed electro-catalysis. Aforementioned functional Pt-CeO_x interface would be activated after 300 cycles of electrochemical pre-treatment which gave the result of high EASA. Pt-CeO_x interface mainly consists of Ce^{4+} species which is different with Pt-CeO_x nano-particles interface. It is because Pt-CeO_x nano-particles/C mainly consists of Ce^{3+} species in the Pt-CeO_x nano-particle interface.

Pt content in the cathode of polymer membrane fuel cell device is from 20 to 50wt% to give high power density[1-2]. However, high cost of Pt electro-catalysts is the major barriers to widespread of fuel cell in a variety of applications.

Fugane et al. improved the ORR activity by using Pt-CeO_x nano-particle interface and proposed the unique mechanism for improvement of ORR activity on Pt[3,4]. In this case, 20wt% Pt loaded CeO_x nano-particle/C electrodes mainly consisted of Ce^{3+} cations[3,4]. It was based on the electrochemical redox reaction ($Ce^{3+} \Leftrightarrow Ce^{4+}$) at room temperature, of which Masuda et al. observed aforementioned key electrochemical redox reaction by using in-situ XANES analysis[5].

To conclude the role of Pt-CeO_x nanowire interface on electrode reaction and decrease the Pt content in the cathode, the activity of oxygen reduction reaction (ORR) observed on Pt-CeO_x nanowire/C was examined in the present chapter. Also, the effect of the amount of Pt in Pt-CeO_x nanowire/C on ORR activity was examined.

5-2. Results and discussion

5-2-1. Interfacial structural features of Pt loaded CeO_x nanowire/C

In Chapter 4, it is concluded that the interstital oxygen sites in the Pt-CeO_x interface on Pt loaded CeO_x nanowire/C electrode are formed and it conctributed to the enhancement of anode property, futher defect structure analysis of Pt-CeO_x nanowire interface on Pt loaded CeO_x nanowire/C electro-catalysts is performed by using EELS analysis technique in Chapter 5. Also, effect of fromation of Pt-CeO_x nanowire interface on Pt loaded CeO_x nanowire/C on improvement of ORR activity is examined in the present chapter.

5-2-1 (a) Cerium M-edge peak analysis

Indentication of cerium valancy in the Pt-CeO_x nanowire interface is important for concluding defect stucutre of Pt-CeO_x hetero-interface on Pt loaded CeO_x nanowire/C electro-catalysts. The fluorite structure mainly consists of tetravalant and trivalent cerium cations. To cocnclude the influcen of oxidation state**s** of cerium cations in Pt-CeO_x nanowire interface on activity of ORR reaction, the valence of Ce cation after electro-chemical pre-treatment (i.e. electrochamical conditioning process) was examined by using EELS. Figure 5-1 shows the energy loss spectra of Ce $M_{4,5}$-edges spectra taken from 50wt%, 10wt%, and 5wt% Pt loaded CeO_x nanowire/C after 300cycle swqeeps in 0.5M H_2SO_4 aqueous solution. The EELS profiles in the Figure 5-1 have two characterstics peaks marked by M_4 and M_5. The intensity ratio of M_5/ M_4 peaks (i.e. I_{M5}/ I_{M4}) represents Ce valance states[6, 7]. The ratio of I_{M5}/ I_{M4} observed for aforementioned three samples were from 0.92 to 1.07, where I_{M4} and I_{M5} are maximum intensities of the peaks. Shoulder features that are known to be characteristic of Ce^{4+} cation can be noted in both peaks (i.e. peaks of CeM_4 and CeM_5), as indicated by using arrows. And the observed peak intensity ratios I_{M5}/ I_{M4} were summarized in Table 5-1.

For pure ceria (i.e. CeO_2), I_{M5}/ I_{M4} value was estimated to be around 1.2[7,8]. Both Figure 5-1 and Table 5-1 indicate that the Pt-CeO_x nanowire interface on the electrochemically pre-treated three Pt loaded CeO_x nanowire/C samples (i.e. 50, 10, and 5wt% Pt loaded CeO_x nanowire/C) mainly consists of Ce^{4+} cation and little amount of trivalent cerium cation (i.e. Ce^{3+}) co-exists in aforementioned interface.

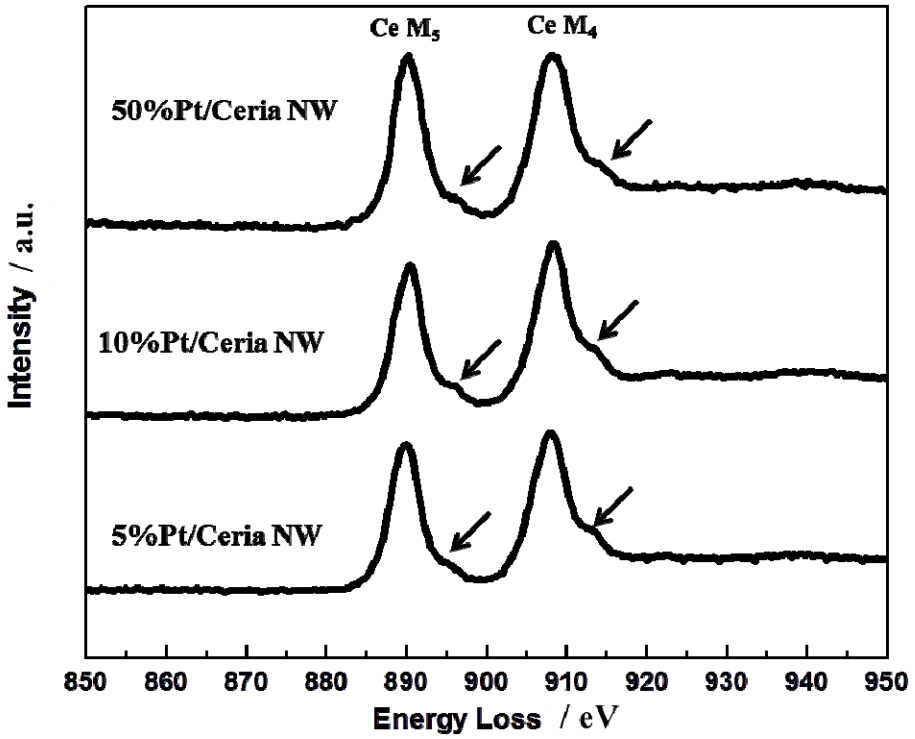

Figure 5-1 EELS spectra of Ce $M_{4,5}$-edge spectra taken from Pt loaded CeO_x nanowire/C samples.

Table 5-1 Estimated I_{M5}/ I_{M4} ratios observed for Pt loaded CeO_x nanowire/C samples.

Pt content (wt%)	I_{M5}/I_{M4}
50	1.07
10	0.926
5	0.925

As mentioned in the introduction of the present chapter (i.e. 5-1. introduction), it will be expected that the observed level of ORR activity on Pt in Pt loaded CeO_x nanowire/C is different from Pt loaded CeO_x nano-particle/C because of quite different oxidation state of Ce cation in the interface in the Pt loaded CeO_x nano-particle/C.

5-2-1 (b). Oxygen K-edge peak analysis.

Since the valence of Ce cation in the interface of Pt loaded CeO_x nano-particle/C mainly consisted of Ce^{4+} (not Ce^{3+}), the local ordering of oxygen vacancies of CeO_x in the Pt-CeO_x nanowire was characterized by using oxygen K-edge spectra analysis. In the Figure 5-2, three featured peaks, labeled by A, B and C, can be observed. Peak A is attributed to oxygen 2*p* states hybridized with Ce 4*f*. Peaks B and C were attributable to oxygen 2*p* states hybridized with Ce 5*d* states under a cubic crystal field[10]. Those two peaks were also believed to be the signature of the tetrahedral arrangement of the oxygen atoms in various isoelectronic oxides[9]. Also, the peak analysis of oxygen K-edge spectra has been successfully applied to determine the oxygen vacancy ordering in CeO_x based system which consists of Ce^{3+} and Ce^{4+} [8, 10, 11]. In this analysis, it has been suggested that the enhancement in the peak intensity ratio between peak B and peak C (I_B/ Ic) could be introduced by the local ordering oxygen vacancies of CeO_x lattice in Pt-CeO_x interface[8].

The peak intensity ratio (I_B/ Ic) between peak B and peak C was examined for the characterization of the local ordering of oxygen vacancies of CeO_x lattice in the Pt-CeO_x nanowire interface in the present work. The integral intensities of peak B and C (i.e. I_B and Ic) were estimated by using energy windows with a width of 2eV, and the peak intensity ratio between peak B and peak C (I_B/ Ic) was calculated.

Figure 5-2 shows EELS oxygen K-edge spectra observed for 5wt%, 10wt% and 50wt% Pt loaded CeO_x nanowire/C samples. Also, I_B/ Ic values observed for aforementioed three samples were summarized in Table 5-2.

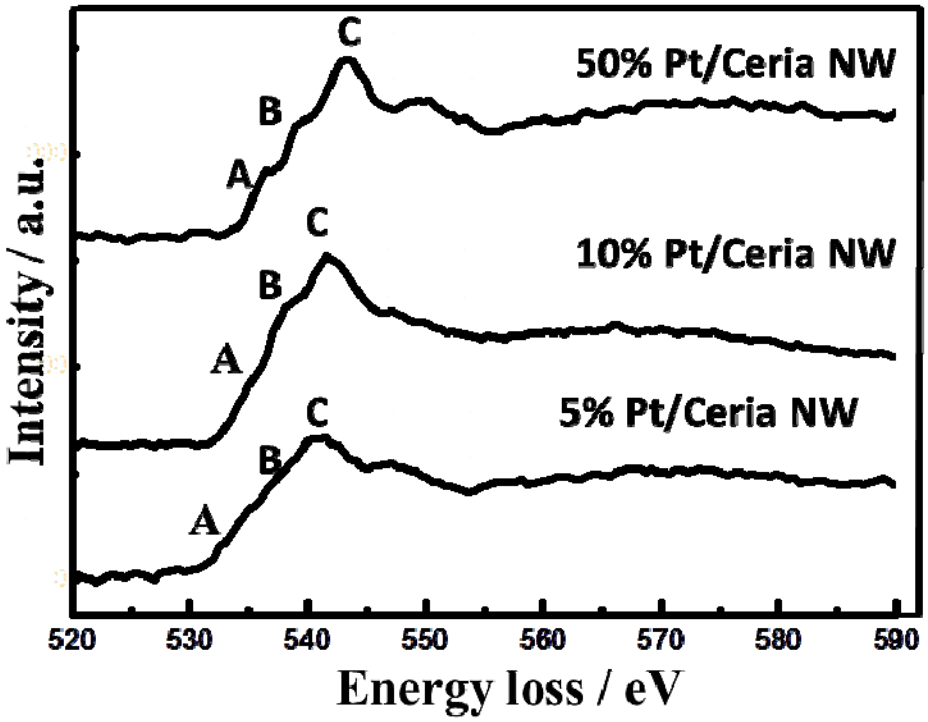

Figure 5-2 EELS oxygen K-edge spectra observed for Pt loaded CeO_x nanowire/C.

Table 5-2 Comparison of I_B/ Ic ratios observed for Pt loaded CeO_x nanowire/C electro-catalysts.

Pt content (wt%)	I_B/I_C
50	0.63
10	0.80
5	0.95

In the case of calculated value for ideal CeO_2 (i.e. Ce^{4+}), the I_B/ Ic ratio was approximately 0.7. The I_B/ Ic ratio observed for 50wt% Pt loaded CeO_x nanowire/C was almost same to the previously reported value for ideal CeO_2. Also other I_B/ Ic ratios observed for 10wt% Pt loaded CeO_x nanowire/C and 5wt% Pt loaded CeO_x nanowire/C were close to aforementioned ideal value, although the observed values for 10wt% Pt loaded CeO_x nanowire/C and 5wt% Pt loaded CeO_x nanowire/C were slightly higher than that of ideal value of CeO_2 (i.e. Ce^{4+}). It suggests that higher level local ordering of oxygen vacancy of CeO_x lattice which is similar to C-type rare earth structure is in the Pt-CeO_x nanowire interface of 5wt% Pt-CeO_x nanowire/C, even though the heterogeneous interface between Pt and CeO_x mainly consists of Ce^{4+} species.

Based on the characterization results of oxygen K-edge spectra observed for Pt-CeO_x nanowire/C specimens, it is concluded that small amount of Ce^{3+} species or some amount of interstitial oxygen which creates the local ordering of oxygen vacancy in the fluorite lattice (i.e. Ce^{4+} lattice) exists in the interface of Pt and CeO_x nanowire.

5-2-2 Oxygen Reduction Reaction (ORR) Activity on Pt/ CeO_x nanowire/C

The hydrodynamic voltamogrammes of ORR observed for 5wt% and 10wt% Pt loaded CeO_x nanowire/C shifted to higher potential region as compared with commercially available 20wt%

Pt/C as shown in Figure 5-3. To characterize higher potential region more than 0.85 V (vs. RHE) in details, the magnified hydrodynamic voltamogrames of ORR were shown in Figure 5-3(b). Those two figures clearly suggests that the observed ORR activity on Pt loaded CeO_x nanowire/C electro catalysts are better than that of commercially available Pt/C. Especially, the magnified figure (i.e. Figure 5-3 (b)) suggests that ORR activities on Pt loaded CeO_x nanowire/C are observed around 1V (vs. RHE). It looks improvement of ORR activity as compared with conventional Pt/C.

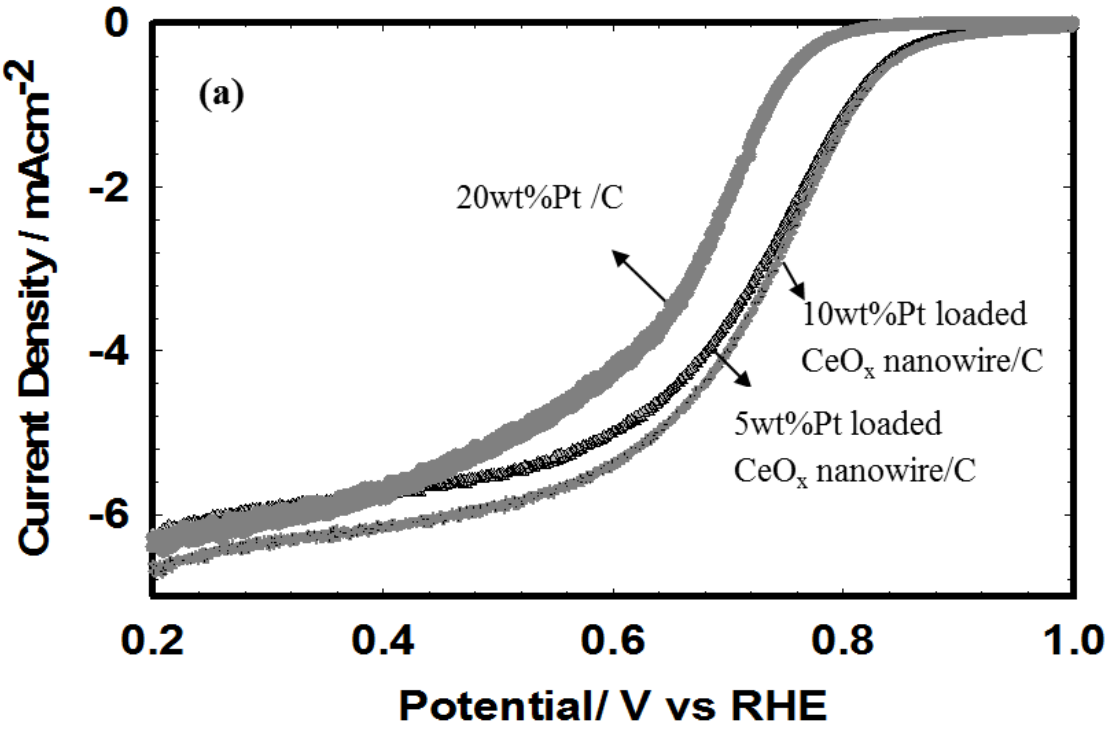

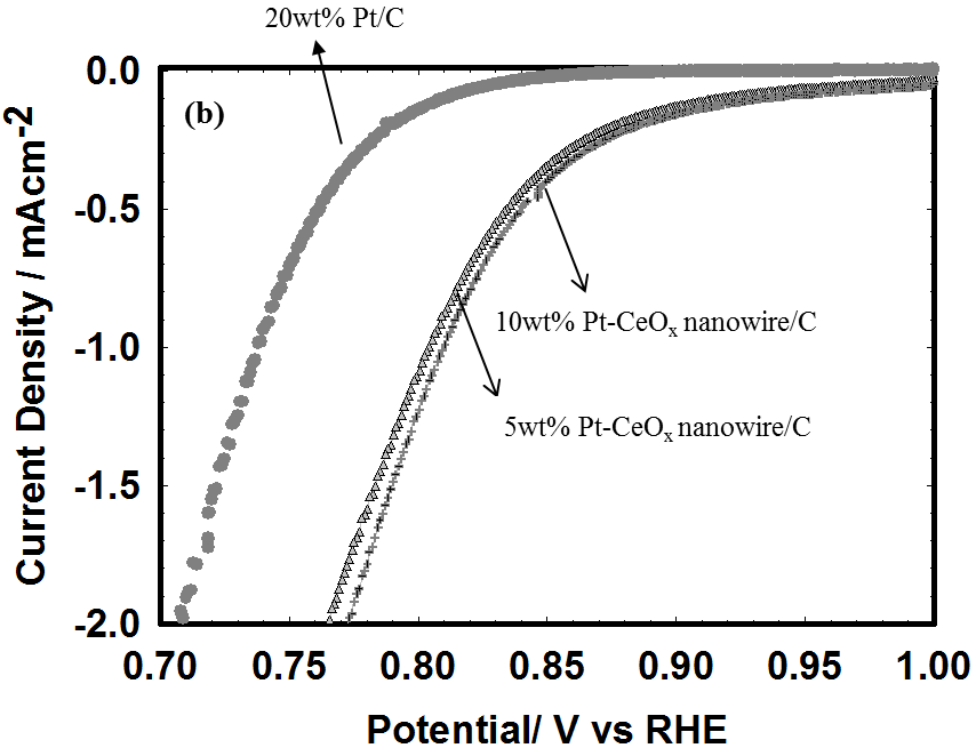

Figure 5-3(a) Hydrodynamic voltamogrammes and **(b)** magnified hydrodynamic voltamogrammes of ORR on commercially available Pt/C and Pt loaded CeO_x nanowire/C electrocatalysts in 0.5M H_2SO_4 aqueous solution at 28°C.

To characterize this improvement of ORR in the high potential region in details, Tafel plots were derived by using the ORR data observed for 50wt% Pt loaded CeO_x nanowire/C, 5wt% Pt loaded CeO_x nanowire/C, 5wt% Pt loaded CeO_x nano-particles/C and commercially available 20wt% Pt/C. Figure 5-4(a) presents Tafel plot observed for 50wt% Pt loaded CeO_x/C and commercially available Pt/C electro-catalysts. Based on this data, it is conclude that ORR activity observed for 50wt% Pt loaded CeO_x nanowire/C is slightly higher than that of commercially available 20wt%

Pt/C electro-catalyst. This small improvement of ORR on 50wt% Pt loaded CeO_x nanowire/C would be attributable to promotion effect of Pt-CeO_x nanowire interface which is formed on Pt.

To examine the effect of enhancement of ORR activities on the formation of Pt-CeO_x nanowire interface, same Tafel plot analysis was performed by using 5wt% Pt loaded CeO_x nanowire/C, and 20wt% Pt/C. In Figure 5-4(b), the unusual two steps of Tafel lines were observed for 5wt% Pt loaded CeO_x nanowire/C. To conclude this unusual result, the Tafel plot was obtained by using ORR activity data observed for CeO_x nanowire/C without Pt catalyst. As demonstrated in Figure 5-4(b), the weak signal of ORR was observed for the surface of CeO_x nanowire/C without Pt. Noisy signal and low kinetic current density were observed as compared with the ORR signal observed for 5wt% Pt loaded CeO_x nanowire/C. It indicates that ORR activity observed for CeO_x nanowire/C without Pt was quite low level. In the case of previously reported Pt loaded CeO_x nanoparticle/C, the remained CeO_x on Pt was quite low level and interface area between Pt and CeO_x was limited. As a consequence, the electrochemistry observed for the previous reported Pt loaded CeO_x nanoparticle/C was not affected by the electrochemistry on remained CeO_x on Pt. The promotion effect of CeO_x by the formation of Pt-CeO_x interface was simply observed in the previous work.

On the other hand, Pt-CeO_x interface area became wide by using reaction space between CeO_x nanowire surface and $Ce(OH)_3$ in the present thesis work which was shown in Chapter 3. The observed EASA for Pt-CeO_x nanowire/C surface was approximately 5 times higher than the previously reported Pt-CeO_x nanoparticle/C surface. This suggests that the remained CeO_x in the Pt- CeO_x nanowire/C electrode became high level as compared with Pt-CeO_x nanoparticle/C. The electrochemistry on CeO_x nanowire/C without Pt affected the slope of Tafel line taken from 5wt% Pt-CeO_x nanowire/C at higher potential region (i.e. more than 0.9V (vs.RHE)) in Figure 5-

4(b). However, the slope of Tafel line observed for 5wt% Pt loaded CeO_x nanowire/C (i.e. -103mVdec^{-1}) was steeper than that of conventional Pt/C (i.e. -60mVdec^{-1}) under 0.9V (vs.RHE). Also, aforementioned Tafel slop observed for 5wt% Pt loaded CeO_x nanowire/C below 0.9V (vs.RHE) was also steeper than that of previously reported 20wt% Pt loaded CeO_x nanoparticle/C (i.e. approximately -73mVdec^{-1}). It suggests that excess over potential of ORR on 5wt% Pt-CeO_x nanowire/C became small as compared with previously reported 20wt% Pt loaded CeO_x nanoparticle/C. Therefore, Tafel line derived from the ORR data which was observed for 5wt% Pt-CeO_x nanowire/C shifted to higher potential side as compared with 20wt% Pt loaded CeO_x nanoparticle/C.

To examine the effect of Pt-CeO_x nanowire interface formation on a lowering of Pt amount in the electro-catalysts, Tafel line derived from the ORR data which was observed for 5wt% Pt-CeO_x nanoparticle/C compared with conventional Pt/C as shown in Figure 5-4(c). This figure clearly indicates that Tafel line derived from 5wt% Pt-CeO_x nanoparticle/C shifted into low potential side as compared with 5wt% Pt-CeO_x nanowire/C which was shown in Figure 5-4(b).

Based on experimental results, it is concluded that Pt amount in Pt-CeO_x electro-catalyst systems can be minimized by formation of Pt-CeO_x nanowire interface on Pt.

In the present work, however, important point is not only improved level of ORR activity observed for 5wt% Pt loaded CeO_x nanowire/C as compared with previously reported Pt-CeO_x nanoparticle/C. The change of Tafel slope observed for 5wt% Pt loaded CeO_x nanowire/C suggests that there are two kinds of Pt active sites on CeO_x nanowire surface, even though the observed Tafel line affected by the electrochemistry of CeO_x nanowire without Pt. If the Pt loaded CeO_x nanowire interface perfectly covered the surface of CeO_x nanowire and there is no bare CeO_x nanowire surface without Pt-CeO_x nanowire interface on the prepared electro-catalyst,

Steep Tafel slope will be observed for 5wt% Pt-CeO_x nanowire surface as well as previously reported electro-catalysts. Also it is expected that Tafel line derived from 5wt% Pt loaded CeO_x nanowire/C surface will be much steeper (i.e over -103mVdec^{-1}) than previously reported electro-catalysts.

To characterize the effect of Pt-CeO_x nanowire interface formation on enhancement of ORR activity on Pt in details and develop the design concept for fabrication of high quality electro-catalysts with high ORR activity, both K-L plot analysis (Figure 5-5(a) to 5-5(e)) and potential dependence of kinetic current density which can be estimated by using intersect point between horizontal axis and vertical axis of K-L plot (Figure 5-6 (a) and (b)) were examined.

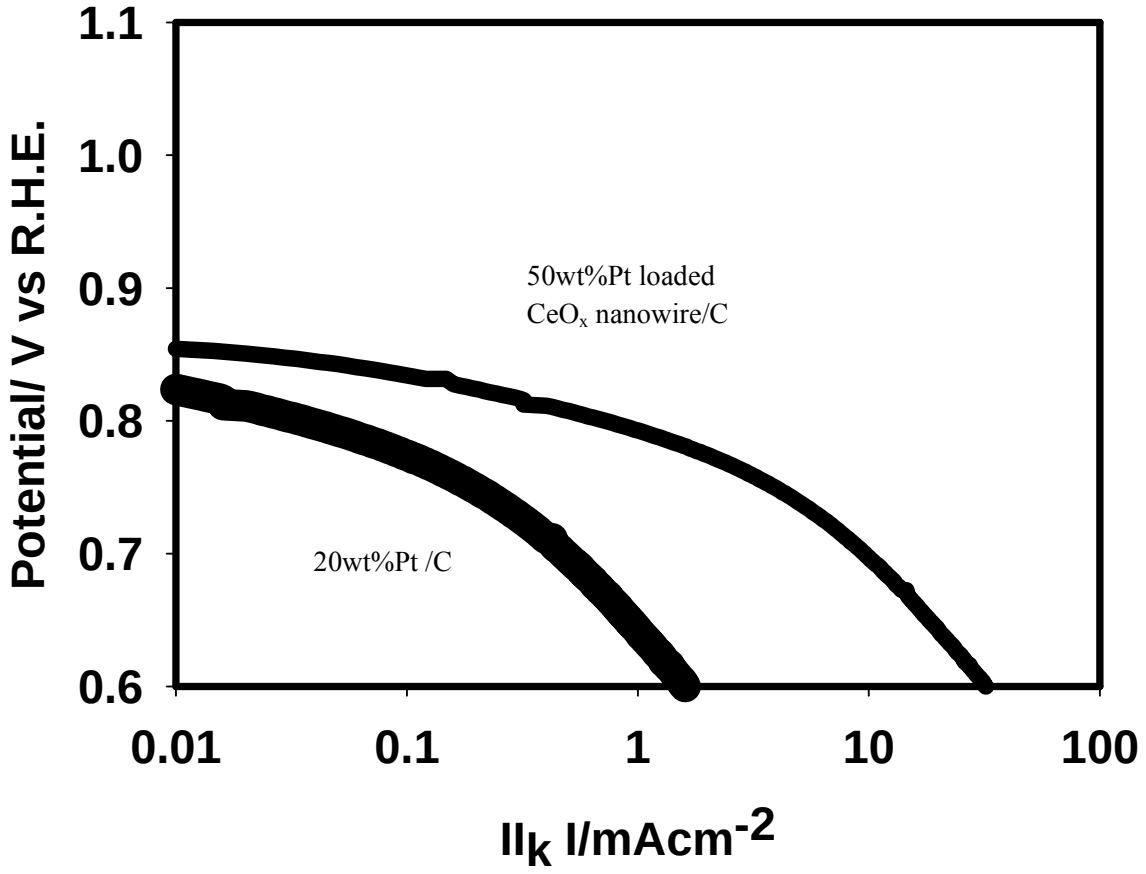

Figure 5-4(a) Tafel plots derived from kinetic current density I_k of 50wt% Pt loaded CeO_x nanowire/C and conventional Pt/C.

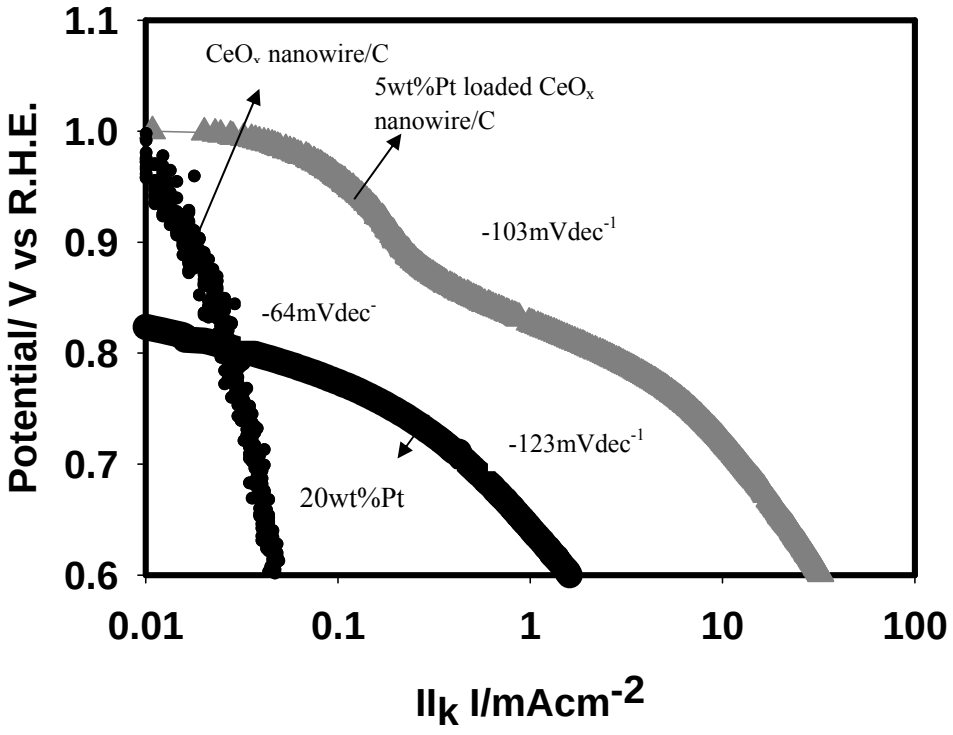

Figure 5-4(b) Tafel plots derived from kinetic current density I_k of 5wt % Pt loaded CeO_x nanowire/C, CeO_x nanowire/C without Pt and conventional Pt/C.

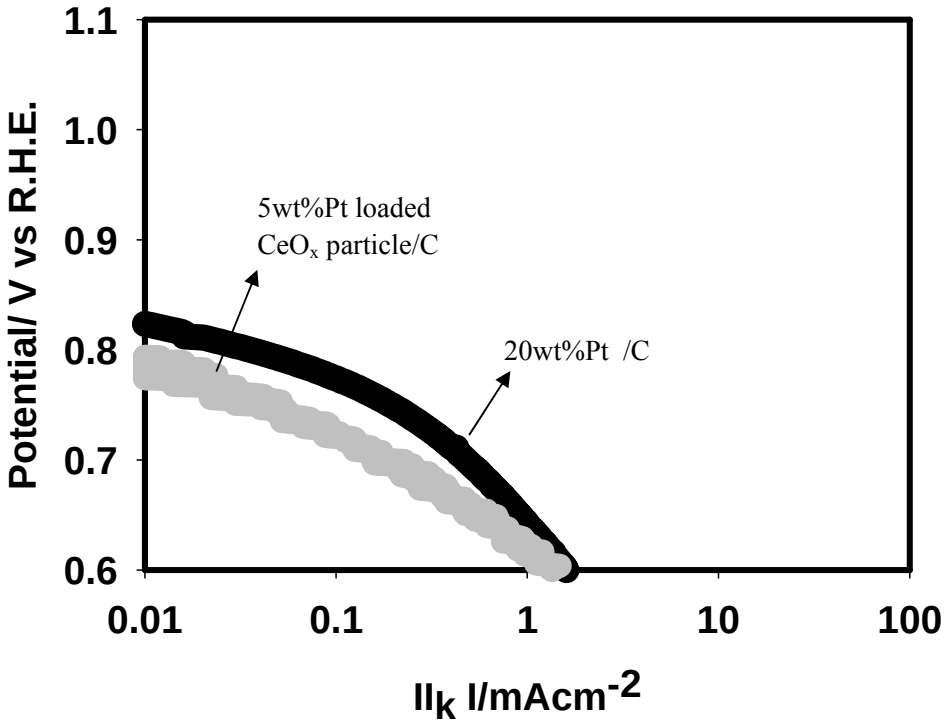

Figure 5-4(c) Tafel plots derived from kinetic current density I_k of 5wt% Pt loaded CeO_x nano-particle/C(grey) and Pt/C(black).

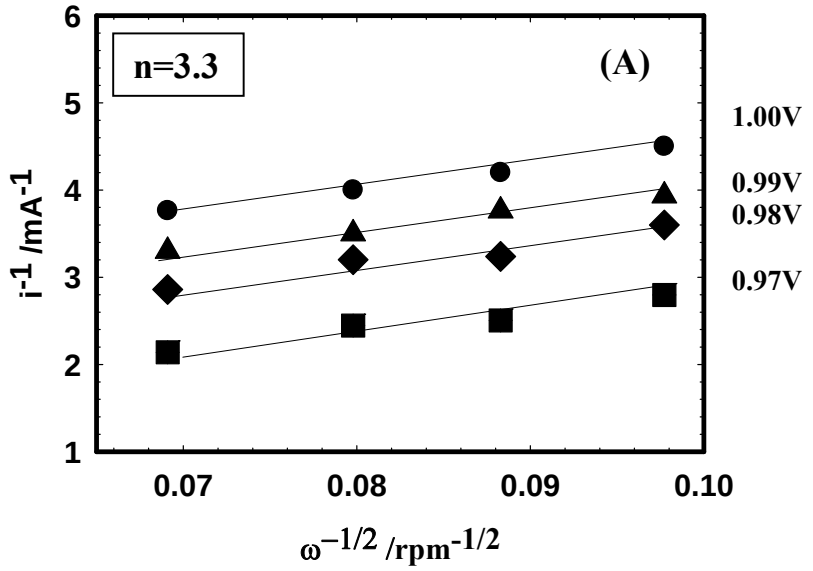

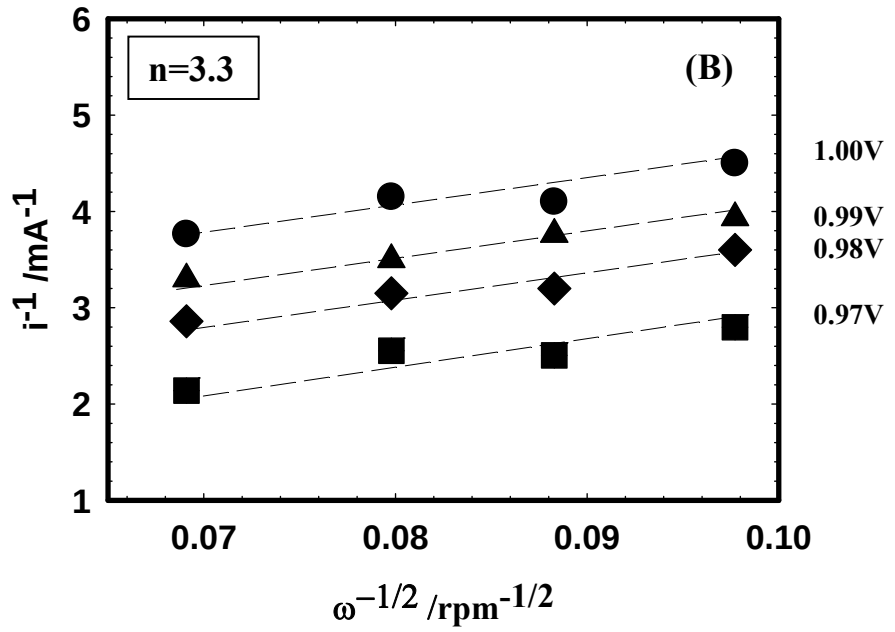

Figure 5-5(a) Kotecky-Levich plots at different potential observed from 5wt% Pt loaded CeO_x nanowire/C (A) and 10wt % Pt loaded CeO_x nanowire/C (B). Observed potential region: 0.97 to 1.00V (vs. RHE).

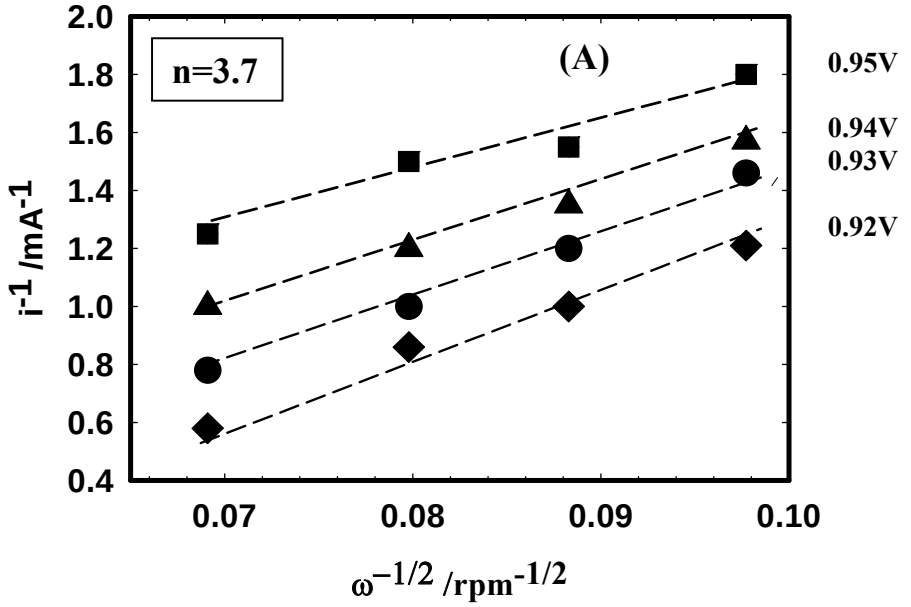

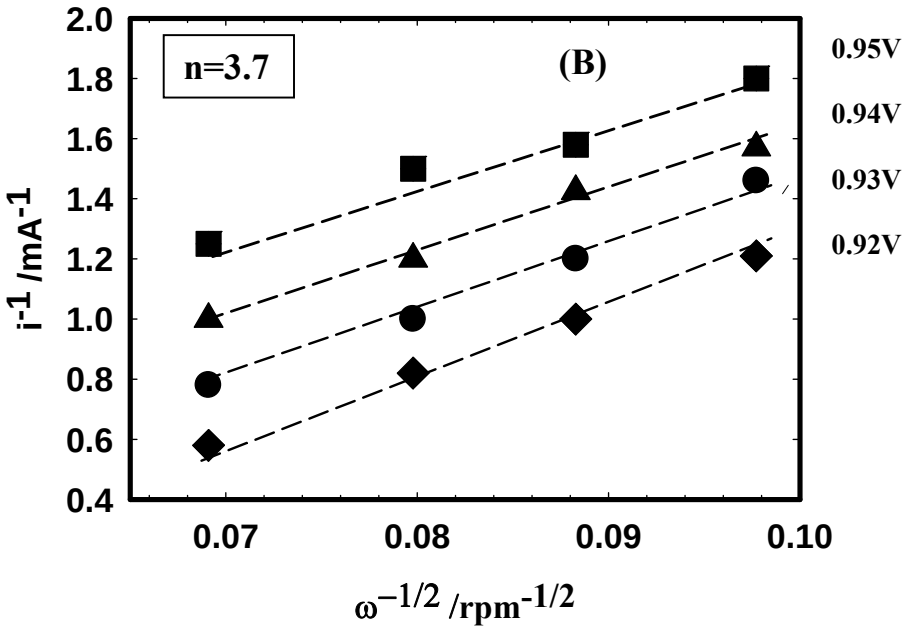

Figure 5-5(b) Kotecky-Levich plots at different potential observed from 5wt% Pt loaded CeO_x nanowire/C (A) and 10wt% Pt loaded CeO_x nanowire/C (B). Observed potential region: 0.92 to 0.95V (vs. RHE).

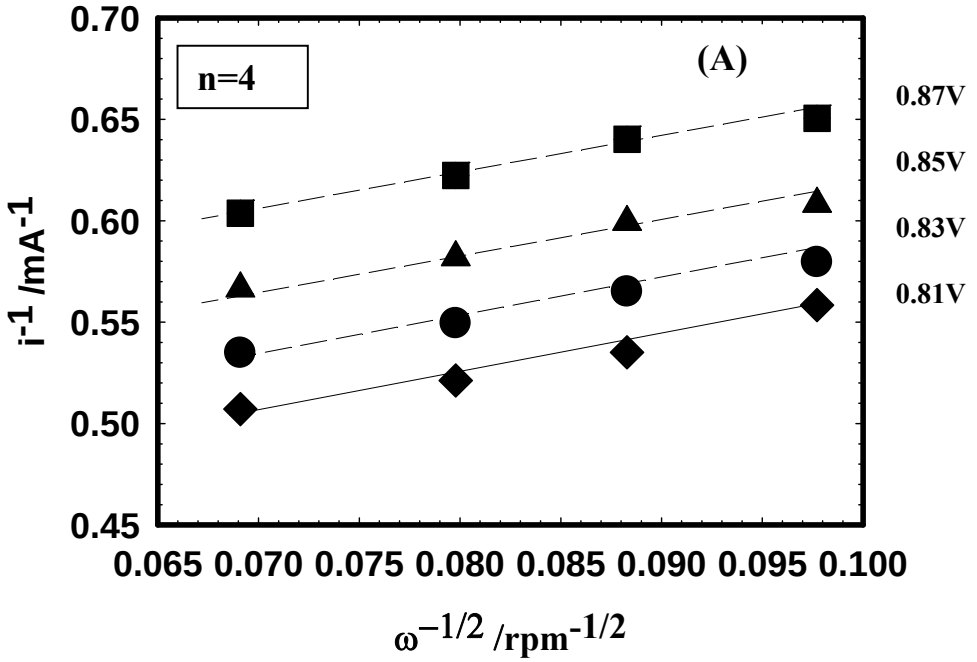

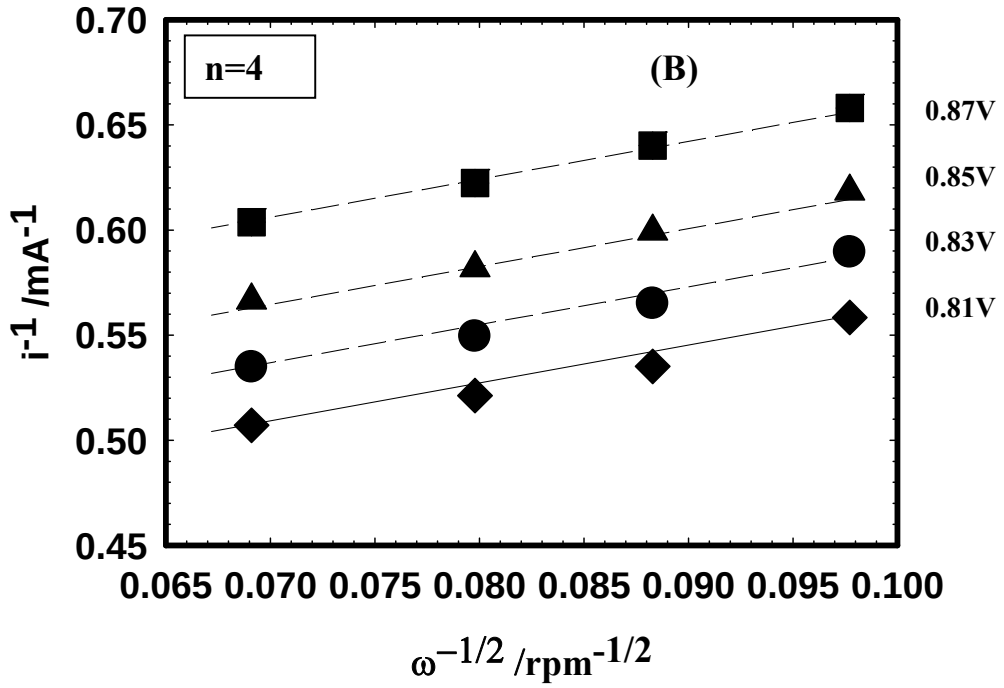

Figure 5-5(c) Kotecky-Levich plots at different potential observed from 5wt% Pt loaded CeO_x nanowire/C (A) and 10wt% Pt loaded CeO_x nanowire/C (B). Observed potential region: 81 to 0.87V (vs. RHE).

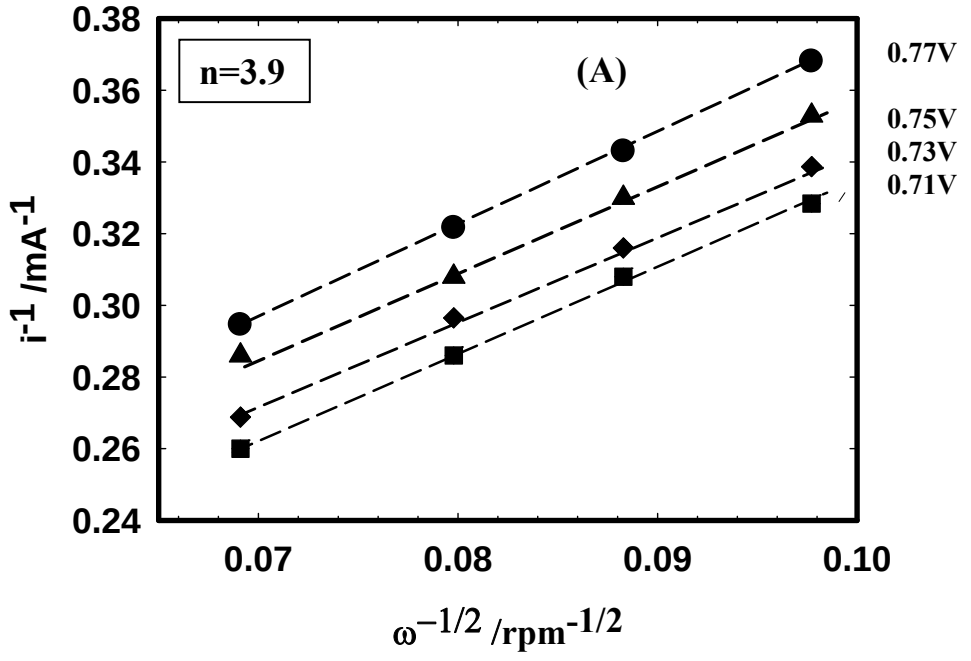

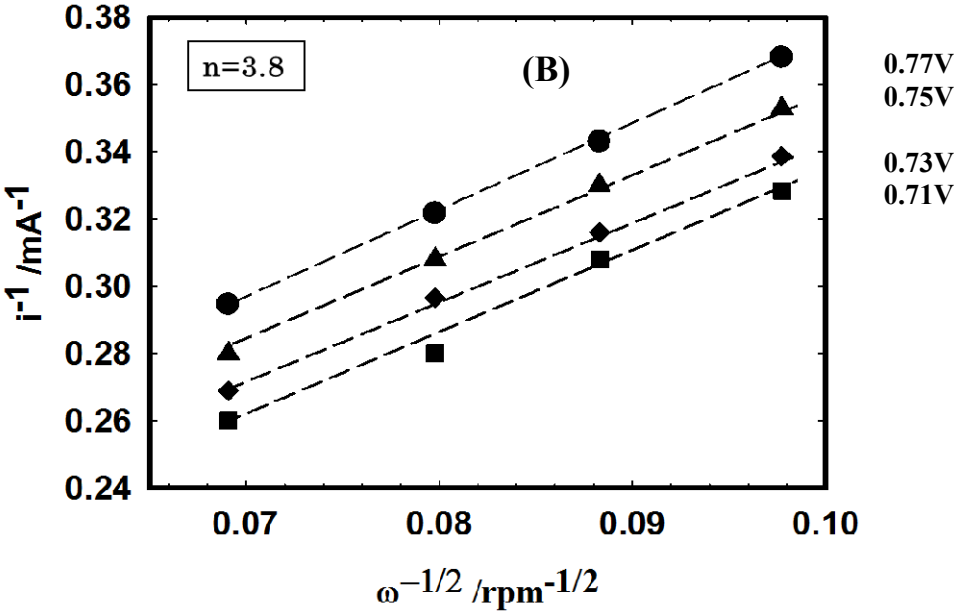

Figure 5-5(d) Kotecky-Levich plots at different potential observed from 5wt% Pt loaded CeO_x nanowire/C (A) and 10wt% Pt loaded CeO_x nanowire/C (B). Observed potential region: 0.71 to 0.77V (vs. RHE).

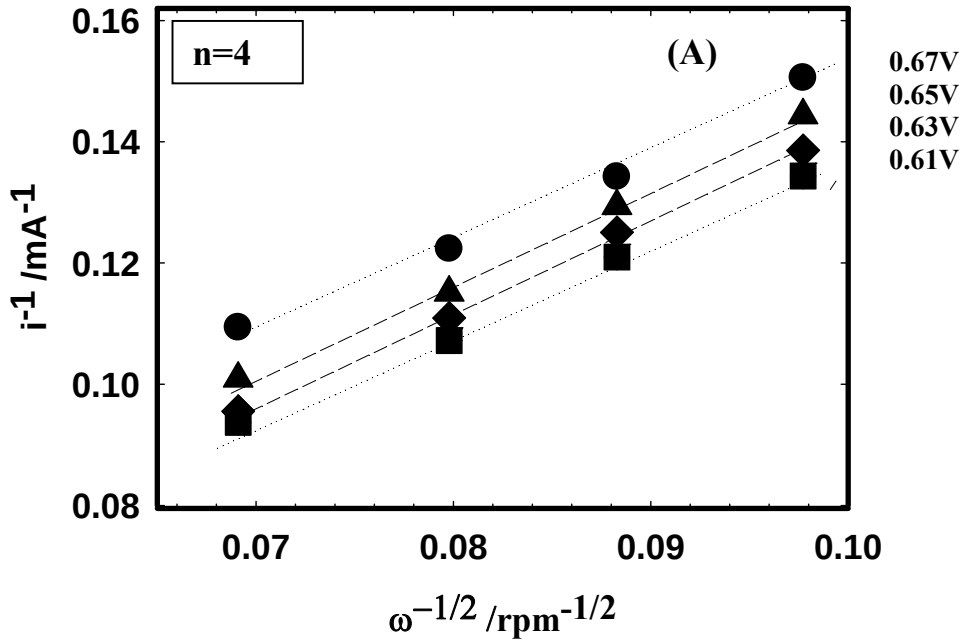

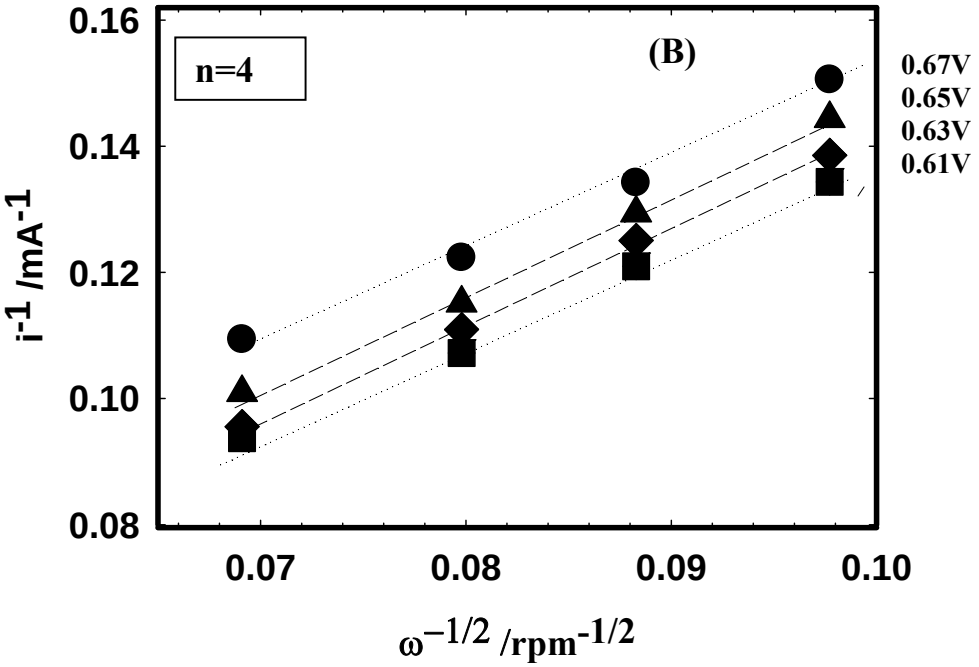

Figure 5-5(e) Kotecky-Levich plots at different potential observed from 5wt% Pt loaded CeO_x nanowire/C (A) and 10wt% Pt loaded CeO_x nanowire/C (B). Observed potential region: 0.61 to 0.67V (vs. RHE).

To analyze the number of electrons in the electrode reactions on 5wt% Pt loaded CeO_x nanowire/C and 10wt% Pt loaded CeO_x nanowire/C, K-L plots were obtained in five cases based on the data of Figure 5-4(b). First one is for analysis of electrochemistry at potential ranging from 0.97 to 1.0V vs. RHE (i.e. Figure 5-5(a)). This is for characterization of one of two steps at higher potential region. Figure 5-5(a) indicates that number of electrons observed for 5wt% and 10wt% Pt loaded CeO_x nanowire/C (i.e. n=3.3) is less than ideal number of electron for formation of H_2O molecule (i.e. n=4). The observed current would be attributable to both ORR reaction and n-type semi-conducting property of CeO_x nanowire/C without Pt. It is hard to use this activity for fuel cell reaction. The second case of K-L plot is for analysis of electrochemistry

at potential ranging from 0.92 to 0.95V vs. RHE (i.e. Figure 5-5(b)). This is for characterization of midway between two steps of Tafel lines obtained from data observed for 5wt% Pt and 10wt% Pt loaded CeO_x nanowire/C electro-catalysts. The estimated n values which were determined from the slopes of lines clearly got close to the ideal number of electron (i.e. n=4) for formation of H_2O molecules in fuel cell reaction. It suggests that ORR activity on Pt can be enhanced at higher potential region (i.e. below 0.95V (vs.RHE)) on the Pt-CeO_x nanowire/C. It is expected that ORR activity on Pt will be still improved if the larger amount of Pt-CeO_x nanowire interface can be created on the electro-catalysts. To characterize other three cases which are for analysis of electrode reactions at potential ranging from 0.81 to 0.87V (vs. RHE), 0.71 to 0.77V (vs. RHE) and 0.61 to 0.67V (vs. RHE) in Figure 5-4(b), the number of electrons were examined in Figure 5-5(c), 5-5(d) and 5-5(e), respectively.

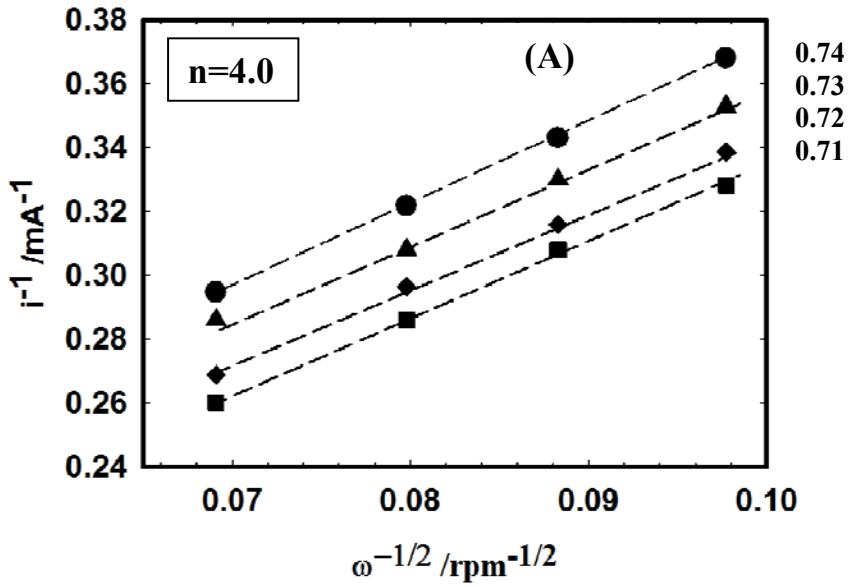

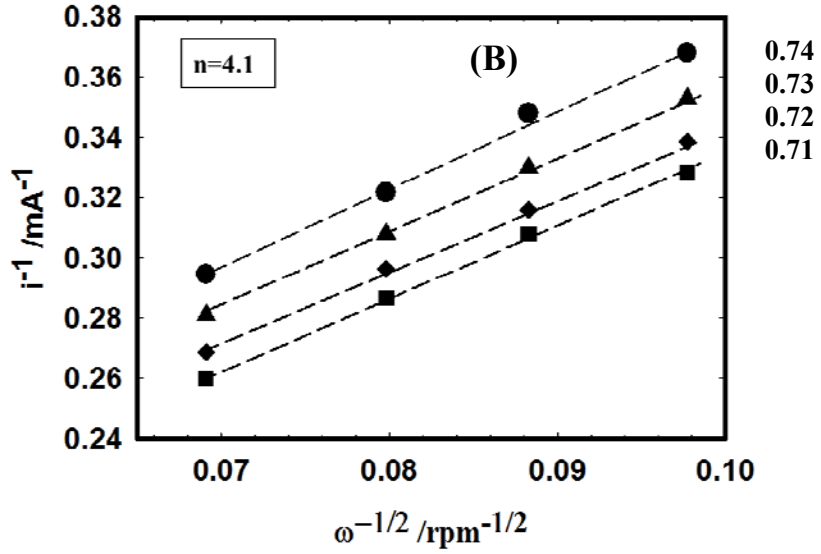

Figure 5-5(f) Kotecky-Levich plots at different potential observed from 50wt% Pt loaded CeO_x nanowire/ C (A) and commercially available Pt /C (Pt content: 20wt %) (B). Observed potential region: 0.71 to 0.74V (vs. RHE).

For comparison of number of electron of ORR observed for 5wt% Pt loaded CeO_x nanowire/C and 10wt% Pt loaded CeO_x nanowire/C with that of 20wt% Pt/C and 50wt% Pt loaded CeO_x nanowire/C, Figure 5-5(f) shows K-L plots obtained from ORR data of aforementioned electro-catalysts. Based on all observed data at potential ranging from 0.61V to 0.87V (vs. RHE) in aforementioned figures, it is concluded that the number of electron in ORR observed for 5wt% Pt loaded CeO_x nanowire/C and 10wt% Pt loaded CeO_x nanowire/C from 0.61 to 0.87V (vs. RHE) is almost equal to ideal number of electron (i.e. n=4) within small deviation due to experimental error.

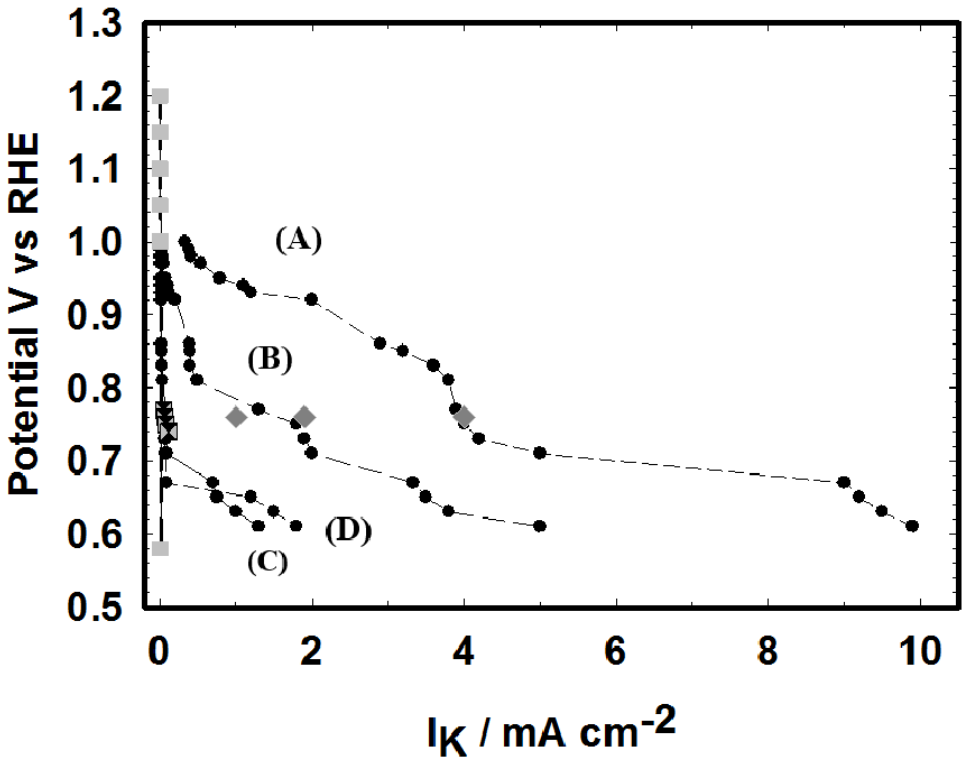

Figure 5-6(a) Kinetic current values obtained from the Koutecky-Levich plots of the 5wt% Pt-CeO_x nanowire/C (A), 50wt% Pt-CeO_x nanowire/C (B), 5wt% Pt-CeO_x nanoparticle/C (C), conventional Pt/C (D), Pt/C-PPy-Pre [15] ■, Pt alloy with Fe,Ni,Co(1:1) [16] ◆, 20wt% Pt-CeO_x nanoparticle/C■.

To characterize I_k values observed at potential ranging from 0.7 to 1.0V (vs. RHE), kinetic current values obtained from the Koutecky-Levich plots of the 5wt% Pt-CeO_x nanowire/C, 50wt% Pt-CeO_x nanowire/C, 5wt% Pt-CeO_x nanoparticle/C, conventional Pt/C and previously reported electrocatalysts were demonstrated in Figure 5-6(a). Also, the magnified Figure 5-6(a) is shown in Figure 5-6(b).

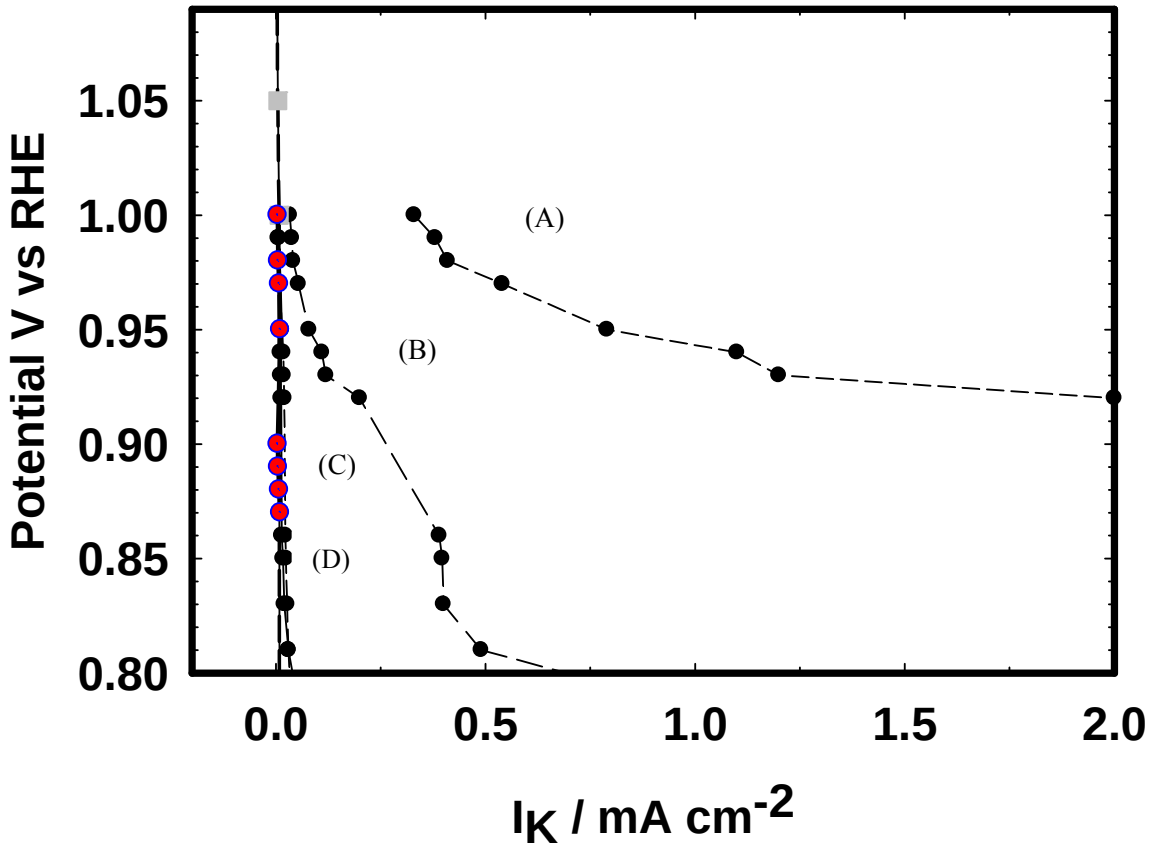

Figure 5-6(b) High shift of kinetic Current values obtained from the Koutecky-Levich plots of the 5wt% Pt-CeO_x nanowire/C (A), 50wt% Pt-CeO_x nanowire/C (B), 5wt% Pt-CeO_x nanoparticle/C (C), conventional Pt/C (D), 20wt% Pt-CeO_x nanoparticle/C ■ and CeO_x nanowire/C ●.

Based on those results, it is concluded that the electrochemistry observed for 5wt% Pt-CeO_x nanowire/C surface in the present thesis work provided us aforementioned new research direction for design of electro-catalyst surface with high quality ORR activity. Namely, it is possible that two kinds of Pt active sites are formed by the different incorporation of Pt into CeO_x lattice. And improvement of ORR and lowering of Pt amount in cathodes would be

possible if aforementioned Pt active sites perfectly covered on the surface of CeO_x nanowire support surface.

In the case of Pt-CeO_x nanoparticle/C cathode, Pt surface oxidation was inhibited by the formation of Pt-CeO_x interface on the samples. To conclude the role of Pt-CeO_x nanowire for improvement of ORR activity on the samples, cyclic voltamogramms in 0.5M H_2SO_4 aqueous solution was examined by using aforementioned three samples (i.e. 5wt%, 10wt% and 50wt% Pt loaded CeO_x nanowire/C) as shown in Figure 5-7. The cyclic voltammogram observed for the surface of conventional Pt/C involved the oxidation and reduction peaks of Pt at 1V (vs. RHE) and 0.7V (vs. RHE), respectively. It is demonstrated in the small window into Fig.5-7.

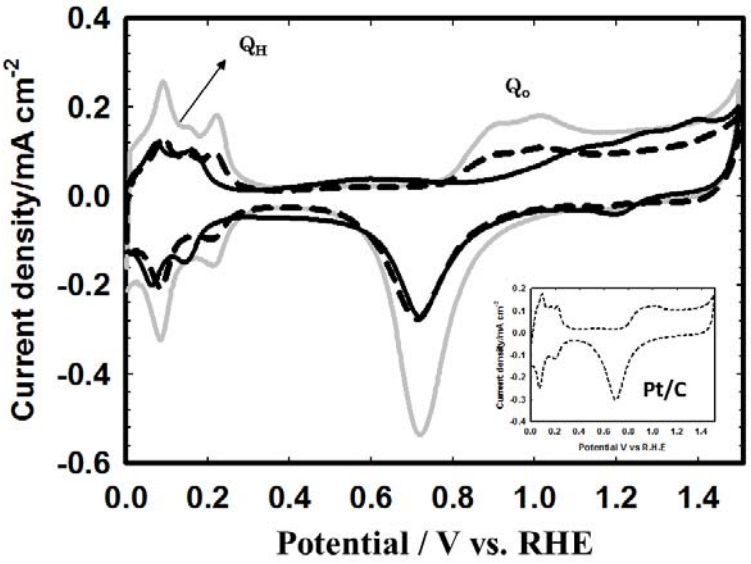

Figure 5-7 Cyclic voltammograms showing Q_O and Q_H area at 300 cycles on GC electrode.

Alternatively, the observed cyclic voltammograms for the 5wt% Pt loaded CeO_x nanowire /C showed only characteristic peaks of desorption peak and adsorption peak of hydrogen on Pt, and the oxidation and reduction of Pt were depressed in the observed cyclic voltammogram. The cyclic voltammogram observed for 10wt% Pt loaded CeO_x nanowire /C was similar to 5wt% Pt loaded CeO_x nanowire/C. The surface oxidation level of Pt can be estimated from the observed

ratio between oxidation charge (Q_O) and hydrogen adsorption charge (Q_H) by assumption of following oxidation reactions on Pt,

$$\mathbf{Pt + H_2O \rightarrow Pt\text{-}OH + H^+ + e^-} \qquad \mathbf{(5\text{-}1)}$$

$$\mathbf{Pt\text{-}OH \rightarrow Pt\text{-}O_{ad} + H^+ + e^-} \qquad \mathbf{(5\text{-}2)}$$

and

$$\mathbf{Pt\text{-}O_{ad} + H_2O \rightarrow PtO_2 + 2H^+ + 2e^-}.^{14} \qquad \mathbf{(5\text{-}3)}$$

The onset potential of OH adsorption on Pt surface is around 0.8V (vs. RHE), and the Pt surface is almost fully covered by aforementioned OH species at around 1.08V (vs. RHE). In this case, the ratio Q_O/Q_H becomes one[13]. Between 1.08 and 1.35V (vs. RHE), the OH species are gradually transformed into Pt-O_{ad} (i.e. adsorbed atomic oxygen) species, the ration Q_O/Q_H becomes 2[13]. At higher potential, stable oxides such as PtO_2 would be formed ($Q_O/Q_H > 2$).[13] To compare the oxidation level of Pt surface in the samples, the Q_O/Q_H observed for the Pt-CeO_x nanowire/C and commercially available Pt/C were shown in Table 5-3. The ratios $Q_O(1)/Q_H$ observed for Pt-CeO_x/CB and Pt/C were 0.3 and 0.7, respectively. Where $Q_O(1)$ is estimated in the potential ranging from 0.8 to 1.08V (vs. RHE) and $Q_O(2)$ is estimated in the potential ranging from 1.08 to 1.35V (vs. RHE). This table indicates that the surface oxidation of Pt in Pt-CeO_x nanowire/C is inhibited as compared with surface oxidation of Pt in the commercially available Pt/C. Also, it is concluded that the surface oxidation of Pt is effectively inhibited in cathodic condition by the formation of interface between Pt and CeO_x nanowire on Pt surface.

Table 5-3 Q_O (1)/Q_H and Q_O(2)/Q_H ratio observed for Pt loaded ceria nanowire at 300cycles on GC electrode.

Pt content (wt%)	$Q_{0(1)}/Q_H$	$Q_{0(2)}/Q_H$
50	**0.7**	**1.6**
10	**0.4**	**0.8**
5	**0.1**	**0.3**
Commercially available Pt/C	1	**2**

The suppression of oxidation of Pt surface was previously reported by using Pt-CeO_x nanoparticles/C cathodes. According to the previously reported case of Pt-CeO_x nano-particles/C, the ORR activity on Pt in Pt-CeO_x nano-particles/C can be improved by aforementioned suppression of oxidation of Pt surface. It is because the main species of Ce^{3+} in Pt-CeO_x interface is oxidized instead of Pt surface. Then the Pt surface can be clean in the cathodic atmosphere. And this idea is experimentally confirmed by using in-situ XAFS analysis[5].

5-3 Conclusion

In this chapter, I showed the defect structural features of Pt-CeO_x nanowire interface of electrochemically pretreated Pt-CeO_x nanowire/C cathode by using EELS data. The EELS analysis clearly tells that the Pt-CeO_x nanowire interface mainly consists of Ce^{4+} species and local ordering of oxygen vacancy of CeO_x lattice in the Pt-CeO_x nanowire interface on Pt.

For the conclusion in the present chapter, the previously reported ORR process is re-introduced in this conclusion as well as chapter 1. In general, ORR process can be explained by using following 4 electron process[14].

$$\mathbf{O_2 + Pt \rightarrow Pt\text{-}O_{2ad}} \quad \textbf{(5-4)}$$

$$\mathbf{Pt\text{-}O_{2ad} + (H^+ + e^-) \rightarrow Pt\text{-}O_2H_{ad} + Pt\text{-}O_{ad}} \quad \textbf{(5-5)}$$

$$\mathbf{Pt\text{-}O_2H_{ad} + (H^+ + e^-) \rightarrow H_2O + Pt\text{-}O_{ad}} \quad \textbf{(5-6)}$$

$$\mathbf{Pt\text{-}O_{ad} + (H^+ + e^-) \rightarrow Pt\text{-}OH_{ad}} \quad \textbf{(5-7)}$$

$$\mathbf{Pt\text{-}OH_{ad} + (H^+ + e^-) \rightarrow H_2O + Pt} \quad \textbf{(5-8)}$$

In the step 2 (i.e. Eq.5-5), the oxide film is formed on Pt, of which electrode reaction is suppressed on Pt/C. Masuda[15] et al. explained that the oxide formation on Pt in Pt-CeO_x nanoparticle/C was suppressed by electrochemical redox reaction between Ce^{3+} and Ce^{4+}. It suggests that Ce^{3+} species is oxidizing to Ce^{4+} species instead of Pt (i.e. Ce^{3+} => Ce^{4+} $+e^-$ reaction) and the ORR activity was enhanced on Pt in Pt loaded CeO_x nanoparticle/C.

In the case of Pt loaded CeO_x nanowire/C, Ce^{4+} species which is analyzed by Ce M-edge spectra of EELS mainly presented in the Pt-CeO_x nanowire interface which would be contribute to enhancement of ORR activity on Pt in Pt-CeO_x nanowire/C. Since small ORR activity on 5wt% Pt-CeO_x nanowire/C surface was observed at higher potential region (i.e. above 0.95V (vs. RHE)), novel promotion effect of CeO_x as compared with previously reported promotion effect of CeO_x in Pt-CeO_x nanoparticle/C can be concluded. So I assumed that two kinds of Pt-CeO_x nanowire interface were formed by different incorporation of Pt into CeO_x lattice. And charge transfer reaction for enhancement of Pt surface activity would be promoted by the electrochemical reduction reaction of interstitial oxygen vacancy site (i.e. O_i') for creation of

lattice site of oxygen (O_o^x) in the Pt-CeO_x nanowire interface as well as the electrochemical formation reaction of Ce^{4+} cation from Ce^{3+} cation in the previously reported Pt-CeO_x nanoparticle interface[3,5]. Then, the surface oxidation reaction on Pt would be inhibited and small ORR activity was observed at higher potential region as compared with previously reported Pt-CeO_x nanoparticle/C electro-catalyst.

In the Chapter 4, the electrochemical reduction reaction such as $\mathbf{1/2O_O^X + e^- => 1/2O^{"}_i}$ which is not only electrochemical reduction reaction of Ce^{4+} cation for formation of Ce^{3+} cation (i.e. $Ce^{4+} + e^- => Ce^{3+}$) was assumed for the conclusion for improvement of activity of methanol electro-oxidation reaction by formation of Pt-CeO_x nanowire interface. In the present Chapter 5, similar oxidation processes (i.e. $\mathbf{1/2\ O^{"}_i => 1/2O_O^X + e^-}$ and $\mathbf{Ce^{3+} => Ce^{4+} + e^-}$) on two kinds of Pt active sites which were formed in the Pt-CeO_x nanowire interface were concluded based on the experimental results.

Below 0.9V (vs.RHE), aforementioned two kinds of Pt active sites which are formed by different incorporation of Pt into CeO_x lattice would contribute to the enhancement of ORR activity on Pt. It is conclude that is why ORR activity observed for 5wt% Pt-CeO_x nanowire/C surface is higher than that on 5wt% Pt-CeO_x nanoparticle/C surface which is shown in Figure 5-4(a).

To develop the design concept of the function of Pt loaded ceria nanowire interface, it is necessary to characterize the bulk interface defect structure which will be discussed in chapter 6 with the help of conclusion in both Chapter 4 and Chapter 5 of the present thesis. The reasonable defect model in the Pt-CeO_x nanowire interface is examined in the next chapter 6 by using defect cluster simulation method.

References

1. J. Zhang, "PEM Fuel Cell Electrocatalysts and Catalyst layer: Fundamentals and Applications", *Springer-Verlag*, **1**, pp.3-4(2008).

2. H. A. Gasteiger, S. S. Kocha, B. Sompalli, and F. T. Wagner, "Activity Benchmarks and Requirements for Pt, Pt-alloy, and Non-Pt Oxygen Reduction Catalysts for PEMFCs", *Appl. Catal. B*, **56**, pp.9-35(2005).

3. K. Fugane, T.Mori, D.R.Ou, A. Suzuki, H.Yoshikawa, T.Masuda, K.Uosaki, Y.Yamashita, S.Ueda, K.Kobayashi, N.Okazaki, I.Matolinova, and V.Matolin, "Activity of Oxygen Reduction Reaction on Small Amount of Amorphous CeO_x Promoted Pt Cathode for Fuel cell Application", *Electrochimica Acta*, **56**, pp.3874-3883(2011).

4. K.Fugane, T.Mori, D.R.Ou, P.F.Yan, F.Ye, H.Yoshikawa, and J.Drennan, "Improvement of Cathode Performance on Pt-CeO_x by Optimization of Electrochemical Pretreatment Condition for PEFC Application", *Langmuir*, **28**, pp.16692-16770(2012).

5. T. Masuda, H. Fukumitsu, K. Fugane, H. Togasaki, D. Matsumura, K. Tamura, Y. Nishihata, H. Yoshikawa, K. Kobayashi, T. Mori, and K. Uosaki, "Role of Cerium Oxide in the Enhancement of Activity for the Oxygen Reduction Reaction at Pt–CeO_x Nanocomposite Electrocatalyst - An in Situ Electrochemical X-ray Absorption Fine Structure Study", *J. Phys. Chem. C* , **116**, pp.10098−10102 (2012).

6. J.A. Fortner, and E.C. Buck, "The Chemistry of the Light Rare-Earth Elements as Determined by Electron Energy Loss Spectroscopy", *Appl. Phys. Lett.*, **6**, pp.3817–3819(1996).

7. L.A.J. Garvie, and P.R. Buseck, "Determination of Ce^{4+}/Ce^{3+} in Electron-beam-damaged CeO_2 by Electron Energy-loss Spectroscopy", *J. Phys. Chem. Solids*, **60**, pp.1943-1947(1999).

8. D.R.Ou, T.Mori, F.Ye, H.Togasaki, M. Miyayama, S. Nakayama, J. Zou, G.J.Auchterlonie, and J.Drennan, "Microstructural Characteristics of SDC Electrolyte Film Supported by Ni–SDC Cermet Anode", *J. Electrochecal Society*, **156**, pp. B825-B830 (2009).

9. F. Jollet, C. Noguera, N. Thromat, M. Gautier, and J.P. Duraud, "Electronic-Structure of Yttrium-Oxide", *Phys. Rev. B.,* **42**, pp.7587–7595(1990).

10. D.R.Ou, T.Mori, F.Ye, J.Zou, G. J.Auchterlonie, and J.Drennan, "Oxygen Vacancy Ordering in Heavily Rare-earth-doped Ceria", *Appl. Phys. Lett.*, **89**, pp.171911-171914(2006).

11. D.R.Ou, T.Mori, F.Ye, J.Zou, G. J.Auchterlonie, and J.Drennan, "Oxygen-vacancy Ordering in Lanthanide-doped Ceria: Dopant-type Dependence and Structure Model", *Phys. Rev. B*, **77**, pp.024108-024116(2008).

12. A.V.Soldatov, T.S.Ivanchenko, S.Della Longa, A.Kotani, Y.Iwamoto, and A.Bianconi, "Crystal-structure Effects in the Ce L3-edge X-ray Absorption Spectrum of CeO_2 Multiple Scattering Resonances and Many-body Final-states", *Phys. Rev. B*, **50**, pp.5074-5080(1994).

13. H. Imai, K. Izumi, M. Matsumoto, Y. Kubo, K. Kato, and Y. Imai, "In situ and Real-time Monitoring of Oxide Growth in a few Monolayers at Surfaces of Platinum Nanoparticles in Aqueous Media", *J. Am. Chem. Soc*, **131**, pp.6293-6300 (2009).

14. J. K. Norskov, J.Rossmeisl, A. Logadottir, L.Lindqvist, J.R. Kitchin, T.Bligaard, and H.Jonsson,"Origin of the Overpotential for Oxygen Reduction at Fuel-cell Cathode", *J.Phys. Chem. B*, **108**, pp.17886- 17892 (2004).

15. S.M.Unni, V.M. Dhavale, V.K. Pillai, and S Kurungot," High Pt Utilization Electrodes for Polymer Electrolyte Membrane Fuel Cells by Dispersing Pt Particles Formed by a Preprecipitation Method on Carbon "Polished" with Polypyrrole", *J.Phys.Chem.C*, **114**, pp. 14654-14661(2010).

16. T.Toda, H. Igarashi, H. Uchida, and M. Watanabe, "Enhancement of the Electro reduction of Oxygen on Pt Alloys with Fe, Ni and Co", *Journal of the Electrochemical Society*, **146**, pp. 3750-3756(1999).

Chapter 6 Defect structural analysis of Pt loaded CeO_x nanowire interface by using atomistic simulation method

6-1 Introduction

The experimental results in previous chapters 4 and 5 showed conspicuous improvement in anode and cathode properties due to the formation of Pt loaded CeO_x nanowire interface with relatively low Pt content in Pt loaded CeO_x nanowire/C electrodes. In the conclusion of those chapters, the electrochemical reduction of lattice oxygen and electrochemical oxidation of interstitial oxygen in the Pt-CeO_x nanowire interface were assumed. In order to develop the conclusion in the present thesis work, the reasonable defect structure model is examined by using atomistic simulation in this chapter 6.

6-2 Results and Discussion

6-2-1 Defect structure simulation in Pt-CeO_x nanowire interface

Since the major cation species in the interface of electrochemically pre-treated samples was Ce^{4+} and Pt^{2+} which were analyzed by EELS and XPS, the simplest defect cluster is assumed based on following Eq.6-1.

$$\mathbf{2PtO + Ce_{ce}^{x} + 4O_O^X + 6V_i^x => 2Pt_i^{\cdot\cdot} + 4O_i'' + 4V_o^{\cdot\cdot} + V_{ce}'''' + CeO_2} \qquad \mathbf{(6\text{-}1)}$$

where Kröger –Vink notation is used for explanation of defect formation reaction in the Pt-CeO_x interface.

According to Eq.6-1, the simplest Frenkel type defect cluster was considered as follows;

Cluster model 1: $2Pt_i^{\cdot\cdot}$-$4O_i''$-$4V_o^{\cdot\cdot}$-V_{ce}''''

To explain this Frenkel type defect cluster model clearly, Figure 6-1(a) and 6-2(b) demonstrates the original fluorite structure and cluster model 1 which is assumed in the Pt-CeO_x interface, respectively.

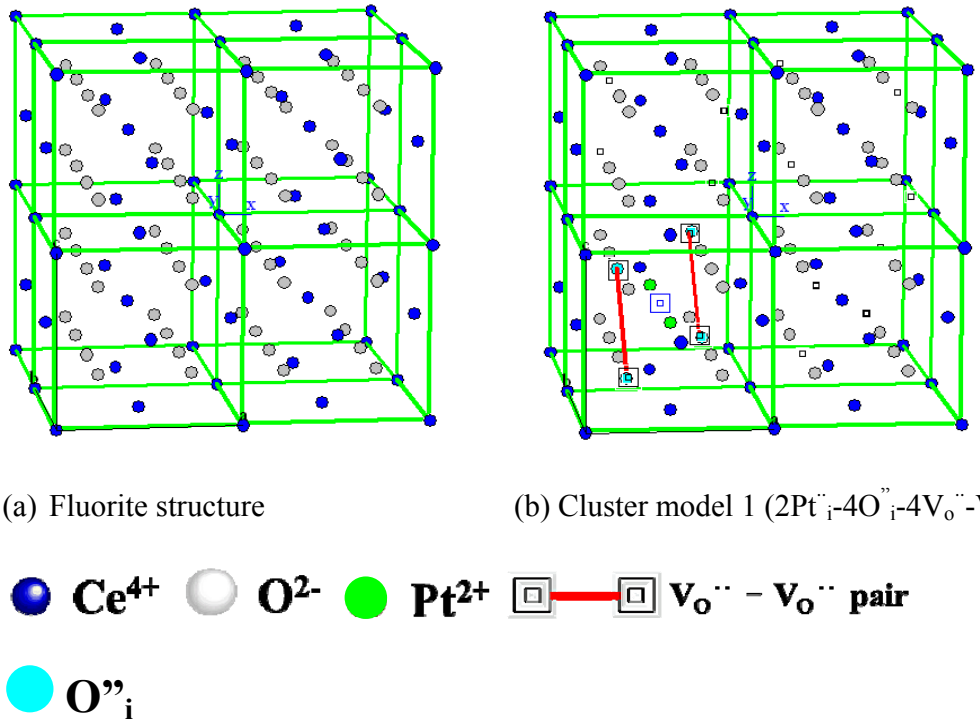

Figure 6-1 Structure model of fluorite lattice (a) and simplest defect structure (cluster model 1) (b).

As I noticed in Chapter 2 (i.e. Experimental), the binding energy (ΔE_b) was calculated in the present thesis work based on Eq. 6-2.

$$\Delta E_b = \sum E_{isolated} - E_{cluster} \qquad (6\text{-}2)$$

where $\sum E_{isolated}$ is the entire defect energy of the cluster in the Pt-CeO_x nanowire interface, ΔE_b is normalized by the total number of defects in the clusters. From Eq.6-2, it can be noticed that a positive binding energy implies a preference of the formation of lattice defect clusters over its individual components. Also, the calculated ΔE_b, $\sum E_{isolated}$ and $E_{cluster}$ are positive values in the calculation of reasonable defect cluster model.

To calculate ΔE_b, isolated defect energies were calculated at first. The calculation results were summarized in Table 6-1.

Table 6-1 Isolated defect energies which were calculated by using GULP code.

Defect species	Isolated defect energy / eV
Cerium vacancy ($V_{ce}^{''''}$)	85.477
Oxygen interstitial (O_i'')	8.999
Oxygen vacancy ($Vo^{\cdot\cdot}$)	15.396
Platinum interstitial ($Pt_i^{\cdot\cdot}$)	-11.176

Table 6-2 Comparison of formation energy of Frenkel pair.

Type of defects	**Present work (eV)**	**Pevious reported data (eV)**[1]
Anion Frenkel-pair $V_o^{\cdot\cdot}+ O_i''$	**3.19(8)**	**3.21**
Cation Frenkel-pair $V_{Ce}''''+ Ce_i^{\cdot\cdot\cdot\cdot}$	**11.13**	**15.94**

To examine the validity of calculation in the present work, anion Frenkel pair and cation Frenkel pair formation energy were compared by using present work data and previously reported data, as shown in Table 6-2.

Formation energy of ($V_o^{\cdot\cdot}+ O_i''$) pair = (15.396+(-8.999))/2 =3.19(8) eV

Formation energy of ($V_{Ce}''''+ Ce_i^{\cdot\cdot\cdot\cdot}$) pair = (85.477+(-63.211))/2=11.13 eV

where the calculared fromation energy of isolated intestial cerium ($Cei^{\cdot\cdot\cdot\cdot}$) was -63.211eV in the present simulation.

Table 6-2 suggests that our calculation data agreed with previously reported data within small misfit in the allowable range. Based on this comparison of calculation results with previously reported data, the formation energy of defect cluster and binding energy were calculated for each defect cluster model.

According to Eq.6-1, the total number of defects in defect cluster model 1 is 11. The local charge on defects is neutral. The output file of present atomistic simulation based on cluster model 1 which is demonstrated in Fig.6-1(b) is listed below.

Table 6-2 Output file list based on cluster model 1.

```
**********************************************
*  Defect calculation for configuration                *
**********************************************
 Total number of defects = 11
 Total charge on defect  =   0.00
 Defect centre is at   0.0000   0.0000   0.0000  Angs
 Region 1 radius =  16.2330      Number of ions =   2742
 Region 2 radius =  32.4660      Number of ions =  18852
Components of defect energy :
--------------------------------------------------------------------------------
 Region 1 - region 1                 = 48.99353 eV
 Region 1 - region 2a (unrelaxed)      = -0.01145 eV
 Region 1 - 2a (relaxed - correction)  = -0.0075 eV
 Region 1 (Total)                    = 48.97457 eV
 Region 2a                          = 0.003758 eV
```

Region 2b = 0.00000000 eV

Total defect energy = 48.97833 eV

Start of defect optimisation :

Cycle: 0 Defect Energy: 82.38483 eV

** Hessian calculated **

Cycle: 1 Defect Energy: 61.67534 eV

** Hessian calculated **

Cycle: 2 Defect Energy: 57.76833 eV

Cycle: 3 Defect Energy: 56.48433 eV

** Hessian calculated **

Cycle: 4 Defect Energy: 49.40939 eV

Cycle: 5 Defect Energy: 49.2161 eV

Cycle: 6 Defect Energy: 49.18113 eV

Cycle: 7 Defect Energy: 49.0089 eV

Cycle: 8 Defect Energy: 48.99057 eV

Cycle: 9 Defect Energy: 48.98529 eV

Cycle: 10 Defect Energy: 48.98611 eV

Cycle: 11 Defect Energy: 48.98587 eV

** Hessian calculated **

Cycle: 12 Defect Energy: 48.9841 eV

Cycle: 13 Defect Energy: 48.98188 eV

Cycle: 14 Defect Energy: 48.98004 eV

Cycle: 15 Defect Energy: 48.97916 eV

Cycle: 16 Defect Energy: 48.97873 eV

Cycle: 17 Defect Energy: 48.97852 eV

Cycle: 18 Defect Energy: 48.97842 eV

Cycle: 19 Defect Energy: 48.97837 eV

Cycle: 20 Defect Energy: 48.97835 eV

Cycle: 21 Defect Energy: 48.97834 eV

** Hessian calculated **

**** Optimisation achieved ****

Final defect energy = 48.97833

Final defect Gnorm = 1.98E-06

Components of defect energy :

Region 1 - region 1 = 48.99353 eV

Region 1 - region 2a (unrelaxed) = -0.01145 eV

Region 1 - 2a (relaxed - correction) = -0.0075 eV

Region 1 (Total) = 48.97457 eV

Region 2a = 0.003758 eV

Region 2b = 0.00000000 eV

Total defect energy = 48.97833 eV

Timing analysis for GULP :

Task / Subroutine Time (Seconds)

Calculation of real space energy and derivatives 0.004

Calculation of real space energy using symmetry 0.008

Calculation for region 1 energy and derivatives (2-b) 5 85.3126

Calculation for region 2a energy 1587.191

Total CPU time 5721.894

As shown in Table 6-1, the number of defect and local charge which were calculated in the present simulation agreed with our model well.

Since the value of $\sum E_{isolated}$ which is calculated by Table 6-1 is 88.6674 (eV), the calculated binding energy (ΔE_b) for cluster model 1 is 3.60 (eV) (i.e. ΔE_b = (88.6674 - 48.978)/11) = 3.60). In the present work, all other configurations of defects based on the defect composition of $\mathbf{2Pt^{\cdot\cdot}_i\text{-}4O^{''}_i\text{-}4V_o^{\cdot\cdot}\text{-}V^{''''}_{ce}}$ in the original fluorite lattice (i.e. Figure 6-2(a)) did not provide us positive values of ΔE_b. It indicates that the defect configuration demonstrated in Figure 6-1(b) is preferable in the fluorite lattice. Figure 6-1(c) demonstrated the crystal structure of C-type rare earth structure which is thermodynamically stable with fluorite structure.

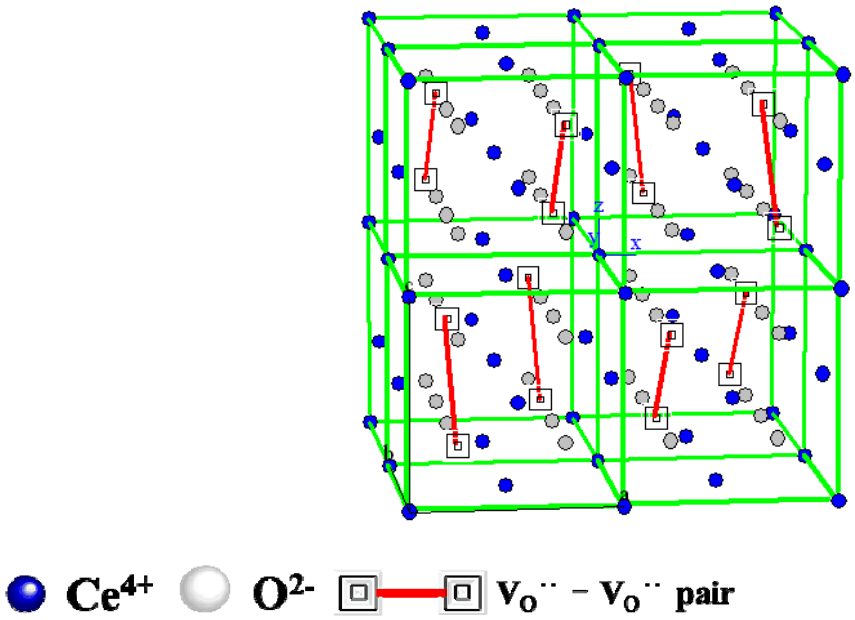

Figure 6-1 (c) Structure model of C-type rare earth structure which can be thermodynamically stable with fluorite lattice (i.e. Figure 6-1(a)).

The oxygen defect configuration in Figure 6-1(b) was similar to that in the part of Figure 6-1(c). Note that the oxygen defect in Figure 6-1(b) was created by the formation of interstitial oxygen site in the fluorite lattice. It means that oxygen defect site is formed by the small shift of lattice oxygen into interstitial site. In the present calculation, aforementioned shift from lattice site was

only 0.05Å. If aforementioned shift was more than 0.1Å, $E_{cluster}$ and ΔE_b values cannot be positive. It indicates that the oxygen interstitial site which is formed by the small shift of oxygen from lattice site is easily formed in the fluorite lattice. Then, the defect cluster (i.e. cluster model 1) can be stabilized in the fluorite lattice.

6-2-2 Development of defect clusters in Pt-CeO_x nanowire interface

Based on the simulation result, it is concluded that cluster model 1 is developing unite for larger cluster in Pt-CeO_x nanowire interface. To conclude the larger cluster, following three defect formation reactions were assumed.

For two combined defect cluster (i.e. cluster model 1 * 2);

$$\mathbf{4PtO + 2Ce_{ce}^{x} + 8O_O^X + 12V_i^x \Rightarrow 4Pt_i^{\cdot\cdot} + 8O_i'' + 8V_o^{\cdot\cdot} + 2V_{ce}'''' + 2CeO_2} \qquad \mathbf{(6\text{-}3)}$$

Expected defect cluster: $\mathbf{4Pt_i^{\cdot\cdot}\text{-}8O_i''\text{-}8V_o^{\cdot\cdot}\text{-}2V_{ce}''''}$ (i.e. cluster model 2)

For three combined defect cluster (cluster model 1*3)

$$\mathbf{6PtO + 3Ce_{ce}^{x} + 12O_O^X + 18V_i^x \Rightarrow 6Pt_i^{\cdot\cdot} + 12O_i'' + 12V_o^{\cdot\cdot} + 3V_{ce}'''' + 3CeO_2} \qquad \mathbf{(6\text{-}4)}$$

Expected defect cluster: $\mathbf{6Pt_i^{\cdot\cdot}\text{-}12O_i''\text{-}12V_o^{\cdot\cdot}\text{-}3V_{ce}''''}$ (i.e. cluster model 3)

For four combined defect cluster (cluster model 1*4)

$$\mathbf{8PtO + 4Ce_{ce}^{x} + 16O_O^X + 24V_i^x \quad 8Pt_i^{\cdot\cdot} + 16O_i'' + 16V_o^{\cdot\cdot} + 4V_{ce}'''' + 4CeO_2} \qquad \mathbf{(6\text{-}5)}$$

Expected defect cluster: $\mathbf{8Pt_i^{\cdot\cdot}\text{-}16O_i''\text{-}12V_o^{\cdot\cdot}\text{-}4V_{ce}''''}$ (i.e. cluster model 4)

To conclude the stable defect clusters in the fluorite lattice, following defect configurations which are based on C-type rare earth structure are assumed. The defect structure models which are assumed in the present work are demonstrated in Figure 6-2(a) to 6-2(c).

(a)

(b)

(c)

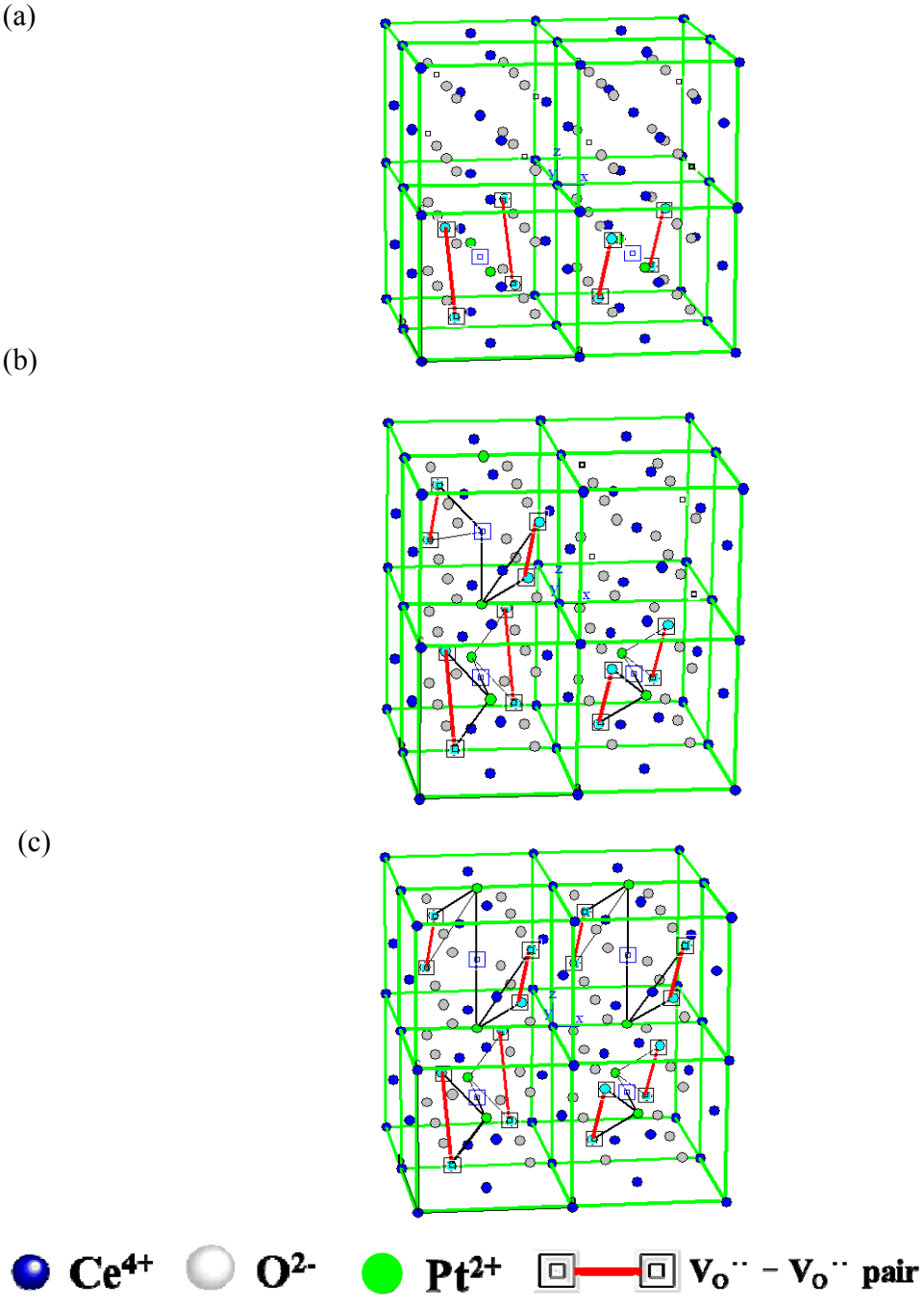

Figure 6-2 Defect structure models of cluster model 2 ($4Pt^{\cdot\cdot}_{i}$-$8O^{''}_{i}$-$8V_{o}^{\cdot\cdot}$-$2V^{''''}_{ce}$) (a), cluster model 3 ($6Pt^{\cdot\cdot}_{i}$-$12O^{''}_{i}$-$12V_{o}^{\cdot\cdot}$-$3V^{''''}_{ce}$) (b) and cluster model 4 ($8Pt^{\cdot\cdot}_{i}$-$16O^{''}_{i}$-$12V_{o}^{\cdot\cdot}$-$4V^{''''}_{ce}$).

Based on the defect configurations in Figure 6-2(a) to 6-2(c), the atomic coordinates for each defect cluster model was fixed in the present atomistic simulation. Then, the cluster formation energies ($\mathbf{E_{cluster}}$) and binding energies ($\mathbf{\Delta E_b}$) were calculated. The output files of defect cluster formation energies ($\mathbf{E_{cluster}}$) for cluster model 2, cluster model 3 and cluster model 4 were listed in Table 6-2(a), 6-2(b) and 6-2(c), respectively.

Table 6-2(a) Output file for cluster formation energy calculation of cluster model 2.

```
**********************************************
*  Defect calculation for configuration     :                    *
**********************************************
 Total number of defects = 22
 Total charge on defect  =   0.00
 Defect centre is at   0.0000   0.0000   0.0000  Angs
 Region 1 radius =  16.2330      Number of ions =   2742
 Region 2 radius =  32.4660      Number of ions =  18852
Components of defect energy :
--------------------------------------------------------------------------------
 Region 1 - region 1                = 165.9317  eV
 Region 1 - region 2a (unrelaxed)      = 1.851933 eV
 Region 1 - 2a (relaxed - correction)  = -3.02342 eV
 Region 1 (Total)                   = 164.7602  eV
 Region 2a                         = 1.512476 eV
 Region 2b                          =      0.00000000 eV
```

Total defect energy = 166.2727 eV

Start of defect optimization:

Cycle: 0 Defect Energy: 166.2727

** Hessian calculated **

Cycle: 1 Defect Energy: 132.91

** Hessian calculated **

Cycle: 2 Defect Energy: 130.003

** Hessian calculated **

Cycle: 3 Defect Energy: 118.0723

** Hessian calculated **

Cycle: 4 Defect Energy: 106.1646

** Hessian calculated **

Cycle: 5 Defect Energy: 104.1346

Cycle: 6 Defect Energy: 103.2673

Cycle: 7 Defect Energy: 102.1834

Cycle: 8 Defect Energy: 100.9519

Cycle: 9 Defect Energy: 99.90116

Cycle: 10 Defect Energy: 98.87778

Cycle: 11 Defect Energy: 97.75441

Cycle: 12 Defect Energy: 96.35936

Cycle: 13 Defect Energy: 95.20838

Cycle: 14 Defect Energy: 94.45977

** Hessian calculated **

Cycle: 15 Defect Energy: 92.01752

Cycle: 16 Defect Energy: 91.94626

Cycle: 17 Defect Energy: 91.92371

Cycle: 18 Defect Energy: 91.91326

Cycle: 19 Defect Energy: 91.90798

Cycle: 20 Defect Energy: 91.90554

Cycle: 21 Defect Energy: 91.90409

Cycle: 22 Defect Energy: 91.90346

Cycle: 23 Defect Energy: 91.90308

Cycle: 24 Defect Energy: 91.90288

** Hessian calculated **

Cycle: 25 Defect Energy: 91.90278

Cycle: 26 Defect Energy: 91.90272

Cycle: 27 Defect Energy: 91.90268

Cycle: 28 Defect Energy: 91.90266

Cycle: 29 Defect Energy: 91.90264

Cycle: 30 Defect Energy: 91.90263

**** Optimisation achieved ****

Final defect energy = 91.90262

Final defect Gnorm = 9.6E-07

Components of defect energy :

Region 1 - region 1 = 91.95221 eV

Region 1 - region 2a (unrelaxed) = 0.095373 eV

Region 1 - 2a (relaxed - correction) = -0.27307 eV

Region 1 (Total) = 91.77452 eV

Region 2a = 0.128105 eV

Region 2b = 0.00000000 eV

Total defect energy = 91.90262 eV

Timing analysis for GULP:

Task / Subroutine	Time (Seconds)
Calculation of real space energy and derivatives	0.004
Calculation of real space energy using symmetry	0.008
Calculation for region 1 energy and derivatives (2-b)	1094.096
Calculation for region 2a energy	3076.104

Total CPU time 9499.526

The calculation result was optimized through the calculation process of 30 cycles. It means that minimum potential energy for formation of defect cluster was fixed by 30 cycle optimization. Based on Eq.6-3, the expected number of defects is 22. The local charge between cations and anions is balanced. Those expected data agreed with the calculation results of output file in Table 6-2(a). Since the value of $\sum E_{isolated}$ for cluster model 2 which is calculated by Table 6-1 is 177.3348 (eV), the calculated binding energy (ΔE_b) for cluster model 2 is 3.88 (eV) (i.e. ΔE_b = (177.3348 – 91.9026)/22) = 3.88).

Table 6-2(b) Output file for cluster formation energy calculation of cluster model 3

****

* Defect calculation for configuration: *

****

Total number of defects = 33

Total charge on defect = 0.00

Defect centre is at 0.0000 0.0000 0.0000 Angs

Region 1 radius = 16.2330 Number of ions = 2742

Region 2 radius = 32.4660 Number of ions = 18852

Components of defect energy :

Region 1 - region 1 = 235.9731 eV

Region 1 - region 2a (unrelaxed) = 4.843747 eV

Region 1 - 2a (relaxed - correction) = -5.80615 eV

Region 1 (Total) = 235.0106 eV

Region 2a = 2.924795 eV

Region 2b = 0.00000000 eV

Total defect energy = 237.9354 eV

Start of defect optimisation :

Cycle: 0 Defect Energy: 237.9354

** Hessian calculated **

Cycle: 1 Defect Energy: 203.7717

** Hessian calculated **

Cycle: 2 Defect Energy: 195.0646

Cycle: 3 Defect Energy: 192.0533

Cycle: 4 Defect Energy: 188.6614

Cycle: 5 Defect Energy: 184.0139

** Hessian calculated **

Cycle: 6 Defect Energy: 170.381

** Hessian calculated **

Cycle: 7 Defect Energy: 166.6481

Cycle: 8 Defect Energy: 163.9677

** Hessian calculated **

Cycle: 9 Defect Energy: 160.2345

** Hessian calculated **

Cycle: 10 Defect Energy: 156.386

Cycle: 11 Defect Energy: 154.2094

Cycle: 12 Defect Energy: 152.5178

Cycle: 13 Defect Energy: 152.3844

** Hessian calculated **

Cycle: 14 Defect Energy: 151.1306

Cycle: 15 Defect Energy: 150.0805

Cycle: 16 Defect Energy: 149.0031

Cycle: 17 Defect Energy: 148.4241

Cycle: 18 Defect Energy: 148.086

Cycle: 19 Defect Energy: 147.2909

Cycle: 20 Defect Energy: 146.2873

Cycle: 21 Defect Energy: 145.0773

Cycle: 22 Defect Energy: 143.8804

Cycle: 23 Defect Energy: 142.5358

** Hessian calculated **

Cycle: 24 Defect Energy: 141.9601

Cycle: 25 Defect Energy: 141.2802

Cycle: 26 Defect Energy: 140.5694

Cycle: 27 Defect Energy: 139.4693

Cycle: 28 Defect Energy: 138.7067

Cycle: 29 Defect Energy: 138.1929

Cycle: 30 Defect Energy: 137.8398

Cycle: 31 Defect Energy: 137.5277

Cycle: 32 Defect Energy: 137.2337

Cycle: 33 Defect Energy: 137.0523

** Hessian calculated **

Cycle: 34 Defect Energy: 136.939

Cycle: 35 Defect Energy: 136.7898

Cycle: 36 Defect Energy: 136.6109

Cycle: 37 Defect Energy: 136.493

Cycle: 38 Defect Energy: 136.4363

Cycle: 39 Defect Energy: 136.4094

Cycle: 40 Defect Energy: 136.3968

Cycle: 41 Defect Energy: 136.3912

**** Optimization achieved ****

Cycle: 42 Defect Energy: 136.3887

Cycle: 43 Defect Energy: 136.3879

** Hessian calculated **

Cycle: 44 Defect Energy: 136.3877

Cycle: 45 Defect Energy: 136.3878

Cycle: 46 Defect Energy: 136.3879

Cycle: 47 Defect Energy: 136.3881

Cycle: 48 Defect Energy: 136.3882

Cycle: 49 Defect Energy: 136.3883

Cycle: 50 Defect Energy: 136.3883

Cycle: 51 Defect Energy: 136.3884

Cycle: 52 Defect Energy: 136.3884

Cycle: 53 Defect Energy: 136.3884

** Hessian calculated **

Cycle: 54 Defect Energy: 136.3885

Cycle: 55 Defect Energy: 136.3885

Final defect energy = 136.3885

Final defect Gnorm = 2.7E-07

Components of defect energy :

Region 1 - region 1 = 136.3144 eV

Region 1 - region 2a (unrelaxed) = 0.457754 eV

Region 1 - 2a (relaxed - correction) = -0.72431 eV

Region 1 (Total) = 136.0478 eV

Region 2a = 0.340657 eV

Region 2b = 0.00000000 eV

Total defect energy = 136.3885 eV

Timing analysis for GULP :

Task / Subroutine Time (Seconds)

Calculation of real space energy and derivatives 0.004

Calculation of real space energy using symmetry 0.008

Calculation for region 1 energy and derivatives (2-b) 2028.559

Calculation for region 2a energy 5812.315

Total CPU time 15658.42

The calculation result was optimized through the calculation process of 55 cycles. Based on Eq.6-4, the expected number of defects is 33. The local charge between cations and anions is balanced. Those expected data agreed with the calculation results of output file in Table 6-2(b). Since the value of $\sum E_{isolated}$ for cluster model 3 which is calculated by Table 6-1 is 200.0022 (eV), the calculated binding energy (ΔE_b) for cluster model 3 is 3.92(7) (eV) (i.e. ΔE_b = (200.0022 – 136.3885)/33) = 3.92(7)).

Table 6-2(c) Output file for cluster formation energy calculation of cluster model 3.

****

* Defect calculation for configuration *

****

Total number of defects = 44

Total charge on defect = 0.00

Defect centre is at 0.0000 0.0000 0.0000 Angs

Region 1 radius = 16.2330 Number of ions = 2742

Region 2 radius = 32.4660 Number of ions = 18852

Start of defect optimization:

Cycle: 0 Defect Energy: 242.2537

** Hessian calculated **

Cycle: 1 Defect Energy: 227.756

** Hessian calculated **

Cycle: 2 Defect Energy: 226.4557

Cycle: 3 Defect Energy: 225.0487

Cycle: 4 Defect Energy: 224.5106

Cycle: 5 Defect Energy: 224.1742

Cycle: 6 Defect Energy: 224.1499

Cycle: 7 Defect Energy: 223.977

Cycle: 8 Defect Energy: 223.3583

Cycle: 9 Defect Energy: 223.2963

Cycle: 10 Defect Energy: 223.0616

Cycle: 11 Defect Energy: 222.6344

** Hessian calculated **

Cycle: 12 Defect Energy: 221.3551

Cycle: 13 Defect Energy: 220.2162

Cycle: 14 Defect Energy: 220.2046

Cycle: 15 Defect Energy: 219.8634

Cycle: 16 Defect Energy: 219.7979

** Hessian calculated **

Cycle: 17 Defect Energy: 193.0628

** Hessian calculated **

Cycle: 18 Defect Energy: 186.7282

Cycle: 19 Defect Energy: 177.1841

Cycle: 20 Defect Energy: 164.3456

** Hessian calculated **

Cycle: 21 Defect Energy: 161.6348

Cycle: 22 Defect Energy: 146.4689

** Hessian calculated **

Cycle: 23 Defect Energy: 146.4619

Cycle: 24 Defect Energy: 146.4566

Cycle: 25 Defect Energy: 146.4441

Cycle: 26 Defect Energy: 146.4308

Cycle: 27 Defect Energy: 146.417

Cycle: 28 Defect Energy: 146.4065

Cycle: 29 Defect Energy: 146.399

Cycle: 30 Defect Energy: 146.3937

Cycle: 31 Defect Energy: 146.3898

Cycle: 32 Defect Energy: 146.3867

** Hessian calculated **

Cycle: 33 Defect Energy: 128.117

** Hessian calculated **

Cycle: 34 Defect Energy: 110.7697

** Hessian calculated **

Cycle: 35 Defect Energy: 109.6028

Cycle: 36 Defect Energy: 108.9723

Cycle: 37 Defect Energy: 108.82

Cycle: 38 Defect Energy: 108.8196

Cycle: 39 Defect Energy: 108.818

Cycle: 40 Defect Energy: 108.8023

Cycle: 41 Defect Energy: 108.7968

Cycle: 42 Defect Energy: 108.7966

Cycle: 43 Defect Energy: 108.7593

Cycle: 44 Defect Energy: 108.7554

** Hessian calculated **

Cycle: 45 Defect Energy: 100.599

Cycle: 46 Defect Energy: 99.99102

Cycle: 47 Defect Energy: 99.94042

Cycle: 48 Defect Energy: 99.94009

** Hessian calculated **

Cycle: 49 Defect Energy: 90.78726

Cycle: 50 Defect Energy: 90.6919

Cycle: 51 Defect Energy: 90.54444

Cycle: 52 Defect Energy: 90.53824

Cycle: 53 Defect Energy: 90.53798

Cycle: 54 Defect Energy: 90.53468

Cycle: 55 Defect Energy: 90.52207

Cycle: 56 Defect Energy: 90.51867

Cycle: 57 Defect Energy: 90.47665

Cycle: 58 Defect Energy: 90.47192

** Hessian calculated **

Cycle: 59 Defect Energy: 90.46798

Cycle: 60 Defect Energy: 90.23369

Cycle: 61 Defect Energy: 90.07832

Cycle: 62 Defect Energy: 90.0615

Cycle: 63 Defect Energy: 90.05712

Cycle: 64 Defect Energy: 90.05519

Cycle: 65 Defect Energy: 90.04312

Cycle: 66 Defect Energy: 90.04078

Cycle: 67 Defect Energy: 89.9994

Cycle: 68 Defect Energy: 89.99468

** Hessian calculated **

Cycle: 69 Defect Energy: 89.98445

Cycle: 70 Defect Energy: 89.7391

Cycle: 71 Defect Energy: 89.58592

Cycle: 72 Defect Energy: 89.56723

Cycle: 73 Defect Energy: 89.56076

Cycle: 74 Defect Energy: 89.55941

Cycle: 75 Defect Energy: 89.54643

Cycle: 76 Defect Energy: 89.54406

Cycle: 77 Defect Energy: 89.50221

Cycle: 78 Defect Energy: 89.4976

** Hessian calculated **

Cycle: 79 Defect Energy: 89.48471

Cycle: 80 Defect Energy: 89.24499

Cycle: 81 Defect Energy: 89.09499

Cycle: 82 Defect Energy: 89.07482

Cycle: 83 Defect Energy: 89.0659

Cycle: 84 Defect Energy: 89.06507

Cycle: 85 Defect Energy: 89.051

Cycle: 86 Defect Energy: 89.04853

Cycle: 87 Defect Energy: 89.00615

Cycle: 88 Defect Energy: 89.00158

** Hessian calculated **

Cycle: 89 Defect Energy: 88.98622

Cycle: 90 Defect Energy: 88.75187

Cycle: 91 Defect Energy: 88.60584

Cycle: 92 Defect Energy: 88.58468

Cycle: 93 Defect Energy: 88.57298

Cycle: 94 Defect Energy: 88.57259

Cycle: 95 Defect Energy: 88.55722

Cycle: 96 Defect Energy: 88.55459

Cycle: 97 Defect Energy: 88.51155

Cycle: 98 Defect Energy: 88.50696

** Hessian calculated **

Cycle: 99 Defect Energy: 88.48931

Cycle: 100 Defect Energy: 88.26

Cycle: 101 Defect Energy: 88.11863

Cycle: 102 Defect Energy: 88.09707

Cycle: 103 Defect Energy: 88.08242

Cycle: 104 Defect Energy: 88.08232

Cycle: 105 Defect Energy: 88.06542

Cycle: 106 Defect Energy: 88.06252

Cycle: 107 Defect Energy: 88.01869

Cycle: 108 Defect Energy: 88.014

** Hessian calculated **

Cycle: 109 Defect Energy: 87.99424

Cycle: 110 Defect Energy: 87.76963

Cycle: 111 Defect Energy: 87.63341

Cycle: 112 Defect Energy: 87.61215

Cycle: 113 Defect Energy: 87.59459

Cycle: 114 Defect Energy: 87.59459

Cycle: 115 Defect Energy: 87.57587

Cycle: 116 Defect Energy: 87.57261

Cycle: 117 Defect Energy: 87.52774

Cycle: 118 Defect Energy: 87.52287

** Hessian calculated **

Cycle: 119 Defect Energy: 87.50124

Cycle: 120 Defect Energy: 87.28105

Cycle: 121 Defect Energy: 87.15046

Cycle: 122 Defect Energy: 87.13025

Cycle: 123 Defect Energy: 87.11013

Cycle: 124 Defect Energy: 87.10998

Cycle: 125 Defect Energy: 87.08912

Cycle: 126 Defect Energy: 87.08535

Cycle: 127 Defect Energy: 87.03912

Cycle: 128 Defect Energy: 87.03396

** Hessian calculated **

Cycle: 129 Defect Energy: 87.01073

Cycle: 130 Defect Energy: 86.79471

Cycle: 131 Defect Energy: 86.66994

Cycle: 132 Defect Energy: 86.65148

Cycle: 133 Defect Energy: 86.62951

Cycle: 134 Defect Energy: 86.62902

Cycle: 135 Defect Energy: 86.6057

Cycle: 136 Defect Energy: 86.60121

Cycle: 137 Defect Energy: 86.5532

Cycle: 138 Defect Energy: 86.5476

** Hessian calculated **

Cycle: 139 Defect Energy: 86.52303

Cycle: 140 Defect Energy: 86.31093

Cycle: 141 Defect Energy: 86.19215

Cycle: 142 Defect Energy: 86.17602

Cycle: 143 Defect Energy: 86.1533

Cycle: 144 Defect Energy: 86.1524

Cycle: 145 Defect Energy: 86.12639

Cycle: 146 Defect Energy: 86.12092

Cycle: 147 Defect Energy: 86.07058

Cycle: 148 Defect Energy: 86.06434

** Hessian calculated **

Cycle: 149 Defect Energy: 86.03877

Cycle: 150 Defect Energy: 85.83045

Cycle: 151 Defect Energy: 85.71756

Cycle: 152 Defect Energy: 85.70417

Cycle: 153 Defect Energy: 85.6821

Cycle: 154 Defect Energy: 85.68091

Cycle: 155 Defect Energy: 85.65228

Cycle: 156 Defect Energy: 85.64554

Cycle: 157 Defect Energy: 85.59233

Cycle: 158 Defect Energy: 85.58516

** Hessian calculated **

Cycle: 159 Defect Energy: 85.55894

Cycle: 160 Defect Energy: 85.35431

Cycle: 161 Defect Energy: 85.24721

Cycle: 162 Defect Energy: 85.23667

Cycle: 163 Defect Energy: 85.21676

Cycle: 164 Defect Energy: 85.21567

Cycle: 165 Defect Energy: 85.18506

Cycle: 166 Defect Energy: 85.17679

Cycle: 167 Defect Energy: 85.11964

Cycle: 168 Defect Energy: 85.11111

** Hessian calculated **

Cycle: 169 Defect Energy: 85.08464

Cycle: 170 Defect Energy: 84.88362

Cycle: 171 Defect Energy: 84.78203

Cycle: 172 Defect Energy: 84.77427

Cycle: 173 Defect Energy: 84.75783

Cycle: 174 Defect Energy: 84.75726

Cycle: 175 Defect Energy: 84.72634

Cycle: 176 Defect Energy: 84.71649

Cycle: 177 Defect Energy: 84.65439

Cycle: 178 Defect Energy: 84.64384

** Hessian calculated **

Cycle: 179 Defect Energy: 84.61765

Cycle: 180 Defect Energy: 84.4203

Cycle: 181 Defect Energy: 84.32387

Cycle: 182 Defect Energy: 84.31856

Cycle: 183 Defect Energy: 84.30633

Cycle: 184 Defect Energy: 84.3063

Cycle: 185 Defect Energy: 84.27805

Cycle: 186 Defect Energy: 84.26729

Cycle: 187 Defect Energy: 84.19958

Cycle: 188 Defect Energy: 84.18603

** Hessian calculated **

Cycle: 189 Defect Energy: 84.16021

Cycle: 190 Defect Energy: 83.96788

Cycle: 191 Defect Energy: 83.87619

Cycle: 192 Defect Energy: 83.87287

Cycle: 193 Defect Energy: 83.86482

Cycle: 194 Defect Energy: 83.86429

Cycle: 195 Defect Energy: 83.84258

Cycle: 196 Defect Energy: 83.83301

Cycle: 197 Defect Energy: 83.76047

Cycle: 198 Defect Energy: 83.74258

** Hessian calculated **

Cycle: 199 Defect Energy: 83.71835

Cycle: 200 Defect Energy: 83.52996

Cycle: 201 Defect Energy: 83.44249

Cycle: 202 Defect Energy: 83.44063

Cycle: 203 Defect Energy: 83.43608

Cycle: 204 Defect Energy: 83.43277

Cycle: 205 Defect Energy: 83.42041

Cycle: 206 Defect Energy: 83.41506

Cycle: 207 Defect Energy: 83.34261

Cycle: 208 Defect Energy: 83.31937

** Hessian calculated **

Cycle: 209 Defect Energy: 83.29739

Cycle: 210 Defect Energy: 83.1131

Cycle: 211 Defect Energy: 83.02916

Cycle: 212 Defect Energy: 83.02825

Cycle: 213 Defect Energy: 83.0261

Cycle: 214 Defect Energy: 83.01735

Cycle: 215 Defect Energy: 83.01335

Cycle: 216 Defect Energy: 83.01275

Cycle: 217 Defect Energy: 82.95207

Cycle: 218 Defect Energy: 82.926

** Hessian calculated **

Cycle: 219 Defect Energy: 82.90599

Cycle: 220 Defect Energy: 82.72491

Cycle: 221 Defect Energy: 82.64362

Cycle: 222 Defect Energy: 82.64324

Cycle: 223 Defect Energy: 82.64239

Cycle: 224 Defect Energy: 82.62679

Cycle: 225 Defect Energy: 82.62655

Cycle: 226 Defect Energy: 82.62509

Cycle: 227 Defect Energy: 82.58807

Cycle: 228 Defect Energy: 82.56884

** Hessian calculated **

Cycle: 229 Defect Energy: 82.54759

Cycle: 230 Defect Energy: 82.36551

Cycle: 231 Defect Energy: 82.28558

Cycle: 232 Defect Energy: 82.2854

Cycle: 233 Defect Energy: 82.28506

Cycle: 234 Defect Energy: 82.264

Cycle: 235 Defect Energy: 82.26372

Cycle: 236 Defect Energy: 82.25616

Cycle: 237 Defect Energy: 82.23837

Cycle: 238 Defect Energy: 82.23101

** Hessian calculated **

Cycle: 239 Defect Energy: 82.203

Cycle: 240 Defect Energy: 82.01376

Cycle: 241 Defect Energy: 81.93412

Cycle: 242 Defect Energy: 81.93401

Cycle: 243 Defect Energy: 81.93381

Cycle: 244 Defect Energy: 81.91016

Cycle: 245 Defect Energy: 81.90914

Cycle: 246 Defect Energy: 81.89692

Cycle: 247 Defect Energy: 81.88696

Cycle: 248 Defect Energy: 81.88487

** Hessian calculated **

Cycle: 249 Defect Energy: 81.8501

Cycle: 250 Defect Energy: 81.65398

Cycle: 251 Defect Energy: 81.57416

Cycle: 252 Defect Energy: 81.57407

Cycle: 253 Defect Energy: 81.57392

Cycle: 254 Defect Energy: 81.54911

Cycle: 255 Defect Energy: 81.54762

Cycle: 256 Defect Energy: 81.53289

Cycle: 257 Defect Energy: 81.52595

Cycle: 258 Defect Energy: 81.52538

** Hessian calculated **

Cycle: 259 Defect Energy: 81.48653

Cycle: 260 Defect Energy: 81.28632

Cycle: 261 Defect Energy: 81.20616

Cycle: 262 Defect Energy: 81.20608

Cycle: 263 Defect Energy: 81.20595

Cycle: 264 Defect Energy: 81.18054

Cycle: 265 Defect Energy: 81.17875

Cycle: 266 Defect Energy: 81.16262

Cycle: 267 Defect Energy: 81.1571

Cycle: 268 Defect Energy: 81.15696

** Hessian calculated **

Cycle: 269 Defect Energy: 81.11607

Cycle: 270 Defect Energy: 80.91224

Cycle: 271 Defect Energy: 80.83164

Cycle: 272 Defect Energy: 80.83157

Cycle: 273 Defect Energy: 80.83145

Cycle: 274 Defect Energy: 80.80565

Cycle: 275 Defect Energy: 80.80367

Cycle: 276 Defect Energy: 80.78667

Cycle: 277 Defect Energy: 80.78195

Cycle: 278 Defect Energy: 80.78194

** Hessian calculated **

Cycle: 279 Defect Energy: 80.74003

Cycle: 280 Defect Energy: 80.53282

Cycle: 281 Defect Energy: 80.45176

Cycle: 282 Defect Energy: 80.45169

Cycle: 283 Defect Energy: 80.45157

Cycle: 284 Defect Energy: 80.42552

Cycle: 285 Defect Energy: 80.42339

Cycle: 286 Defect Energy: 80.40579

Cycle: 287 Defect Energy: 80.4016

Cycle: 288 Defect Energy: 80.40159

** Hessian calculated **

Cycle: 289 Defect Energy: 80.35917

Cycle: 290 Defect Energy: 80.14874

Cycle: 291 Defect Energy: 80.06717

Cycle: 292 Defect Energy: 80.06712

Cycle: 293 Defect Energy: 80.06699

Cycle: 294 Defect Energy: 80.04076

Cycle: 295 Defect Energy: 80.03853

Cycle: 296 Defect Energy: 80.02051

Cycle: 297 Defect Energy: 80.01668

Cycle: 298 Defect Energy: 80.01665

** Hessian calculated **

Cycle: 299 Defect Energy: 79.97399

Cycle: 300 Defect Energy: 79.76043

Cycle: 301 Defect Energy: 79.67836

Cycle: 302 Defect Energy: 79.67831

Cycle: 303 Defect Energy: 79.67819

Cycle: 304 Defect Energy: 79.65181

Cycle: 305 Defect Energy: 79.6495

Cycle: 306 Defect Energy: 79.63112

Cycle: 307 Defect Energy: 79.62757

Cycle: 308 Defect Energy: 79.62749

** Hessian calculated **

Cycle: 309 Defect Energy: 79.58476

Cycle: 310 Defect Energy: 79.36817

Cycle: 311 Defect Energy: 79.28558

Cycle: 312 Defect Energy: 79.28553

Cycle: 313 Defect Energy: 79.2854

Cycle: 314 Defect Energy: 79.2589

Cycle: 315 Defect Energy: 79.25653

Cycle: 316 Defect Energy: 79.23788

Cycle: 317 Defect Energy: 79.23455

Cycle: 318 Defect Energy: 79.23441

** Hessian calculated **

Cycle: 319 Defect Energy: 79.19163

Cycle: 320 Defect Energy: 78.97207

Cycle: 321 Defect Energy: 78.88897

Cycle: 322 Defect Energy: 78.88892

Cycle: 323 Defect Energy: 78.88879

Cycle: 324 Defect Energy: 78.86224

Cycle: 325 Defect Energy: 78.85981

Cycle: 326 Defect Energy: 78.84093

Cycle: 327 Defect Energy: 78.83776

Cycle: 328 Defect Energy: 78.83757

** Hessian calculated **

Cycle: 329 Defect Energy: 78.79479

Cycle: 330 Defect Energy: 78.57232

Cycle: 331 Defect Energy: 78.48868

Cycle: 332 Defect Energy: 78.48863

Cycle: 333 Defect Energy: 78.4885

Cycle: 334 Defect Energy: 78.46183

Cycle: 335 Defect Energy: 78.45937

Cycle: 336 Defect Energy: 78.44027

Cycle: 337 Defect Energy: 78.43726

Cycle: 338 Defect Energy: 78.43701

** Hessian calculated **

Cycle: 339 Defect Energy: 78.3942

Cycle: 340 Defect Energy: 78.16887

Cycle: 341 Defect Energy: 78.0847

Cycle: 342 Defect Energy: 78.08466

Cycle: 343 Defect Energy: 78.08452

Cycle: 344 Defect Energy: 78.05778

Cycle: 345 Defect Energy: 78.05529

Cycle: 346 Defect Energy: 78.03602

Cycle: 347 Defect Energy: 78.03312

Cycle: 348 Defect Energy: 78.03282

** Hessian calculated **

Cycle: 349 Defect Energy: 77.98995

Cycle: 350 Defect Energy: 77.76181

Cycle: 351 Defect Energy: 77.6771

Cycle: 352 Defect Energy: 77.67706

Cycle: 353 Defect Energy: 77.67691

Cycle: 354 Defect Energy: 77.65008

Cycle: 355 Defect Energy: 77.64743

Cycle: 356 Defect Energy: 77.62796

Cycle: 357 Defect Energy: 77.62517

Cycle: 358 Defect Energy: 77.6248

** Hessian calculated **

Cycle: 359 Defect Energy: 77.58183

Cycle: 360 Defect Energy: 77.35095

Cycle: 361 Defect Energy: 77.26569

Cycle: 362 Defect Energy: 77.26566

Cycle: 363 Defect Energy: 77.2655

Cycle: 364 Defect Energy: 77.23867

Cycle: 365 Defect Energy: 77.23613

Cycle: 366 Defect Energy: 77.21651

Cycle: 367 Defect Energy: 77.2138

Cycle: 368 Defect Energy: 77.21337

** Hessian calculated **

Cycle: 369 Defect Energy: 77.17026

Cycle: 370 Defect Energy: 76.9366

Cycle: 371 Defect Energy: 76.8508

Cycle: 372 Defect Energy: 76.85076

Cycle: 373 Defect Energy: 76.85059

Cycle: 374 Defect Energy: 76.82361

Cycle: 375 Defect Energy: 76.82105

Cycle: 376 Defect Energy: 76.80124

Cycle: 377 Defect Energy: 76.79863

Cycle: 378 Defect Energy: 76.79813

** Hessian calculated **

Cycle: 379 Defect Energy: 76.75475

Cycle: 380 Defect Energy: 76.51857

Cycle: 381 Defect Energy: 76.43222

Cycle: 382 Defect Energy: 76.43219

Cycle: 383 Defect Energy: 76.43201

Cycle: 384 Defect Energy: 76.405

Cycle: 385 Defect Energy: 76.40243

Cycle: 386 Defect Energy: 76.38244

Cycle: 387 Defect Energy: 76.37991

Cycle: 388 Defect Energy: 76.37934

** Hessian calculated **

Cycle: 389 Defect Energy: 76.33564

Cycle: 390 Defect Energy: 76.09697

Cycle: 391 Defect Energy: 76.01007

Cycle: 392 Defect Energy: 76.01004

Cycle: 393 Defect Energy: 76.00984

Cycle: 394 Defect Energy: 75.98272

Cycle: 395 Defect Energy: 75.98013

Cycle: 396 Defect Energy: 75.95997

Cycle: 397 Defect Energy: 75.95751

Cycle: 398 Defect Energy: 75.95687

** Hessian calculated **

Cycle: 399 Defect Energy: 75.91271

Cycle: 400 Defect Energy: 75.6715

Cycle: 401 Defect Energy: 75.58404

Cycle: 402 Defect Energy: 75.58401

Cycle: 403 Defect Energy: 75.5838

Cycle: 404 Defect Energy: 75.55668

Cycle: 405 Defect Energy: 75.5541

Cycle: 406 Defect Energy: 75.53374

Cycle: 407 Defect Energy: 75.53135

Cycle: 408 Defect Energy: 75.53063

** Hessian calculated **

Cycle: 409 Defect Energy: 75.48602

Cycle: 410 Defect Energy: 75.24231

Cycle: 411 Defect Energy: 75.15429

Cycle: 412 Defect Energy: 75.15427

Cycle: 413 Defect Energy: 75.15404

Cycle: 414 Defect Energy: 75.12683

Cycle: 415 Defect Energy: 75.12423

Cycle: 416 Defect Energy: 75.10368

Cycle: 417 Defect Energy: 75.10136

Cycle: 418 Defect Energy: 75.10055 **

Hessian calculated **

Cycle: 419 Defect Energy: 75.05536

Cycle: 420 Defect Energy: 74.80908

Cycle: 421 Defect Energy: 74.72048

Cycle: 422 Defect Energy: 74.72046

Cycle: 423 Defect Energy: 74.72021

Cycle: 424 Defect Energy: 74.69287

Cycle: 425 Defect Energy: 74.69027

Cycle: 426 Defect Energy: 74.66951

Cycle: 427 Defect Energy: 74.66725

Cycle: 428 Defect Energy: 74.66635

** Hessian calculated **

Cycle: 429 Defect Energy: 74.62051

Cycle: 430 Defect Energy: 74.37164

Cycle: 431 Defect Energy: 74.28249

Cycle: 432 Defect Energy: 74.28247

Cycle: 433 Defect Energy: 74.2822

Cycle: 434 Defect Energy: 74.25481

Cycle: 435 Defect Energy: 74.2522

Cycle: 436 Defect Energy: 74.23121

Cycle: 437 Defect Energy: 74.22902

Cycle: 438 Defect Energy: 74.22802

** Hessian calculated **

Cycle: 439 Defect Energy: 74.18145

Cycle: 440 Defect Energy: 73.93

Cycle: 441 Defect Energy: 73.84028

Cycle: 442 Defect Energy: 73.84027

Cycle: 443 Defect Energy: 73.83998

Cycle: 444 Defect Energy: 73.81254

Cycle: 445 Defect Energy: 73.80995

Cycle: 446 Defect Energy: 73.78872

Cycle: 447 Defect Energy: 73.78659

Cycle: 448 Defect Energy: 73.78548

** Hessian calculated **

Cycle: 449 Defect Energy: 73.73805

Cycle: 450 Defect Energy: 73.48391

Cycle: 451 Defect Energy: 73.3936

Cycle: 452 Defect Energy: 73.39358

Cycle: 453 Defect Energy: 73.39327

Cycle: 454 Defect Energy: 73.36567

Cycle: 455 Defect Energy: 73.36307

Cycle: 456 Defect Energy: 73.34158

Cycle: 457 Defect Energy: 73.33952

Cycle: 458 Defect Energy: 73.33828

** Hessian calculated **

Cycle: 459 Defect Energy: 73.28989

Cycle: 460 Defect Energy: 73.03301

Cycle: 461 Defect Energy: 72.94214

Cycle: 462 Defect Energy: 72.94212

Cycle: 463 Defect Energy: 72.94179

Cycle: 464 Defect Energy: 72.91414

Cycle: 465 Defect Energy: 72.91154

Cycle: 466 Defect Energy: 72.88978

Cycle: 467 Defect Energy: 72.88778

Cycle: 468 Defect Energy: 72.88641

** Hessian calculated **

Cycle: 469 Defect Energy: 72.83698

Cycle: 470 Defect Energy: 72.57736

Cycle: 471 Defect Energy: 72.48589

Cycle: 472 Defect Energy: 72.48588

Cycle: 473 Defect Energy: 72.48552

Cycle: 474 Defect Energy: 72.45767

Cycle: 475 Defect Energy: 72.45506

Cycle: 476 Defect Energy: 72.43299

Cycle: 477 Defect Energy: 72.43106

Cycle: 478 Defect Energy: 72.42953

** Hessian calculated **

Cycle: 479 Defect Energy: 72.37891

Cycle: 480 Defect Energy: 72.11643

Cycle: 481 Defect Energy: 72.02438

Cycle: 482 Defect Energy: 72.02437

Cycle: 483 Defect Energy: 72.02398

Cycle: 484 Defect Energy: 71.99604

Cycle: 485 Defect Energy: 71.99343

Cycle: 486 Defect Energy: 71.97105

Cycle: 487 Defect Energy: 71.96918

Cycle: 488 Defect Energy: 71.96747

** Hessian calculated **

Cycle: 489 Defect Energy: 71.91554

Cycle: 490 Defect Energy: 71.65015

Cycle: 491 Defect Energy: 71.5575

Cycle: 492 Defect Energy: 71.55749

Cycle: 493 Defect Energy: 71.55708

Cycle: 494 Defect Energy: 71.52893

Cycle: 495 Defect Energy: 71.52632

Cycle: 496 Defect Energy: 71.50359

Cycle: 497 Defect Energy: 71.50179

Cycle: 498 Defect Energy: 71.49989

** Hessian calculated **

Cycle: 499 Defect Energy: 71.44659

Cycle: 500 Defect Energy: 71.17826

Cycle: 501 Defect Energy: 71.08502

Cycle: 502 Defect Energy: 71.08501

Cycle: 503 Defect Energy: 71.08457

Cycle: 504 Defect Energy: 71.05629

Cycle: 505 Defect Energy: 71.05369

Cycle: 506 Defect Energy: 71.03059

Cycle: 507 Defect Energy: 71.02886

Cycle: 508 Defect Energy: 71.02674

** Hessian calculated **

Cycle: 509 Defect Energy: 70.97173

Cycle: 510 Defect Energy: 70.70026

Cycle: 511 Defect Energy: 70.60641

Cycle: 512 Defect Energy: 70.6064

Cycle: 513 Defect Energy: 70.60592

Cycle: 514 Defect Energy: 70.57739

Cycle: 515 Defect Energy: 70.57477

Cycle: 516 Defect Energy: 70.55125

Cycle: 517 Defect Energy: 70.54961

Cycle: 518 Defect Energy: 70.54722

** Hessian calculated **

Cycle: 519 Defect Energy: 70.49046

Cycle: 520 Defect Energy: 70.21588

Cycle: 521 Defect Energy: 70.12144

Cycle: 522 Defect Energy: 70.12143

Cycle: 523 Defect Energy: 70.12093

Cycle: 524 Defect Energy: 70.09239

Cycle: 525 Defect Energy: 70.08981

Cycle: 526 Defect Energy: 70.06582

Cycle: 527 Defect Energy: 70.06426

Cycle: 528 Defect Energy: 70.06156

** Hessian calculated **

Cycle: 529 Defect Energy: 70.00269

Cycle: 530 Defect Energy: 69.72512

Cycle: 531 Defect Energy: 69.63009

Cycle: 532 Defect Energy: 69.63008

Cycle: 533 Defect Energy: 69.62955

Cycle: 534 Defect Energy: 69.6006

Cycle: 535 Defect Energy: 69.59795

Cycle: 536 Defect Energy: 69.57345

Cycle: 537 Defect Energy: 69.57198

Cycle: 538 Defect Energy: 69.56892

** Hessian calculated **

Cycle: 539 Defect Energy: 69.50765

Cycle: 540 Defect Energy: 69.22702

Cycle: 541 Defect Energy: 69.13138

Cycle: 542 Defect Energy: 69.13138

Cycle: 543 Defect Energy: 69.13081

Cycle: 544 Defect Energy: 69.10167

Cycle: 545 Defect Energy: 69.09901

Cycle: 546 Defect Energy: 69.07393

Cycle: 547 Defect Energy: 69.07257

Cycle: 548 Defect Energy: 69.06909

** Hessian calculated **

Cycle: 549 Defect Energy: 69.00524

Cycle: 550 Defect Energy: 65.62941

Cycle: 551 Defect Energy: 65.62941

** Hessian calculated **

Cycle: 552 Defect Energy: 65.46188

Cycle: 553 Defect Energy: 65.36345

Cycle: 554 Defect Energy: 65.35853

Cycle: 555 Defect Energy: 65.35435

Cycle: 556 Defect Energy: 65.35394

Cycle: 557 Defect Energy: 65.35073

Cycle: 558 Defect Energy: 65.33831

Cycle: 559 Defect Energy: 65.31955

Cycle: 560 Defect Energy: 65.27123

Cycle: 561 Defect Energy: 65.25121

** Hessian calculated **

Cycle: 562 Defect Energy: 65.24991

Cycle: 563 Defect Energy: 65.04783

Cycle: 564 Defect Energy: 64.98654

Cycle: 565 Defect Energy: 64.97215

Cycle: 566 Defect Energy: 64.96557

Cycle: 567 Defect Energy: 64.93716

Cycle: 568 Defect Energy: 64.93345

Cycle: 569 Defect Energy: 64.9293

Cycle: 570 Defect Energy: 64.89033

Cycle: 571 Defect Energy: 64.86134

** Hessian calculated **

Cycle: 572 Defect Energy: 64.85935

Cycle: 573 Defect Energy: 64.66255

Cycle: 574 Defect Energy: 64.60385

Cycle: 575 Defect Energy: 64.59103

Cycle: 576 Defect Energy: 64.58594

Cycle: 577 Defect Energy: 64.54627

Cycle: 578 Defect Energy: 64.54599

Cycle: 579 Defect Energy: 64.54595

Cycle: 580 Defect Energy: 64.526

Cycle: 581 Defect Energy: 64.50613

** Hessian calculated **

Cycle: 582 Defect Energy: 64.50519

Cycle: 583 Defect Energy: 64.31252

Cycle: 584 Defect Energy: 64.25538

Cycle: 585 Defect Energy: 64.243

Cycle: 586 Defect Energy: 64.2384

Cycle: 587 Defect Energy: 64.19023

Cycle: 588 Defect Energy: 64.19016

Cycle: 589 Defect Energy: 64.18922

Cycle: 590 Defect Energy: 64.18215

Cycle: 591 Defect Energy: 64.17481

** Hessian calculated **

Cycle: 592 Defect Energy: 64.1748

Cycle: 593 Defect Energy: 63.98289

Cycle: 594 Defect Energy: 63.9266

Cycle: 595 Defect Energy: 63.91368

Cycle: 596 Defect Energy: 63.90875

Cycle: 597 Defect Energy: 63.85537

Cycle: 598 Defect Energy: 63.85519

Cycle: 599 Defect Energy: 63.85381

Cycle: 600 Defect Energy: 63.85061

Cycle: 601 Defect Energy: 63.84753

** Hessian calculated **

Cycle: 602 Defect Energy: 63.84741

Cycle: 603 Defect Energy: 63.65241

Cycle: 604 Defect Energy: 63.59674

Cycle: 605 Defect Energy: 63.58284

Cycle: 606 Defect Energy: 63.57711

Cycle: 607 Defect Energy: 63.51934

Cycle: 608 Defect Energy: 63.51923

Cycle: 609 Defect Energy: 63.51849

Cycle: 610 Defect Energy: 63.51652

Cycle: 611 Defect Energy: 63.51444

** Hessian calculated **

Cycle: 612 Defect Energy: 63.51427

Cycle: 613 Defect Energy: 63.31981

Cycle: 614 Defect Energy: 63.26499

Cycle: 615 Defect Energy: 63.24984

Cycle: 616 Defect Energy: 63.24299

Cycle: 617 Defect Energy: 63.18049

Cycle: 618 Defect Energy: 63.18047

Cycle: 619 Defect Energy: 63.18038

Cycle: 620 Defect Energy: 63.1791

Cycle: 621 Defect Energy: 63.17739

** Hessian calculated **

Cycle: 622 Defect Energy: 63.17731

Cycle: 623 Defect Energy: 62.98532

Cycle: 624 Defect Energy: 62.93146

Cycle: 625 Defect Energy: 62.91492

Cycle: 626 Defect Energy: 62.90672

Cycle: 627 Defect Energy: 62.83878

Cycle: 628 Defect Energy: 62.83875

Cycle: 629 Defect Energy: 62.83861

Cycle: 630 Defect Energy: 62.83799

Cycle: 631 Defect Energy: 62.8367

** Hessian calculated **

Cycle: 632 Defect Energy: 62.8367

Cycle: 633 Defect Energy: 62.6477

Cycle: 634 Defect Energy: 62.59672

Cycle: 635 Defect Energy: 62.5787

Cycle: 636 Defect Energy: 62.569

Cycle: 637 Defect Energy: 62.49498

Cycle: 638 Defect Energy: 62.4948

Cycle: 639 Defect Energy: 62.49362

Region 1 - region 1 = 237.6224 eV

Region 1 - region 2a (unrelaxed) =13.61886 eV

Region 1 - 2a (relaxed - correction) = 191.9488 eV

Region 1 (Total) = 443.1901 eV

Region 2a = -380.697 eV

Region 2b = 0.00000000 eV

Total defect energy = 62.49283 eV

Timing analysis for GULP :

Task / Subroutine Time (Seconds)

Calculation of real space energy and derivatives 0.008

Calculation of real space energy using symmetry 0.008

Calculation for region 1 energy and derivatives (2-b) 31118.66

Calculation for region 2a energy 92144.27

Total CPU time 177201.9

The calculation result was optimized through the calculation process of 642 cycles. Based on Eq.6-5, the expected number of defects is 44. The local charge between cations and anions is balanced. Those expected data agreed with the calculation results of output file in Table 6-2(b). Since the value of $\sum E_{isolated}$ for cluster model 4 which is calculated by Table 6-1 is 354.6696 (eV), the calculated binding energy (ΔE_b) for cluster model 4 is 6.64 (eV) (i.e. ΔE_b = (354.6696 – 62.49283)/44) = 6.64).

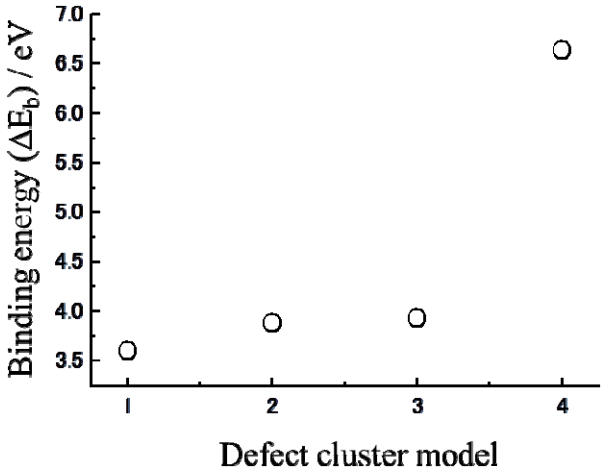

Figure 6-3 Calculated binding energies for defect cluster models (i.e. model 1 to model 4).

Figure 6-3 summarized the binding energies which were calculated by using the data of Tables 6-2 (a) to 6-2 (c). This figure indicates that the defect cluster model 1 is bulding unite for development of clusters and the defect cluster model 3 is the most stable defect clsuters in Pt-CeO_x nanowire interface.

In the defect model of the present work, we assumed that the oxygen defect configulation follows the defect strucutre of C-type rare earth strucutre. To confirm the validity of this assumption, the configulation of oxygen defect in model 3 was slightly changed as shown in Figure 6-4. In Fig.6-4, the oxygen defect configulation in region IV is just copy of that in region I. It is not equal to the oxygen defect configulation in C-type rare earth strucutre.

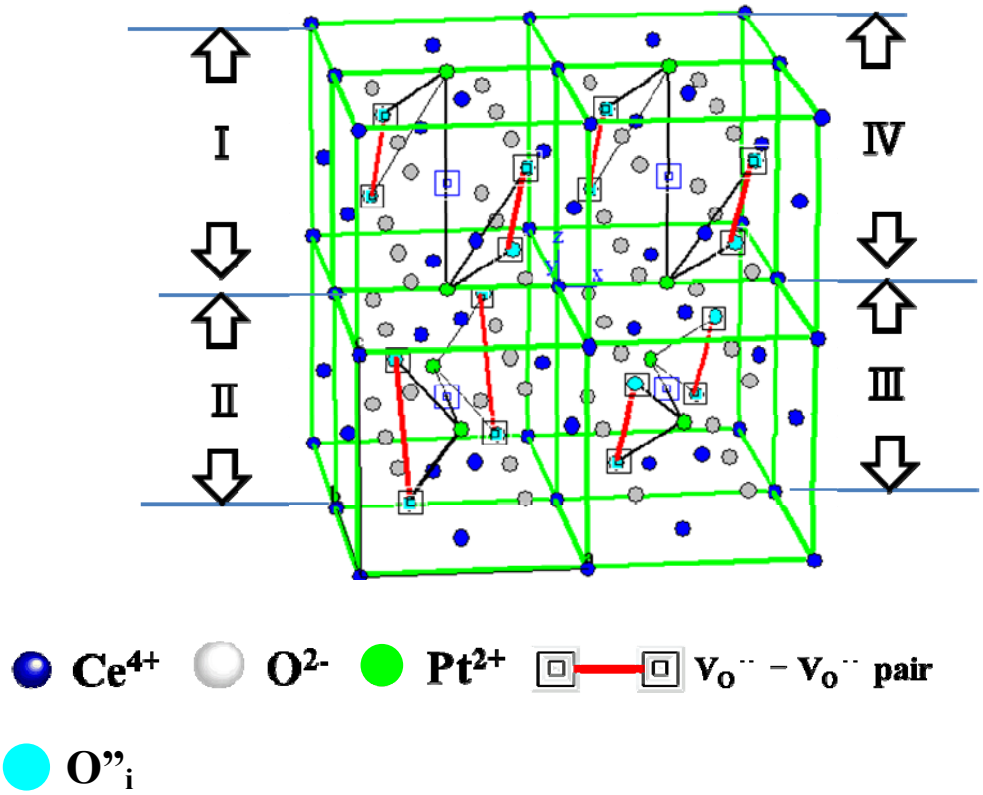

Figure 6-4 Defect cluster model 4’ with incorrect oxygen defect configulation as compared with C-type rare earth strucutre.

Based on this defect cluster model 4’, the binding energy were calculated. The obtained binding energy was 3.92(7) eV which is almost same to the binding energy calculated for defect cluster model 3. The binding energy for defect cluster model 4’ is plotted in Figure 6-4 togather with the binding energies for defect clutser model 1, model 2 and model 3 in Figure 6-5. This figure

cleary indicates that the the oxygen defect configulation in Pt-CeO_x nanowire follows the defect strucutre of C-tyepe rare earth strucutre, as shown in Figure 6-6.

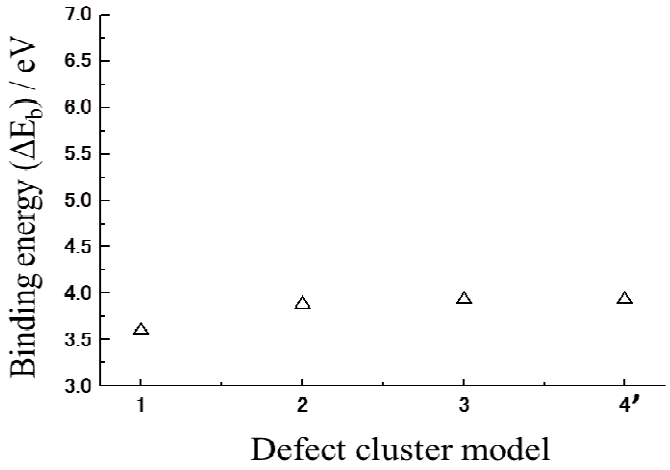

Figure 6-3 Calculated binding energies for defect cluster models (i.e. model 1 to model 4').

(a) (b)

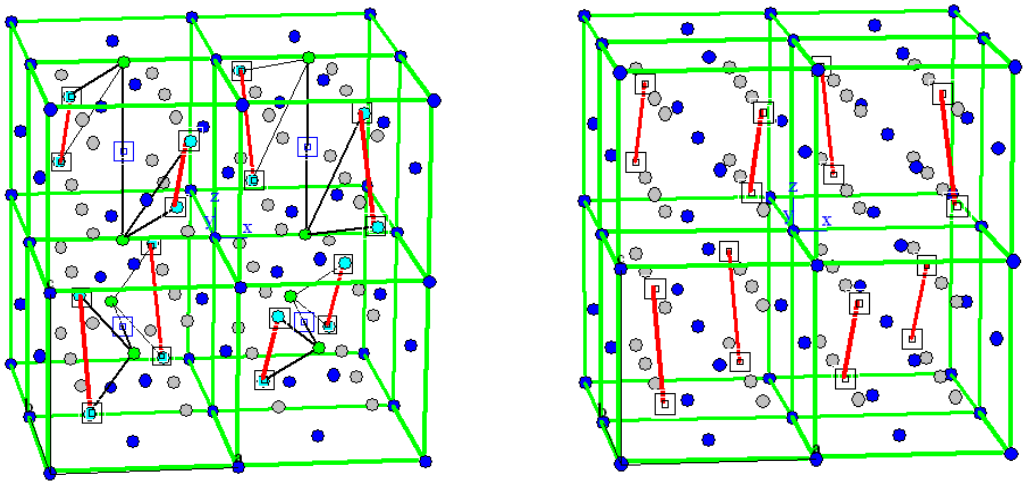

Figure 6-4 Defect cluster model 4 (a) and C-type rare earth strucutre (b). Symbols in the figure are as same as Figure 6-4.

Based on all defect simulation results, it is concluded that small shift of oxygen from lattice site (i.e. 0.05Å) makes interstitial oxygen defect and this interstitial oxygen site makes defect clusters stable in the fluroite lattice in the Pt-CeO_x nanowire interface.

The present atomistic simulation partially supported the conclusion in Chapter 4 and Chapter 5 of the presnet thesis work. Based on the atomistic simulation results, the electrochemical oxidation of oxygen site of the CeO_x lattice in Pt-CeO_x nanowire interface (i.e. $\mathbf{O_O^x + 2e^- => O''_i}$) can be assumed as well as electrochemical oxidation of Ce^{4+} site of the CeO_x lattice in Pt-CeO_x nanowire interface (i.e. $Ce^{4+} + \mathbf{e^-} => Ce^{3+}$) which was shown in the conclusion of Chapter 4. Also, the electrochemical reduction of interstitial oxygen site (i.e. $\mathbf{O''_i => O_O^x + 2e^-}$) can be assumed as well as electrochemical reduction of Ce^{3+} site of the CeO_x lattice in Pt-CeO_x naowire interface (i.e. $Ce^{3+} => Ce^{4+} + e^-$) which was shown in the conclusion of Chapter 5. However, more detail defect structure simulation for top surface area (from first layer to 5^{th} layer of sureface) should be performed by using similar atomistic simulation. After defect interface structure which includes both sureface area and deeper area was fully examined, the crystallographic information about the Pt-CeO_x nanowire interface has to be considered for calculation of the band structure and density of state (DOS) which can be calculated by using first priciple method. Based on the calculation results, ideal EELS profiles for oxygen K-edge spectra and Ce $M_{4,5}$-edge spectra will be fixed. Then, the effect of Pt-CeO_x naowire interface formation on the charge transfer phenomena will become clear.

Based on the atomistic simulation results about Pt-CeO_x nanowire interface, the preliminary design concept has been developed. It is expected that perfect desgin concept will be developed by continuous work based on the results of present thesis works.

6-3 Conclusion

In the Chapter 6, we proposed the defect cluster model based on XPS and EELS analysis data. Frenkel defect type cluster model was considered in the presnet chapter. It is because Pt–CeO_x nanowire interface mainly consists of Ce^{4+} and Pt^{2+} species. Based on the proposed model, the binding energies were calculated by using atomistic simulation with GULP code. The present atomistic simulation results indicate that the interstitial oxygen defect site is easily formed in the fluorite lattice by dissolution of Pt^{2+} cations into CeO_x lattice. It is because the shift of oxygen from lattice site to interstitial site is just 0.05Å. This sift of oxygen atom position in the CeO_x lattice (i.e. $\mathbf{O''_i <=> O_O^x + 2e^-}$) would be much easier than the formation of shcottky defect of oxygen by the electrochemical redox reaction between Ce^{3+} and Ce^{4+} (i.e. $\mathbf{Ce^{3+} <=> Ce^{4+} + e^-}$) in CeO_x lattice. The strong ligand mechanim for enhancement of methanol electro-oxidation reaction on Pt (in Chapter 4) and oxygen reduction reaction on Pt (in Chapter 5) would be conspecuously improved by the electrochemical oxidation and reduction of lattice defects in CeO_x in Pt and CeO_x nanowire interface on Pt. It is concluded that the present atomistic simuation results partially supported the conclusion of Chapter 4 and Chapter 5. The experimental results in Chapter 6 suggest that the design of Frenkel type defect strucutre in Pt and CeO_x interface is key for the enhancement of anode and cathode properties in fuel cell reaction.

Since electron is localized on Ce^{3+} in CeO_x and electrical strucutre of CeO_x with Ce^{3+} and Ce^{4+} cations becomes heterogeneous, the band structure calculation for the defect interface which consists of CeO_x with Ce^{3+} and Ce^{4+} will be complicated. Also, the atomistic simulation about surface structure of CeO_x is complicated as well. As a consequnece of this, the deeper area from top surface was concluded by using atomistic simulation method for development of conclusion

in the present thesis work. Based on the all experimental results, it is expected that high quality electro-catalysts will be able to fabricate by using present desgin concept.

References

1. A. Walsh, S M. Woodley, C. R. A. Catlow, A. A. Sokol, "Potential energy landscapes for anion Frenkel-pair formation in ceria and india" *Solid State Ionics*, **184**, pp.52–56(2011)

2. K.Fugane, T.Mori, D.R.Ou, P. Yan , F. Yei, H. Yoshikawa and J.Drennan, "Improvement of Cathode Performance on Pt-CeO_x by Optimization of Electrochemical Pretreatment Condition for PEFC Application", *Langmuir*, **28**, pp 16692-16700 (2012).

3. D. J. Binks and R. W. Grimes, "Incorporation of Monovalent Ions in ZnO and Their Influence on Varistor Degradation", *J. Am. Ceram. Soc*., **76**, pp. 2370- 2372 (1993).

4. V. Bulter, C. R. Catlow, B. E. Fender, and J. H. Harding, "Dopant ion radius and ionic conductivity in cerium dioxide", *Solid State Ionics*, **8**, pp. 109-113 (1983).

5. S. Vyas, R. W. Grimes, D. H. Gay, and A. L. Rohl, "Structure, Stability and Morphology of Stoichiometric Ceria Crystallites", *J. Chem. Soc. Faraday Trans*., **94**, pp. 427 -434(1998).

6. M. Born and J. E. Mayer, "Zur Gittertheorie der Ionenkristalle", *Z. Phys*., **75**, pp.1-5 (1932).

7. M. R. Welton and W. Barndt, "A LEED Study of the MgO (100) Surface: Identification of a Finite Rumple", *J. Phys. C,* **15**, pp.5691-5700 (1982).

8. P. P. Ewald, "Die Berchnung optischer und elektrostatischer Gitterpotentiale", *Ann. Phys*, **64**, pp. 253-257 (1921).

9. B. G. Dick and A. W. Overhauser, "Theory of the dielectric constants of alkali I halide crystals, *Phys. Rev*., **112**, 90-103 (1958).

10 .G. V. Lewis and C. R. Catlow," Potential models for ionic oxides", *J. Phys. C*, **18**, pp.1149 - 1161(1985).

Chapter 7 Conclusion

In the present thesis, the preparation and characterization of hetero-interface between Pt and CeO_x nanowires on Pt were performed and influence of the formation of Pt-CeO_x nanowire interface on Pt on the improvement of anode and cathode properties in fuel cell reactions was discussed.

In the chapter 3, I discussed about the growth process of CeO_x nanowire. In the first step of the formation process of CeO_x nanowire, the formation of micelle like structure which consists of soft template CTAB, $CeCl_3$ and urea was observed and gentle oxidation of $CeCl_3$ gave rise $Ce(OH)_3$ in that micelle like structure. Eventually, fine CeO_x nanowires were formed through slow oxidation of Ce $(OH)_3$ in the micelle like structure by using alcohothermal process. After preparation of CeO_x nanowire, TEM analysis indicates that $Ce(OH)_3$ species were formed on the CeO_x nanowire in the reducing process and covered the surface of CeO_x nanowire. Since $Ce(OH)_3$ layer which covered the CeO_x nanowire surface shows the basic property in the aqueous solution as well as $(OH)^-$ species on CeO_x nanowire, it is concluded that K_2PtCl_4 salt as resources of Pt particle is sandwiched between aforementioned $Ce(OH)_3$ layer and CeO_x nanowire surface. The interface between $Ce(OH)_3$ layer and CeO_x nanowire surface would be acid–base reaction space at atomic scale for fabrication of large amount of Pt-CeO_x nanowire interface.

In contrast, the reaction space on previously reported Pt-CeO_x nanoparticle/C was limited to the contact point of Pt nanoparticle and CeO_x nanoparticle (i.e. point contact between Pt and CeO_x). So, after Pt loading procedure, the Pt particles were captured by surface space of CeO_x nanowire due to the acid-base interaction at the interface.

The large amount of Pt-CeO_x nanowire interface on Pt was fabricated in the Chapter 3 for application of electro-catalysis in the fuel cell reaction. In other words, the surface of CeO_x

nanowire can be active nano-reaction stage for fabrication of Pt-CeO_x interface and provide the surface of electro-catalysts the large amount of Pt-CeO_x interface on Pt as active site. That is unique role of CeO_x nanowire which cannot be observed on the surface of nano-sized CeO_x particles**.** Also, it is concluded that the Pt-CeO_x nanowire interface is activated by the electro-chemical pretreatment process for removal of impurities such as $Ce(OH)_3$ from Pt-CeO_x nanowire/C surface and enhancement of anode and cathode properties in the fuel cell reactions on Pt is expected by formation of Pt-CeO_x nanowire interface.

To develop the conclusion in Chapter 3, influence of difference of electrochemical pretreatment condition on the surface composition and crystal phase of Pt-CeO_x interface on Pt was examined. After the electrochemical pretreatment of Pt-CeO_x nanowire/C surface, the main species of Ce cation in the Pt-CeO_x nanowire interface was Ce^{4+} which is quite different from Pt loaded CeO_x nanoparticle/C case. Based on experimental results, it is concluded that Pt-CeO_x nanowire interface which has different defect structure as compared with Pt-CeO_x nanoparticle interface in Pt loaded CeO_x particles/C was formed and it contributes to improvement of methanol electro-oxidation reaction activity and oxygen reduction reaction activity on Pt.

From the experimental results in Chapter 4, I concluded that the formation of interface between Pt and CeO_x contributed to the improvement of the electrochemical active surface area (EASA) and methanol electro-oxidation property on Pt. In the case of 5wt% Pt loaded CeO_x nanowire/C, the observed EASA was approximately 5 times higher than 5wt% Pt loaded CeO_x nanoparticles/C. Also, the amount of Pt in Pt-CeO_x nanowire/C was reduced without decrease of activity of methanol electro-oxidation reaction on Pt-CeO_x nanowire/C as compared with Pt-CeO_x nanoparticle/C. Based on the experimental results about the improvement of methanol electro-oxidation activity which was observed on 5wt% Pt-CeO_x nanowire/C, the multifunction

such as electrochemical reduction reaction of both Ce^{4+} (i.e. $\mathbf{Ce^{4+} + e^{-} => Ce^{3+}}$) and lattice oxygen (i.e. $\mathbf{1/2O_O^X + e^{-} => 1/2\ O^{"}_i}$) in Pt-CeO_x nanowire interface was assumed on the active site on Pt-CeO_x nanowire/C. Aforementioned two kinds of active sites around Pt which was formed by different incorporation of Pt in the CeO_x of the Pt-CeO_x nanowire interface would contribute to both of a lowering of onset potential of methanol electro-oxidation reaction and enhancement of current peak intensity ratio of forward and backward sweep (I_f / I_b) which were close to conventional PtRu/C. I concluded the basic mechanism of improvement of activities of methanol electro-oxidation reaction based on the results of the electrochemistry measurement and the in-situ FT-IR observation which is direct observation of methanol electro-oxidation reaction on Pt. In the previously reported Pt-CeO_x nano-particle/C system, CeO_x which is electrode support would convert CO_x by taking electron from Pt-(CO) species. It means that the electrochemical reduction reaction of Ce^{4+} to Ce^{3+} (i.e. $\mathbf{Ce^{4+} + e^{-} => Ce^{3+}}$) was assumed on the Pt–$CeO_x$ nanoparticle/C electro-catalysts. In the case of Pt-CeO_x nanoparticles/C, however, this proposed mechanism was not obviously observed in the activity measurement of methanol electro-oxidation reaction because of low level Pt-CeO_x interface area and small amount of Ce^{4+} species in the interface.

In contrast, Pt-CeO_x nanowire/C with high Pt-CeO_x interface area would have two kinds of Pt active sites whose activity could be promoted by both electrochemical reduction reactions of Ce^{4+} (i.e. $\mathbf{Ce^{4+} + e^{-} => Ce^{3+}}$) and lattice oxygen (i.e. $\mathbf{1/2O_O^X + e^{-} => 1/2O^{"}_i}$) on Pt-$CeO_x$ nanowire/C interface. It is concluded that lower onset potential of methanol electro-oxidation reaction and higher current peak intensity ratio of forward and backward sweep (I_f / I_b) which were close to the conventional PtRu/C were observed by the formation of multifunctional active

sites (i.e. two kinds of active sites by different incorporation of Pt in the CeO_x) on the Pt-CeO_x nanowire/C.

After confirming improvement in methanol electro-oxidation reaction activity of Pt in Pt loaded CeO_x nanowire/C, the influence of the formation of Pt-CeO_x nanowire interface on enhancement of activity of oxygen reduction reaction (ORR) on Pt was examined. In the case of Pt loaded CeO_x nanowire/C, Ce^{4+} species which is analyzed by using Ce M-edge spectra in EELS analysis mainly presented in the Pt-CeO_x nanowire interface which would contribute to enhancement of ORR activity on Pt in Pt-CeO_x nanowire/C. Since small ORR activity on 5wt% Pt-CeO_x nanowire/C surface was observed at higher potential region (i.e. above 0.95V (vs. RHE)), novel promotion effect of formation of Pt-CeO_x nanowire interface on improvement of ORR activity on Pt was concluded as compared with previously reported promotion effect of CeO_x in Pt-CeO_x nanoparticle/C. I assumed that two kinds of Pt active sites were formed by different incorporation of Pt into CeO_x lattice in Pt-CeO_x nanowire interface and they contributed to the promotion of charge transfer reaction for enhancement of Pt surface activity. Based on the experimental results, it is conclude that ORR activity on Pt is promoted by the electrochemical oxidation processes which are oxidation reaction of interstitial oxygen site (i.e. $\mathbf{1/2O''_i}$ => $\mathbf{1/2O_O^X + e^-}$) and oxidation reaction of Ce^{3+} cation (i.e. $\mathbf{Ce^{3+} => Ce^{4+} + e^-}$) on aforementioned which were expected in the Pt-CeO_x nanowire interface. Then, ORR activity observed for 5wt% Pt-CeO_x nanowire/C surface would become higher as compared with that on 5wt% Pt-CeO_x nanoparticle/C surface below 0.9V (vs. RHE).

To develop the conclusion in Chapter 4 and Chapter 5, the atomistic simulation for the development of defect structure model in the Pt-CeO_x nanowire interface was peformed in chapter 6 with help of GULP code. In Chapter 6, I proposed the defect cluster model based on

XPS and EELS analysis data. Frenkel defect type cluster model was considered in Chapter 6. It is because Pt–CeO_x nanowire interface mainly consists of Ce^{4+} and Pt^{2+} species. Based on the proposed model, the binding energies were calculated by using atomistic simulation with GULP code. The present atomistic simulation results indicate that the interstitial oxygen defect site is easily formed in the fluorite lattice by dissolution of Pt^{2+} cations into CeO_x lattice. It is because the shift of oxygen from lattice site to interstitial site is just 0.05Å. This shift of oxygen atom position in the CeO_x lattice (i.e. $\mathbf{O''_i} <=> \mathbf{O_O^x} + \mathbf{2e^-}$) would be much easier than the formation of shcottky defect of oxygen by the electrochemical redox reaction between Ce^{3+} and Ce^{4+} (i.e. $\mathbf{Ce^{3+}} <=> \mathbf{Ce^{4+}} + \mathbf{e^-}$) in CeO_x lattice. The strong ligand mechanim for enhancement of methanol electro-oxidation reaction activity on Pt (in Chapter 4) and oxygen reduction reaction activity on Pt (in Chapter 5) would be conspecuously improved by the electrochemical oxidation and reduction of lattice defects in CeO_x in Pt and CeO_x nanowire interface on Pt. It is concluded that the present atomistic simuation results partially supported the conclusion of Chapter 4 and Chapter 5. The experimental results in Chapter 6 suggest that the design of Frenkel type defect strucutre in Pt and CeO_x interface is key for the enhancement of anode and cathode properties in fuel cell reaction.

In the present thesis, the ehnacement of methaol electro-oxidation reaction activity and ORR activity on Pt were observed by formation of novel Pt-CeO_x nanowire interface which mainly consists of Ce^{4+} cation and highly ordered oxygen vancay of CeO_x lattice in the Pt-CeO_x nanowire interface. With the help of the atomistic simulation analysis, I examined the defect structure of Pt-CeO_x nanowire interface in the present thesis. Also, the role of aforemtioned novel defect interface strucutre on enhacement of electrocatalysis activity in the fuel cell reactions was concluded based on the resulsts of atomistic simulation. Based on all experimental

resulsts in the present thesis work, it is found that a design of bulk Frenkel defect strucutre in the hetero-interface of active metal Pt and CeO_x nanowire support is important for developing electrocatalysts with less Pt amount in the fuel cell reactions.